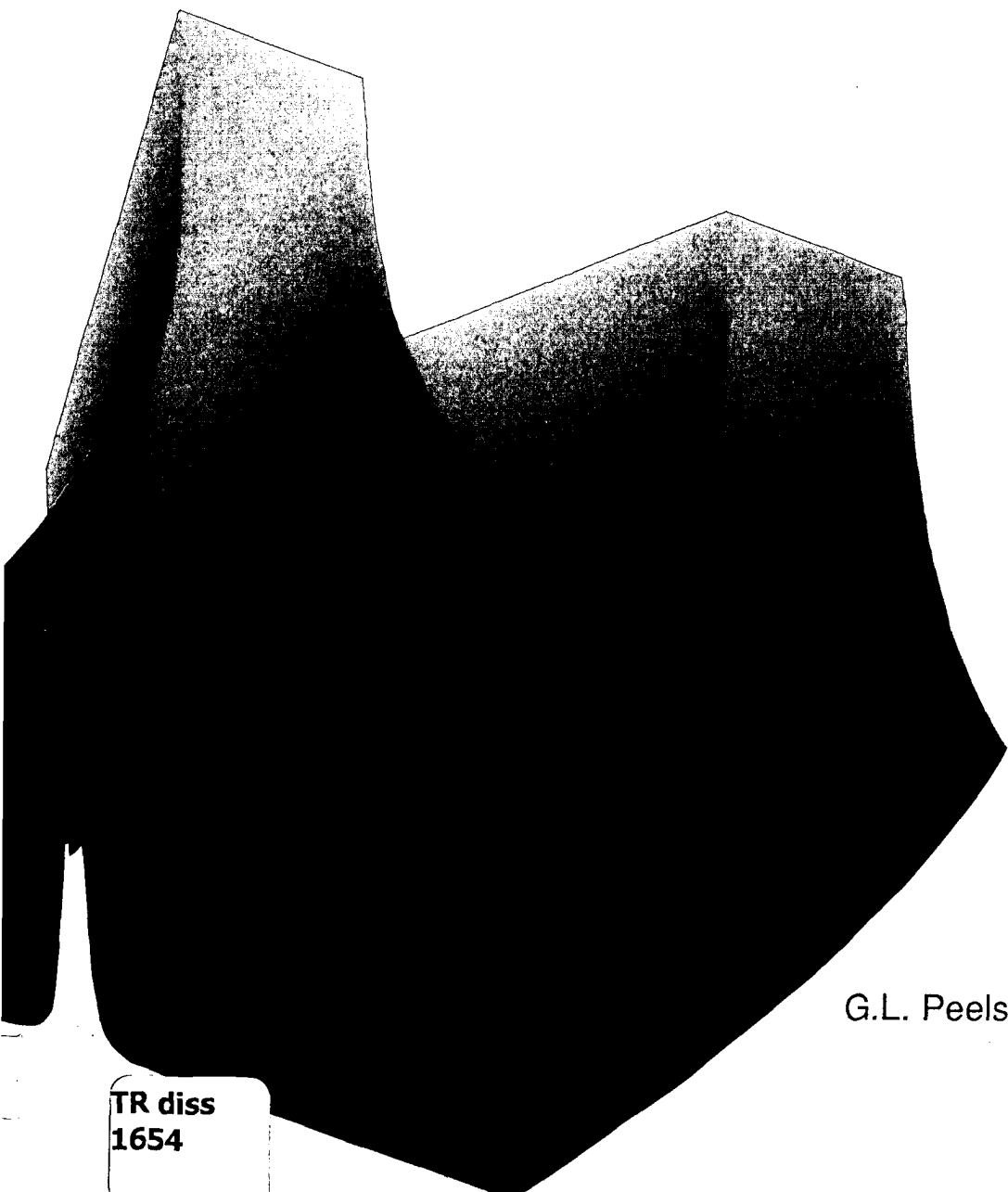


**TRUE AMPLITUDE WAVE FIELD EXTRAPOLATION  
WITH APPLICATIONS IN SEISMIC  
SHOT RECORD REDATUMING**



G.L. Peels

TR diss  
1654

True amplitude wave field extrapolation with applications  
in seismic shot record redatuming

65553

3078783

TR diss 658

**TRUE AMPLITUDE WAVE FIELD EXTRAPOLATION  
WITH APPLICATIONS IN SEISMIC  
SHOT RECORD REDATUMING**



**PROEFSCHRIFT**

ter verkrijging van de graad van doctor  
aan de Technische Universiteit Delft,  
op gezag van de Rector Magnificus,  
prof.dr.s. P.A. Schenck,  
in het openbaar te verdedigen  
ten overstaan van een commissie,  
aangewezen door het College van Dekanen  
op donderdag 15 september 1988 te 10.00 uur door

**GEORGE LAURENS PEELS**

geboren te Zoetermeer  
natuurkundig ingenieur

Gebotekst Zoetermeer / 1988

**TR diss  
1654**

Dit proefschrift is goedgekeurd door de promotor

prof.dr.ir. A.J. Berkhout

Copyright © 1988, by Jason Geosystems, Delft, The Netherlands.

All rights reserved. No part of this publication may be reproduced, stored in a retrieval system or transmitted in any form or by any means, electronic, mechanical, photocopying, recording or otherwise, without the prior written permission of the author, G.L. Peels, Jason Geosystems B.V., P.O. Box 596, 2600 AN Delft, The Netherlands.

CIP-DATA KONINKLIJKE BIBLIOTHEEK, DEN HAAG

Peels, George Laurens

True amplitude wave field extrapolation with applications in seismic shot record redatuming / George Laurens

Peels.-

[S.l. : s.n.] (Zoetermeer : Gebotekst). - III.

Thesis Delft. - With ref. - With summary in Dutch

ISBN 90-9002347-X

SISO 562 UDC 550.34 (043.3)

Subject headings: seismology, wave field extrapolation, redatuming

printed in The Netherlands by: N.K.B. Offset bv, Bleiswijk

*Opgedragen  
aan mijn ouders*

# LIST OF CONTENTS

	<b>INTRODUCTION</b> . . . . .	1
	0.1 Model driven processing . . . . .	2
	0.2 Wave propagation . . . . .	4
	0.3 The redatuming . . . . .	5
<b>1</b>	<b>A MODEL FOR THE OVERBURDEN WAVE PROPAGATION EFFECTS</b> . . . . .	7
	1.1 Introduction . . . . .	7
	1.2 The parameterization . . . . .	8
	1.3 The macro model . . . . .	10
<b>2</b>	<b>WAVE FIELD EXTRAPOLATION</b> . . . . .	31
	2.1 Introduction . . . . .	31
	2.2 Forward wave propagation . . . . .	32
	2.3 Interpretation of the Kirchhoff integral . . . . .	36
	2.4 A comparison of the Kirchhoff integral and the Rayleigh integral . . . . .	38
	2.5 The Green's function . . . . .	44
	2.6 Recursive versus non-recursive extrapolation . . . . .	49
	2.7 One-way versus two-way field extrapolation . . . . .	51
	2.8 A 2-D approximation for a 3-D world . . . . .	52
<b>3</b>	<b>INVERSE WAVE FIELD PROPAGATION</b> . . . . .	55
	3.1 Introduction . . . . .	55
	3.2 Inverse extrapolation through a planar homogeneous layer . . . . .	56
	3.3 Inverse extrapolation through an inhomogeneous medium . . . . .	60
	3.4 Inverse wave field extrapolation for arbitrarily inhomogeneous media . . . . .	69
	3.5 Recursive application of the full Kirchhoff integral for recursive inverse wave field extrapolation . . . . .	73

<b>4</b>	<b>THE REDATUMING</b>	91
4.1	The forward model	93
4.2	The target response $X$	97
4.3	The redatuming	100
4.4	Redatuming with the full Kirchhoff operator	104
4.5	Application of redatuming in layer replacement	108
4.6	Redatuming and migration	109
<b>5</b>	<b>APPLICATION OF THE REDATUMING</b>	113
5.1	The effects of geophone spread and spatial sampling on migration and redatuming	113
5.2	Strong dip in lateral velocity variations, a synthetic example	144
5.3	Dome structure, a synthetic example	150
5.4	A real data example	153
	<b>APPENDIX</b>	169
	<b>REFERENCES</b>	173
	<b>SUMMARY</b>	175
	<b>SAMENVATTING</b>	177
	<b>CURRICULUM VITAE</b>	179

# PREFACE

The laboratory of seismics and acoustics at Delft University has been involved in industry sponsored research into inversion techniques for detailed delineation of reservoirs. For these types of techniques high quality reflection data is required. The overburden wave propagation effects however, distort the reflection events from the target zone. A true zero offset section at a datum just over the target, without the overburden wave propagation effects, is to be preferred over a surface zero offset section. Therefore, several years ago research has been initiated into redatuming techniques at Delft University. Special focus was put on the preservation of the amplitude information in the redatuming, because of the reservoir delineation which would use the redatumed zero offset data.

Later on research activities into wave equation based 3-D depth migration, 3-D redatuming, multiple elimination and macro model verification have been intensified in the industry sponsored research project TRITON. I think the close cooperation between the people in this project has been very beneficial for research presented in this thesis and the other key research area's in TRITON.

I would like to thank my promotor prof. Berkhout for his indications of the directions of the research and the interesting discussions on the macro model. Special thanks are due to Kees Wapenaar for the many discussions and suggestions.

Furthermore I would like to thank the Marathon Oil company for providing me with the water tank data set and Ad van der Schoot for providing me with the different stacks for this data set. Also I would like to thank Jason Geosystems for allowing me to continue the work on my thesis after I had left the university. In preparing several of the figures for this thesis I had terrific help from Tiny van der Werff and Vladimir Budejicky for which I would like to thank them.

Delft, September 1988

---

## INTRODUCTION

In the search for fossil fuels surface measurements are carried out in order to determine the subsurface structure and rock properties. Various methods for doing these surface measurements are available. In the magnetic methods the subsurface structure is derived from small changes in the earth magnetic field. The gravitational methods use changes in the earth gravitational field to determine the subsurface structure. However these methods can only resolve large structural changes. The seismic method allows for small (down to meters) structural changes to be resolved from the measurements. In the seismic method a seismic source generates waves propagating into the subsurface. Since the subsurface is discontinuous with respect to the properties determining the wave propagation, the source waves are reflected at the structures in the subsurface. Therefore the measured wave field at the surface contains information on the structures in the subsurface. The acquisition geometry and signal to noise ratios however make an interpretation of the registered wave field in terms of a depth model very difficult. Extensive data processing of the registered wave field is carried out in order to obtain an image of the subsurface structures. The processed data is presented in a section. An interpreter uses this section together with other information to determine the location and size of possible hydrocarbon reservoirs or coal seams. A correct image with respect to the lateral and depth positioning of the structures as well as the strength of the reflectors is important for the correct delineation of the reservoir. An incorrect well location is very expensive both in terms of money for the oil company and career opportunities of the interpreter.

The registered wave field in seismic techniques is an 'image' of the subsurface in a space-time coordinate system. The vertical axis is the time and not depth. Going from time to depth requires the elimination of various wave propagation effects. The commonly used time migration will cause the reflection response to move both horizontally and vertically in the section. Also it will cause diffraction energy from diffractors to collapse. The result is however not yet an image in depth. The vertical axis is still time. A depth migration is computationally more expensive but it does produce an image in depth. This image is a map of the reflectivity properties of the whole subsurface area under investigation. However for the target zone high detail is required both in terms of reflectivity properties as well as elastic properties. With current acquisition techniques and migration techniques insufficient detail structure is resolved from the data. For this purpose inversion techniques have been developed such as proposed by van Riel and Berkhout [1985] and still are being refined and extended. These techniques aim at going beyond the resolution of the seismic data. Unfortunately reservoirs are situated up to several kilometers below the surface. So the reflection response which is input to these inversion techniques is distorted because of the overburden wave propagation effects. In order to have better quality input data for the inversion or detailed interpretation these overburden wave propagation effects should be eliminated.

In the redatuming procedure the surface data is brought to a new datum (figure 0.1). By choosing this new datum just over the target zone a clear and undistorted reflection response is obtained. The wave propagation effects of the overburden are eliminated. The redatuming should of course preserve the amplitude and travel time information of the surface data in order to obtain the true reflection response of the target. The key issues in the redatuming are the subsurface model and the elimination of the wave propagation effects. For the redatuming the approach of model driven processing is applicable.

## 0.1 MODEL DRIVEN PROCESSING

A seismic data processing sequence contains different types of processing. Most of these processing algorithms require only the data as input. Processing parameters are obtained by maximizing some coherency criterion. For the stacking processes, the stacking velocities are obtained by applying different stacking velocities to selected CMP panels. The velocity for which a reflection event is properly aligned after normal move out correction is the stacking velocity. For depth migration and redatuming an initial depth model is required before the actual processing takes place. These processing algorithms require both the data as well as a depth model as input. So the position of the reflectors is both input as well as output to the depth migration and redatuming algorithms. The apparent contradiction may be solved by identifying the requirements for the input depth model. It turns out that this input depth model is a sparse

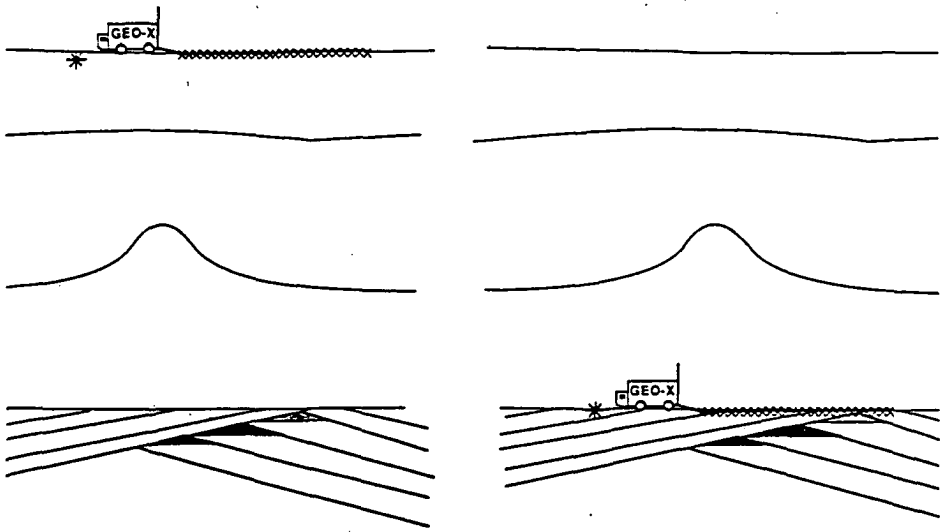


Figure 0.1 The purpose of redatuming is to bring down the acquisition surface to a level just over the area of interest. The overburden wave propagation effects are eliminated from the data.

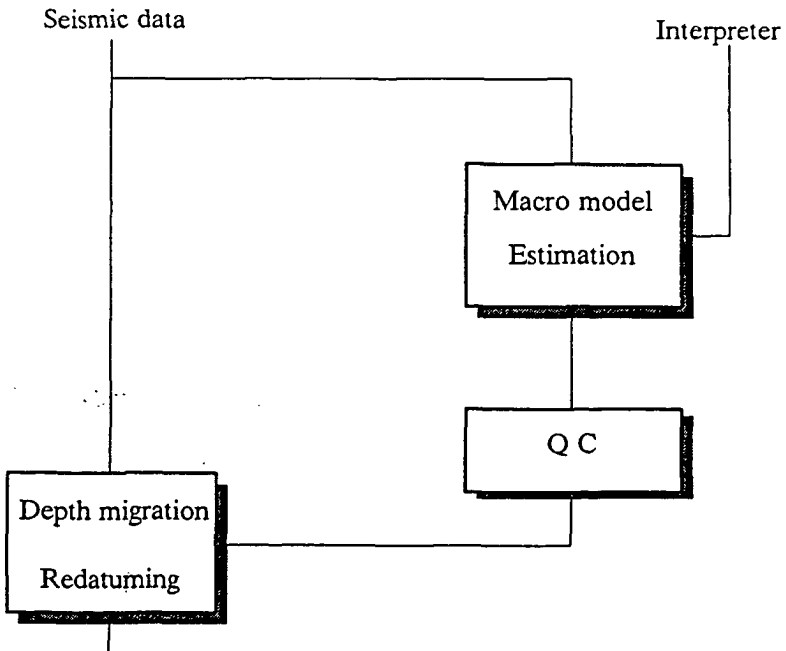


Figure 0.2 In the model driven processing the estimation of the macro model is carried out separately from the processing. If a good macro model has been found, the expensive processing takes place.

model and should be determined with special techniques. This sparse depth model, which we will call the macro subsurface model, is used to model the wave propagation through the subsurface. The approach in which the depth model is obtained separately from the actual processing will be referred to as model driven processing.

The model driven processing is schematically represented in figure 0.2. Input to the model driven processing is again only the seismic data. The depth model or macro model for the redatuming could be obtained with tomographic techniques. An interpreter should identify the major structures in the subsurface in for instance a stacked section. The tomographic techniques should estimate the true positions of these major structures in depth as well as the interval velocities. This macro model is a sparse model since it does not contain detailed structures such as thin layers. If the travel times modeled in the macro model correspond to the travel times of the main reflection events in the seismic data, the depth migration will yield an optimal result. So by examining the data mismatch between modeled reflection travel times and measured travel times the quality of the depth model may be examined. If the data mismatch is sufficiently small the depth migration result will be optimum. In this way only a single depth migration run is required.

The depth model used in the migration or redatuming is useful for an interpreter as well. The positions of the major structures and the interval velocities in this model helps the interpreter to determine the general geological structures in the area.

In chapter 1 of this thesis various properties of the macro model will be discussed. The medium properties determining the wave propagation and the reflection characteristics are separated. The macro model for describing the wave propagation effects contains the trend information from the acoustic velocity profile. The full elastic case has not been considered for this thesis. Various modeling experiments have been carried out to investigate the effects of detailed fluctuations in the velocity profile on the wave propagation properties.

## **0.2 WAVE PROPAGATION**

The wave propagation is a key issue for the redatuming. In chapter 2 wave propagation modeling operators are discussed. The wave propagation operators are based on the Kirchhoff integral. In the macro model a number of interfaces are identified which may be several wave lengths apart. The Kirchhoff integral allows for the wave field to be extrapolated over large distances in a single extrapolation step. The wave field extrapolation operators used in this thesis are based on the one-way wave equation. Although wave propagation based on the two-way wave equation is more accurate, the one-way extrapolation operators have been chosen because of their robustness. The Green's function and its relation to the wave field extrapolation will be discussed in this chapter as well. The freedom in choice of the Green's function is an

important tool in obtaining the most suited wave field extrapolation operator for specific geometries or applications.

In chapter 3 the inverse wave propagation is discussed. The wave field which has been registered by the geophones should be back propagated to bring it down to the new datum. Special attention has been paid to the preservation of amplitude information in the inverse wave field extrapolation. The commonly used matched inverse Rayleigh operator or Kirchoff approximation does not handle the amplitudes of the wave field properly. An inverse wave extrapolation operator which preserves the amplitude information in the inverse extrapolation is obtained by choosing an appropriate Green's function. If this integral is applied recursively in a layer to layer extrapolation, even the boundary conditions are incorporated. The transmission effects at acoustic impedance contrasts are automatically eliminated.

### 0.3 THE REDATUMING

The redatuming procedure is discussed in chapter 4. Firstly the forward model of a seismic dataset is discussed. In matrix notation a relation between the surface shots, the surface

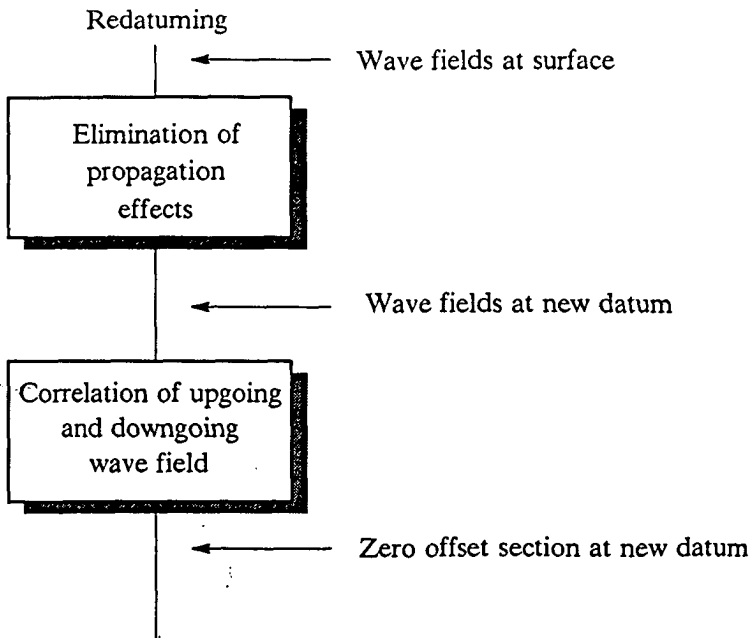


**Figure 0.3** In the redatuming surface shot records are brought down to the new datum through an inverse, wave field propagation. At the new datum a true zero offset section is obtained by correlation of up going and down going wavefields.

geophone data and the subsurface structures is determined. Through inversion of these equations a relation between the shot records at the surface and the shot records at the new datum is obtained. The redatuming procedure is outlined in figure 0.3. For the elimination of the wave propagation effects the wave field extrapolation operators derived in chapter 3 are used. Special attention has been paid to the data organization in the redatuming. Berryhill (1984) proposed a redatuming procedure which requires the data to be reorganized from a common shot gather configuration to a common receiver gather organization. This results in a huge overhead and tremendous input/output in an actual implementation, particularly if the method would be extended for 3-D applications. However in this thesis a shot record based redatuming is proposed. Each shot is redatumed separately, allowing for a highly efficient implementation and very well suited for parallel processing.

In chapter 5 the redatuming is applied to both synthetic as well as real data. In practice the geophone cable length is limited, resulting in a partly lost reflection response. In the experiments discussed in the first sections of chapter 4, the cable length and geophone spread is varied. Only part of the reflectivity information is reconstructed if limited surface data is considered. The synthetic redatuming experiments have been carried out on shot records obtained with finite difference modeling. The last experiment involves real data modeled in a water tank. The macro model for this data set has been obtained with travel time inversion. The redatuming resulted in a reconstruction of the zero offset section for the deepest reflector. The overburden wave propagation effects have been eliminated, resulting in a high quality section, which is superior over the surface zero offset section.

## 1

---

## A MODEL FOR THE OVERBURDEN WAVE PROPAGATION EFFECTS

### 1.1 INTRODUCTION

In the seismic experiment an acoustic wave field is sent into the earth in order to examine the subsurface structures. Since the wave field propagates through the subsurface, information about the subsurface may be extracted from the registered wave field. From the reflection of the wave field at the subsurface structures an image of the subsurface could be reconstructed. This image is not complete since not all of the structures are resolved from the seismic data. The dimensions of the smallest structures which can be resolved from the seismic data alone are comparable to the size of the seismic wavelet (figure 1.1). A model describing the wave propagation through the subsurface is important for the reconstruction of the subsurface structures. For the description of wave propagation through the subsurface the following problems are considered. From physical relations such as the equation of motion and the stress-strain relation a description of the wave propagation is found. This problem is considered in the next chapter. The other problem concerns the parameterization of the subsurface. Looking at the subsurface on a microscopic scale results in a very detailed description of the subsurface. This detail may not be significant for the wave propagation which is relevant for the migration or the redatuming problem. So the scale at which the subsurface is considered should be changed. If fewer detail is considered, the parameterization becomes more sparse. The purpose is to find a parameterization which is sufficient to model the wave propagation effects relevant for our problem.

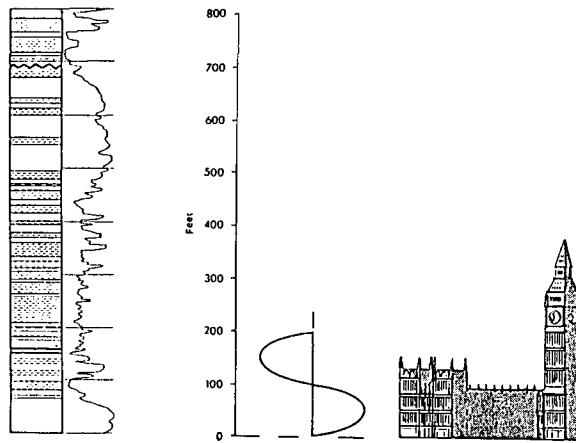


**Figure 1.1** The lithological log, a seismic wavelet and a well known building in London shown on the same scale, give some idea of the size of the structures which may be resolved from seismic data.

In this chapter a parameterization of the subsurface which is sufficient for describing the wave propagation effects is investigated. Both migration and redatuming techniques require the wave propagation effects to be eliminated.

An intelligent subsurface parameterization will allow for simplifications such that the propagation of the waves of interest is still described accurately enough. Because of the simplifications the mathematics become more simple and the inverse problem for the wave field back propagation is more easily found. The approach may no longer be exact, but if the errors are sufficiently small this is acceptable.

## 1.2 THE PARAMETERIZATION

For the modeling of the acoustic wave propagation through the earth a representation of this earth is required. The representation should be convenient and sufficient to describe the propagation effects which are of interest. A parameterization of the earth on a molecular scale could be chosen. The distribution of molecules is very dense compared to the seismic scale. So this parameterization is not useful since it is too elaborate. If we increase our scale another description or parameterization could be chosen. If we look at the earth through a microscope, fine layers and structure become visible. However this representation is still too detailed for most geophysical applications. A less detailed description is required. A visual inspection of a core

from a borehole also shows some fine layering. However these layers are still quite small compared to the seismic wavelet. In general an even more sparse representation or parameterization of the earth is taken for the geophysical applications (figure 1.2).

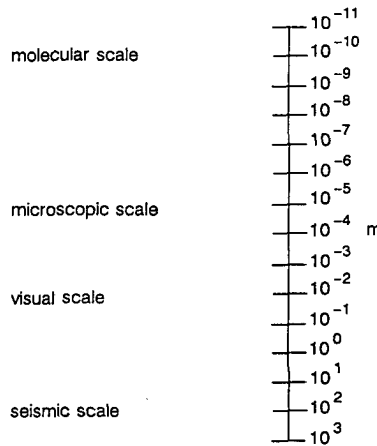


**Figure 1.2** Different scales could be considered for the parameterization of the medium. However a sparse, not to detailed representation is preferred for the evaluation of propagation effects.

In depth migration and inverse scattering type of applications, a representation of the velocity and density as a function of the spatial coordinates is chosen. Usually the detail which is incorporated into the velocity model does is larger than the seismic wavelet. Although the seismic scale is too coarse to contain all the detailed features which exist in the actual medium, the parameterization is an acceptable representation of the true medium for most geophysical applications.

In the case of the wave propagation through an overburden the propagation effects should be modeled. A parameterization should be chosen which is sufficient to describe the wave propagation effects. The macro model is defined to be a representation of the subsurface which satisfies this condition. A geological interpretation of the macro model is only of minor interest. So the representation does not need to have an exact relation with the true medium. In specific cases a stack of homogeneous layers has approximately the same propagation effects as a single layer with a velocity gradient. This stack of layers could be an acceptable parameterization,

although it does not reflect the true structure. So the parameterization is not intended to be a complete and accurate description of the true earth. It should only be sufficient to describe some effect related to the data. In molecular physics a similar approach is followed. Different models or representations of an atom exist. Different representations are used to describe different effects. The various models are not mutually exclusive. In the seismic case the macro model is used to describe the wave propagation. Other, more detailed representations should for instance be used for stratigraphic interpretations. In the next section a parameterization of the overburden specifically for the wave propagation will be discussed.

### 1.3 THE MACRO MODEL

In the previous section it has been argued that the parameterization of the overburden should allow for a sufficiently accurate description of the wave propagation effects. In the seismic reflection response the major events are related to strong impedance contrasts. Usually only few of these strong reflection events occur. So a parameterization of the subsurface consisting of several layers will be chosen.

From depth migration we know that a model of the earth consisting of a several layers with simple velocity profiles turns out to describe the wave propagation sufficiently well. The reflection is imaged correctly even for small structures ( in this case small is of the order of magnitude of the wave length). The velocity distribution in the layers may range from homogeneous to simple velocity gradients for most structures.

Since the macro model should have a parameterization which is sufficient to describe the wave propagation effects. These effects and the properties of the earth which determine the wave propagation should be investigated. For this purpose consider the following identification of the propagation effects in relation to the medium properties:

- The propagation properties which are determined by the trend in the medium properties of the earth. These properties determine the transmission effects of the medium.
- The reflectivity properties which are determined by the detail in the medium properties of the earth. These properties determine the reflection effects of the medium.

In order to extract the detail in the model or the trend information different estimation techniques should be used. The trend information can be obtained through tomographic techniques. Either the transmitted wave field is measured in order to estimate the trend information or offset information is used in surface experiments. The trend information is a sparse parameterization of the subsurface. Low frequency structural information is considered for this parameterization.

The detail in the model could be obtained through seismic depth migration or inverse scattering techniques. In general these techniques require the trend information as input as well as the seismic data itself. The wave propagation effects between the acquisition surface and the depth level of interest are eliminated before the reflectivity or the acoustic or elastic properties

are estimated. In general the trend information is more sparse than the detail. The detail contains the more high frequent structural information (figure 1.3). Unfortunately the trend information and the detail information which may be recovered from the seismic data is limited. The amount of detail is limited because the seismic sources are bandlimited and high frequent seismic waves are strongly attenuated. Furthermore not all of the trend information may be resolved from the seismic data because the reflected wave field is registered over a limited distance. Also the range of dips at which the wave fields travel through the subsurface is limited.

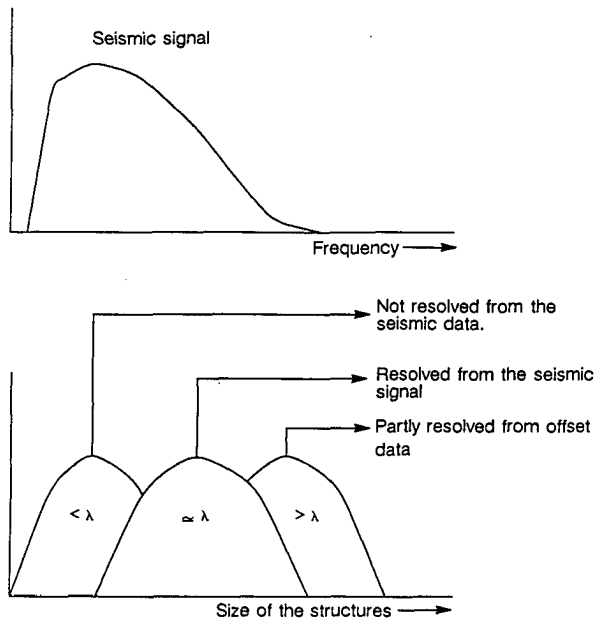


**Figure 1.3** The size of the structures in the subsurface in relation to the bandwidth of the seismic signal. Structures smaller than the seismic wavelet can not be resolved from the seismic data alone. Structures larger than the seismic wavelet can only be partly resolved from offset data.

In depth migration and redatuming techniques the wave field propagation through the overburden should be eliminated. In the case of migration the overburden are the structures overlying the depth level at which imaging should occur. In the case of redatuming the overburden are the structures overlying the new datum. The acquisition level is brought down from the surface to the new datum. In order to invert for the wave propagation effects of the overburden a parameterization of the overburden structures for the description of wave propagation effects of the overburden should be determined. The inverse problem of eliminating the wave propagation effects is solved in chapter 3 by inverting for the modeling relations. The

parameterization of the overburden should be adequate to describe the wave propagation effects through the overburden sufficiently well. For redatuming the reflection properties of the overburden are of no interest, since only the propagation needs to be inverted for. The reflection properties of the target zone below the overburden need to be determined. So only a *propagation model* of the overburden is required.

In order to obtain an adequate parameterization of the subsurface, the properties determining the wave propagation effects should be examined more closely. Therefore the acoustic impedance profiles will be considered. For the full elastic case all elastic parameters should be regarded. However for this thesis we limit ourselves to the acoustic case. Consider the velocity profile from figure 1.4.

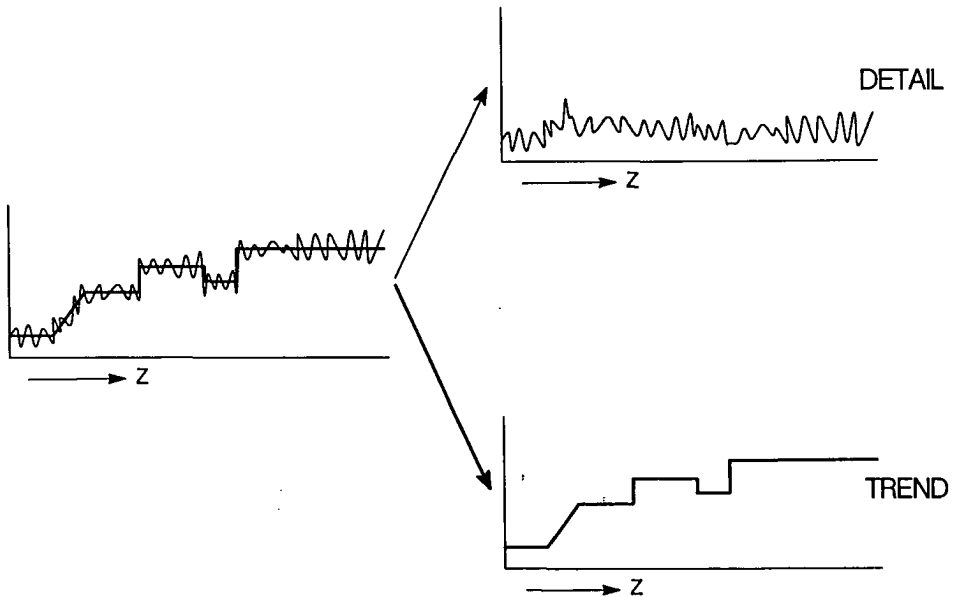


**Figure 1.4** The detail and trend information in a velocity profile are considered separately for their relation to the wave propagation.

The profile is very detailed compared to the wave length of the seismic signal. The detail goes even beyond the bandwidth of the seismic signal. The acoustic impedance profile also shows a trend. The travel time of the seismic events in the registered response are related to this

trend. The detail in the velocity function will average out in a zero travel time effect. The detailed variations in the acoustic impedance profile are related to the small reflection events in the response. Although a gradient in the velocity profile will cause the wave field to propagate back at turning planes, in practice most of the reflection occurs at sharp changes in acoustic impedance. In figure 1.5 the differentiation between properties determining the wave propagation and the properties determining the reflectivity has been visualized.

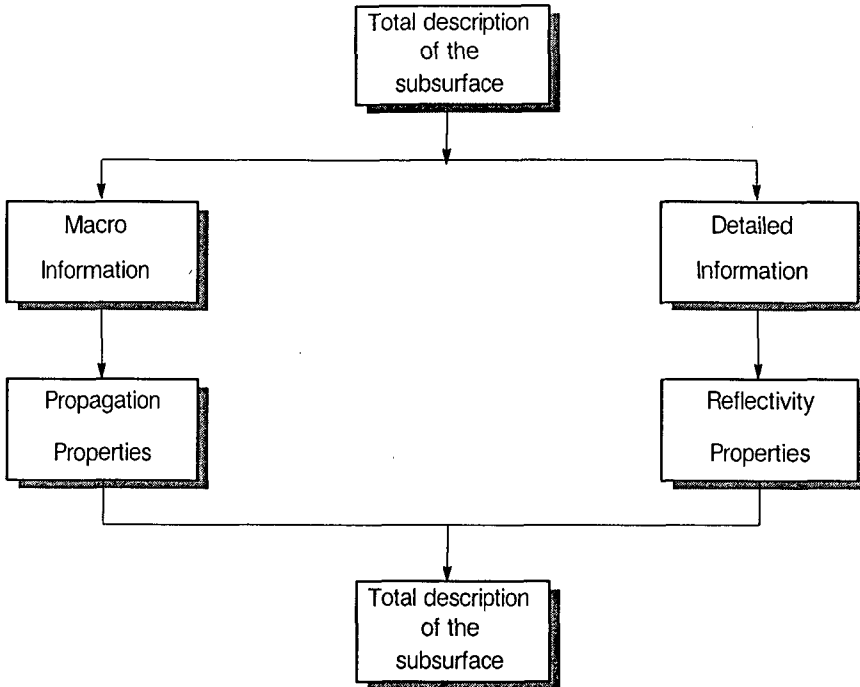


**Figure 1.5** The total description of the subsurface is split up in macro information and detail information. The macro information is related to the propagation properties and the detail information is related to the reflectivity properties.

The parameterization of the subsurface which is adequate to describe the propagation effects of the overburden requires only the trend in the acoustic impedance model to be considered. The subsurface models which sufficiently well describe the overburden wave propagation effects and are parameterized accordingly, will be referred to as macro models. These models may be obtained from the data with tomographic techniques such as travel time inversion as has been shown by Van der Made [1987]. The macro models may be considered to be a sparse parameterization of the true subsurface.

In order to verify that the trend information is sufficient to describe the wave propagation effects properly several modeling experiments have been carried out. These experiments are not

intended to be a sound proof of the assumption that the propagation properties are determined by the trend information, but serve as a set of cases to get a feeling for the relation between the (frequency) information in the velocity profiles and the effect on wave propagation. We expect that the size of the detail compared to the wave length of the seismic wave field influences the wave propagation. Also the type of perturbation such random detail and correlated detail will have different effects on the wave propagation. Therefore the effects for several types of model perturbations on the overburden wave propagation has been examined.

For the high frequency approximation the travel time for a wave field propagating through the perturbed velocity model is given by

$$\tau = \int \frac{1}{c} ds \quad , \quad (1.1)$$

where the integration takes place along the ray path  $s$ .

The velocity function contains the velocity trend  $c_0$  and the velocity detail  $\delta c$ .

$$c = c_0 + \delta c \quad . \quad (1.2)$$

Substitution in (1.1) gives

$$\tau = \int \frac{1}{c_0 + \delta c} ds \quad , \quad (1.3)$$

or

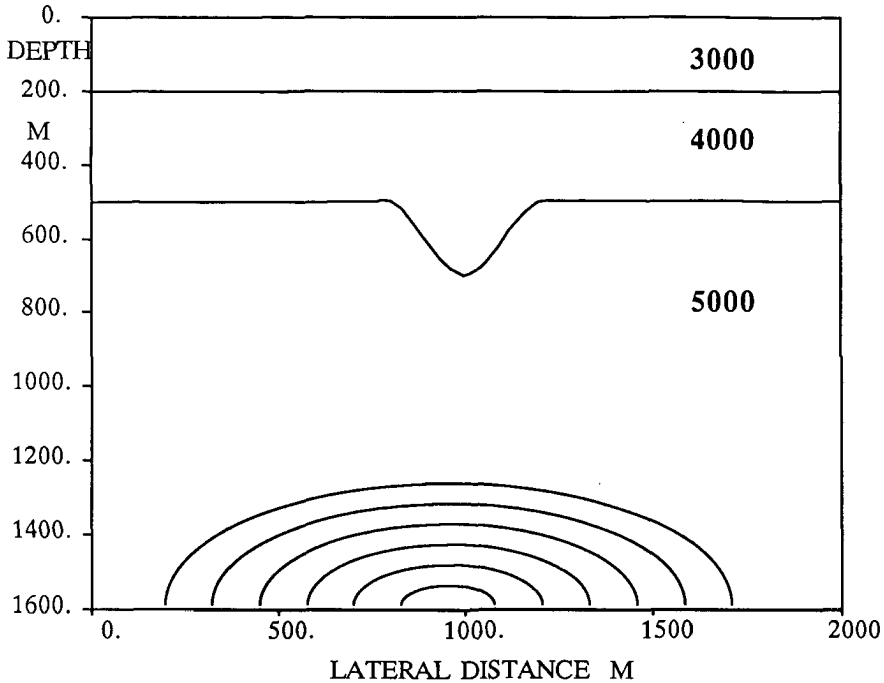
$$\tau = \int \frac{1/c_0}{1 + \delta c/c_0} ds \quad . \quad (1.4)$$

With  $\delta c \ll c_0$  this may be approximated by

$$\tau = \int \frac{1}{c_0} \left( 1 - \frac{\delta c}{c_0} \right) ds \quad . \quad (1.5)$$

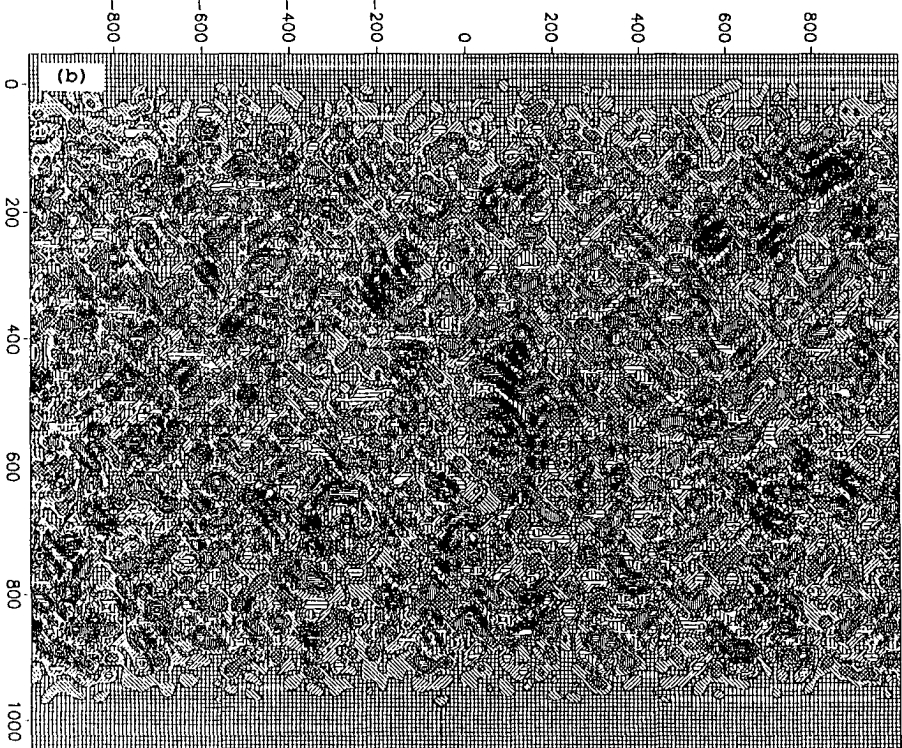
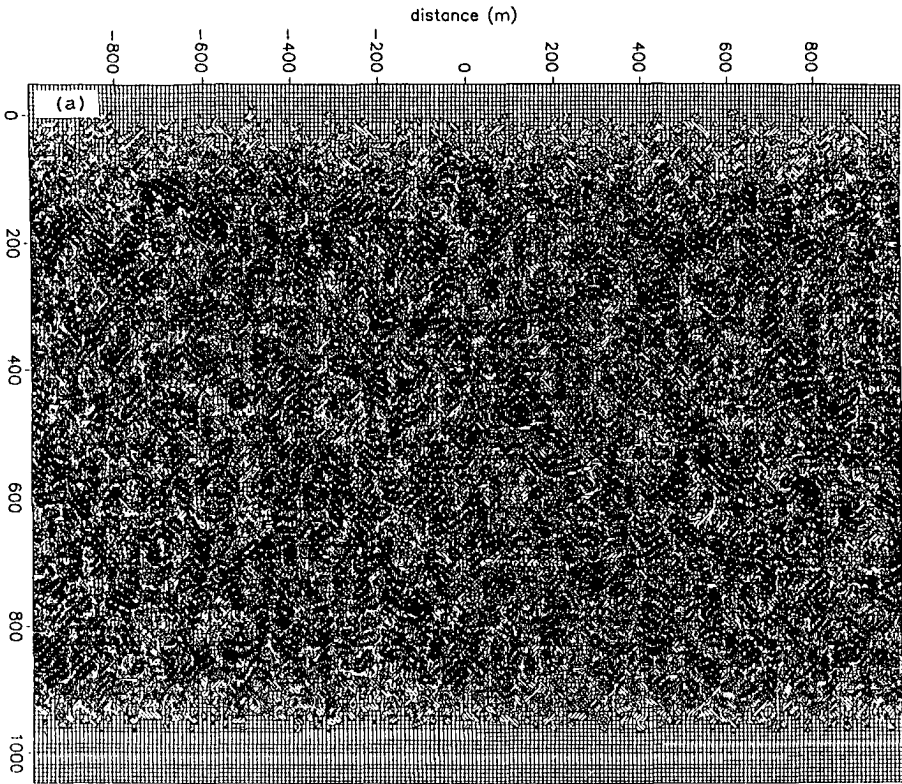
If the velocity detail  $\delta c$  has a zero average along the ray path, the travel time effect will be zero.

For the modeling experiment a macro model is defined containing a synclinal structure as shown in figure 1.6. In order to simulate detail in the velocity model spatially bandlimited (both in  $x$  and  $z$  direction) gaussian noise is added to this macro velocity model. The gaussian noise is equivalent to velocity anomalies in the velocity profile. A source is placed below the syncline at a depth of 2000 m. A finite difference modeling scheme with absorbing boundary conditions for all grid boundaries is used to obtain the modeled response at the surface for the perturbed velocity profile. The velocity perturbation is windowed in the depth direction such that the medium in the vicinity of the sources and receivers is homogeneous. This way the source strength for each source point does not vary because of velocity variations in the source region.



**Figure 1.6** The macro model for the wave propagation modeling experiments. Velocity variations are added in the region between 200 m and 1000 m depth. The wave field which has propagated through the macro model is registered at the surface.

By varying the strength of the velocity perturbation the effect of the detail in the model on the wave propagation is examined. The average size of the detail compared to the wave length is also related to the wave propagation effect. The size of the velocity anomalies is also varied. In the modeling experiments the following sizes are taken:  $\ll \lambda$ ,  $< \lambda$ ,  $\pm \lambda$ ,  $> \lambda$ . The velocity perturbations are shown in figure 1.7. A vertical velocity profile for each perturbation is shown in figure 1.8. The velocity perturbations are added to the macro model velocity distribution. The wave field is then modeled for the composite velocity distribution. For each of the different velocity perturbations four modeling experiments are carried out. For these four experiments the velocity perturbation is scaled to  $\pm 125$  m/s,  $\pm 250$  m/s,  $\pm 500$  m/s and  $\pm 750$  m/s. So in total sixteen modeling experiments are carried out for the random velocity perturbation. For the  $\pm 125$  m/s experiment the registered wave field for each of the perturbations is shown in figure 1.9. The registered wave field is undistorted for all the velocity perturbations. So this level of velocity perturbations does not influence the wave propagation for all types of perturbations



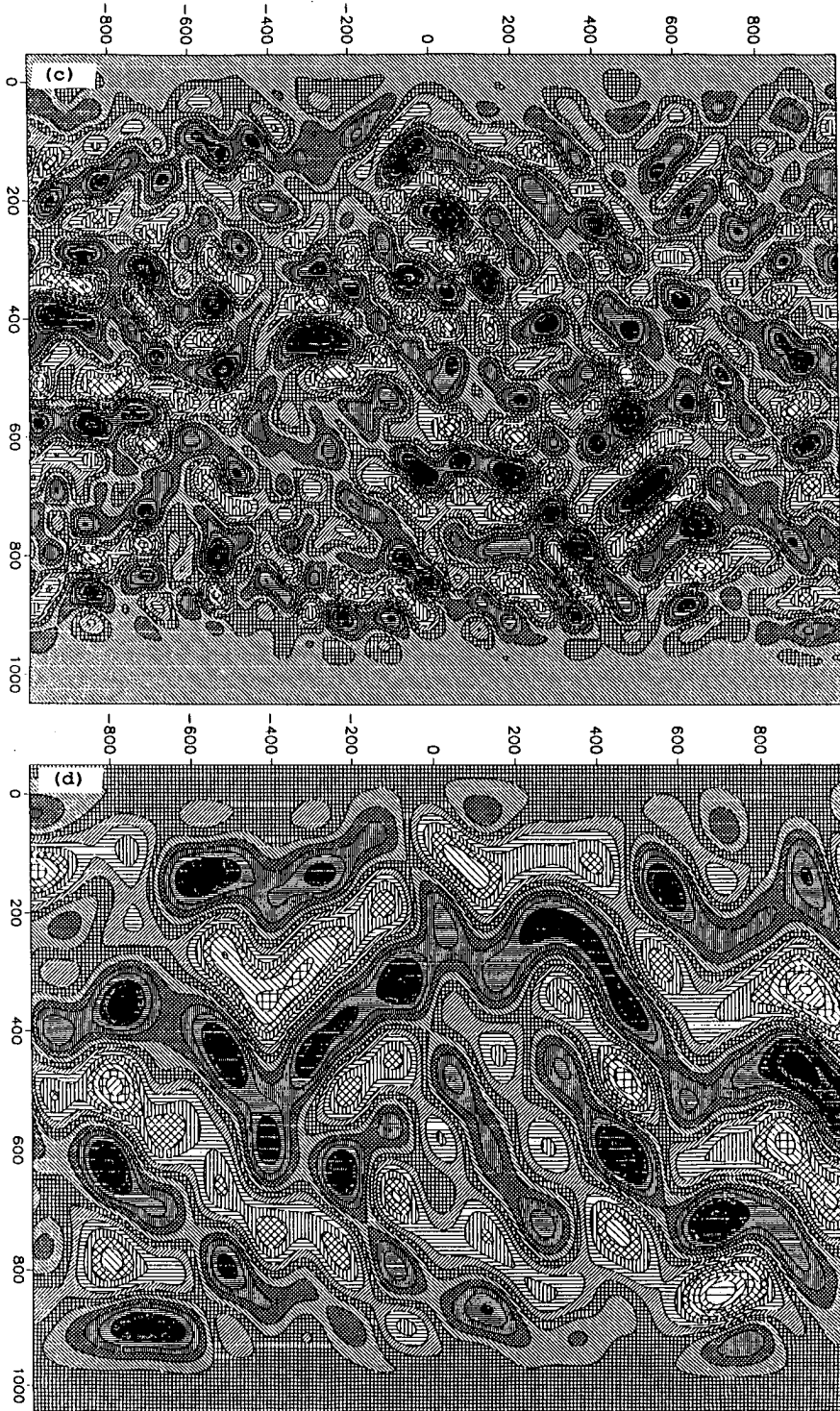


**Figure 1.7** The velocity variations which are added to the macro model to examine the effects on the wave propagation. The size of the velocity anomalies ranges from  $\ll \lambda$  in (a) through  $< \lambda$  in (b) and  $\cong \lambda$  (c) to  $> \lambda$  in (d).

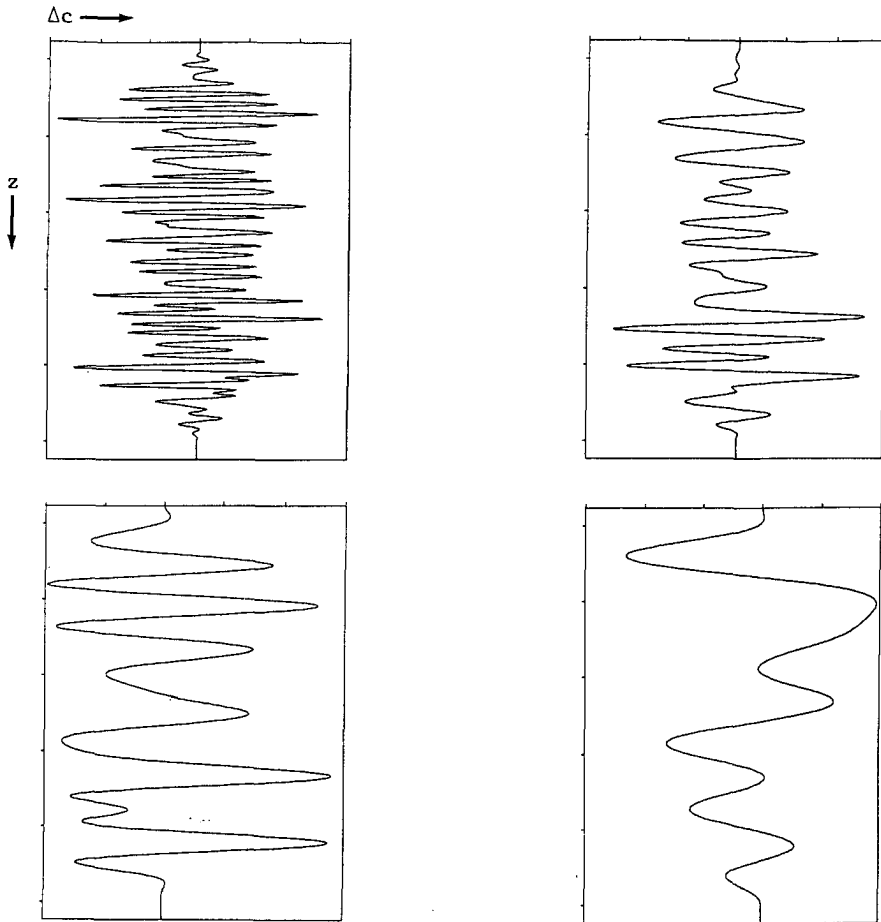


Figure 1.8 A vertical velocity profile from the perturbations from figure 1.7.

ranging from fine ( $\ll \lambda$ ) to coarse ( $> \lambda$ ). The variation in the detail has been increased to  $\pm 250$  m/s in figure 1.10. Again the registered wave field is undistorted. For the  $> \lambda$  perturbation minor distortion is present in the propagated wave field. However this distortion is well below the noise levels present in field data. Consequently velocity variations of  $\pm 250$  m/s for velocity anomalies ranging from  $\ll \lambda$  to  $> \lambda$  do not influence the wave propagation significantly. In the case of variations of  $\pm 500$  m/s the detailed perturbations do not influence wave propagation (figure 1.11). However for the  $\cong \lambda$  and  $> \lambda$  perturbations the propagated wave field is distorted. In the case of the  $\cong \lambda$  perturbation this distortion is again small to practical noise levels. For the  $> \lambda$  perturbation the distortion is becoming more significant as can be seen in figure 1.12. In this figure the propagated wave field for an unperturbed macro model

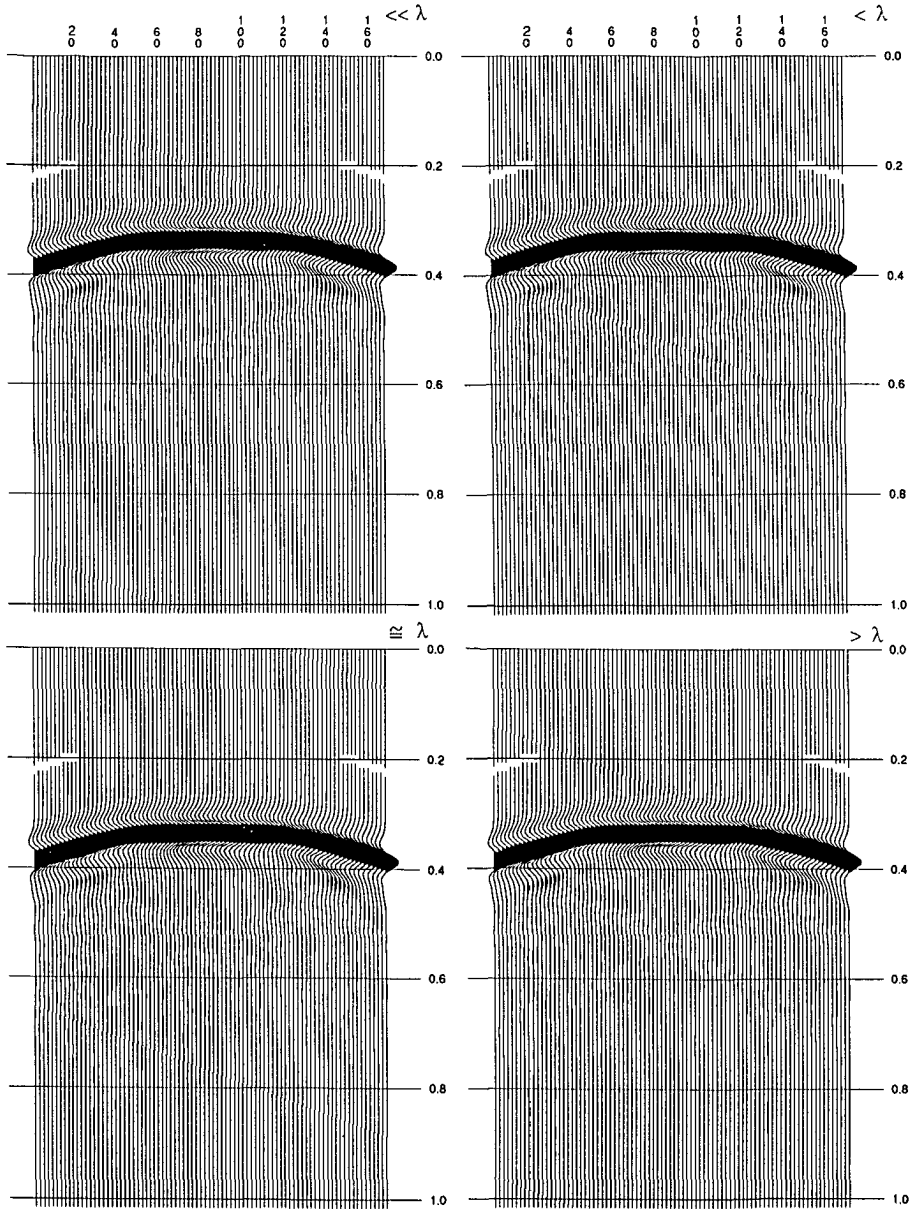
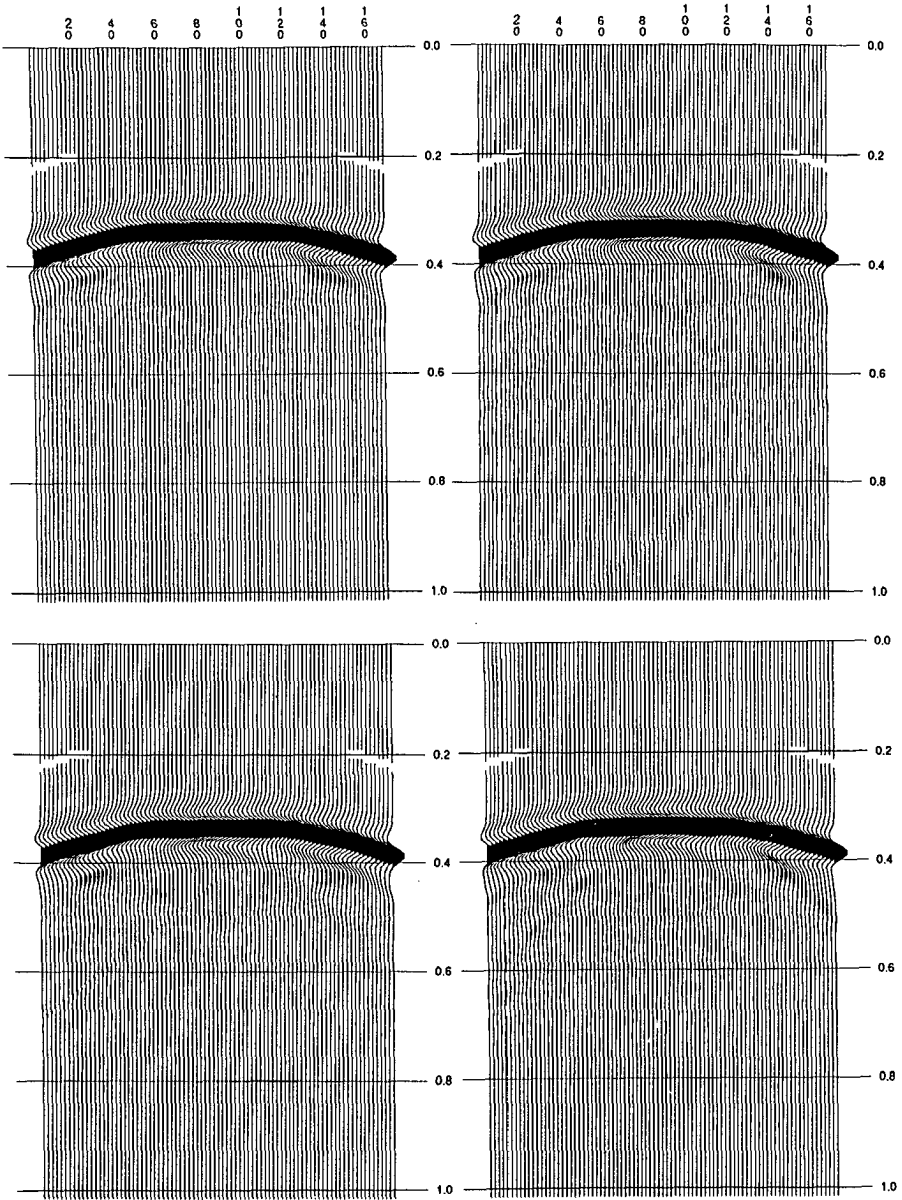
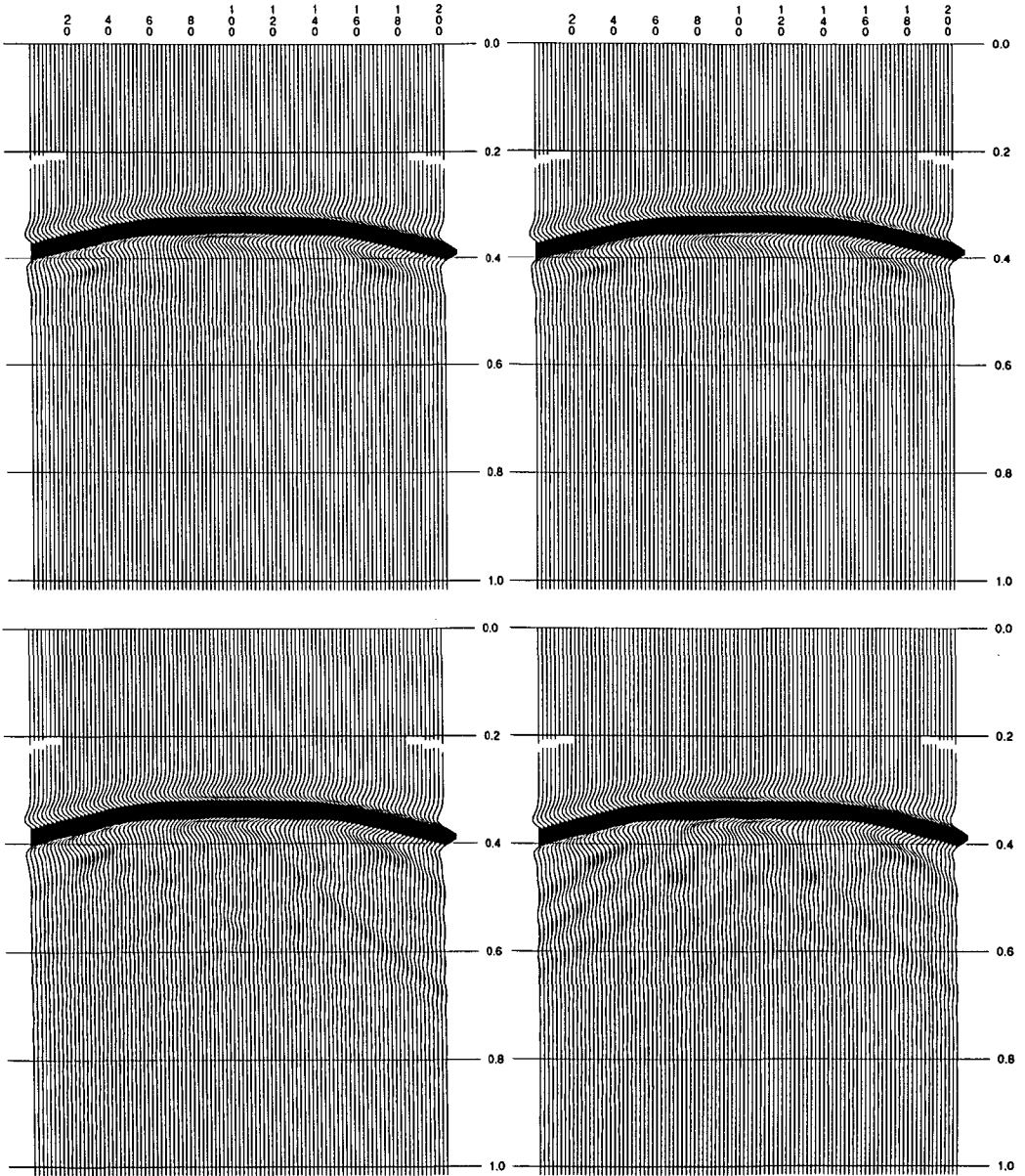


Figure 1.9 The propagated wave field for the  $\ll \lambda$ ,  $< \lambda$ ,  $\cong \lambda$  and  $> \lambda$  perturbation at a strength of  $\pm 125$  m/s.



**Figure 1.10** The propagated wave field for the  $\ll \lambda$ ,  $< \lambda$ ,  $\cong \lambda$  and  $> \lambda$  perturbation at a strength of  $\pm 250$  m/s.



**Figure 1.11** The propagated wave field for the  $\ll \lambda$ ,  $< \lambda$ ,  $\cong \lambda$  and  $> \lambda$  perturbation at a strength of  $\pm 500$  m/s.

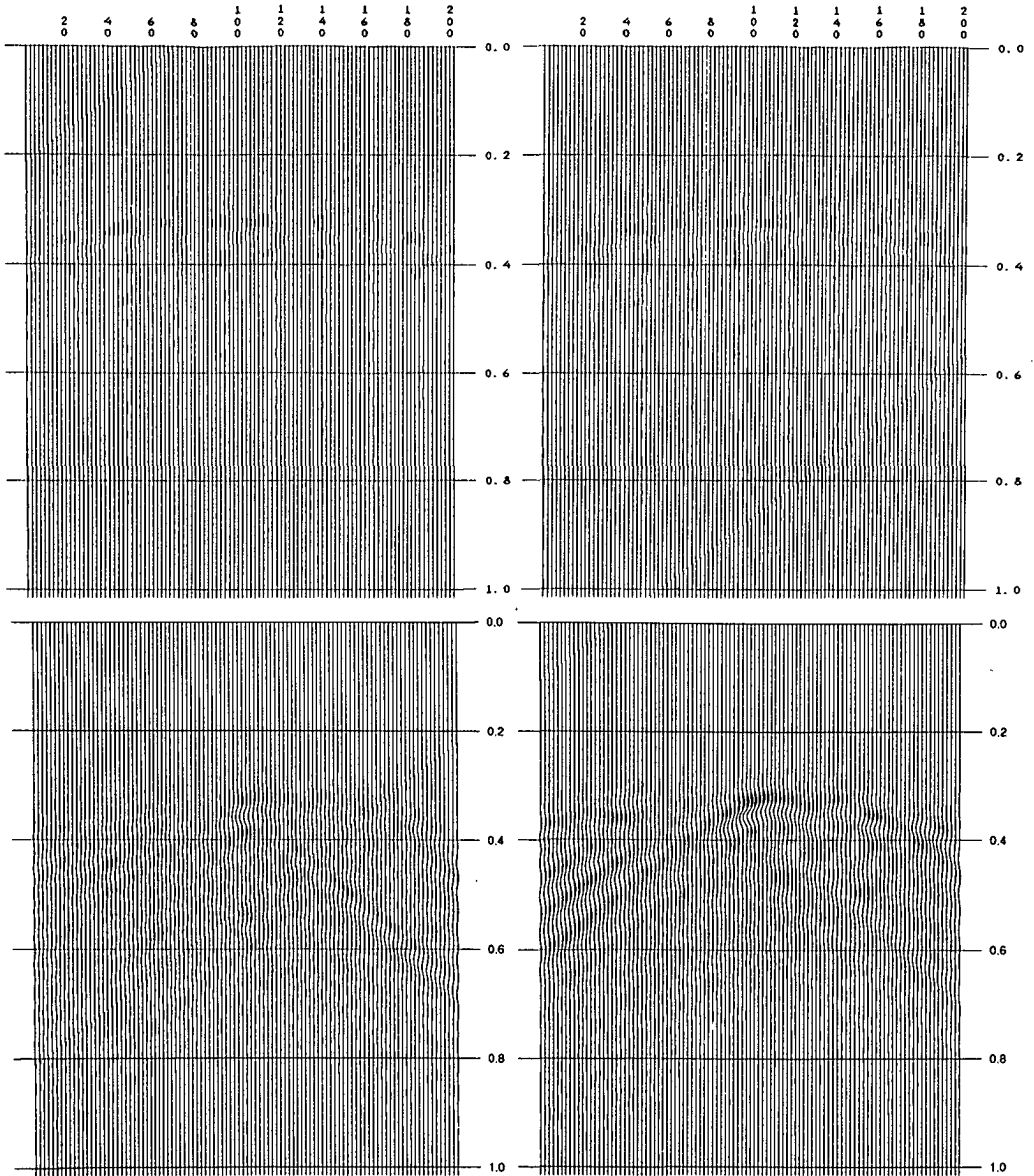


Figure 1.12 The propagated wave fields in the unperturbed velocity model has been subtracted from the wave fields from figure 1.11.

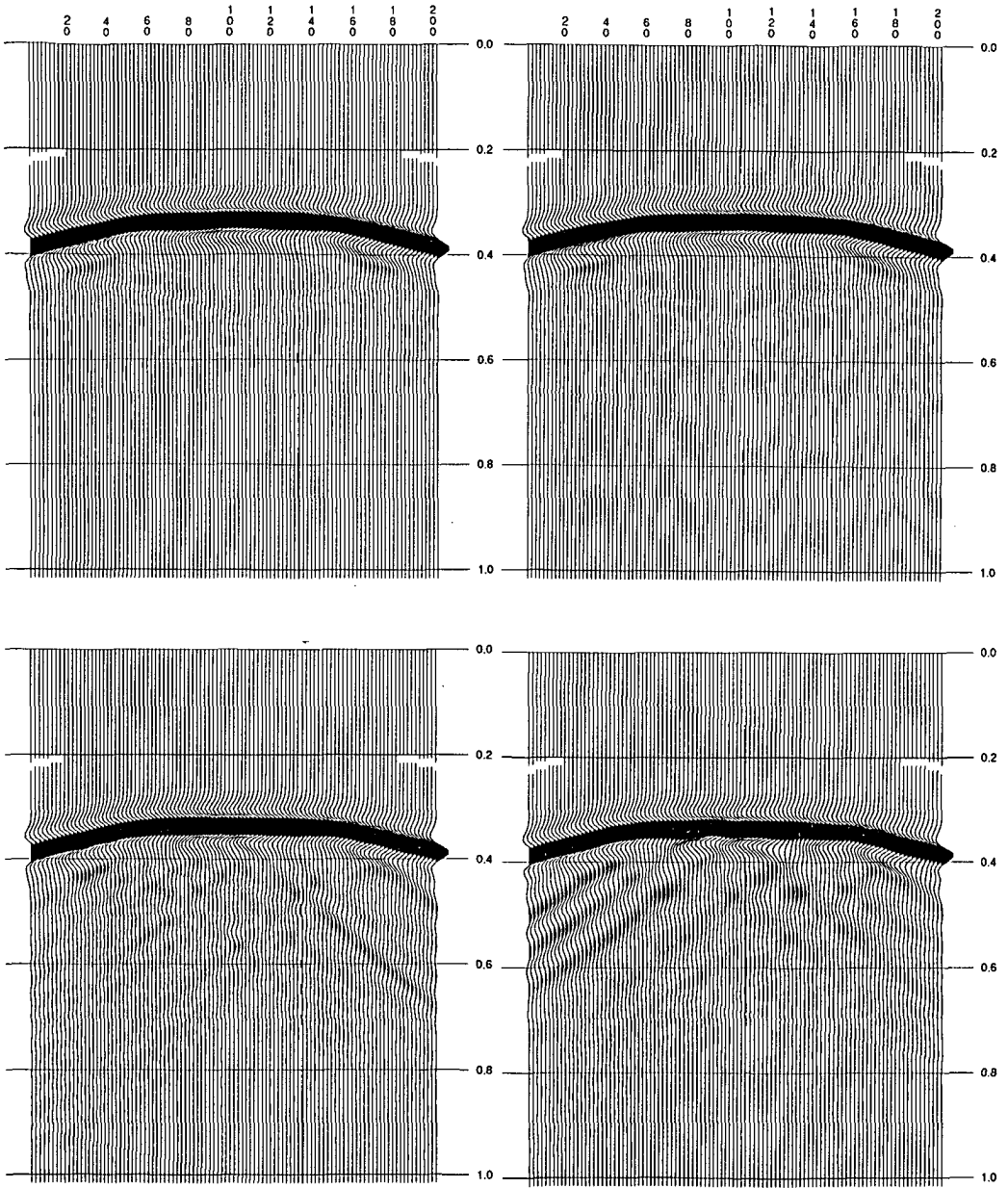


Figure 1.13 The propagated wave field for the  $\ll \lambda$ ,  $< \lambda$ ,  $\cong \lambda$  and  $> \lambda$  perturbation at a strength of  $\pm 750$  m/s.

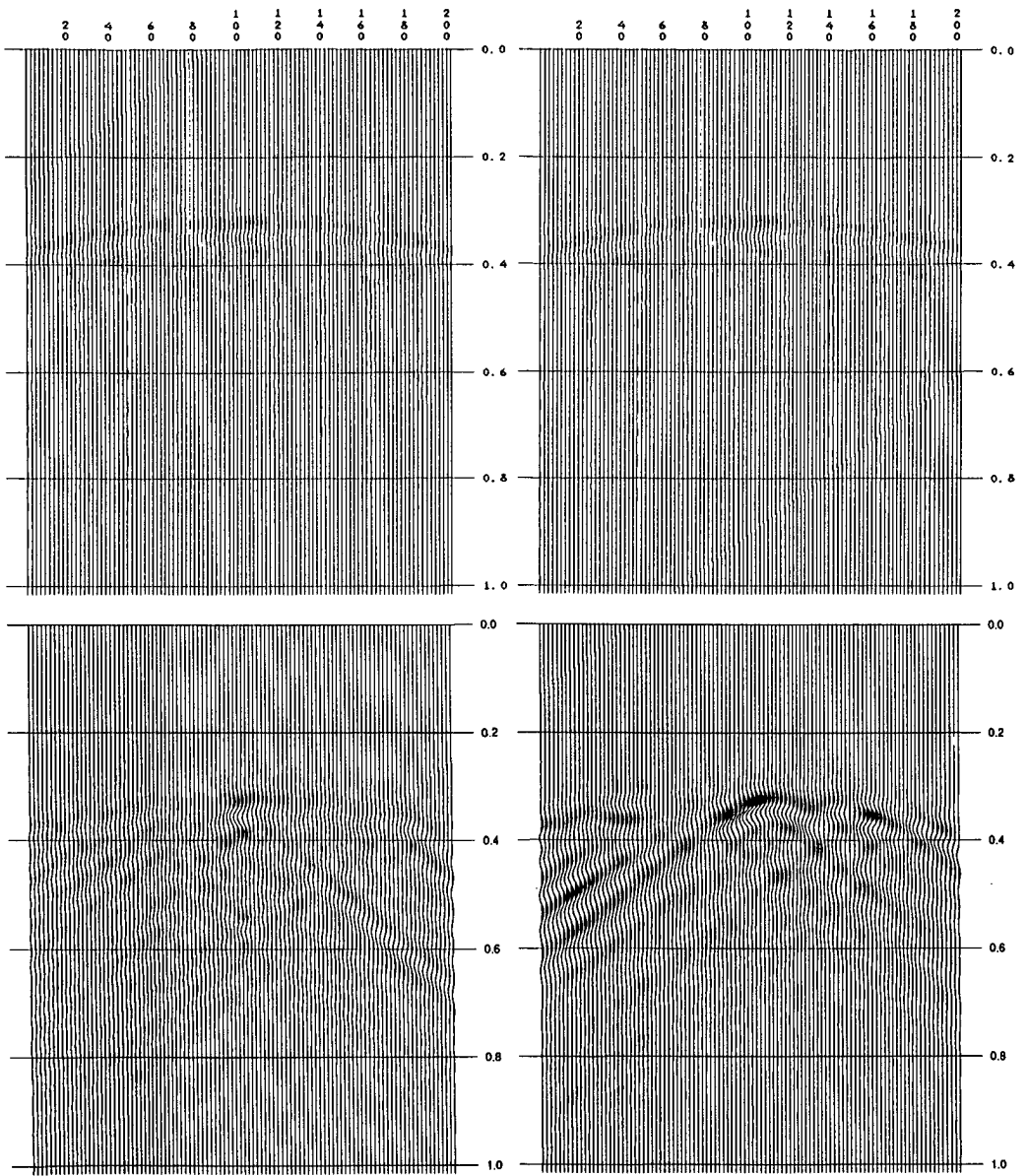


Figure 1.14 The propagated wave fields in the unperturbed velocity model has been subtracted from the wave fields from figure 1.13.

has been subtracted from the wave field obtained with the perturbed velocity model. For the  $\pm 750$  m/s perturbation the distortion for the  $\ll \lambda$  and the  $< \lambda$  perturbations is still quite insignificant (figure 1.13). For the  $\pm \lambda$  and the  $> \lambda$  perturbation the distortion is more pronounced. The character of the distortion is very similar to the response of a distribution of point diffractors (figure 1.14). So the velocity perturbation causes diffraction tails to appear in the response. From these experiments we get an indication that detailed information in the velocity profile ( $< \lambda$ ) does not significantly influence the propagation properties. Even for larger perturbations ( $> \lambda$ ) the propagation properties are not changed for small ( $< 250$  m/s) velocity changes. In case of increasing velocity changes for large velocity anomalies diffraction events occur in the propagated wave field. The conclusions are summarized in table 1.1.

**Table 1.1**

The wave propagation distortion for different random velocity perturbations.

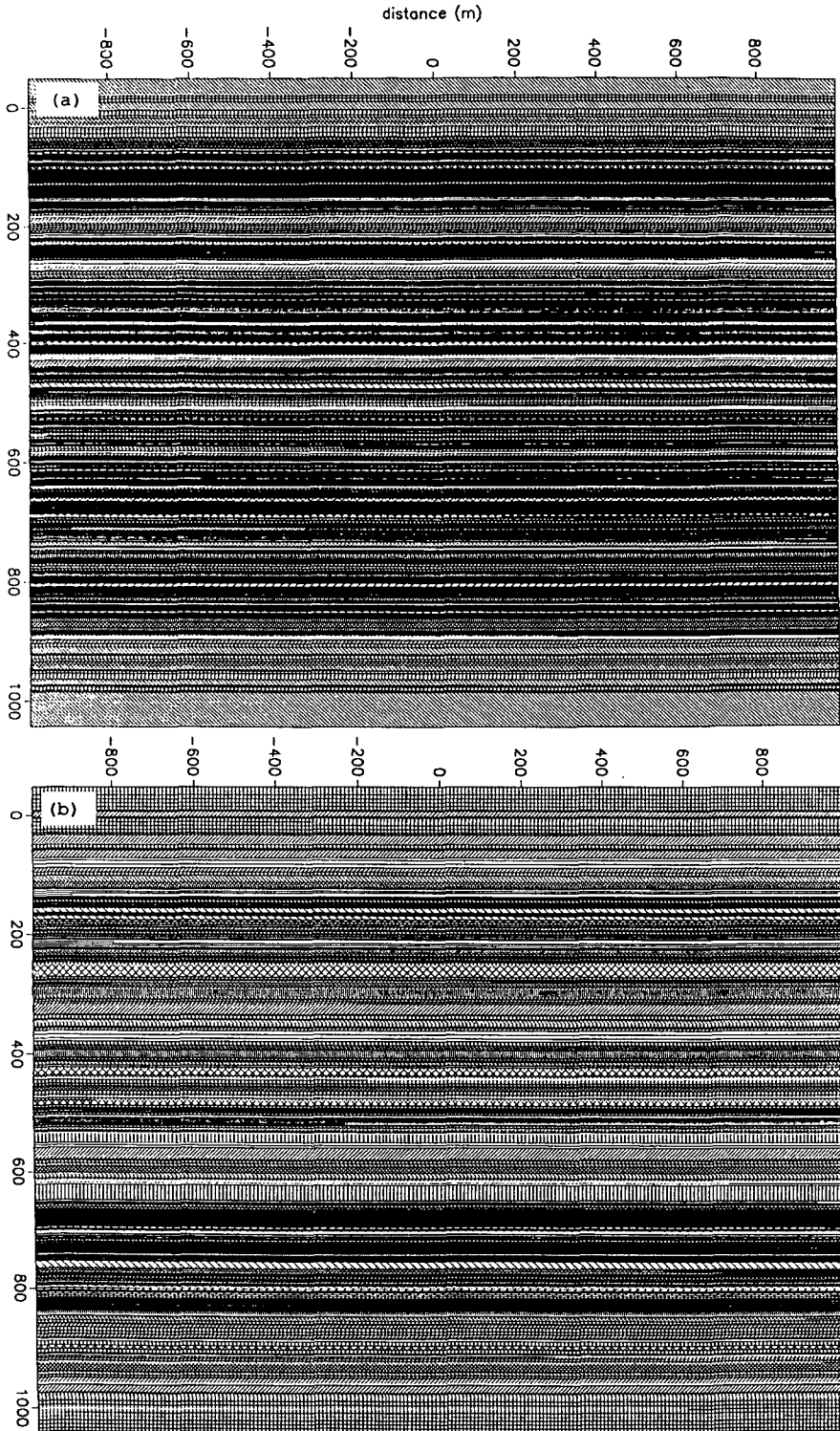
A + indicates no wave propagation distortion.

A +/- indicates some wave propagation distortion, but comparable to noise.

A - indicates strong wave propagation distortion.

	$\ll \lambda$	$< \lambda$	$\cong \lambda$	$> \lambda$
125 m/s	+	+	+	+
250 m/s	+	+	+	+/-
500 m/s	+	+	+/-	-
750 m/s	+	+	-	-

Apart from fully random perturbations correlated detail has also been added to the macro model. One vertical random velocity perturbation is extended laterally resulting in a finely layered velocity perturbation. This perturbation is strongly laterally coherent as occurs in the true subsurface as well. The different perturbations are shown in figure 1.15. Again the size of the velocity anomalies is varied from  $\ll \lambda$  to  $> \lambda$ . The transmitted wave field for the  $\pm 500$  m/s perturbations is shown in figures 1.16. The propagated wave field shows not the distortions which are present in the propagated wave field for the randomly perturbed velocity model. However for the strong lateral coherent velocity perturbations the travel time effect is not zero. In figure 1.17 the center trace for the  $\cong \lambda$  perturbation of strengths  $\pm 125$  m/s through  $\pm 750$  m/s is shown. The response shifts in time and decreases in amplitude as the perturbation increases. In figure 1.18 the amplitude cross sections for the propagated wave field in the



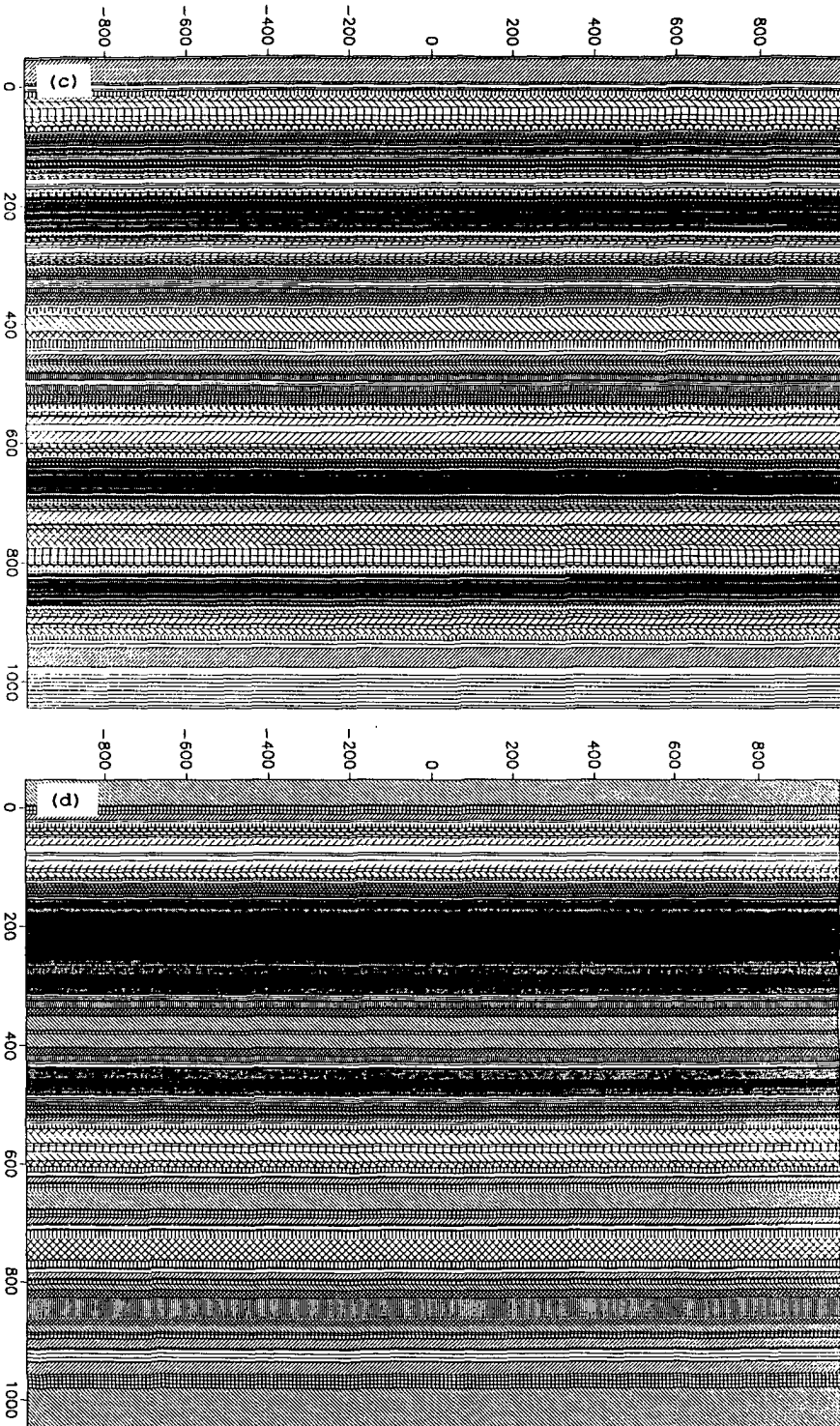


Figure 1.15 Lateral velocity perturbations of dimensions  $\ll \lambda$ ,  $< \lambda$ ,  $\cong \lambda$  and  $> \lambda$  have been added to the macro model to study the effect of coherent velocity anomalies on the wave propagation.

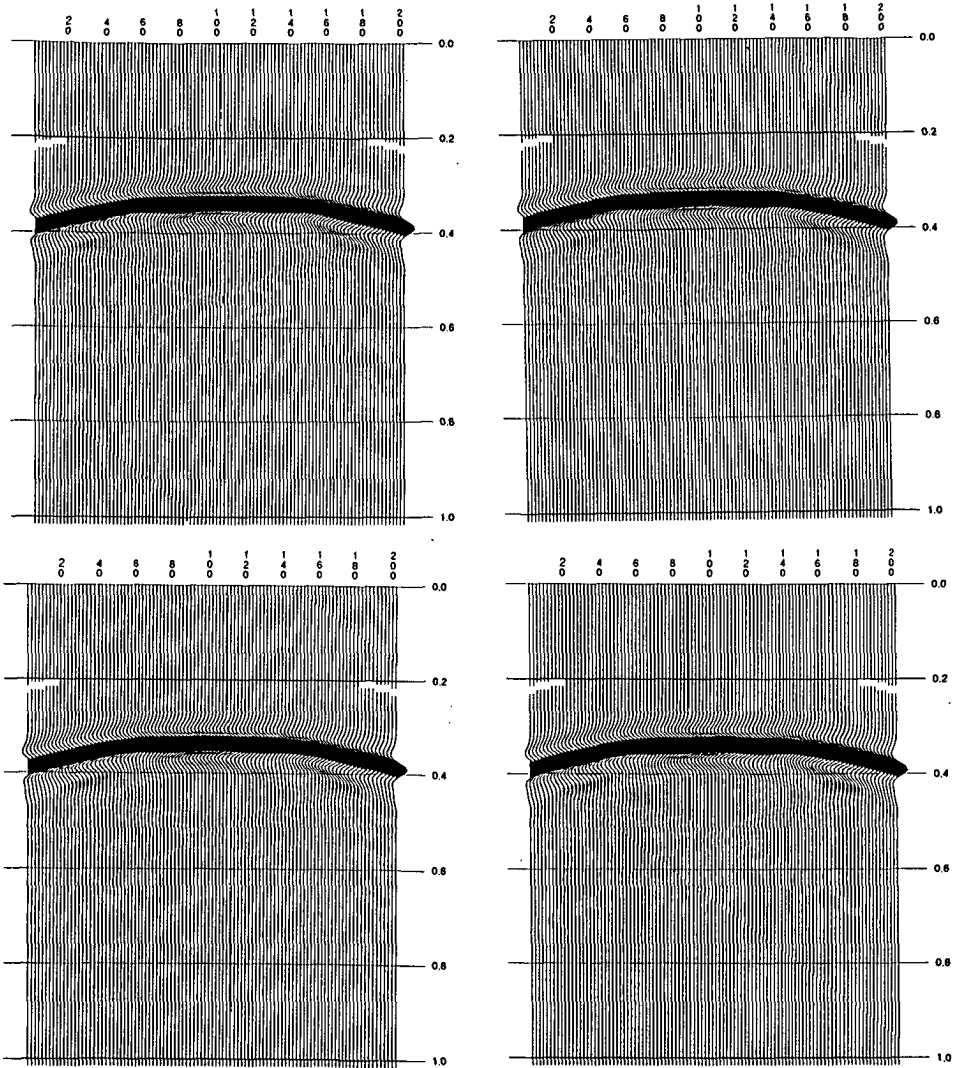
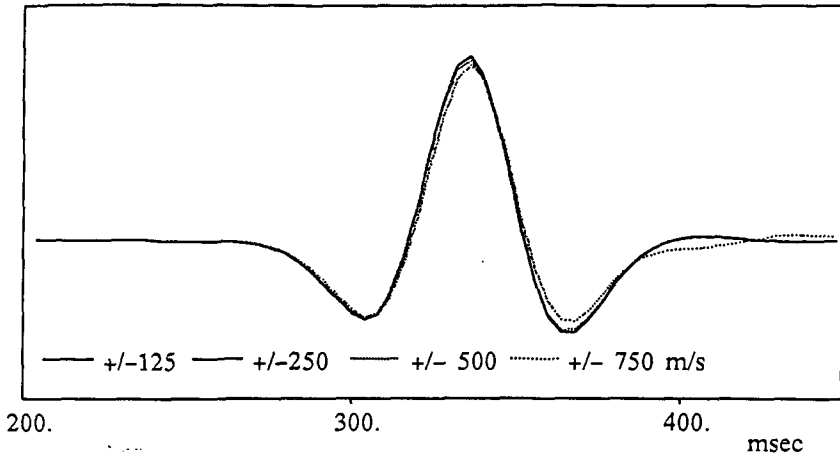
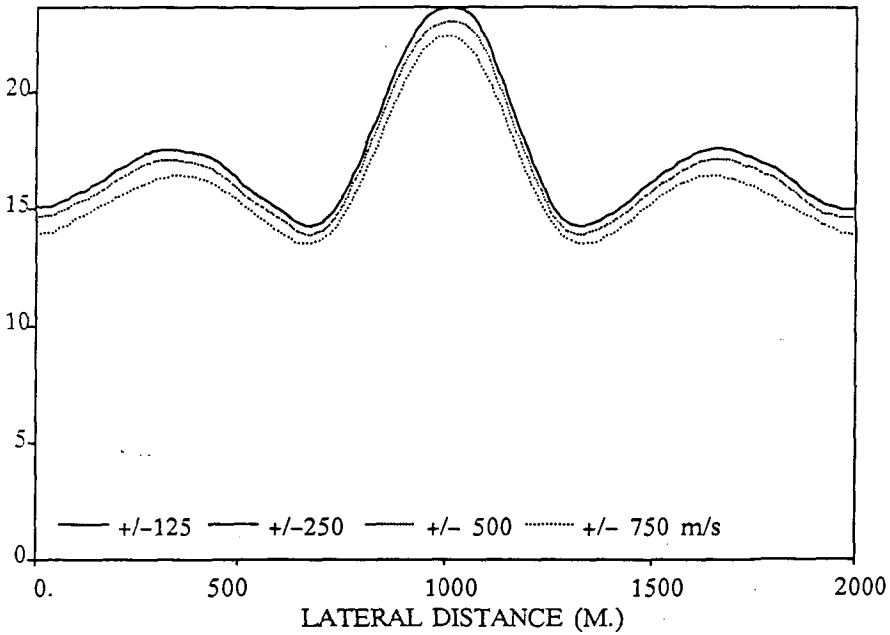


Figure 1.16 The propagated wave field for the  $\ll \lambda$ ,  $< \lambda$ ,  $\cong \lambda$  and  $> \lambda$  coherent velocity perturbation at a strength of  $\pm 500$  m/s.



**Figure 1.17** The middle trace from the propagated wave fields for the  $\cong \lambda$  perturbation at  $\pm 125$  m/s,  $\pm 250$  m/s,  $\pm 500$  m/s and  $\pm 750$  m/s strength, shows a travel time shift which increases with increasing velocity variations.



**Figure 1.18** The amplitude cross section for the propagated wave field in the  $\cong \lambda$  perturbed velocity model. The perturbation strength ranges from  $\pm 125$  m/s to  $\pm 750$  m/s. For the strong velocity anomalies the amplitude of the propagated wave field is biased.

perturbed velocity model is compared to the propagated wave field in the unperturbed velocity model. In these amplitude cross sections the envelope of the signal has been taken and the maximum in each trace is plotted as a function of the lateral position. From the figures we can see that for large velocity perturbations an amplitude bias occurs for the  $\cong \lambda$  and  $> \lambda$  type of perturbations. For the smaller velocity perturbations the amplitude bias becomes insignificant.

**Table 1.2**

The wave propagation distortion for different lateral coherent velocity perturbations.

A + indicates no wave propagation distortion.

A +/- indicates some wave propagation distortion, but comparable to noise.

A - indicates strong wave propagation distortion.

	$\ll \lambda$	$< \lambda$	$\cong \lambda$	$> \lambda$
125 m/s	+	+	+	+
250 m/s	+	+	+	+/-
500 m/s	+	+	+/-	-
750 m/s	+	+	-	-

For the laterally coherent velocity perturbation the modeling results are summarized in table 1.2. The travel time shift which occurred for the strong perturbations can easily be compensated by modifying the interval velocities slightly. The macro model is sufficient for describing the wave propagation properties of the subsurface in the case of laterally coherent velocity perturbations.

The experiments give a clear indication that the wave propagation properties of a medium are determined by the trend information in the velocity function. The detail in the velocity profile does not significantly influence the propagation of a wave field. The sparse parameterization used in the macro model is therefore a sufficient representation of the medium for describing the wave propagation properties.

---

## WAVE FIELD EXTRAPOLATION

### 2.1 INTRODUCTION

The wave field extrapolation is very important in migration and redatuming. In a seismic experiment the wave field is registered at only a few locations on the surface or on a well. Whereas for the migration and redatuming the wave field should be known throughout the subsurface. The registered wave field should be propagated or back propagated into the subsurface by applying wave field extrapolation operators.

In one-way wave propagation an extrapolation in the direction of propagation away from the sources requires different operators from the extrapolation towards the sources. In this chapter the forward extrapolation away from the sources will be discussed.

The wave field extrapolation operators will be based on the Kirchhoff integral. Quite often one of the terms of the Kirchhoff integral is dropped, resulting in the Kirchhoff approximation. The error in this approximation will be investigated. The Green's function which appears in the Kirchhoff integral will be examined more closely. By choosing different Green's functions an extrapolation operator may be found which is more suited for a certain problem. A trade off exists between the effort to be put in obtaining a suitable Green's function and the effort it takes to actually propagate the wave field.

## 2.2 FORWARD WAVE PROPAGATION

The propagation of the wave field away from the source is described by the forward wave propagation.

For loss-less inhomogeneous fluids the wave equation follows from the linearized stress-strain relation

$$K \nabla \cdot \mathbf{V} = -j\omega P \quad (2.1)$$

and the linearized equation of motion

$$\frac{1}{\rho} \nabla P = -j\omega \mathbf{V} \quad (2.2)$$

where  $P = P(x,y,z,\omega)$  denotes the Fourier transform of the acoustic pressure  $p(x,y,z,t)$ ,  $\mathbf{V} = \mathbf{V}(x,y,z,\omega)$  denotes the Fourier transform of the particle velocity  $\mathbf{v}(x,y,z,t)$ .  $\rho = \rho(x,y,z)$  describes the mass density distribution and  $K = K(x,y,z)$  describes the bulk compression modulus distribution. These two relations can be combined to obtain the well-known frequency domain representation of the acoustic wave equation.

$$\rho \nabla \cdot \left( \frac{1}{\rho} \nabla P \right) + k^2 P = 0 \quad (2.3)$$

where

$$k = \frac{\omega}{c} \quad (2.4)$$

with

$$c = \sqrt{\frac{K}{\rho}} \quad (2.5)$$

The propagation velocity distribution is described by  $c(x,y,z)$ .

In order to arrive at the Kirchhoff integral equation define a domain  $V$  bounded by a surface  $S$  and outward pointing normal  $\mathbf{n}$ . Now define Green's functions which satisfy the following equation in  $V$

$$\rho \nabla \cdot \left( \frac{1}{\rho} \nabla G(\mathbf{r}, \mathbf{r}_A, \omega) \right) + k^2 G(\mathbf{r}, \mathbf{r}_A, \omega) = -4\pi\rho\delta(\mathbf{r} - \mathbf{r}_A) \quad (2.6)$$

with  $\mathbf{r} = (x,y,z)$

where  $\mathbf{r}_A = \mathbf{r}(x_A, y_A, z_A)$  is an arbitrary point  $A$  in  $V$ . So  $G$  represents the pressure associated with the wave field resulting from a point source in  $A$ .

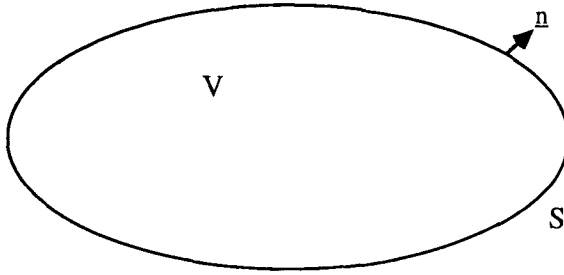


Figure 2.1 Bounded domain V for theorem of Gauss.

The theorem of Gauss states that

$$\int_V (\nabla \cdot \mathbf{a}) dV = \int_S \mathbf{a} \cdot \mathbf{n} dS \quad (2.7)$$

Now define the vector field  $\mathbf{a} = \mathbf{a}(\mathbf{r}, \mathbf{r}_A, \omega)$  in V such that

$$\mathbf{a} = gP\nabla G - qG\nabla P \quad (2.8)$$

q is some space variant function. So

$$\nabla \cdot \mathbf{a} = \nabla \cdot (q\nabla G)P + q\nabla G \cdot \nabla P - \nabla G \cdot q\nabla P - G\nabla \cdot q\nabla P \quad (2.9)$$

If we assume V to be source free for the wave field P and using equation (2.3) and (2.6) it follows

$$\nabla \cdot \mathbf{a} = -4\pi P \delta(\mathbf{r} - \mathbf{r}_A) \quad (2.10)$$

so after applying the theorem of Gauss

$$P(\mathbf{r}_A, \omega) = -\frac{1}{4\pi} \int_S \frac{1}{\rho(\mathbf{r})} \left[ P(\mathbf{r}, \omega) \frac{\partial G(\mathbf{r}, \mathbf{r}_A, \omega)}{\partial n} - \frac{\partial P(\mathbf{r}, \omega)}{\partial n} G(\mathbf{r}, \mathbf{r}_A, \omega) \right] dS \quad (2.11)$$

Relation (2.11) represents the Kirchhoff integral. It states that if the wave field is known on a closed surface S which does not enclose any sources, the wave field may be calculated at any point inside V. If sources would exist inside V a volume integral over all sources should be included in relation 2.11. In seismics however the measurements are never available on a closed surface. Therefore generally a configuration is taken consisting of an infinite surface  $S_0$  and a hemisphere  $S_1$  with a radius R going to infinity as shown in figure 2.2. Since V should be

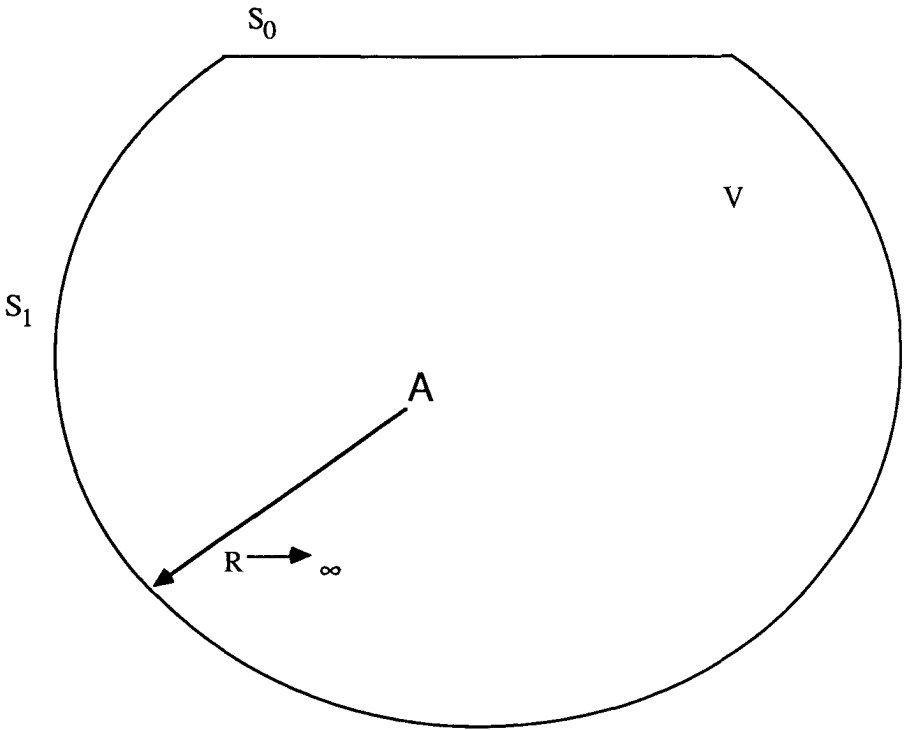


Figure 2.2 Modified surface  $S$  to eliminate contributions from  $S_1$  to the Kirchhoff integral over  $S_0$  and  $S_1$ .

source free all sources should be located in the upper half space above  $S_0$ . The Sommerfeld radiation condition states that the contribution of the Kirchhoff integral over the hemisphere goes to zero if the radius  $R$  goes to infinity. So the Kirchhoff integral over  $S$  may be replaced by an integral over a plane surface  $S_0$  at  $z_0$ .

$$P(\mathbf{r}_A, \omega) = -\frac{1}{4\pi} \int_{S_0} \frac{1}{\rho} \left[ \frac{P \partial G}{\partial n} - \frac{\partial P}{\partial n} G \right] dS \quad (2.12)$$

As shown by Berkhout and Wapenaar (1988) Rayleigh type integrals for the geometry shown in figure 2.2 may be derived from the full Kirchhoff integral under the following surface condition

$$\frac{\partial \rho}{\partial z} = 0, \quad \frac{\partial c}{\partial z} = 0 \quad \text{at } z_0 . \quad (2.13)$$

These conditions are equivalent to a reflection free surface. The wave equation at  $z_0$  now becomes

$$\frac{\partial^2}{\partial z^2} P + \rho \frac{\partial}{\partial y} \left( \frac{1}{\rho} \frac{\partial P}{\partial y} \right) + \rho \frac{\partial}{\partial x} \left( \frac{1}{\rho} \frac{\partial P}{\partial x} \right) + k^2 P = 0 . \quad (2.14)$$

The wavefield  $P(\mathbf{r}, \omega)$  is always spatial and temporal bandlimited in practical situations. The partial differentiation may be represented by a spatial convolution if only a limited bandwidth is considered (Berkhout, 1982).

$$\frac{\partial^2 P}{\partial z^2} + H_2 * P = 0 \quad \text{at } z = z_0 , \quad (2.15)$$

with

$$H_2 = \left[ k^2 d_0(x, y) + d_2(x) + d_2(y) - \frac{\partial \ln \rho}{\partial x} d_1(x) - \frac{\partial \ln \rho}{\partial y} d_1(y) \right]_{z_0} , \quad (2.16)$$

where  $d_0$ ,  $d_1$  and  $d_2$  are defined according to

$$\frac{\partial P}{\partial y} = d_1(y) * P \quad \frac{\partial P}{\partial x} = d_1(x) * P , \quad (2.17)$$

$$\frac{\partial^2 P}{\partial x^2} = d_2(x) * P \quad \frac{\partial^2 P}{\partial y^2} = d_2(y) * P , \quad (2.18)$$

$$d_0(x, y) = \delta(x) \delta(y) . \quad (2.19)$$

The total wave field and the Green's functions may be split up into up going  $P^-$  and down going  $P^+$  components

$$P = P^+ + P^- \quad (2.20)$$

Each component satisfies the one-way wave equations

$$\frac{\partial P^+}{\partial z} + j H_1 * P^+ = 0 , \quad (2.21)$$

$$\frac{\partial P^-}{\partial z} - j H_1 * P^- = 0 , \quad (2.22)$$

with

$$H_1 * H_1 = H_2 \quad . \quad (2.23)$$

Note that without lateral velocity and density variations at  $z = z_0$ ,  $H_1$  is given by

$$\tilde{H}_1(k_x, k_y, z_0, \omega) = \iint H_1(x, y, z, \omega) e^{j(k_x x + k_y y)} dx dy \quad , \quad (2.24)$$

so

$$\tilde{H}_1(k_x, k_y, z_0, \omega) = \sqrt{k^2(z_0) - k_x^2 - k_y^2} \quad . \quad (2.25)$$

A similar wave field decomposition is carried out for the Green's function

$$G = G^+ + G^- \quad , \quad (2.26)$$

with

$$\frac{\partial G^+}{\partial z} = -j H_1 * G^+ \quad , \quad (2.27)$$

$$\frac{\partial G^-}{\partial z} = +j H_1 * G^- \quad . \quad (2.28)$$

By choosing the medium for the Green's function homogeneous above  $S_0$  the down going Green's function vanishes.

$$G^+ = 0 \quad . \quad (2.29)$$

After substitution of the one-way wave field components in the Kirchhoff integral the Rayleigh I integral may be derived

$$P(r_A, \omega) = -\frac{1}{2\pi} \int_S \frac{1}{\rho(r)} \frac{\partial P^+(r, \omega)}{\partial z} G^-(r, r_A, \omega) dS \quad . \quad (2.30)$$

In a similar way the Rayleigh II integral may be derived

$$P(r_A, \omega) = -\frac{1}{2\pi} \int_S \frac{1}{\rho(r)} P^+(r, \omega) \frac{\partial G^-(r, r_A, \omega)}{\partial z} dS \quad . \quad (2.31)$$

For a more rigorous discussion on the derivation of these integrals the reader is referred to Berkhout and Wapenaar (1988).

### 2.3 INTERPRETATION OF THE KIRCHHOFF INTEGRAL

In the previous sections the Kirchhoff integral and the Rayleigh integrals have been derived. In this section and the following sections some important characteristics of these integrals will be examined. Consider again the Kirchhoff integral ( equation 2.11)

$$P(r_A, \omega) = -\frac{1}{4\pi} \int_S \frac{1}{\rho} \left[ P \frac{\partial G}{\partial n} - G \frac{\partial P}{\partial n} \right] dS \quad (2.32)$$

As discussed earlier this integral equation states that the wave field inside a closed volume  $V$  bounded by the surface  $S$  (figure 2.3) may be calculated from the pressure and normal

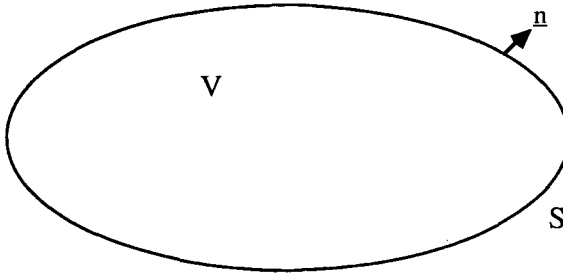


Figure 2.3 Bounded volume  $V$  for the Kirchhoff integral.

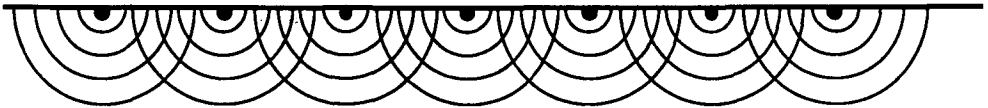


Figure 2.4 According to Huygens' principle each point on  $S$  acts as a secondary point source.

component of the particle velocity distribution at the surface  $S$ . No knowledge about the true sources outside  $S$  is required whatsoever. The interpretation is similar to the Huygens' principle. On the surface  $S$  each point acts as a secondary source (figure 2.4). The wave field in  $V$  is a superposition of the secondary sources. These secondary sources would however cause a wave field to propagate both inward in  $V$  as well as outward. But because of the second term in the Kirchhoff integral the outward propagating waves are eliminated.

## 2.4 A COMPARISON OF THE KIRCHHOFF INTEGRAL AND THE RAYLEIGH INTEGRAL

A wave field extrapolation based on the Kirchhoff integral requires knowledge about both the pressure distribution as well as the distribution of the normal component of the particle velocity (equation 2.11).

$$P(\mathbf{r}_A, \omega) = -\frac{1}{4\pi} \int_S \frac{1}{\rho(\mathbf{r})} \left[ P(\mathbf{r}, \omega) \frac{\partial G(\mathbf{r}, \mathbf{r}_A, \omega)}{\partial n} - \frac{\partial P(\mathbf{r}, \omega)}{\partial n} G(\mathbf{r}, \mathbf{r}_A, \omega) \right] dS \quad (2.33)$$

Under certain conditions discussed in the next section of this chapter, the Rayleigh integral (equation 2.31) may be used instead of the full Kirchhoff integral.

$$P(\mathbf{r}_A, \omega) = \frac{1}{2\pi} \int_S \frac{1}{\rho(\mathbf{r})} P^+(\mathbf{r}, \omega) \frac{\partial G^-(\mathbf{r}, \mathbf{r}_A, \omega)}{\partial n} dS \quad (2.34)$$

The Rayleigh integral or Kirchhoff approximation is often applied in extrapolation and migration procedures. However, if the surface over which the Rayleigh integral is evaluated is not flat some of the assumptions made in the derivation of the Rayleigh integral are violated. So in general the Rayleigh integral is no longer valid for these geometries. A different Green's

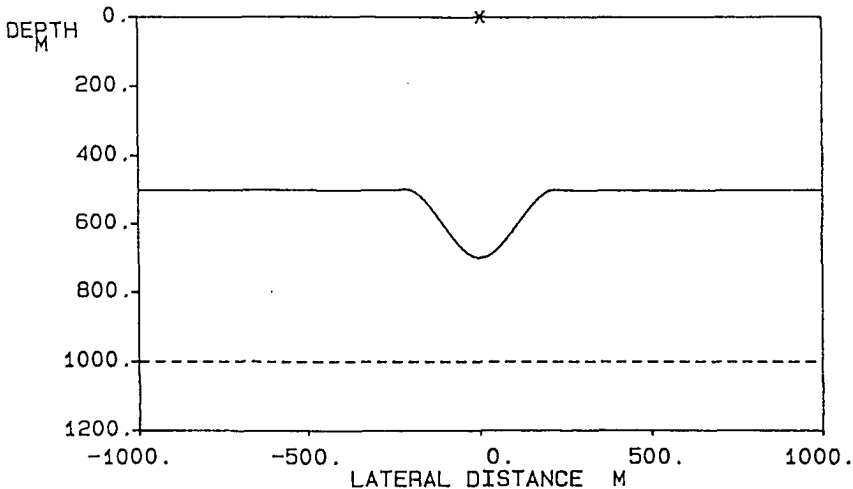


**Figure 2.5** Geometry to compare the Kirchhoff integral with the Rayleigh integral. The source (\*) at  $z = 0$  m generates a wave field. The wave field at the synclinal interface is extrapolated to  $z = 1000$  m with both the Kirchhoff as well as the Rayleigh integral.

function may be chosen in order to make the Rayleigh integral valid. However the Green's function will become more complex as will be discussed in the next section. For a specific configuration of a homogeneous space and a source in  $A$  both the Kirchhoff integral and the Rayleigh integral have been applied. The wave field at the surface  $S_0$  is extrapolated to  $S_1$ .

In figure 2.6 the wave field at  $S_0$  is shown. Due to the undulated character of the surface the response at  $S_0$  is non-hyperbolic. The extrapolated wave field is shown in figure 2.7a for the full Kirchhoff integral and in figure 2.7b for the Rayleigh integral. The direct wave field at  $S_1$  is shown in figure 2.7c.

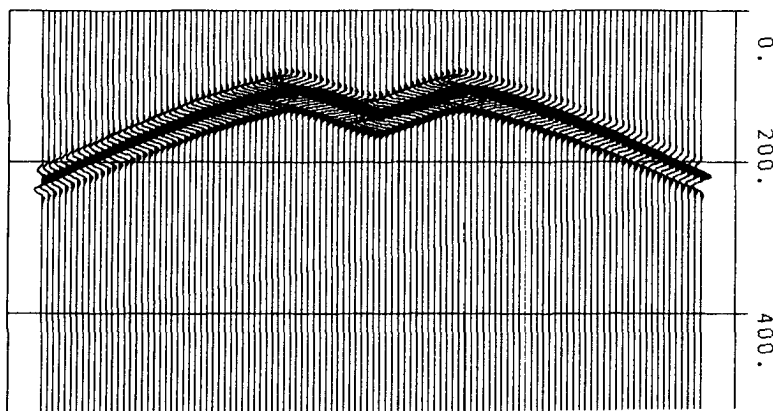


**Figure 2.6** The pressure wave field at the synclinal interface from figure 2.5 due to a source at  $z = 0$  m.

In figure 2.8 the amplitude cross section for the Kirchhoff extrapolated response is compared to the direct source wave field. The travel times as well as the amplitudes are correct for the Kirchhoff based extrapolation operator. For the Rayleigh based wave field extrapolation operator the response at  $S_1$  shown in figure 2.7b is seriously distorted. An additional event is present on both sides of the apex of the hyperbole. This event is caused by a wave field propagating from  $S_0$  into the upper half space but still towards  $S_1$  as shown in figure 2.9.

As discussed in the section on the interpretation of the Kirchhoff integral the two terms in the Kirchhoff integral ensure the correct direction of propagation away from the surface and the source. In terms of Huygen's principle: the secondary sources at  $S$  should only cause a wave field to propagate away from the source for the homogeneous medium. In case of the Rayleigh integral only one term is present. The secondary sources  $S_0$  cause a wave field to propagate in

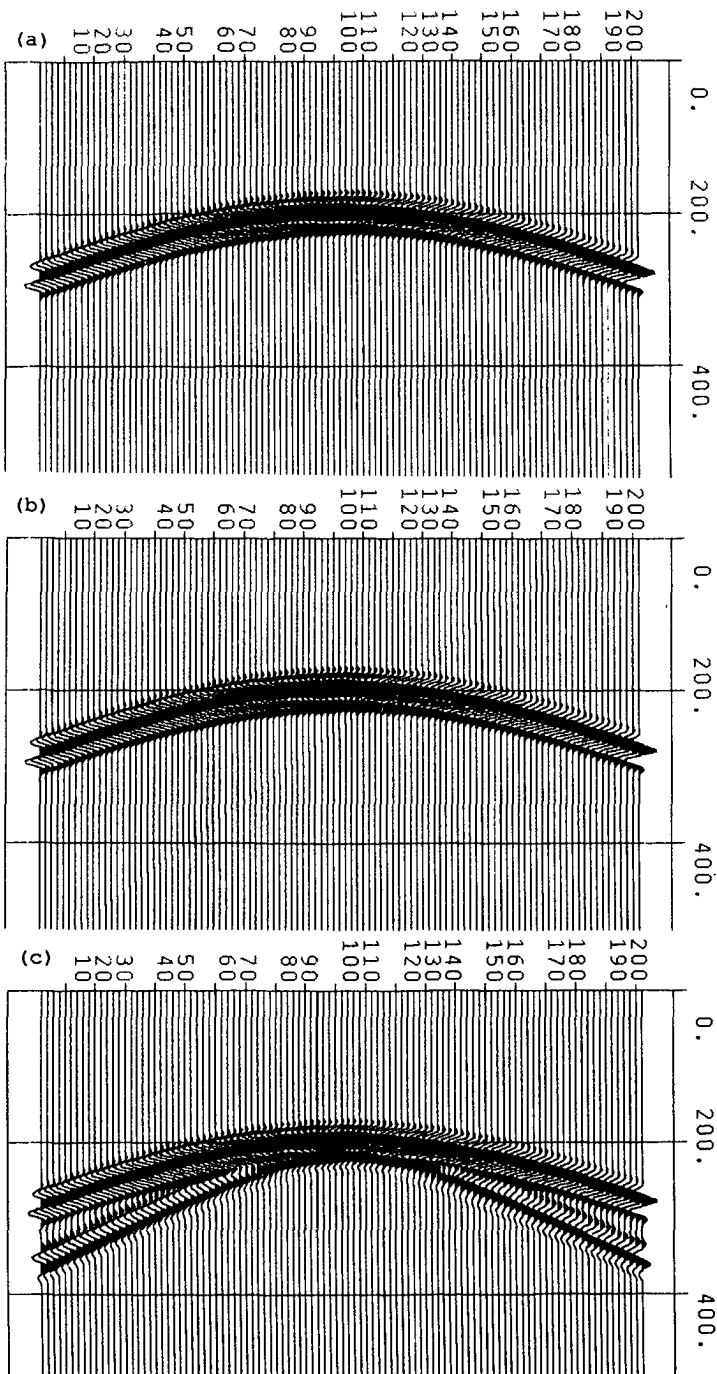


**Figure 2.7** The wave field at  $z = 1000$  m according to the analytical solution (a), the Kirchhoff integral (b) and the Rayleigh integral (c).

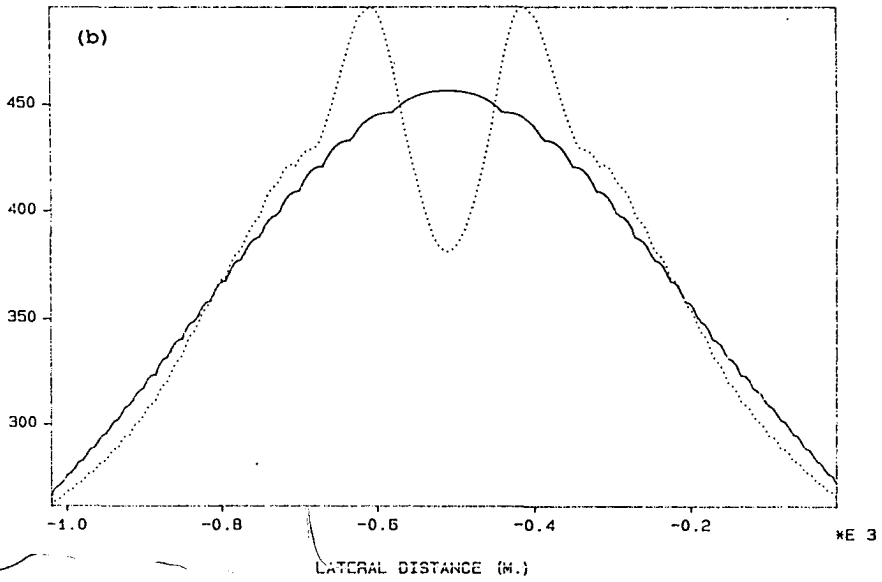
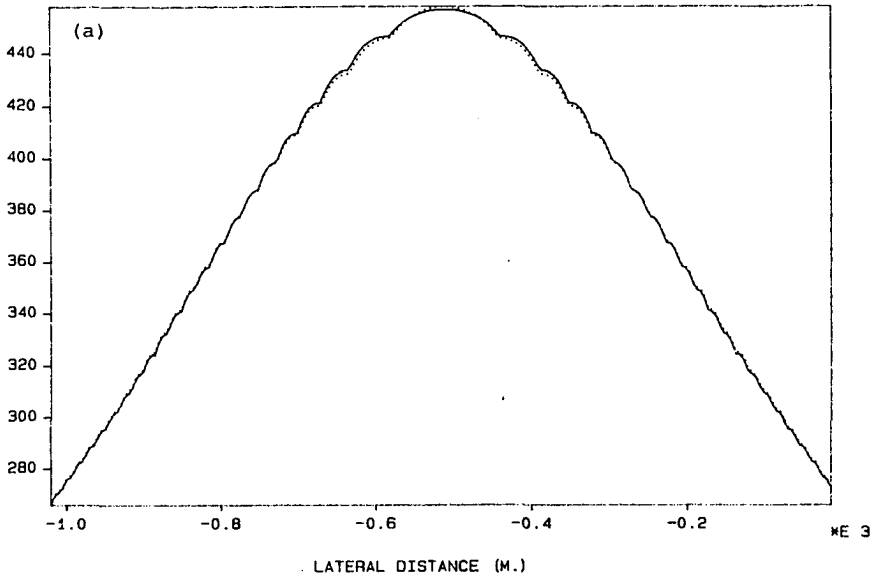


**Figure 2.8** The amplitude cross sections of the wave field at  $z = 1000$  m obtained with the Kirchhoff integral (a, dotted) compared to the analytical solution (a, solid). In figure b the result obtained with the Rayleigh integral (dotted) is compared with the analytical solution (solid).

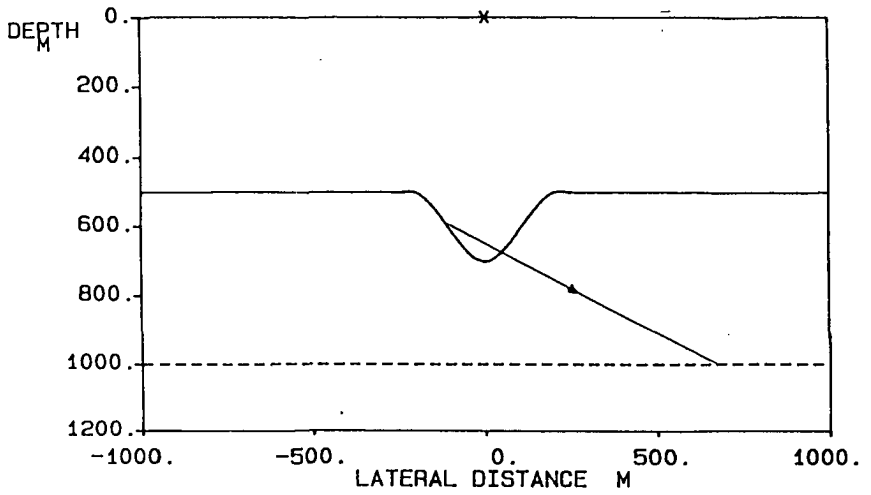


**Figure 2.9** The additional event in the Rayleigh extrapolated wave field is explained by contributions from the dipping part of the anticline.

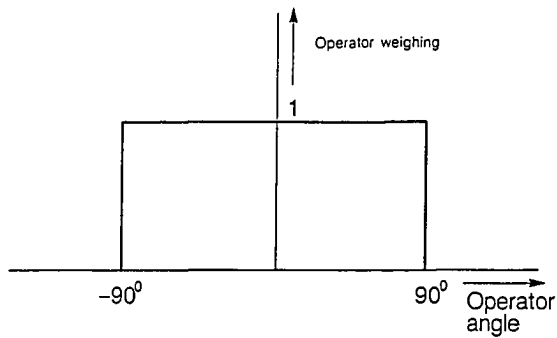


**Figure 2.10** The operator angle is limited to  $\pm 90^\circ$  with respect of the normal to the surface to eliminate contributions as indicated in figure 2.9.

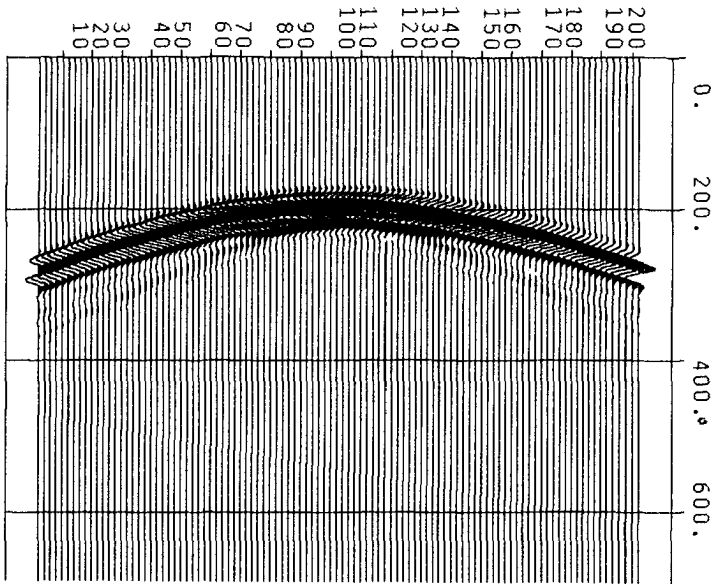


Figure 2.11 Wave field at  $z = 1000$  m obtained with the Rayleigh integral using a  $\pm 90^\circ$  operator angle limitation.

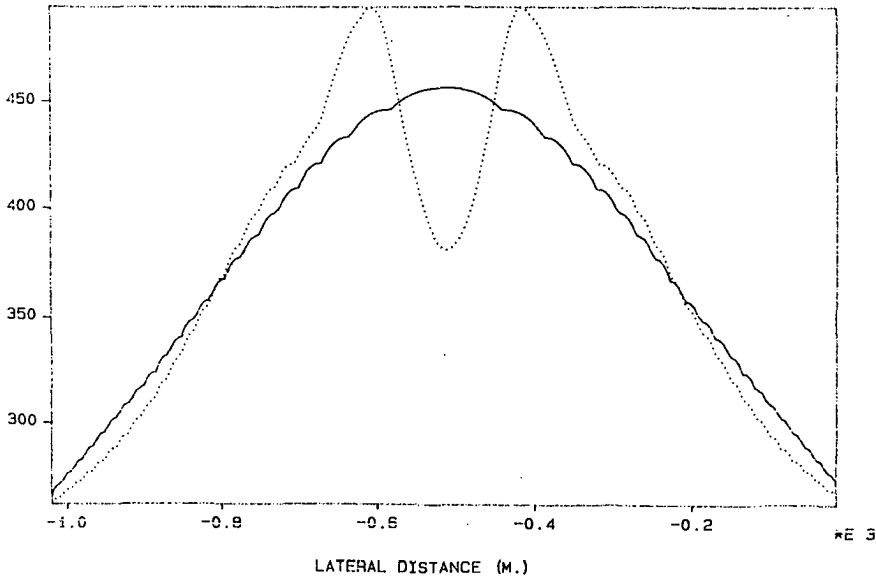


Figure 2.12 Amplitude cross section for the data from figure 2.11. The Rayleigh  $90^\circ$  result (dotted) is compared to the analytical solution (solid).

both directions. One way of suppressing the additional event is to put an additional weighing coefficient in the Rayleigh integral. This coefficient should be zero for angles between  $\mathbf{r}$  and  $\mathbf{n}$  of less than  $-90^\circ$  or over  $90^\circ$  and one for angles between  $-90^\circ$  and  $90^\circ$  (figure 2.10). Thus effectively limiting the operator angle to  $-90^\circ$  to  $90^\circ$ .

With this additional weighing coefficient the additional event disappears as shown in figure 2.11. However, the amplitude cross section shown in figure 2.12 shows incorrect amplitudes for the wave field extrapolated with a Rayleigh based propagation operator.

So for wave field extrapolation from a non-planar interface the full Kirchhoff integral should be used if the amplitude information should be preserved. If the Rayleigh integral is used an operator angle limitation should be applied to suppress artifacts. However, the amplitude information is not suppressed. In the next section the Green's function will be discussed.

## 2.5 THE GREEN'S FUNCTION

One intuitively would think that the propagation properties of the medium should be in the Kirchhoff integral. Well, the Green's functions may be interpreted as an impulse response of the medium at the surface  $S$  due to a point source in  $A$ . A strong analogy with the filter theory exists. In order to obtain the transfer function of a filter, a  $\delta$  pulse is used as input. The measured output is the transfer function. This procedure is identical to the derivation of the Green's function (figure 2.13). In order to obtain the output of the filter for an arbitrary input, the transfer function is convolved with the input signal. In the Kirchhoff integral the impulse response  $G$  is spatially convolved with the input wave field. In inverse extrapolation which will be discussed in the next chapter the purpose is to eliminate the wave propagation effects of the medium and do an inverse filtering for the propagation effects.

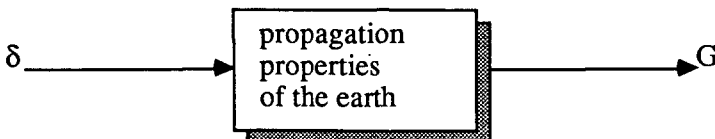


**Figure 2.13** The Green's function is obtained by applying a dirac source to the medium. In filter theory a similar method is used to obtain the transfer function of a filter.

One can also observe some aspects of the important reciprocity properties in acoustic wave field theory. The Green's function is obtained by placing a point source in point  $A$  and register the response at the surface  $S$ . For the extrapolation the response at point  $A$  due to point sources

on the surface  $S$  is required. However, because of reciprocity this is equivalent to a point source in  $A$  and registration on  $S$ .

Another interesting property about the Green's function is that the properties of the medium should be identical to the actual medium inside  $V$  only. Outside  $V$  any medium properties could be chosen for  $G$ . Usually one would take the medium outside  $V$  to be homogeneous to simplify the calculations for  $G$ . Consider the geometry of figure 2.14a consisting of a homogeneous space with some source in  $B$  a volume bounded by  $S$ . The Green's function for calculating the wave field in  $A$  from the wave field on  $S$  is straight forward. A homogeneous medium would be taken inside and outside  $V$ . The Green's function only contains the direct wave field from  $A$  to the surface  $S$ . Now change the medium for calculating  $G$  by including a reflecting surface outside  $V$  (figure 2.14b). The wave field in  $A$  should be unchanged. However the Green's function changed since it now contains a scattered component as well as the direct component. A different Green's function is applied to the same wave field and should give the same wave field in  $A$ , since only the medium for  $G$  has been changed; not the actual medium. This apparent contradiction is solved if the contributions of the Kirchhoff integral for each part of  $S$  to the

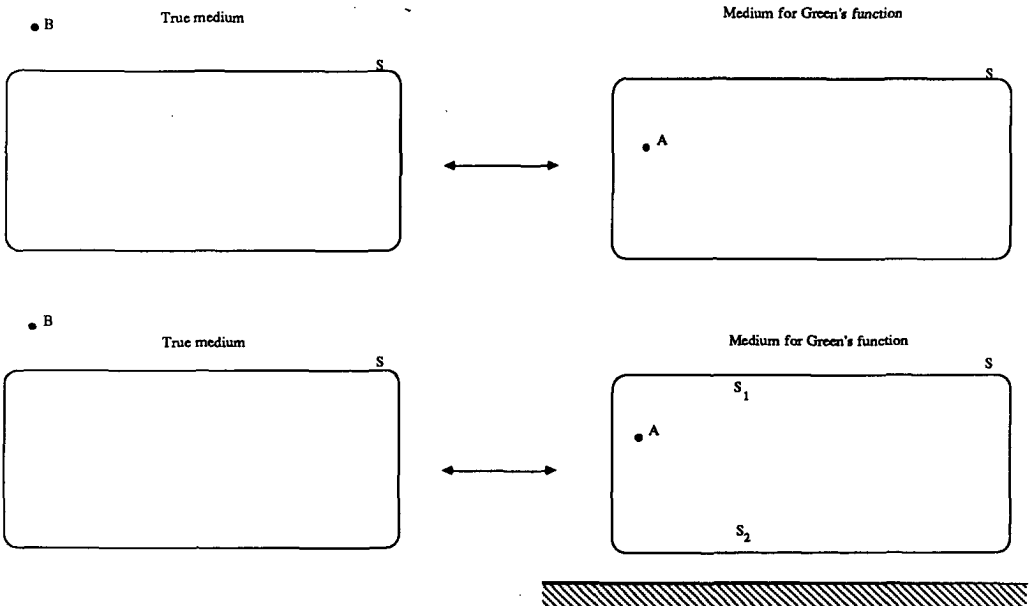


**Figure 2.14** Outside the volume  $V$  bounded by  $S$  the medium for the Green's function may be freely chosen. Both the upper and lower choice for the Green's function will result in the correct wave field in any point inside  $S$ .

wave field in A is examined separately. This procedure will also be followed later on for obtaining inverse extrapolation operators. By analysis of the various contributions in the  $k_x$ - $\omega$  domain, it can easily be verified that for  $S_1$ , the upper part of S the up going (scattered) part of the Green's function applied to the down going wave field cancels the up going part of the Green's function on  $S_2$  applied to the wave field at  $S_2$ . So only the direct part of the Green's function contributes to the wave field in A. Therefore the wave field in A is the same for both choices of the Green's function.

Changing the medium for the Green's function outside V is a very powerful tool for obtaining a more suitable extrapolation operator. The Kirchhoff integral contains two terms. One term involves the pressure wave field on S and a spatial derivative of the Green's function. The second term contains the normal component of the particle velocity and the Green's function. As discussed in a previous section the two terms in the Kirchhoff integral become identical in the case of specific surface geometry and may be replaced by only one term. In the case of a curved surface a different approach should be used to eliminate one of the terms in the Kirchhoff integral. If on  $S_0$  (figure 2.15) boundary conditions for G are chosen such that either

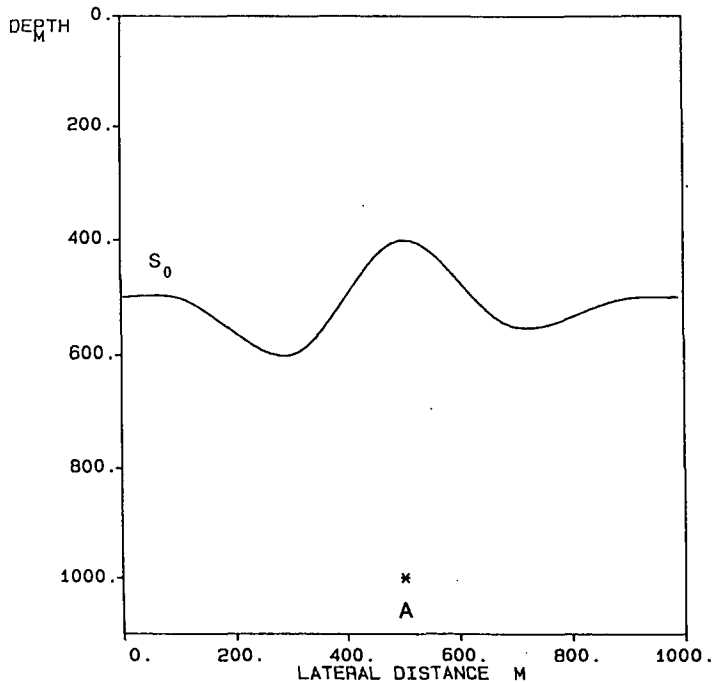


**Figure 2.15** By choosing the boundary condition  $G = 0$  on  $S_0$ , one term in the Kirchhoff integral is eliminated.

$G$  or  $\partial G/\partial n$  vanishes only one term of the Kirchhoff integral remains. Since we are free to choose the medium for  $G$  outside  $V$ , specifying boundary conditions on  $S$  is no approximation. A boundary condition

$$G = 0 \quad \text{on } S, \quad (2.35)$$

corresponds to a free surface. Note that the Green's function becomes more complex for the arbitrarily curved surface than for the planar surface. This is illustrated for the geometry from figure 2.16. The medium is homogeneous. Consider two cases in which the surface on which

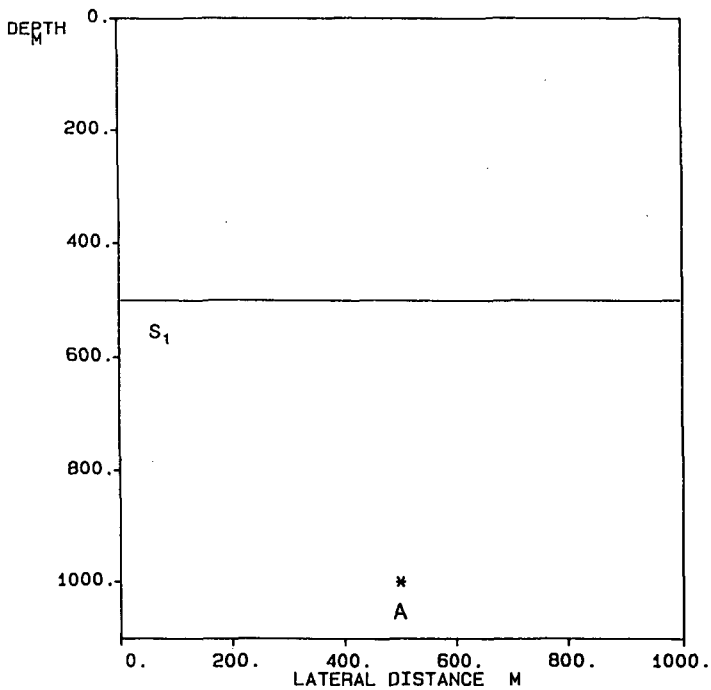


**Figure 2.16** For a planar surface and a homogeneous medium below  $S_1$ , the Green's function may be determined analytically.

the wave field is known is either planar ( $S_1$ ) or curved ( $S_0$ ). In order to obtain the wave field in  $A$  from *only* the pressure data on  $S_0$  or  $S_1$  a suitable Green's function should be used. In the case of a planar surface the Green's function may be derived analytically

$$\frac{\partial G}{\partial n} = -2\rho \frac{1 + jkr}{r^2} \cos \theta e^{-jkr} , \quad (2.36)$$

with

$$r = |\mathbf{r} - \mathbf{r}_A| \quad (2.37)$$

and

$$\cos \theta = \frac{z - z_A}{|r|} . \quad (2.38)$$

This Green's function is shown in figure 2.17.

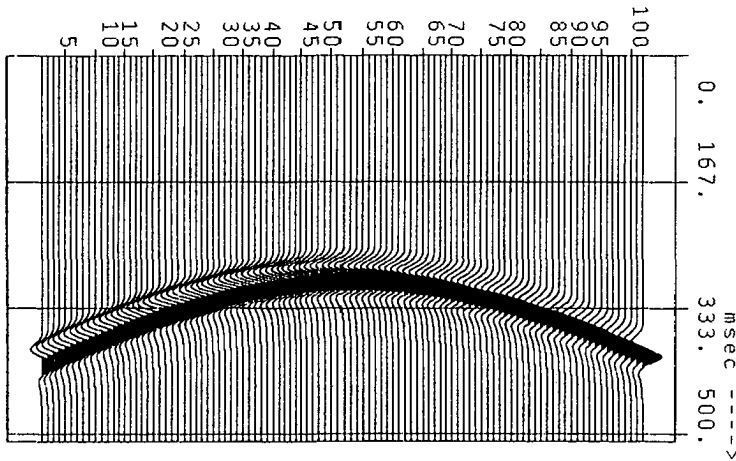


Figure 2.17 The derivative of the Green's function at the surface  $S_1$  from figure 2.16.

For the curved surface the Green's function can not be derived analytically since the boundary condition  $G = 0$  on  $S$  results in direct waves from the dirac source in point  $A$  as well as reflection from the free surface  $S_1$ . However with a finite difference modeling technique the Green's function can be found. The result is shown in figure 2.18. Note that both Green's functions are not caused by dirac sources in  $A$  since a high bandwidth source cannot be modeled with finite differences. However the source spectrum is according to the dirac source for the bandwidth of interest.

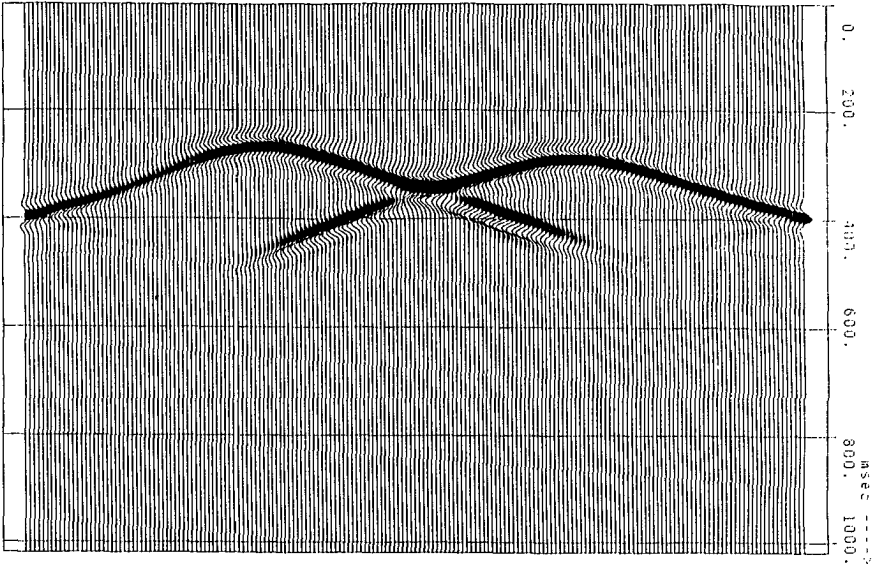
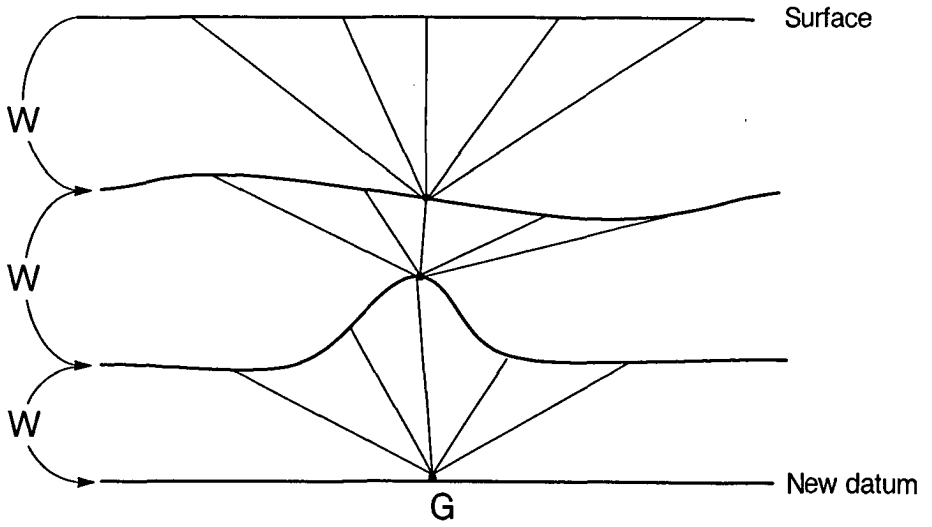


Figure 2.18 The derivative of the Green's function at the surface  $S_0$  from figure 2.15.

## 2.6 RECURSIVE VERSUS NON-RECURSIVE EXTRAPOLATION

In order to extrapolate a wave field with the Kirchhoff integral (2.11) the Green's function should be known. For subsurface models discussed in chapter 1 two different wave field extrapolation procedures are of interest. A recursive extrapolation or a non-recursive extrapolation (figures 2.19 and 2.20). The model is defined as a stack of layers with a relatively simple velocity profile in each layer. The Green's function for each layer may be derived analytically for most simple velocity profiles. In the next sections will be shown that under the assumptions of one-way wave field propagation this procedure has some nice properties when used for inverse wave field extrapolation. The wave field is extrapolated from interface to interface. At each interface the boundary conditions should be met.

In case of the non-recursive wave field extrapolation procedure the wave field is extrapolated from the surface to the target zone in one step. The Green's function contains the propagation effects of the complete overburden structure including transmission effects at the interfaces. An analytical expression for the Green's function is not available for most structures. A numerical modeling procedure for obtaining the Green's functions is therefore required. Accurate



**Figure 2.19** For the recursive extrapolation the wave field is extrapolated from interface to interface.

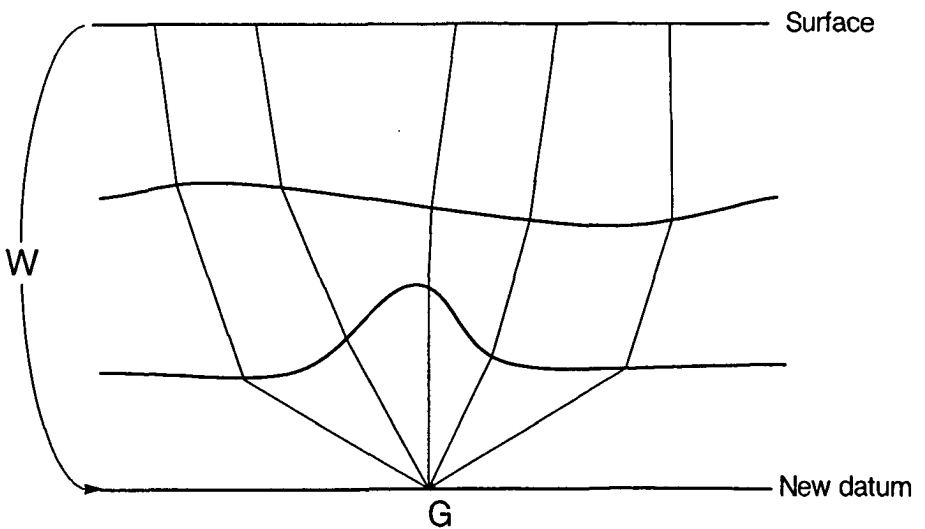


**Figure 2.20** In the non-recursive extrapolation the wave field is extrapolated across many interfaces. The Green's functions should contain the propagation effects of all layers.

modeling procedures based on finite difference approximation of the wave equation are computationally expensive. Ray tracing type of modeling techniques that are based on a high frequency approximation of the wave equation may be feasible for the non-recursive wave field extrapolation. However this has not been studied for this thesis. The recursive extrapolation has been applied in all redatuming experiments. For a discussion on non-recursive wave field extrapolation in redatuming the reader is referred to the TRITON project progress reports (1986, 1987, 1988).

## 2.7 ONE-WAY VERSUS TWO-WAY FIELD EXTRAPOLATION

In migration and inversion different types of wave field extrapolation techniques are applied. A one-way extrapolation technique is employed or a two-way extrapolation technique. In the one-way extrapolation the total wave field is decomposed in up going and down going waves. The up going and down going waves are supposed to propagate independently. This is an approximation since in general interaction does occur especially for waves traveling at high angles in case of velocity gradients. However, for models as discussed in chapter 1 the interaction takes place at the interfaces at which up going and down going waves are coupled through the boundary conditions. Outside the inhomogeneous regions in the subsurface model the up going and down going waves may be extrapolated separately.

$$P^+(z_1) = W^+(z_1, z_0) P^+(z_0) \quad , \quad (2.39)$$

$$P^-(z_0) = W^-(z_0, z_1) P^-(z_1) \quad , \quad (2.40)$$

where  $W^+(z_1, z_0)$  and  $W^-(z_0, z_1)$  are extrapolation operators for up going and down going waves respectively. The one-way wave extrapolation techniques are very robust with respect to model errors. A slightly mispositioned reflector causes only a small distortion in the extrapolated wave field propagation. At acoustic impedance contrasts coupling of up going and down going waves occurs. The boundary conditions should be met explicitly. The multiple reflections are not handled properly. They could be eliminated by applying multiple elimination techniques such as proposed by Berkhout (1982) and currently being developed in the TRITON project (1986, 1987, 1988).

In two-way wave field extrapolation techniques the total wave field is considered. Both up going and down going waves are extrapolated simultaneously. Since the total wave field is continuous across acoustic impedance contrasts the boundary conditions are included implicitly. So transmission effects and multiple reflections are incorporated. A drawback of two-way wave equation based extrapolation techniques is the sensitivity to model errors. In the two-way wave equation based inverse extrapolation the multiple reflections are eliminated as the

extrapolation depth increases. If however a reflector is mispositioned the multiple reflections according to the true depth model occur at different times than the multiple reflections according to the erroneous migration model. This results in a serious distortion of the extrapolated wave field. Since the depth model used for the redatuming is a propagation model and not a reflection model, the reflector positioning may not be that accurate. Therefore for our purpose a robust one-way wave equation based extrapolation technique is preferred over a two-way wave equation based extrapolation operator.

## 2.8 A 2-D APPROXIMATION FOR A 3-D WORLD

The earth is a three dimensional structure. Efforts to obtain an accurate image of the earth's subsurface should be based on 3-D models. However in seismics quite a lot of 2-D surveys have been carried out. Nowadays 3-D seismics is becoming more popular. The processing of the data from a 3-D survey requires a huge computational capacity which has only become available in the last decade through super computers like a CRAY. The study into redatuming with an emphasis on the preservation of the amplitude information presented in this thesis has been implemented for 2-D. Although the theoretical base for the redatuming is 3-D a 2-D approximation has been chosen because of the available computational capacity. A 3-D redatuming procedure is currently being developed within the TRITON (1986, 1987, 1988) project.

The 2-D approximation may still give good results in practice if the subsurface is laterally invariant in the cross line direction. No out of plane events will distort the seismic reflection data. Because of the assumption of the wave field being constant in the cross line direction a difference in geometrical spreading for 3-D ( $1/r$ ) and 2-D ( $1/\sqrt{r}$ ) occurs causing an incorrect scaling of the data during extrapolation. For a specific target depth local amplitude changes along a reflector are directly related to changes in acoustic impedance along the reflector. A more accurate approach for 2-D surveys is the  $2^{1/2}$  D approximation proposed by Bleistein (1984). Again the earth is assumed to be invariant in the cross line direction. However the wave field is not assumed constant in this direction. A geometrical spreading effect is included. The amplitude behaviour for a  $2^{1/2}$  D redatuming may be more accurate for dipping structures. The  $2^{1/2}$  D approximation has not been studied for this thesis. The differences are summarized in table 2.1.

**Table 2.1**  
Geometrical spreading effects and medium assumption  
for 2-D, 2<sup>1/2</sup>-D and 3-D wave propagation.

3-D	2-D	2 <sup>1/2</sup> -D
Spherical spreading (1/r)	Cylindrical spreading (1/√r)	Spherical spreading (1/r)
Velocity and density variations in x, y and z	Velocity and density variations in x and z	Velocity and density variations in x and z

For 2-D the Kirchhoff integral (2.11) and the Rayleigh integral (2.31) should be modified. The integration in the cross line direction should be carried out to go from 3-D to 2-D. The derivation is shown in appendix A. For the geometry shown in figure 2.21 the 3-D Kirchhoff integral is given by

$$P(\mathbf{r}_2, \omega) = \frac{1}{4\pi} \int_S \frac{1 + jkr}{r^2} \cos(\varphi_1) e^{-jkr} P(\mathbf{r}_1, \omega) + j\omega\rho_0 V_n(\mathbf{r}_1, \omega) \frac{e^{-jkr}}{r} dS, \quad (2.41)$$

for the Green's function a homogeneous layer has to be taken

$$G = -\rho \frac{e^{-jkr}}{r}, \quad (2.42)$$

$$r = |\mathbf{r}_1 - \mathbf{r}_2|.$$

The 2-D Kirchhoff integral is given by

$$P(\mathbf{r}_2, \omega) = \frac{1}{4\pi} \int_L -jk\pi \cos \varphi_1 H_1^{(2)}(kr) P(\mathbf{r}_1, \omega) + \omega\rho_0\pi H_0^{(2)}(kr) V_n(\mathbf{r}_1, \omega) dL, \quad (2.43)$$

in which H<sub>0</sub><sup>(2)</sup> and H<sub>1</sub><sup>(2)</sup> represent Hankel functions.

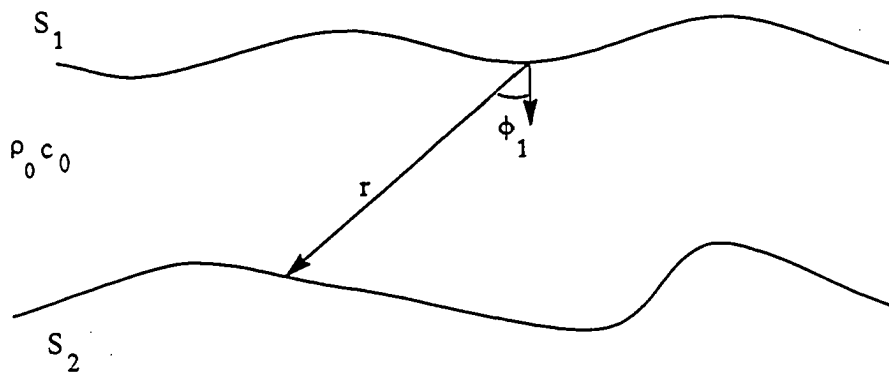


**Figure 2.21** The geometry for the 2-D extrapolation operator. The medium inbetween of the two interfaces is homogeneous.

---

## INVERSE WAVE FIELD PROPAGATION

### 3.1 INTRODUCTION

Generally an inverse wave field extrapolation operator is derived by inverting the forward extrapolation operator. In this chapter an inverse extrapolation operator is derived directly from the wave equation and the theorem of Gauss. Recursive application of this operator yields a correct amplitude behaviour for the primary propagating waves. For a non-recursive application of the inverse extrapolation operator, it will be shown that for arbitrarily inhomogeneous media the amplitude errors are of the second order.

In seismics or any other field in which echo acoustical measurements are carried out, the registration surface does usually not coincide with the area of interest. In surface seismics the measurements are carried out at the surface whereas the reservoirs may be located up to several kilometers below the surface. In order to determine the potential of a reservoir the rock properties in the target area should be determined. The acoustic response, which is related to the rock properties, propagates from the target zone to the surface. In the previous chapter the forward wave propagation has been discussed. However, in order to solve for the medium properties given the response and the source wave field, the forward problem has to be inverted. For the wave field propagation a band limited inverse extrapolation operator is found by taking the complex conjugate of the forward operator. The approach is commonly known as matched inverse. Unfortunately the inversion is only valid for planar interfaces. For an arbitrarily inhomogeneous medium the inversion of the forward operator may become very

complicated. The matched inverse has been used by various authors (Schneider [1978], Castle [1982], Carter and Frazer [1984], Wiggins [1984], Berryhill [1984]) for the inverse wave field extrapolation through complicated media. This inverse operator is commonly accepted to handle the phase properly. However the amplitude handling of the inverse wave propagation operator is hardly ever considered. In the next sections the matched inverse will be briefly discussed. Furthermore an inverse propagation operator will be examined which also holds for curved layer boundaries. This inverse operator will be derived directly from the theorem of Gauss and the wave equation instead of inverting for the forward problem. The amplitude behaviour of this generalized 'Kirchhoff summation' operator will be investigated. It will be shown that for an arbitrarily inhomogeneous medium the amplitude errors are of the second order.

### 3.2 INVERSE EXTRAPOLATION THROUGH A PLANAR HOMOGENEOUS LAYER

In this section the inverse extrapolation through a horizontal layer is discussed. The amplitude behaviour of this operator is investigated for comparison with the 'generalized Kirchhoff summation' operator which will be derived later on. The matched inverse back propagation operator is often used in migration or redatuming schemes. For a rigorous discussion the reader is referred to Berkhout [1982]. For the forward model consider an upward traveling wave field  $P^-(\mathbf{r}, \omega)$  at a planar surface  $S_0$  (figure 3.1). The up going wave field at  $S_0$  is obtained by applying the Rayleigh II integral to the wave field at  $S_1$ .

$$P_0^-(\mathbf{r}_0, \omega) = \int_{S_1} W(\mathbf{r}_0, \mathbf{r}_1, \omega) P^-(\mathbf{r}_1, \omega) dS_1(\mathbf{r}_1) \quad (3.1)$$

where

$$W(\mathbf{r}_0, \mathbf{r}_1, \omega) = \frac{1}{2\pi} \frac{1 + jk\Delta r}{\Delta r^2} \cos \theta e^{-jk\Delta r} \quad (3.2)$$

with

$$\mathbf{r}_0 = (x, y, z_0)$$

$$\mathbf{r}_1 = (x', y', z_1)$$

$$\Delta r = |\mathbf{r}_0 - \mathbf{r}_1| = \sqrt{(x - x')^2 + (y - y')^2 + \Delta z^2}$$

$$\Delta z = z_1 - z_0$$

$$\cos \theta = \Delta z / r$$

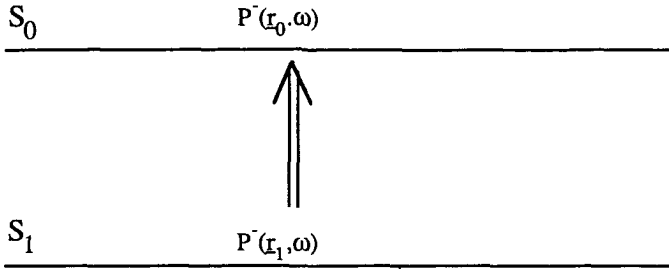


Figure 3.1 The wave field at S1 may be extrapolated to S0 with the phase shift operator.

The integral is equivalent to a two dimensional convolution over  $x$  and  $y$  so

$$P^-(x, y, z_0, \omega) = W(x, y, \Delta z, \omega) * P^-(x, y, z_1, \omega) \quad (3.3)$$

By transforming the operator and the wave field to the wave number domain the convolution becomes a multiplication

$$\tilde{P}^-(k_x, k_y, z_0, \omega) = \tilde{W}(k_x, k_y, \Delta z, \omega) \tilde{P}^-(k_x, k_y, z_1, \omega) \quad (3.4)$$

with

$$\tilde{W}(k_x, k_y, \Delta z, \omega) = e^{-jk_z \Delta z} \quad (3.5)$$

and

$$\begin{aligned} k_z &= \sqrt{k^2 - k_x^2 - k_y^2} & \text{for } k^2 \geq k_x^2 + k_y^2 \\ k_z &= -j\sqrt{k_x^2 + k_y^2 - k^2} & \text{for } k^2 < k_x^2 + k_y^2 \end{aligned} \quad (3.6)$$

The transformed operator is the well known phase shift operator. By applying this operator to the data on a planar surface a wave field propagation over a depth step  $\Delta z$  occurs. For the propagating waves ( $k_x^2 + k_y^2 \leq k^2$ ) the amplitude of the operator is 1 independent of the extrapolation step  $\Delta z$ . For the evanescent waves ( $k_x^2 + k_y^2 > k^2$ ) the amplitude decays exponentially (figure 3.2).

The inverse wave field extrapolation operator  $F$  should invert for the wave propagation effects

$$\tilde{W} F = I \quad (3.7)$$

An inverse wave field operator  $F$  for the phase shift operator is given by

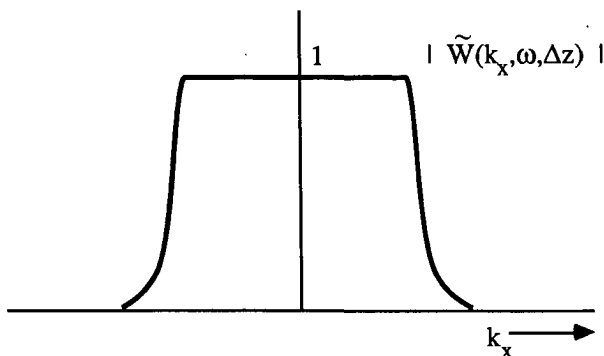


Figure 3.2 The amplitude of the phase shift operator in the  $k_x$ - $\omega$  domain is 1 for the propagating waves.

$$\tilde{F}(k_x, k_y, \Delta z, \omega) = \frac{1}{\tilde{W}(k_x, k_y, \Delta z, \omega)} \quad (3.8)$$

Accuracy and stability should always be investigated for an inverse wave propagation operator. This inverse operator is accurate since

$$\tilde{W} \tilde{F} = 1 \quad (3.9)$$

However, for the evanescent part of the wave field this inverse operator increases exponentially with  $\Delta z$ . Therefore it is not a stable operator and can not be applied to noisy data. In order to stabilize the inverse operator the following approximation is often made

$$\langle \tilde{F}(k_x, k_y, \Delta z, \omega) \rangle = \tilde{W}^*(k_x, k_y, \Delta z, \omega) \quad (3.10)$$

This operator is an exact inverse for the propagating waves. For the evanescent waves the operator is not correct (figure 3.4).

$$\tilde{W} \tilde{W}^* = \begin{cases} 1 & \text{for } k_x^2 + k_y^2 \leq k^2 \\ \rightarrow 0 & \text{for } k_x^2 + k_y^2 > k^2 \end{cases} \quad (3.11)$$

So  $\tilde{W}^*$  is a stable spatially band limited approximation of  $F$ . In general the spatial band limitation will restrict the maximum obtainable spatial resolution. For a more extensive discussion on the resolution in the migration problem the reader is referred to Berkhout [1984].

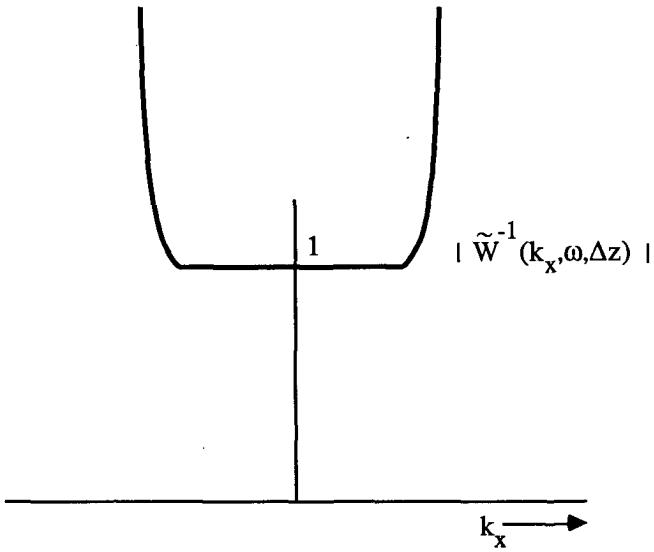


**Figure 3.3a** The inverse of the phase shift operator is unstable for the evanescent waves. The amplitude increases exponentially.

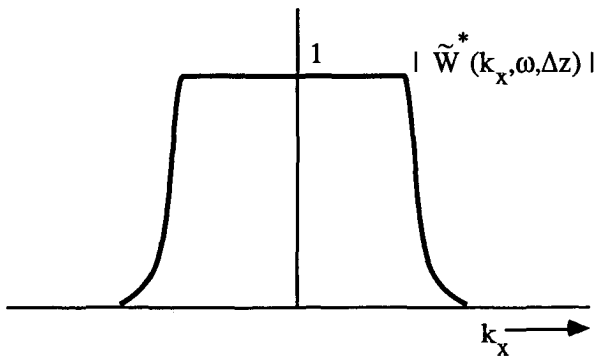


**Figure 3.3b** The matched inverse phase shift operator is a stable operator.

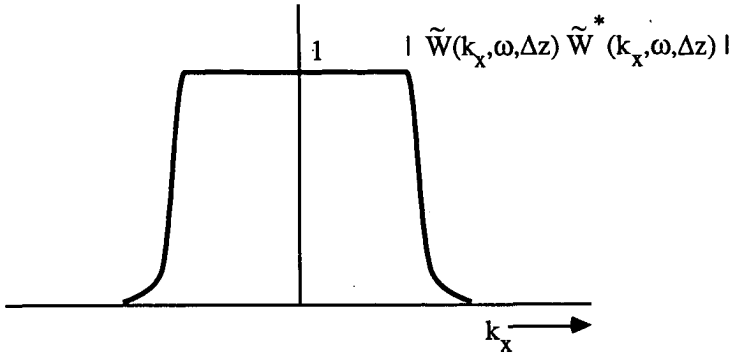


**Figure 3.4** The matched inverse phase shift operator correctly inverts for the propagation effects for the propagating waves. The evanescent waves are not handled correctly.

### 3.3 INVERSE EXTRAPOLATION THROUGH AN INHOMOGENEOUS MEDIUM

In this section the inverse extrapolation for non-planar interfaces and inhomogeneous media is discussed. Since the Rayleigh integral is not valid for curved surfaces the full Kirchhoff integral (equation 2.11) should be applied. However in the problem of inverting the Kirchhoff integral the number of unknowns is twice the number of knowns. The pressure  $P$  is known whereas both pressure and particle velocity on  $S$  should be calculated. Even if both  $P$  and  $V_n$  are measured the equations will not be independent. So inverting the forward problem does not seem to be a solution for the inverse propagation from non-planar interfaces. Therefore an alternative approach should be followed. Again the Kirchhoff integral is derived but now for different Green's functions. Consider the geometry from figure 3.5.

In the previous chapter the Green's functions should satisfy the following wave equation

$$\rho \nabla \cdot \left( \frac{1}{\rho} \nabla G \right) + k^2 G = -\rho 4\pi \delta(\mathbf{r} - \mathbf{r}_A) \quad (3.12)$$

For the inverse wave propagation a slightly modified Green's function is used. These Green's functions  $G$  should satisfy the following equation in the bounded domain  $V$

$$\rho^* \nabla \cdot \left( \frac{1}{\rho^*} \nabla G \right) + k^{*2} G = -\rho^* 4\pi \delta(\mathbf{r} - \mathbf{r}_A) \quad (3.13)$$

For a loss-less medium  $\rho(\mathbf{r})$  and  $k(\mathbf{r})$  are real and the Green's function  $G$  defined by the last equations is identical to the Green's function defined by equation 3.12. For lossy media, the

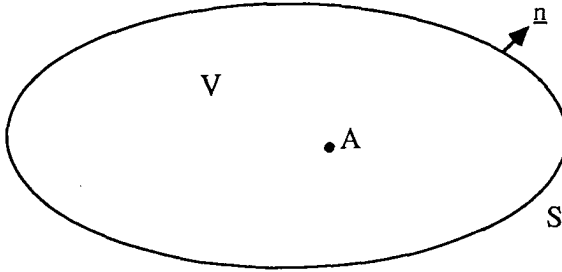


Figure 3.5 Bounded domain V for the Kirchhoff integral.

medium parameters  $\rho(\mathbf{r})$  and  $k(\mathbf{r})$  should be taken complex valued. A small negative imaginary part should be added to wave number according to

$$k(\mathbf{r}) = k_0(\mathbf{r}) (1 - j\eta) \quad \text{with } \eta \ll 1. \quad (3.14)$$

To get an idea what the Green's functions look like, consider a homogeneous medium. The forward propagation solution to the above equations are respectively

$$G(\mathbf{r}, \mathbf{r}_A, \omega) = \frac{\rho(\mathbf{r}) e^{-jk_0|\mathbf{r}-\mathbf{r}_A|}}{|\mathbf{r}-\mathbf{r}_A|} e^{-k_0\eta|\mathbf{r}-\mathbf{r}_A|} \quad (3.15)$$

and

$$G'(\mathbf{r}, \mathbf{r}_A, \omega) = \frac{\rho^*(\mathbf{r}) e^{-jk_0|\mathbf{r}-\mathbf{r}_A|}}{|\mathbf{r}-\mathbf{r}_A|} e^{+k_0\eta|\mathbf{r}-\mathbf{r}_A|} \quad (3.16)$$

The absorption which occurs in lossy media is described by the term  $e^{-k_0\eta|\mathbf{r}-\mathbf{r}_A|}$ . In addition to the spherical divergence this exponential causes an amplitude decay for the Green's wave field propagating away from the source point  $\mathbf{r}_A$ . The second solution contains the term  $e^{+k_0\eta|\mathbf{r}-\mathbf{r}_A|}$  which represents an amplitude increase for waves propagating away from the source in  $\mathbf{r}_A$ . This solution is physically unacceptable, so it should be rejected.

The back propagating solutions to the above wave equations are

$$G^*(\mathbf{r}, \mathbf{r}_A, \omega) = \frac{\rho^*(\mathbf{r}) e^{+jk_0|\mathbf{r}-\mathbf{r}_A|}}{|\mathbf{r}-\mathbf{r}_A|} e^{-k_0\eta|\mathbf{r}-\mathbf{r}_A|} \quad (3.17)$$

and

$$G^*(\mathbf{r}, \mathbf{r}_A, \omega) = \frac{\rho e^{+jk_0|\mathbf{r}-\mathbf{r}_A|}}{|\mathbf{r}-\mathbf{r}_A|} e^{+k_0\eta|\mathbf{r}-\mathbf{r}_A|} \quad (3.18)$$

Since this wave field  $G$  propagates towards  $\mathbf{r}_A$  the term  $e^{-k_0\eta|\mathbf{r}-\mathbf{r}_A|}$  represents an amplitude increase. Therefore this solution is physically not acceptable. The other solution contains the exponential term  $e^{+k_0\eta|\mathbf{r}-\mathbf{r}_A|}$  which represents an amplitude attenuation for the wave field propagating towards  $\mathbf{r}_A$ . So this back propagating Green's function is an acceptable solution the wave equation given in relation (3.13).

With the back propagating Green's function a second version of the Kirchhoff integral will be derived. In the previous chapter the Kirchhoff integral has been derived using the forward propagating Green's function. Similar to the derivation in the previous chapter define a vector  $\mathbf{a}$  field in  $V$

$$\mathbf{a} = \frac{1}{\rho} \nabla G^* - \frac{1}{\rho} G^* \nabla P \quad (3.19)$$

After application of the theorem of Gauss (2.7) to this vector field and substituting equations (2.3) and (3.13) the following integral equation is obtained.

$$P(\mathbf{r}_A, \omega) = \frac{-1}{4\pi} \int_S \frac{1}{\rho} \left[ P \left( \frac{\partial G^*}{\partial n} \right) - \left( \frac{\partial P}{\partial n} \right) G^* \right] dS \quad (3.20)$$

This integral equation is identical to the Kirchhoff integral from equation 2.11 except for the complex conjugate Green's functions. Again as for the forward propagation operator the configuration of a closed surface is not suited for the seismic application. The wave field is only known for a part of the surface. At this point in the forward modeling a geometry of a hemisphere and a non-planar surface was chosen. However since the hemisphere could enclose sources (inverse extrapolation is towards the sources) which would make the integral invalid, this geometry should not be used here. For the inverse extrapolation consider the geometry depicted in figure 3.6.

The pressure and particle velocity is assumed to be known at the surface  $S_0$  of infinite extend. Consider a closed surface with the shape of a pillar box. The top of the box is the acquisition surface  $S_0$ . The bottom of the box is  $S_1$ . The rim of the box  $S_\infty$  is at infinity. Furthermore all (secondary) sources are located below  $S_1$ . Since  $S_\infty$  is of finite extend and located at infinity, the contribution of the pressure at  $A$  from this surface vanishes. So for the configuration of figure 3.6 the Kirchhoff integral from equation 3.20 may be replaced by

$$P(\mathbf{r}_A, \omega) = P_0(\mathbf{r}_A, \omega) + P_1(\mathbf{r}_A, \omega) \quad , \quad (3.21)$$

with

$$P_0(\mathbf{r}_A, \omega) = \frac{-1}{4\pi} \int_{S_0} \frac{1}{\rho} \left[ P \left( \frac{\partial G^*}{\partial n} \right) - \left( \frac{\partial P}{\partial n} \right) G^* \right] dS \quad , \quad (3.22)$$

$$P_1(\mathbf{r}_A, \omega) = \frac{-1}{4\pi} \int_{S_1} \frac{1}{\rho} \left[ P \left( \frac{\partial G^*}{\partial n} \right) - \left( \frac{\partial P}{\partial n} \right) G^* \right] dS \quad . \quad (3.23)$$

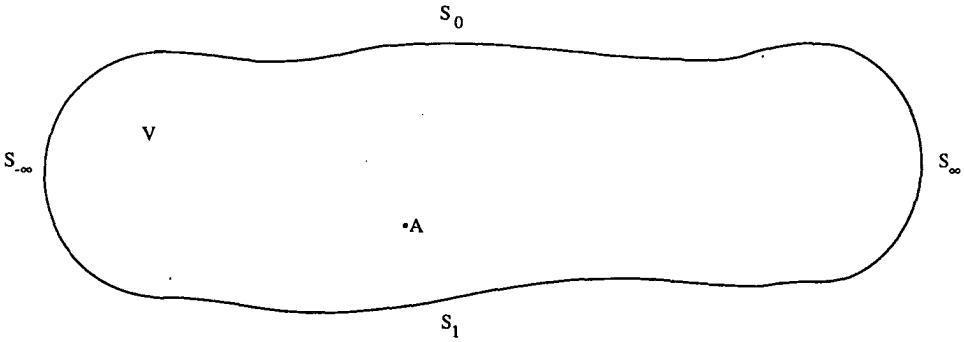


**Figure 3.6** Geometry for deriving an inverse Kirchhoff extrapolation operator. The volume V has the shape of a pilar box, a cross section is shown.

Moving  $S_1$  to infinity similar to the derivations for the forward model will cause V to contain sources. So the Kirchhoff integral in equation 3.23 will not be valid. However because of contributions over  $S_1$  the integral is still not suited for wave field extrapolation purposes. The wave field is only known at  $S_0$ . Therefore the integral over  $S_1$  (3.23) should be investigated more closely.

In order to simplify the evaluation of the integral over  $S_1$  a slightly different geometry should be chosen. The surface  $S_1'$  is now planar and horizontal (figure 3.7) instead of curved. At surface  $S_1'$  the total wave field may be split up in an up going (-) and down going (+) components.

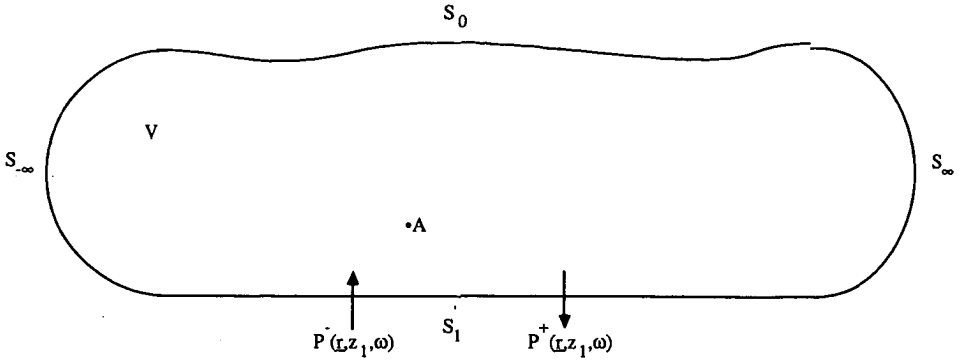


Figure 3.7 The surface  $S_1$  from figure 3.6 is replaced by a planar surface  $S_1'$ .

$$P(\mathbf{r}, \mathbf{r}_1, \omega) = P^+(\mathbf{r}, \mathbf{r}_1, \omega) + P^-(\mathbf{r}, \mathbf{r}_1, \omega) \quad , \quad (3.24)$$

$$G(\mathbf{r}, \mathbf{r}_1, \omega) = G^+(\mathbf{r}, \mathbf{r}_1, \omega) + G^-(\mathbf{r}, \mathbf{r}_1, \omega) \quad , \quad (3.25)$$

with

$$\mathbf{r}_1 = (x, y, z_1) \text{ and } \mathbf{r} = (x, y, z) \quad . \quad (3.26)$$

Suppose the medium is loss-less and homogeneous in an infinite region around  $z = z_1$ .

$$\begin{aligned} \nabla \rho &= 0 \\ \nabla c &= 0 \end{aligned} \quad \text{at } z = z_1 \quad . \quad (3.27)$$

The up and down going wave field satisfy the one-way wave equations (2.21) and (2.22). A slightly modified version of Parseval's theorem reads

$$\iint_{-\infty}^{\infty} A(x, y) B^*(x, y) dx dy = \frac{1}{2\pi} \iint_{-\infty}^{\infty} \tilde{A}(k_x, k_y) \tilde{B}^*(k_x, k_y) dk_x dk_y \quad , \quad (3.28)$$

with  $A$  and  $B$  being some space dependent function and the 2-D spatial Fourier transform is defined by

$$\tilde{A}(k_x, k_y) = \iint_{-\infty}^{\infty} A(x, y) e^{j(k_x x + k_y y)} dx dy \quad . \quad (3.29)$$

Furthermore for the  $z$  derivatives we may write

$$\frac{\partial P}{\partial z}(\mathbf{r}, \omega) = jk_z \tilde{P}(k_x, k_y, z_1, \omega) \quad , \quad (3.30)$$

with

$$k_z = \sqrt{k^2 - k_x^2 - k_y^2} \quad . \quad (3.31)$$

Applying Parseval's theorem and substitution of equation (2.23) yields

$$P_1(\mathbf{r}_A, \omega) = -\frac{1}{\rho} F_A^{-1} \left\{ \left[ \tilde{P}^+ + \tilde{P}^- \right] jk_z * \left[ -\tilde{G}^{*+} + \tilde{G}^{*-} \right] - jk_z \left[ \tilde{P}^+ - \tilde{P}^- \right] \left[ \tilde{G}^{*+} + \tilde{G}^{*-} \right] \right\}_{z_1} \quad . \quad (3.32)$$

By making the area below  $S_1'$  reflection free for the Green's functions no up going waves will occur at  $S_1'$  so

$$\rho(x, y, z > z_1) = \rho(x, y, z_1) \quad , \quad (3.33)$$

$$c(x, y, z > z_1) = c(x, y, z_1) \quad , \quad (3.34)$$

therefore  $G^- = 0$ .

Note that no assumptions are made by choosing a homogeneous medium below  $S_1'$ . So the above equation becomes

$$P_1(\mathbf{r}_A, \omega) = -\frac{2}{\rho} F_A^{-1} \left( \left[ \tilde{P}^+ + \tilde{P}^- \right] jk_z \left[ -\tilde{G}^+ \right] - jk_z \left[ \tilde{P}^+ - \tilde{P}^- \right] \tilde{G}^+ \right)_{z_1} \quad . \quad (3.35)$$

Now consider the evanescent and the propagation waves separately. For the propagating waves at  $S_1'$ ,  $k_z^*(z_1) = k_z(z_1)$  since  $k_x^2 + k_y^2 \leq k^2(z_1)$ . So

$$P_1(\mathbf{r}_A, \omega) = +\frac{2}{\rho} F_A^{-1} \left[ jk_z \tilde{G}^{*+} \tilde{P}^+ \right] \quad . \quad (3.36)$$

For the evanescent waves  $k_x^2 + k_y^2 > k^2(z_1)$ , so  $k_z^* = -k_z$  at  $z_1$ .

$$P_1(\mathbf{r}_A, \omega) = -\frac{2}{\rho} F_A^{-1} \left[ jk_z \tilde{G}^{*+} \tilde{P}^- \right] \quad . \quad (3.37)$$

Deriving an analytical expression for the inverse Fourier transform for  $P_1(\mathbf{r}_A, \omega)$  is quite difficult since the expression changes around  $k_x^2 + k_y^2 = k^2(z_1)$ . However if we assume  $A$  to be not too close to  $S_1'$  the contributions for the evanescent waves may be neglected compared to the propagating waves. So relation 3.36 is used for all values of  $k_x$  and  $k_y$ . So

$$P_1(\mathbf{r}_A, \omega) \cong \frac{2}{\rho} F_A^{-1} \left[ jk_z \tilde{G}^{*+} \tilde{P}^+ \right] \quad , \quad (3.38)$$

or

$$P_1(\mathbf{r}_A, \omega) \cong \frac{2}{\rho} \int_{S_1} \frac{\partial G^{*+}}{\partial z}(\mathbf{r}, \mathbf{r}_A, \omega) P^+(\mathbf{r}, \omega) dS' \quad (3.39)$$

This relation is identical to equation 3.23 except for the evanescent part of the wave field. Next we consider the special case of a homogeneous medium inside  $V$  and above  $S_0$ . Since the wave field at  $S_1'$  only contains up going waves,  $P_1^+ = 0$ . There are no contributions from  $S_1'$  to the wave field in  $A$  and  $P_1(\mathbf{r}_A, \omega) \cong 0$ . The wave field in  $A$  is obtained by an integral over  $S_0$  only

$$P_0(\mathbf{r}_A, \omega) = -\frac{1}{4\pi} \int_{S_0} \frac{1}{\rho} \left[ P \left( \frac{\partial G^*}{\partial n} \right) - \left( \frac{\partial P}{\partial n} \right) G^* \right] dS \quad (3.40)$$

Since only data at the acquisition surface is required, this inverse extrapolation operator is well suited for the seismic application. The pressure and normal component of the particle velocity  $V_n$  on  $S_0$  are used to obtain the wave field in point  $A$  which is closer to the sources than the acquisition surface. So an extrapolation to the sources may be carried out. Since the integral over  $S_0$  gives the correct wave field in  $A$  for the propagating waves, the integral over  $S_1$  may be neglected. So relation 3.40 holds for any shape of  $S_1$ . The inverse extrapolation from an arbitrarily curved surface  $S_0$  to an arbitrarily curved surface  $S_1$  through a homogeneous medium is therefore achieved by applying the integral equation 3.41 for all points on  $S_1$ . The integral is a full Kirchhoff type of integral involving both the pressure as well as the particle velocity. This relation could be interpreted as the matched inverse Kirchhoff integral because of the complex conjugate Green's functions. Since no approximations have been made the integral describes a *true amplitude* inverse wave field propagation for the propagating waves in homogeneous media. The incorrect handling of the evanescent waves results in a limited spatial resolution due to spatial band limitations. Note that this inverse extrapolation operator has not been obtained by inverting the forward operator but is derived directly from the theorem of Gauss. The validity of the matched inverse Kirchhoff integral is shown for a simple geometry in the following experiment. Consider a 2-D medium depicted in figure 3.8a with 2-D wave propagation. The pressure and normal component of the particle velocity of a dipole line source at  $z_2$  are measured at the curved surface  $S_0$ . The pressure response is shown in figure 3.8b. In order to obtain the wave field on  $S_1$  or  $S_2$  the wave field at  $S_0$  should be inverse extrapolated towards the source. The matched inverse Kirchhoff integral is applied to the pressure field and normal component of the particle velocity on  $S_0$  for all points  $A$  on  $S_1$  and  $S_2$ . The inverse extrapolation yields the hyperbolically shaped dipole response at  $S_1$  as shown in figure 3.9c. An amplitude cross section for this response is depicted in figure 3.9d. The maximum in each trace is plotted as a function of the lateral position. The amplitude of the response matches exactly the analytical

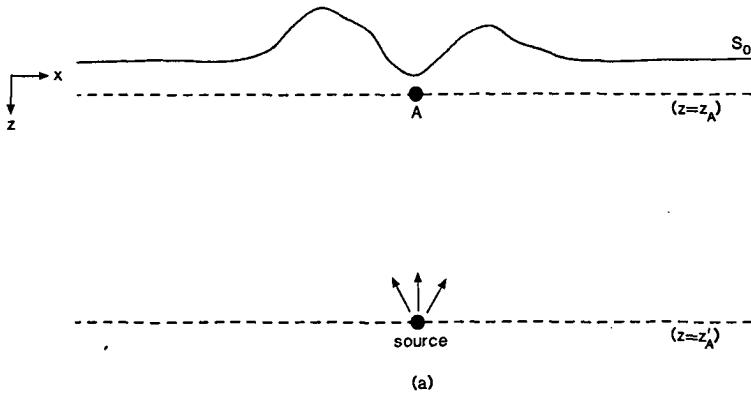


**Figure 3.8a** Geometry for inverse extrapolation of the wave field at  $S_0$  to  $S_1$ . The wave field is caused by a source at  $S_2$ . The wave field is therefore extrapolated towards the source.

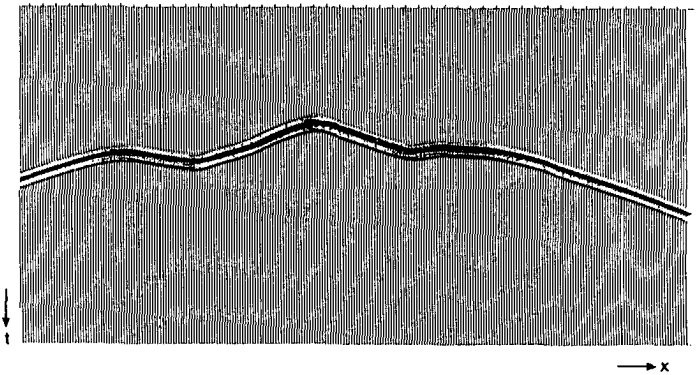


**Figure 3.8b** The wave field at  $S_0$  from figure 3.8.

response shown as the solid line. Only at the left and right spatial boundary deviations occur due to the limited aperture. This would not occur if  $S_0$  would be of infinite extent. If the data is extrapolated to the source level  $S_2$  the response shown in figure 3.9e is obtained. The level to which the wave field is extrapolated is close to the source so one of the assumptions made in the derivation of the inverse full Kirchhoff operator is violated. The inverse extrapolated wave field at the source is smeared out. In figure 3.9f the real part of the central frequency component is shown as a function of the lateral position. The true source is a spatial delta function. The smearing is due to the incorrect extrapolation of the evanescent wave field. The inverse extrapolation from  $S_0$  to  $S_1$  has also been carried out with the Rayleigh integral. This is the commonly used inverse extrapolation operator which involves the pressure only. The Rayleigh

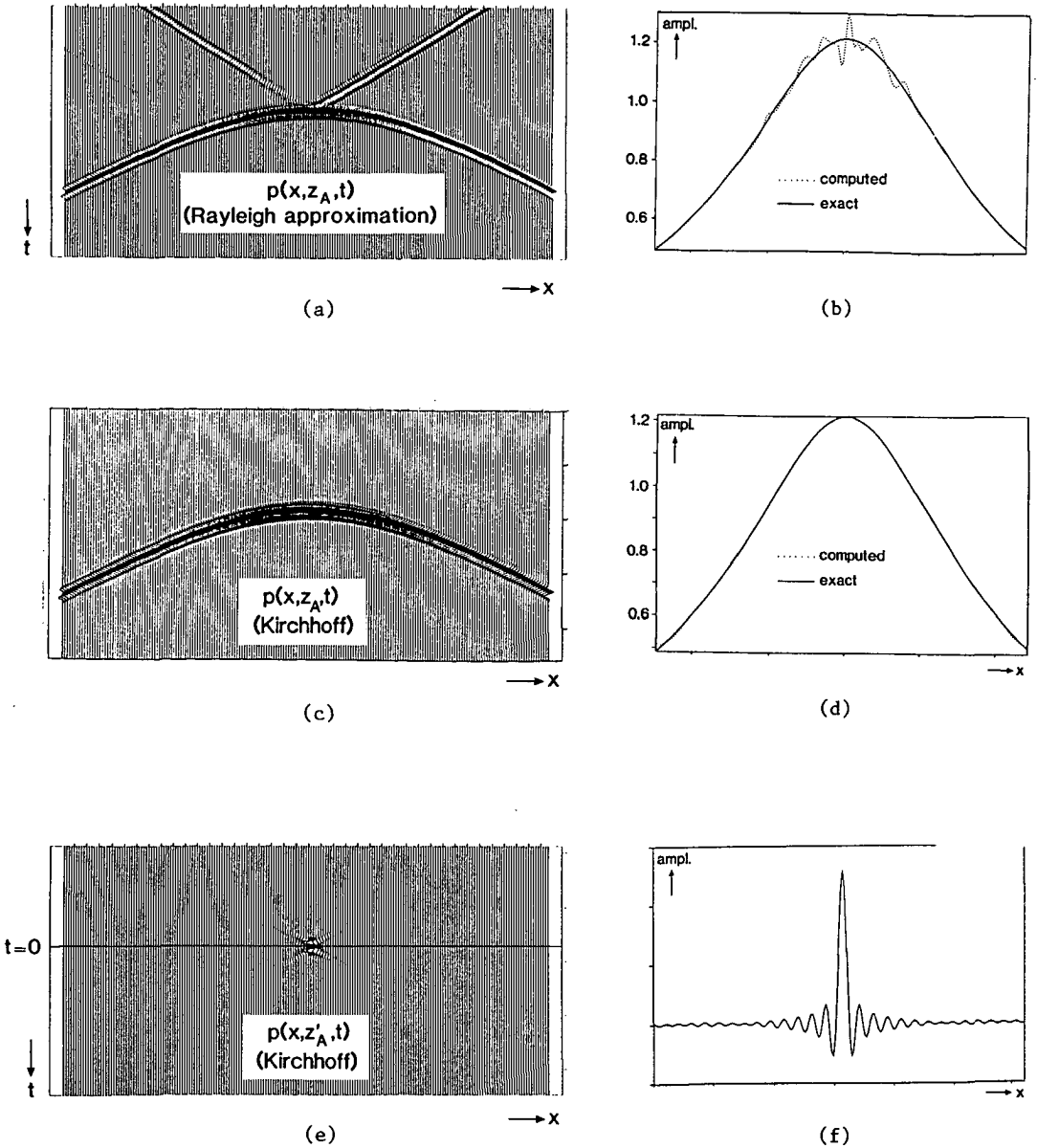


**Figure 3.9** The inverse extrapolated wave field at  $S_1$  obtained with a Rayleigh inverse wave field extrapolation operator (a), a full Kirchhoff inverse wave field extrapolation operator (c). The amplitude cross section allow for a comparison between the amplitudes of the inverse extrapolated wave field (dotted) and the analytical solution (solid). The lowest figures shows the inverse extrapolated wave field at  $S_2$  obtained with the Kirchhoff integral. In (f) the real part of the central frequency component from the data in (e) is shown.

inverse extrapolation operator is obtained by dropping the  $\partial P/\partial n$  from equation 3.40 and replace  $P(\mathbf{r},\omega)$  by  $2P(\mathbf{r},\omega)$

$$P_0(\mathbf{r}_A,\omega) = -\frac{1}{2\pi} \int_{S_0} \frac{1}{\rho} \left[ P \left( \frac{\partial G^*}{\partial n} \right) \right] dS \quad . \quad (3.41)$$

The inverse extrapolated wave field at  $S_1$  obtained with this inverse operator is shown in figure 3.9a. The hyperbolic response is present in this data as well as some significant artifacts. In the amplitude cross section shown in figure 3.9b strong amplitude deviations compared to the analytical response are present. So the amplitude information in inverse extrapolation is not preserved by the Rayleigh type of operators. The full Kirchhoff operator should be applied. This operator is particularly suited for recursive inverse extrapolated in the macro model discussed in chapter 1. The layers in the macro model are homogeneous. So true amplitude inverse extrapolation from interface to interface is accomplished by applying the full Kirchhoff inverse extrapolation operator to the pressure and normal component of the particle velocity at each interface. The problem of the boundary conditions which occurs when passing through each layer interface will be discussed in section (3.5).

### 3.4 INVERSE WAVE FIELD EXTRAPOLATION FOR ARBITRARILY INHOMOGENEOUS MEDIA

In the previous section an inverse extrapolation operator for curved surfaces and homogeneous media enclosed by  $V$  has been derived. The only approximation has been the incorrect handling of the evanescent waves. However for the seismic application the medium is not homogeneous. So if the full Kirchhoff inverse extrapolation operator from equation 3.40 is used in inhomogeneous media an approximation is made. In this section the error related to this approximation is investigated.

In the derivation of the full Kirchhoff inverse wave field extrapolation operator the contributions of the integral over  $S_1'$  (figure 3.10) are investigated. Since all sources are below  $S_1'$  the wave field at  $S_1'$  is up going only provided the medium is homogeneous. If however the medium is inhomogeneous down going waves at  $S_1'$  do occur due to scattering of the up going waves at inhomogeneities above  $S_1'$ . Therefore the integral over  $S_1'$  (equation 3.39) will not vanish. In order to analyze the contribution of the integral over  $S_1'$  to the wave field in  $A$  the Green's function will be split up into two components.  $G_D$  is related to the direct waves in the Green's function.  $G_S$  is associated to the waves in the Green's function which have been scattered by the inhomogeneities in the medium ( figure 3.10). So

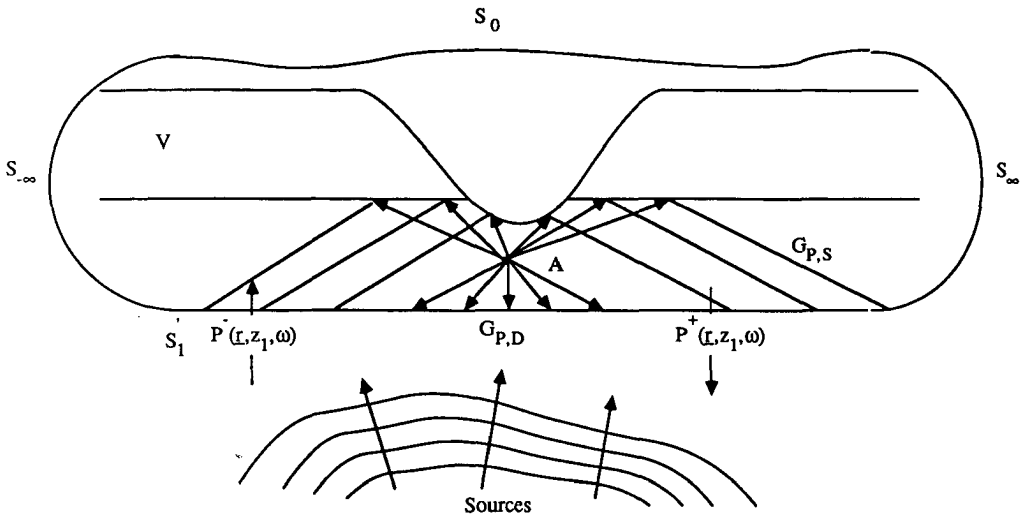


**Figure 3.10** The direct and scattered components for the Green's function at  $S_1'$  for an arbitrarily inhomogeneous medium inside  $V$ .

$$G(\mathbf{r}, \mathbf{r}_A, \omega) = G_D(\mathbf{r}, \mathbf{r}_A, \omega) + G_S(\mathbf{r}, \mathbf{r}_A, \omega) \quad \text{at } S_1' \quad (3.42)$$

Furthermore assume that the wave field  $P_1(\mathbf{r}_A, \omega)$  may be split up into down going and up going waves. So

$$P_1(\mathbf{r}_A, \omega) = P_1^+(\mathbf{r}_A, \omega) + P_1^-(\mathbf{r}_A, \omega) \quad (3.43)$$

and

$$P_1^+(\mathbf{r}_A, \omega) = -\frac{1}{2\pi} \int_{S_1'} \frac{1}{\rho} \left[ P^+(\mathbf{r}, \omega) \frac{\partial G_D^*(\mathbf{r}, \mathbf{r}_A, \omega)}{\partial n} \right] dS \quad (3.44)$$

$$P_1^-(\mathbf{r}_A, \omega) = -\frac{1}{2\pi} \int_{S_1'} \frac{1}{\rho} \left[ P^+(\mathbf{r}, \omega) \frac{\partial G_S^*(\mathbf{r}, \mathbf{r}_A, \omega)}{\partial n} \right] dS \quad (3.45)$$

From figure 3.10 it can be seen that the back propagating Green's functions  $G_D^*$  and  $G_S^*$  converge to  $A$  from opposite directions. Therefore  $P_1^+$  and  $P_1^-$  represent down going and up going waves in  $A$ . The total wave field in  $A$  includes contributions from  $S_0$  as well

$$P(\mathbf{r}_A, \omega) = P_0(\mathbf{r}_A, \omega) + P_1^+(\mathbf{r}_A, \omega) + P_1^-(\mathbf{r}_A, \omega) \quad (3.46)$$

Provided the medium is non-reflecting in the small region between A and  $S_1'$ ,  $P_0(\mathbf{r}_A, \omega)$  is an up going wave field only

$$P_0(\mathbf{r}_A, \omega) = P_0^-(\mathbf{r}_A, \omega) \quad (3.47)$$

For the seismic application the down going waves in A cannot be reconstructed from an integral over the wave field on  $S_0$  only. Since no data is available at  $S_1'$  no contributions to the wave field in A can be computed for this surface. Therefore we have to make the following approximation for the seismic situation

$$P^-(\mathbf{r}_A, \omega) \cong P_0^-(\mathbf{r}_A, \omega) \quad (3.48)$$

or with relations 3.21, 3.22, 3.23 and 3.46.

$$P^-(\mathbf{r}_A, \omega) \cong -\frac{1}{4\pi} \int_{S_0} \frac{1}{\rho} \left[ P \left( \frac{\partial G^*}{\partial n} \right) - \left( \frac{\partial P}{\partial n} \right) G^* \right] dS \quad (3.49)$$

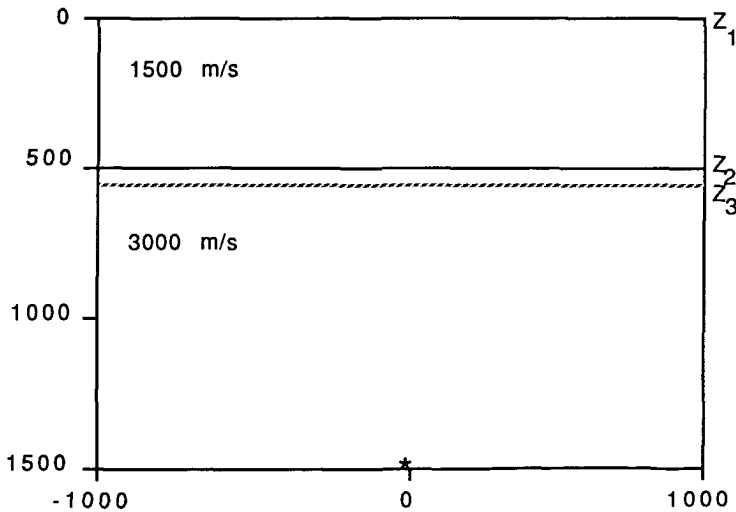


**Figure 3.11** The inverse extrapolation through an inhomogeneous medium. At  $z = 0$  m the wave field is registered from a line source at  $z = 1500$  m. The wave field is inverse extrapolated to  $z_3$  across an acoustic impedance contrast at  $z_2$ .

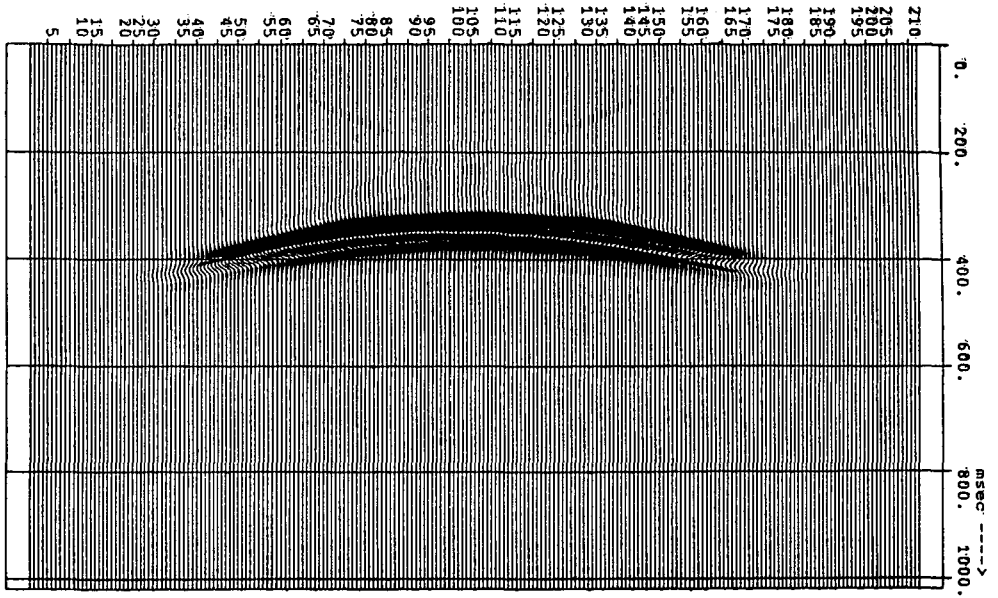


Figure 3.12 The inverse extrapolated wave field at  $z_3$ .

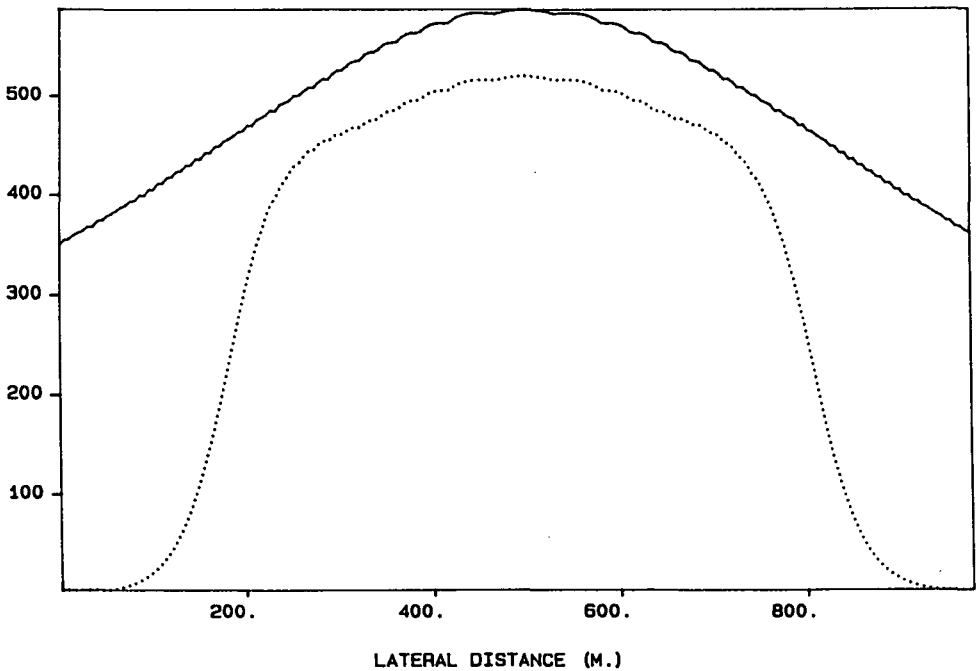


Figure 3.13 The amplitude cross section for the data from figure 3.12 (dotted). The amplitude difference between the inverse extrapolated wave field and the analytical solution (solid) is of the order of  $R^2$ .

The part of the up going wave field in A which has been neglected  $P_1^-(\mathbf{r}_A, \omega)$  is, according to relation 3.45, proportional to the product of the scattered wave  $P^+(\mathbf{r}, \omega)$  at  $S_1'$  and the Green's function  $G_{P,S}^*$  at  $S_1$ . So the magnitude of the neglected wave field is proportional to multiple reflected waves. It is therefore two orders of magnitude lower than  $P_0^-(\mathbf{r}_A, \omega)$ .

An inverse wave field extrapolation through an inhomogeneous medium of the primary wave field from a curved surface  $S_0$  is achieved by applying the generalized 'Kirchhoff summation' operator from equation 3.49. The amplitude errors are of the second order so multiply reflected waves should be neglected. Furthermore the evanescent waves are neglected as well. Finally only the up going wave field is reconstructed. This operator is well suited for the seismic application since the main interest for migration and redatuming is inverse extrapolation of primary waves.

The full Kirchhoff inverse wave field extrapolation operator has been applied to the wave field at  $z_1$  in an inhomogeneous 2-D medium shown in figure 3.11. A dipole line source is located in point L. A layer interface is present at level  $z_2$ . The inverse wave field extrapolation with the integral from equation 3.49 brings the wave field from  $z_1$  to  $z_3$ . Since the medium between  $z_1$  and  $z_3$  is not homogeneous the inverse extrapolation operator is an approximation. The extrapolated wave field at  $z_3$  is shown in figure 3.12. The response is hyperbolicly shaped. The amplitude cross section for this response is depicted in figure 3.13. Comparison with the analytical wave field shows an amplitude error of the order  $R^2$ , where  $R$  denotes the reflection coefficient. So the non recursive application of the full Kirchhoff integral in inhomogeneous media yields an error of the magnitude of multiply reflected waves. However when the integral is applied recursively the amplitude information will be preserved as will be discussed in the next section.

### 3.5 RECURSIVE APPLICATION OF THE FULL KIRCHHOFF INTEGRAL FOR RECURSIVE INVERSE WAVE FIELD EXTRAPOLATION

In the previous sections the application of the full Kirchhoff inverse extrapolation has been discussed. If the medium through which the wave field is inverse extrapolated is homogeneous the full Kirchhoff inverse extrapolation operator is exact for the propagating waves. If the medium is inhomogeneous this operator is no longer correct resulting in amplitude errors of the order of the multiply reflected waves. However if the macro model description of the subsurface is used a recursive extrapolation from interface to interface may be carried out. In one-way wave field extrapolation techniques the boundary conditions are usually not satisfied. Normally, if the wave field is extrapolated across an acoustic impedance contrast, the boundary conditions should be explicitly incorporated. It will be shown in this section that in case of the recursive

wave field extrapolation the up going wave field is correctly inverse extrapolated ( except for the evanescent) without explicitly incorporating the boundary conditions.

Consider in figure 3.14 some upward traveling wave field which has been registered at the surface  $S_1$ . In order to obtain the up going wave field at A, the wave field at  $S_1$  will be inverse extrapolated recursively. For the first extrapolation step consider the medium enclosed by  $S_1$  and  $S_2$ . On  $S_1$  the wave field is known. The wave field just above  $S_2$  should be calculated.

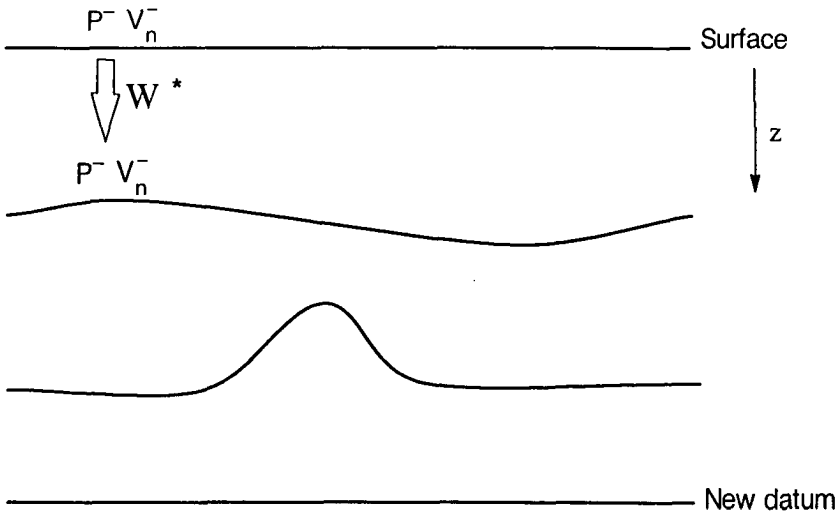


**Figure 3.14** In the recursive extrapolation the upgoing wave field at the surface is extrapolated to the first interface. The upgoing wave field just above the first interface is obtained.

Since the medium enclosed by  $S_1$  and  $S_2$  is homogeneous the full Kirchhoff inverse extrapolation operator could be applied for many points on  $S_2$  without making any approximations. For the next extrapolation step the wave field at  $S_2$  is extrapolated to  $S_3$ . However since the wave field above  $S_2$  is known the velocity contrast at  $S_2$  lies inside the closed volume of the Kirchhoff integral. Application of the integral to the wave field above  $S_2$  yields amplitude errors of the order of magnitude of the multiply reflected waves as discussed in the previous section. So the wave field just below  $S_2$  should be known. Since the wave field originates from sources below  $S_3$  the only wave field above  $S_2$  is an up going wave field. Therefore the total primary wave field above  $S_2$  is known.

$$\begin{aligned}
 P_{\downarrow S_2}(\mathbf{r}, \omega) &= P_{\downarrow S_2}^-(\mathbf{r}, \omega) \\
 V_{n\downarrow S_2}(\mathbf{r}, \omega) &= V_{n\downarrow S_2}^-(\mathbf{r}, \omega)
 \end{aligned}
 \quad \text{just above } S_2 \quad (3.50)$$

Since the wave field is continuous across  $S_2$  the total wave field below  $S_2$  is identical to the total wave field above  $S_2$ .

$$P_{\uparrow S_2}(\mathbf{r}, \omega) = P_{\downarrow S_2}^-(\mathbf{r}, \omega) \quad (3.51)$$

$$V_{n\uparrow S_2}(\mathbf{r}, \omega) = V_{n\downarrow S_2}^-(\mathbf{r}, \omega) \quad (3.52)$$

Just below  $S_2$  the wave field may split up in up going waves and down going waves (figure 3.15)

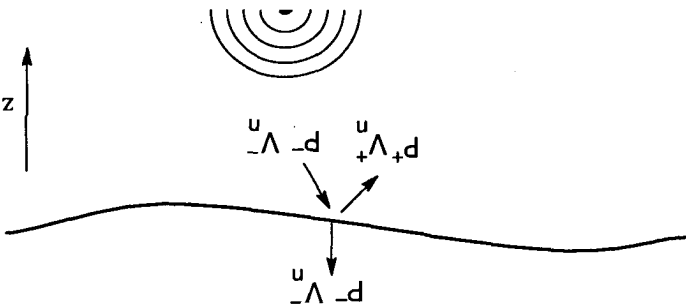


**Figure 3.15** Since the total wave field is continuous across an acoustic boundary condition, the upgoing wave field above the interface equals the upgoing and downgoing wave field just below the interface.

$$P_{\uparrow S_2}(\mathbf{r}, \omega) = P_{\uparrow S_2}^+(\mathbf{r}, \omega) + P_{\uparrow S_2}^-(\mathbf{r}, \omega) \quad (3.53)$$

$$V_{n\uparrow S_2}(\mathbf{r}, \omega) = V_{n\uparrow S_2}^+(\mathbf{r}, \omega) + V_{n\uparrow S_2}^-(\mathbf{r}, \omega) \quad (3.54)$$

Since we are interested in the up going wave field only, the down going wave field component is undesired. If the boundary conditions would be taken into account the up going wave field below  $S_2$  could be calculated from the up going wave field above  $S_2$ . Since incorporating boundary conditions is quite difficult in one-way schemes, this is not a good solution. However

application of the full Kirchhoff inverse extrapolation operator with an up going Green's function to the total wave field just below  $S_2$  yields the up going wave field on  $S_3$  (figure 3.16).

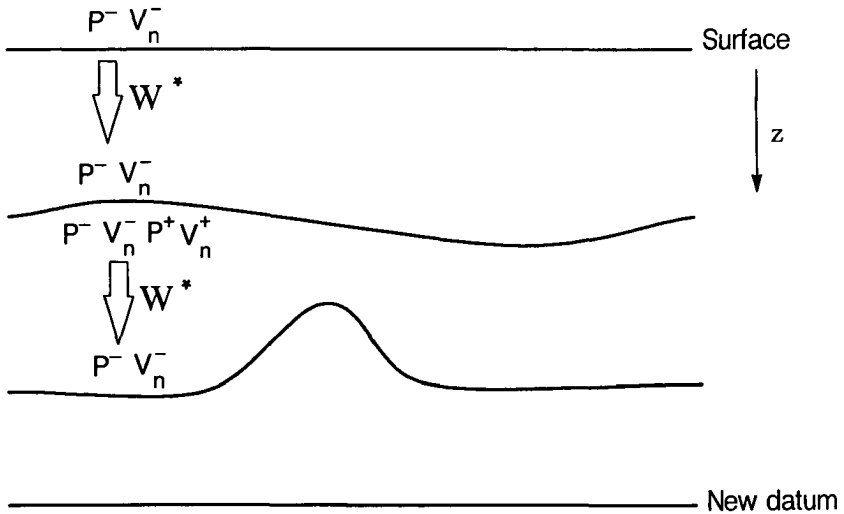


**Figure 3.16** An inverse extrapolation of the total wave field just below the first interface with one-way Green's functions causes the downgoing wave field to be eliminated.

The down going wave field components do not interact with up going Green's functions and are cancelled during the inverse extrapolation. The undesired down going wave field is eliminated. So for the configuration of a stack of homogeneous layers and buried secondary sources recursive inverse wave field extrapolation of the primary up going wave field yields the correct up going wave field for the propagating waves at a deeper level. The wave propagation effects for curved layer interfaces and boundary conditions are all handled correctly.

For an experimental verification of the recursive inverse wave field extrapolation consider the configuration from figure 3.17. A wave field originating from line source  $L$  propagates to the receivers at level  $z_1$ . An impedance contrast exists at  $z_2$ . The wave field is recursively inverse extrapolated from the receivers to level  $z_3$ , where it is compared to the analytical wave field. The first extrapolation step involves inverse wave propagation from  $z_1$  to  $z_2$  with the full Kirchhoff inverse wave field extrapolation operator and a propagation velocity  $c_1 = 1500$  m/s. The

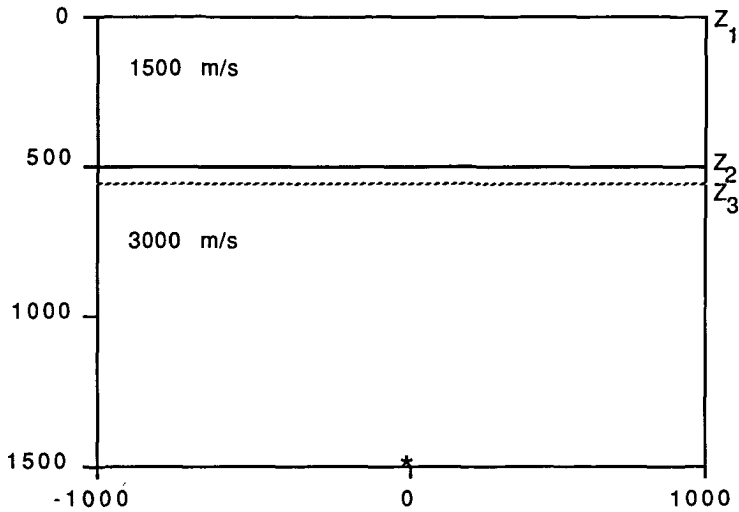


**Figure 3.17** The same geometry as in figure 3.11 for a recursive full Kirchhoff inverse extrapolation across an acoustic impedance contrast.

extrapolated wave field is then inverse propagated from  $z_2$  to  $z_3$  with a propagation velocity  $c_0 = 2000$  m/s. The pressure of the inverse extrapolated wave field at  $z_2$  is shown in figure 3.18. The amplitude cross section is compared to the analytical wave field shown as a solid line is depicted in figure 3.19a. For the area in which the wave field has been back propagated the amplitude match is perfect. Some side lobes effect occur due to aperture truncation. If the recursive inverse wave propagation is carried out with the commonly used Rayleigh operator involving the pressure data only, the amplitude behavior is not correct as shown in the amplitude cross section in figure 3.19b. Because this operator does not handle the boundary conditions correctly.

For the plane layer model the validity of the correct amplitude behavior of the recursive full Kirchhoff operator is easily verified analytically. Computations in the  $k_x$ - $\omega$  domain allows for an easy analysis. For a dipole source  $S$  at  $z_s$  (figure 3.20) the wave field at the receivers is given by

$$P_r(k_x, \omega) = e^{-jk_{z,1} |z_r - z_i|} T(k_{z,1}, k_{z,0}) e^{-jk_{z,0} |z_i - z_s|} \quad (3.55)$$

with

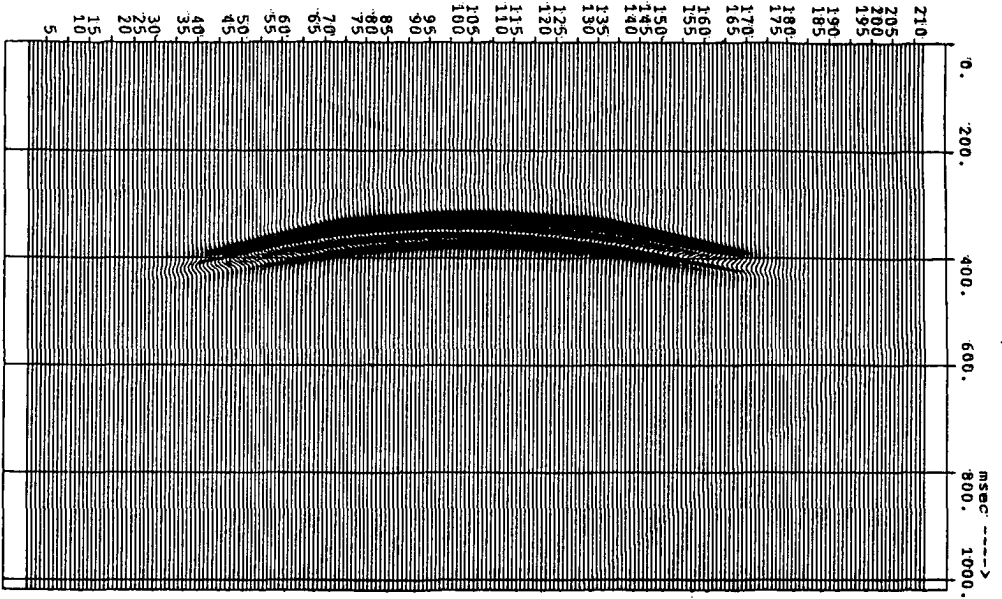


Figure 3.18 The inverse extrapolated wave field at  $z_3$ .

$$k_{z,0} = \sqrt{k_0^2 - k_x^2}$$

$$k_0 = \omega/c_0$$

$$k_{z,1} = \sqrt{k_1^2 - k_x^2}$$

$$k_1 = \omega/c_1$$

The transmission operator  $T(k_{z,1}, k_{z,0})$  for the transmission from the lower halfspace to the upper halfspace is given by

$$T(k_{z,1}, k_{z,0}) = \frac{2\rho_1 jk_{z,0}}{\rho_1 jk_{z,0} + \rho_0 jk_{z,1}} \tag{3.56}$$

For the Kirchhoff extrapolation both pressure and particle velocity data are required

$$V_z(k_x, \omega) = \frac{jk_z}{j\omega\rho} P(k_x, \omega) \tag{3.57}$$

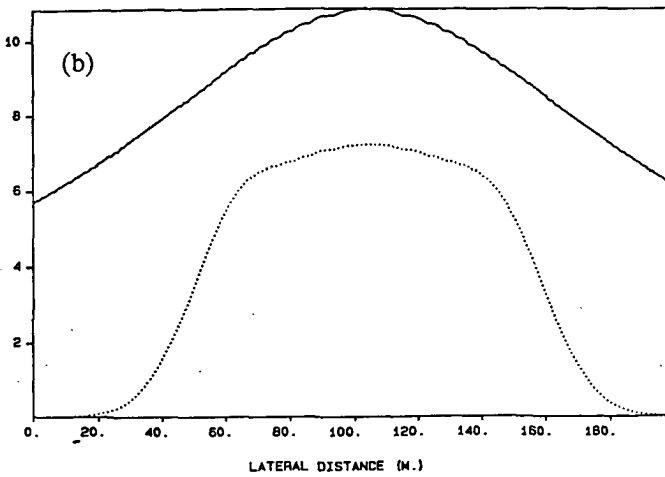
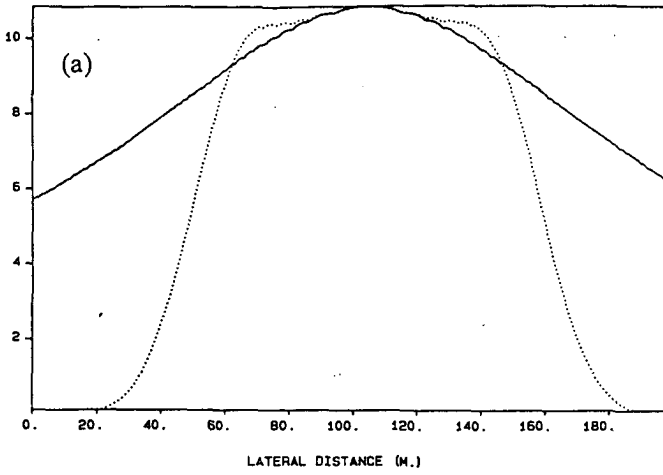


**Figure 3.19** The amplitude cross section for the recursively full Kirchhoff inverse extrapolated data from figure 3.18 (dotted) is compared to the analytical solution (solid) in a. For the data in b the Rayleigh integral has been used for the inverse extrapolation. The boundary conditions are not handled correctly for this operator.

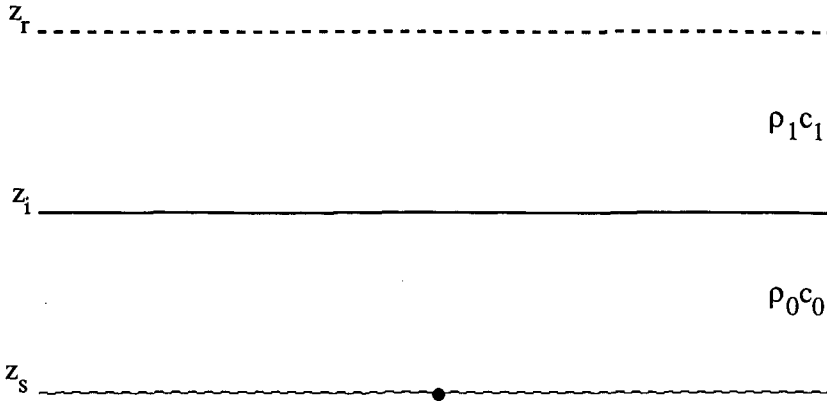


**Figure 3.20** Geometry for an analytical verification of the recursive full Kirchhoff inverse wave field extrapolation across acoustic impedance contrasts.

So

$$V_{zr}(k_x, \omega) = \frac{jk_{z,1}}{j\omega\rho_1} P_r(k_x, \omega) \quad (3.58)$$

The Green's function is given by

$$G = \frac{1}{2jk_z} e^{-jk_z \Delta z} \quad (3.59)$$

The inverse extrapolation considering the propagating waves only from the receivers at  $z_d$  to  $z_i$  is achieved by

$$P_i(k_x, \omega) = \frac{1}{2} e^{+jk_{z,1}|z_r-z_i|} P_r(k_x, \omega) + \frac{1}{2} \frac{1}{jk_{z,1}} e^{+jk_{z,1}|z_r-z_i|} j\omega\rho_1 V_{zr}(k_x, \omega) \quad (3.60)$$

or, by substituting 3.55 and 3.58

$$P_i(k_x, \omega) = T(k_{z,1}, k_{z,0}) e^{-jk_{z,1}|z_r-z_s|} \quad (3.61)$$

Similarly,

$$V_{z,1}(k_x, \omega) = \frac{jk_{z,1}}{j\omega\rho_1} P_1(k_x, \omega) \quad (3.62)$$

The next step of the recursive inverse extrapolation yields

$$P_a(k_x, \omega) = \frac{1}{2} e^{+jk_{z,0}|z_1-z_a|} P_i(k_x, \omega) + \frac{1}{2} \frac{1}{j\omega\rho_0} \frac{e^{+jk_{z,0}|z_1-z_a|} jk_{z,1}}{jk_{z,0}j\omega\rho_1} P_i(k_x, \omega) , \quad (3.63)$$

or after substitution of 3.56 and 3.60

$$P_a(k_x, \omega) = \frac{1}{2} e^{+jk_{z,0}|z_1-z_a|} T(k_{z,1}, k_{z,0}) e^{-jk_{z,0}|z_1-z_s|} + \frac{1}{2} \frac{r_0 jk_{z,1}}{r_1 jk_{z,0}} e^{+jk_{z,0}|z_1-z_a|} T(k_{z,1}, k_{z,0}) e^{-jk_{z,0}|z_1-z_s|} , \quad (3.64)$$

or

$$P_a(k_x, \omega) = \frac{1}{2} \left[ 1 + \frac{r_0 jk_{z,1}}{r_1 jk_{z,0}} \right] T(k_{z,1}, k_{z,0}) e^{-jk_{z,0}|z_1-z_a|} , \quad (3.65)$$

or after substitution of 3.56

$$P_a(k_x, \omega) = e^{-jk_{z,0}|z_1-z_a|} \quad k^2 > k_x^2 , \quad (3.66)$$

which is the wave field at level  $z_a$  due to a dipole source at  $z_s$ . So the wave propagation effects and the boundary conditions have been handled correctly in the recursive Kirchhoff inverse wave field extrapolation.

For the geometry from figure 3.21 with the curved layer interface the recursive inverse wave field extrapolation has also been applied. A line source  $S$  is located at a depth level of 1500 m. The receivers are located on top of an anticlinal structure. The wave field should be backpropagated to level  $z_2$ . The wave field has been modeled with a finite difference modeling scheme. Therefore the boundary conditions have been properly handled in the forward modeling for this laterally varying subsurface model. The pressure response at the receivers is shown in figure 3.22. In order to identify both events several snap shots of the finite difference modeling are shown in figure 3.23. The second event in the response is associated with an internal reflection in the anticlinal structure as indicated in figure 3.24. For the recursive inverse wave field extrapolation the registered wave field is back propagated to the layer interface. According to the boundary conditions the total wave field is continuous across the acoustic impedance contrast. Since the total wave field above the anticline consists of the up going wave field only. The total wave field below the anticline (consisting of the up going direct wave field from the source and the scattered wave field) equals the up going wave field just above the anticline. Another inverse extrapolation step applied to the wave field at the anticline will eliminate the down going wave field and reconstruct the up going wave field at level  $z_2$  as shown in figure 3.25. So the internal reflection in the anticline has been eliminated since the

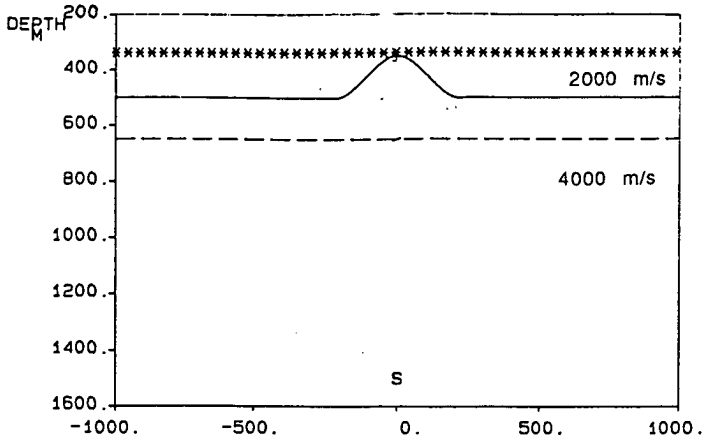


Figure 3.21 Geometry for recursive inverse wave field extrapolation across a curved interface. At  $z = 300$  m the wave from a source at  $z = 1500$  m is registered. This wave field is inverse extrapolated to  $z_2$ .

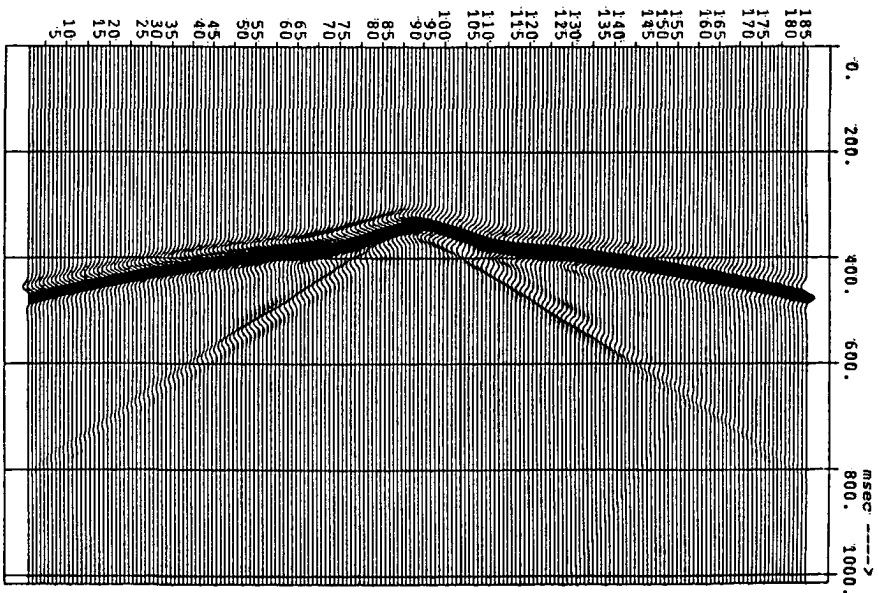
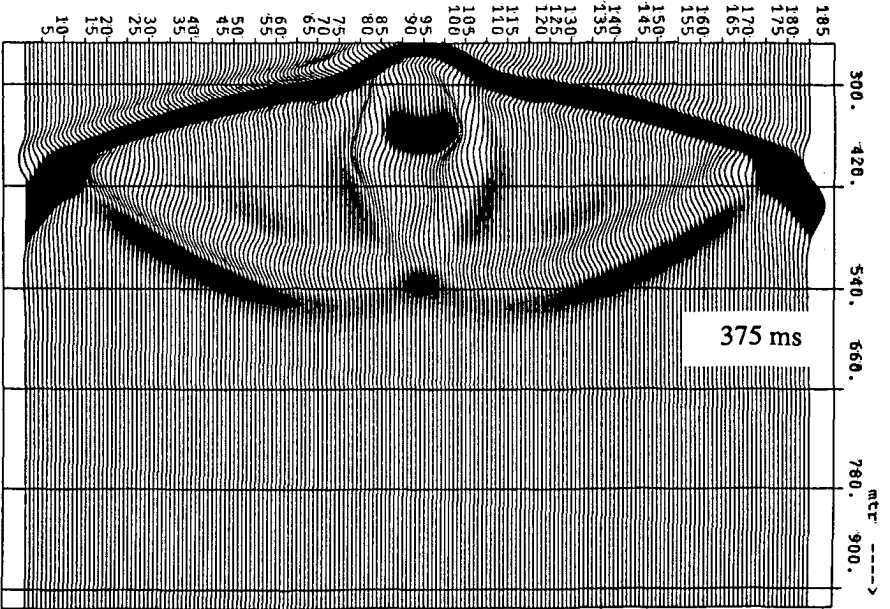
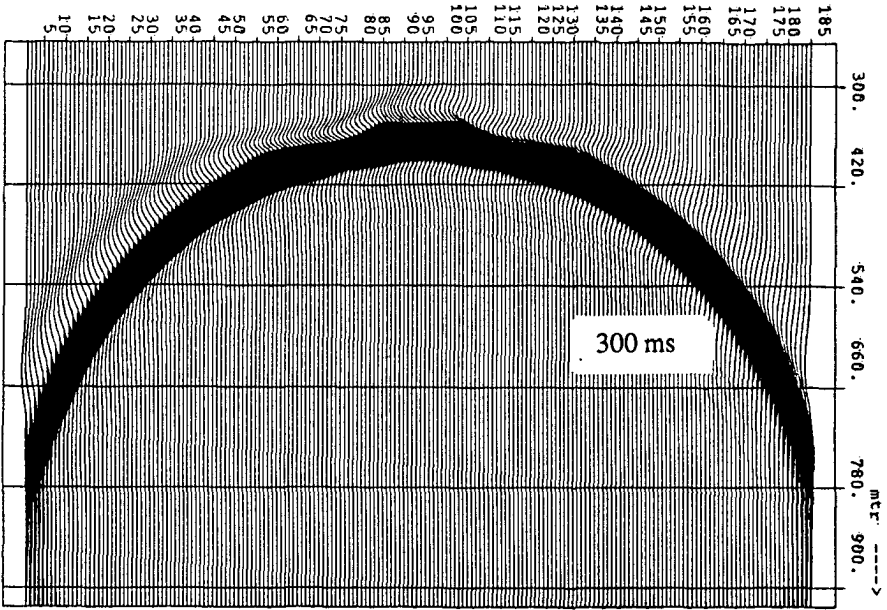
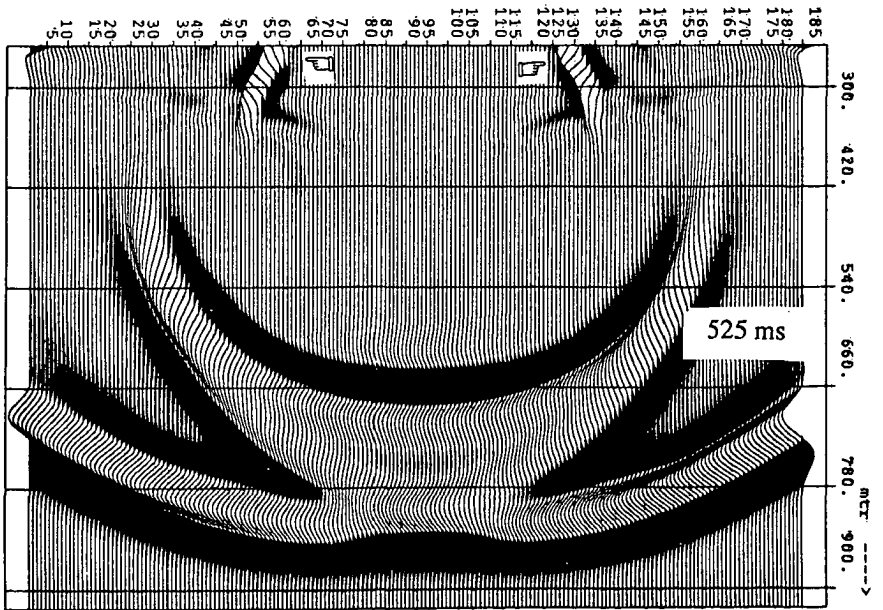
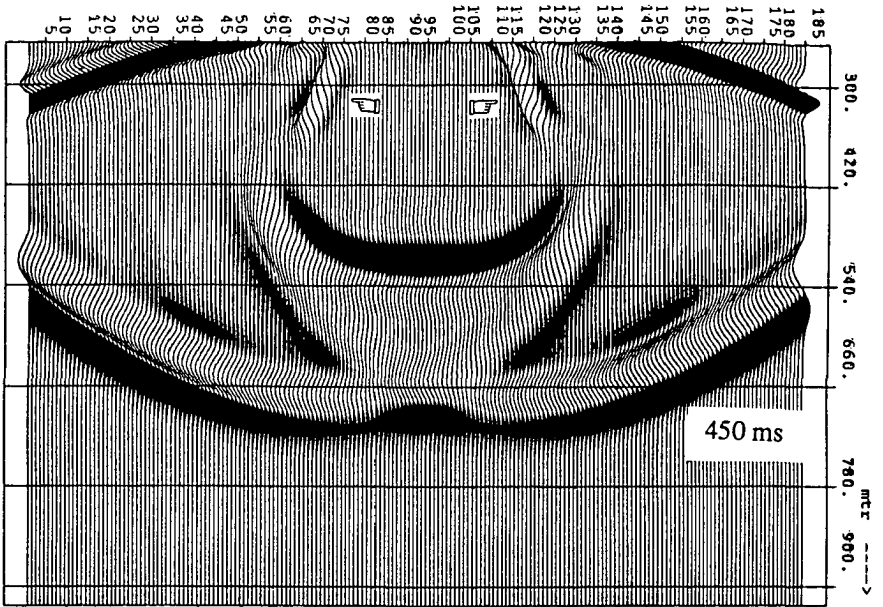


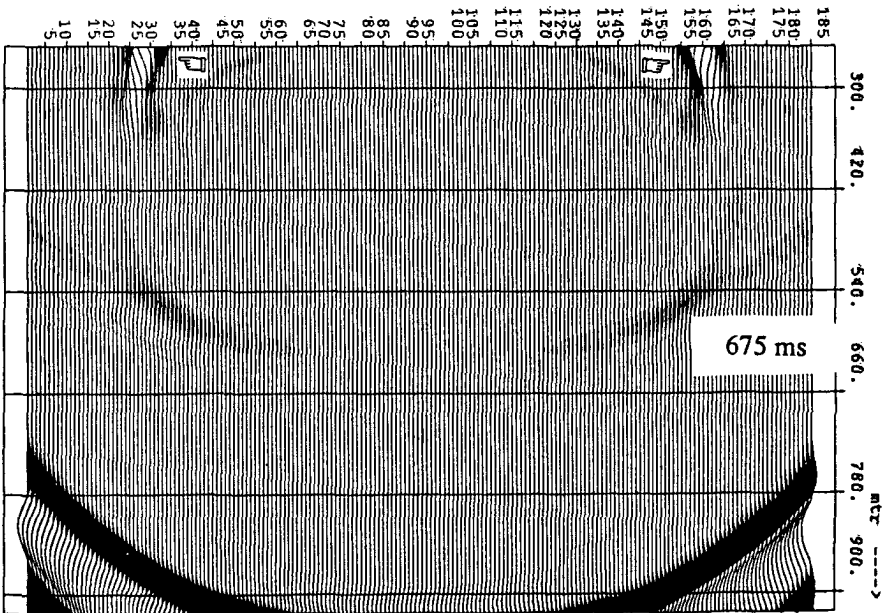
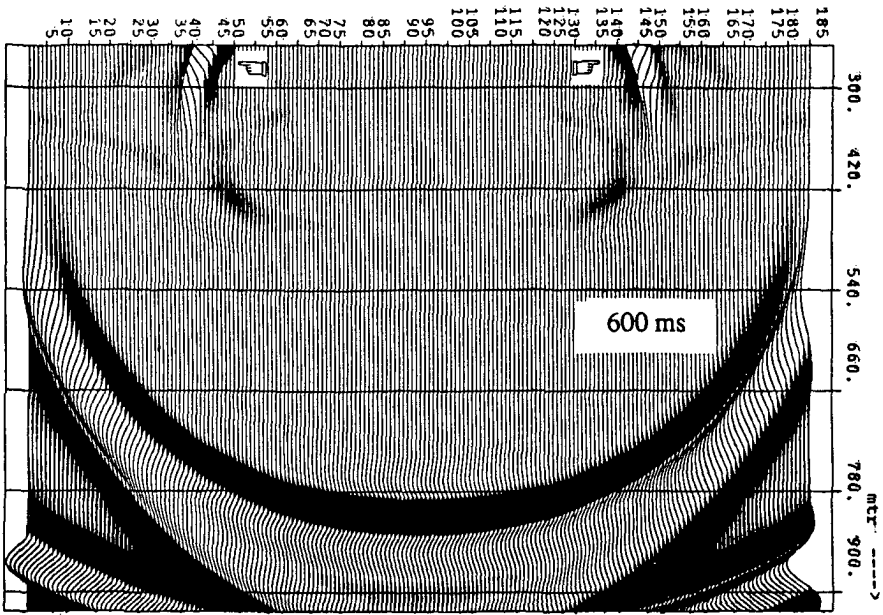
Figure 3.22 The registered data at  $z = 300$  m obtained with finite differences modeling.



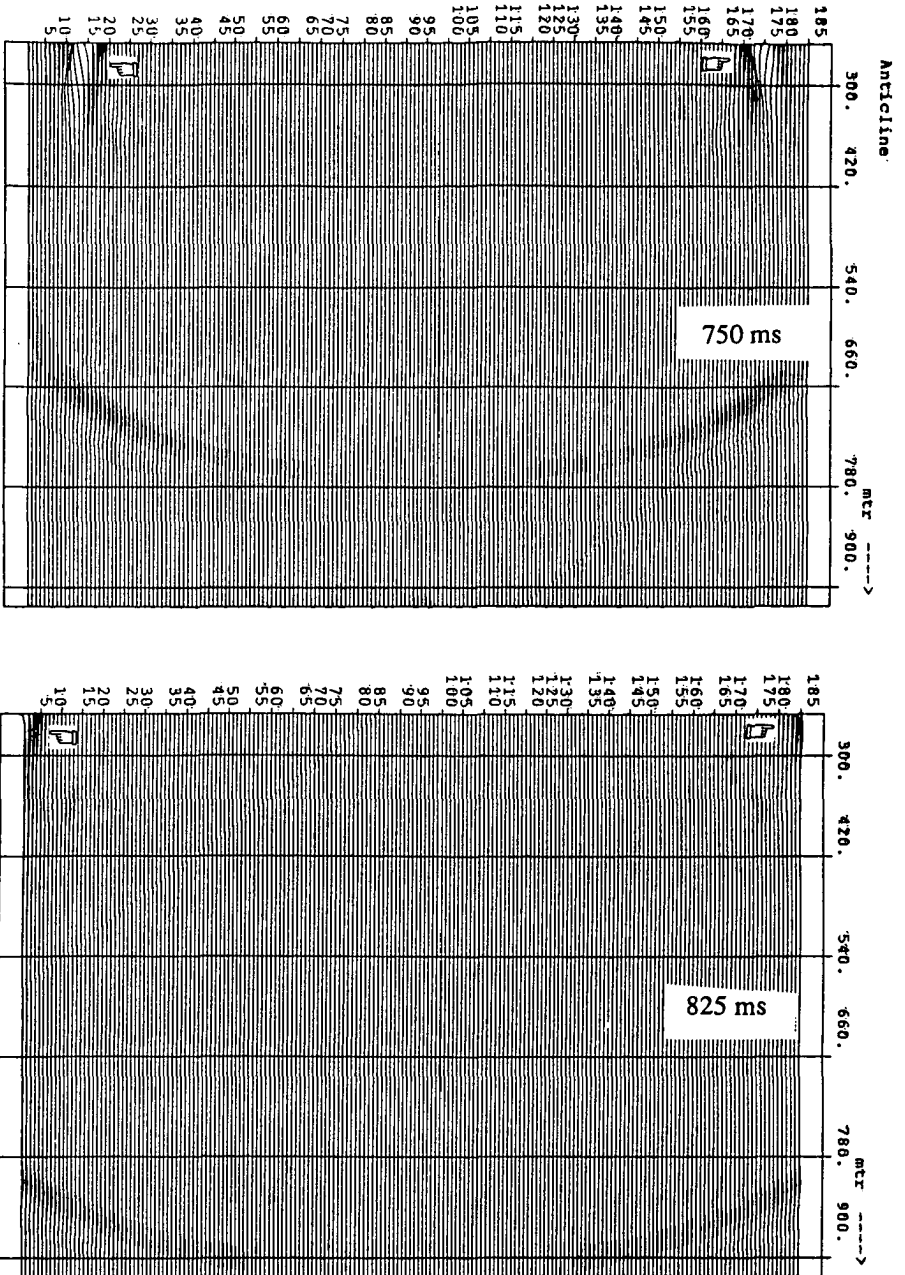
3.23a



3.23b



3.23c



3.23d

Figure 3.23 Time snap shots of the wave field in the subsurface allow for an identification of all events. The second event in figure 3.22 is caused by an internal reflection in the anticlinal structure.

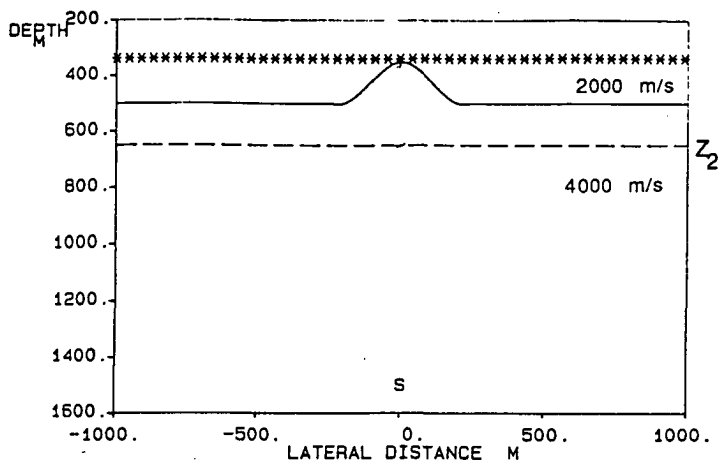


Figure 3.24 A raypath for the internal reflection in the anticlinal structure.

boundary conditions were met and the amplitude information is preserved. The amplitude cross section in figure 3.26 shows a comparison with the analytical wave field. The amplitude level of the recursively inverse extrapolated wave field compares good with the analytical wave field shown as a solid line. So the recursive application of the full Kirchhoff operator correctly inverse extrapolates the wave field. The wave propagation effects as well as the transmission effects are properly handled even for curved layer interfaces. Some deviations occur because some of the waves have propagated out of the registration aperture due to the interface curvature. The inverse wave field extrapolation has also been carried out with the Rayleigh operator involving the pressure data only. The result depicted in figure 3.27 shows an additional event because this operator is not valid for curved interfaces. Furthermore the amplitude cross section presented in figure 3.28 shows the incorrect amplitude handling of this operator because the boundary conditions were not met. The non recursive inverse extrapolation operator as discussed in a section (3.4) has also been applied for this geometry. The back propagated wave field at level  $z_2$  is shown in figure 3.29. No additional events are present in this response. The amplitude cross section (figure 3.30) shows an amplitude difference compared to the analytical wave field. The difference in amplitude corresponds to the error of the order of  $R^2$  due to the fact that this operator is not exact.

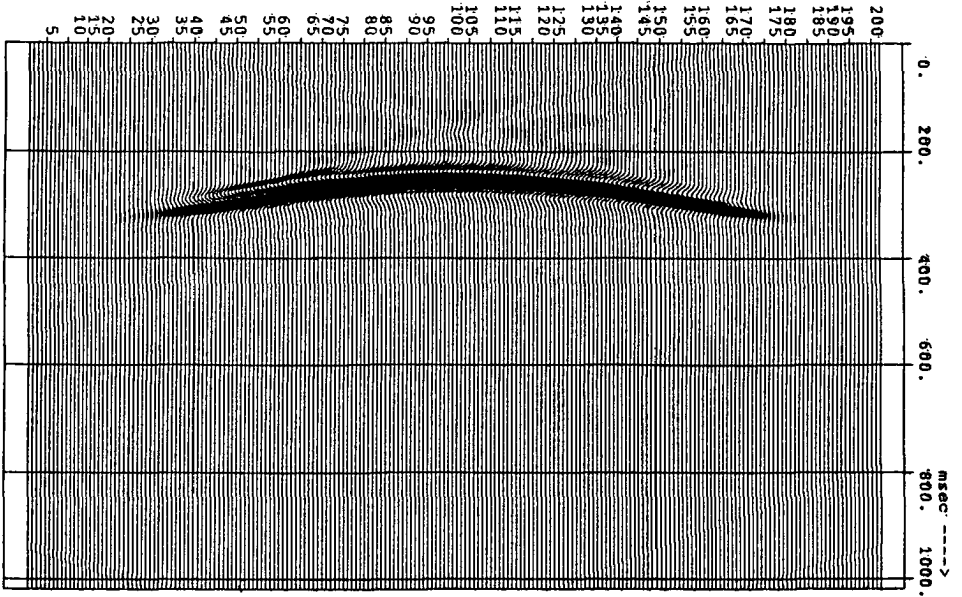


Figure 3.25 The recursive full Kirchhoff inverse extrapolated wave field at  $z_2$ .

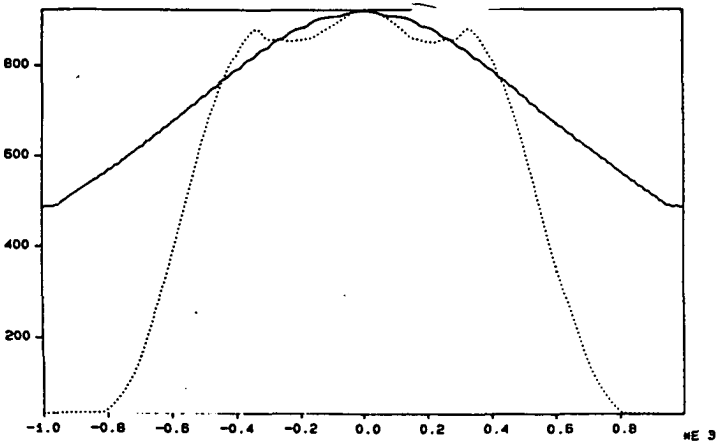


Figure 3.26 The amplitude cross section for the data from figure 3.25 (dotted) compared to the analytical solution (solid). Because of the aperture limitation only part of the wave field is reconstructed.

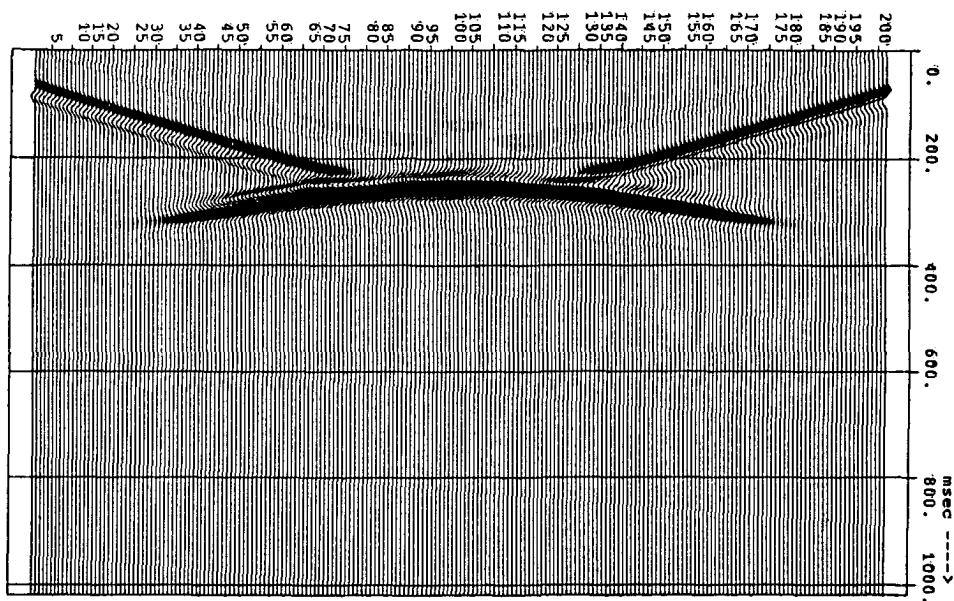


Figure 3.27 The recursive Rayleigh inverse extrapolated wave field at  $z_2$ . An undesired additional event is present.

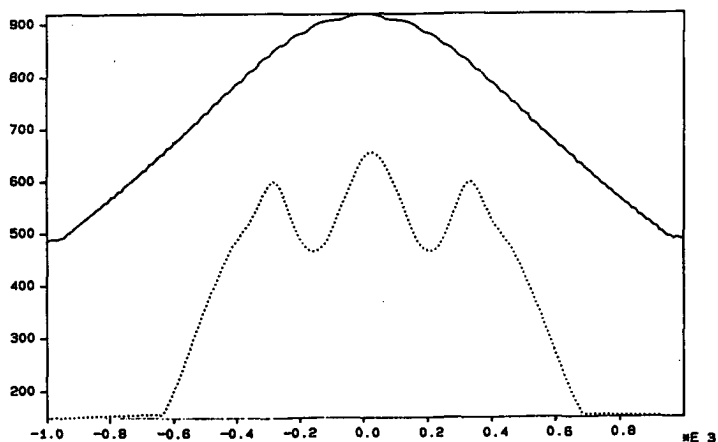


Figure 3.28 The amplitude cross section for the data from figure 3.27 (dotted) is compared to the analytical solution (solid). The amplitude information is not preserved in the inverse extrapolation.

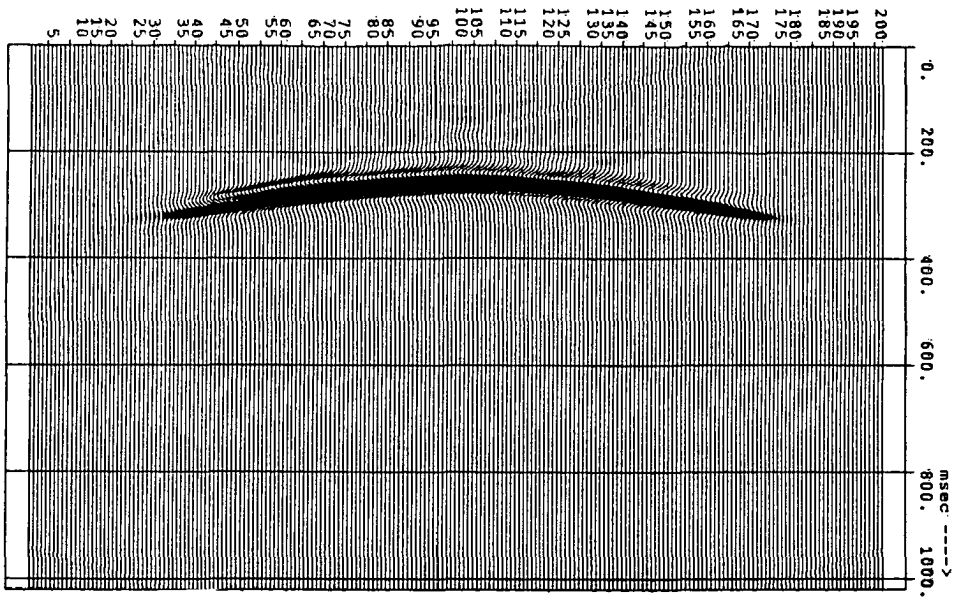


Figure 3.29 The non-recursive inverse extrapolated wave field at  $z_2$ .

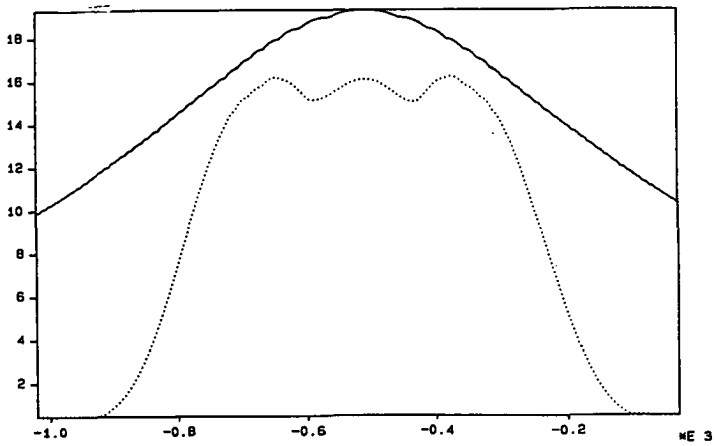


Figure 3.30 The amplitude cross section for the data from figure 3.29 (dotted) is compared with the analytical solution (solid). The difference corresponds to an amplitude error of the order of  $R^2$ .

## 4

---

## THE REDATUMING

In seismics the hydrocarbon reservoirs and the source and detectors are separated by an overburden. This overburden consists of up to several kilometers of earth. The reflection response of the zone of interest, the reservoir, is distorted because of overburden wave propagation effects. A more preferable configuration would consist of source and detectors directly over the target zone. So instead of a datum at the surface a datum within the subsurface is required. A redatuming of the surface data should bring down the sources and detectors for the seismic experiments from the surface to a new datum over the target zone. For this purpose, the overburden wave propagation effects should be eliminated from the seismic data.

In this chapter the redatuming procedure is discussed. For the redatuming, wave propagation effects should be eliminated. In the previous chapters forward wave field and inverse wave field extrapolation have been discussed. In surface seismics the source and the detectors are located at the surface. Reflected waves from the subsurface structures are registered at the surface. In the first sections of this chapter a forward model for describing the reflection response at the surface due to a source at the surface is described. In the forward formulation the overburden wave propagation and the reflection at the target zone should be clearly separated in order to be able to obtain an inverse relation. In this inverse relation the overburden wave propagation effects should be eliminated and an undistorted target zone reflection response should be obtained.

The matrix notation will be used in the derivation of the redatuming procedure. The advantage of this notation is its simplicity and clarity. Furthermore, compared to a formulation in terms of integrals, the matrix notation is closer to a computer implementation. All matrices are

monochromatic, so only one frequency component of the data and the operators is considered in the matrix relations. The monochromatic geophone data for frequency  $\omega_j$  is represented by a data vector  $\mathbf{p}$  (see also figure 4.1)

$$\mathbf{p}(z_0) = \left( P(x_1, z_0, \omega_j), P(x_2, z_0, \omega_j), \dots, P(x_n, z_0, \omega_j) \right)^T \quad (4.1)$$

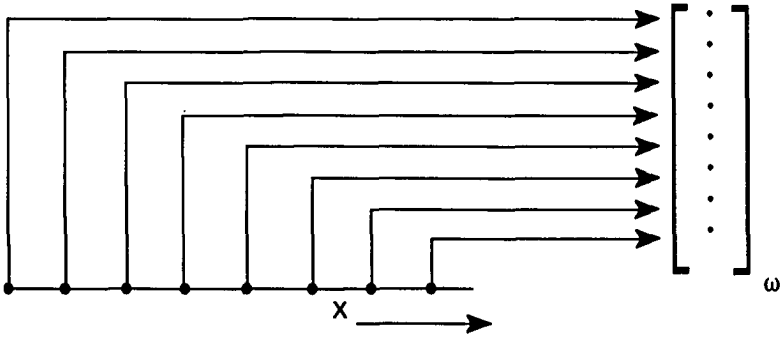


**Figure 4.1** Each element of a data vector contains a complex valued monochromatic data point corresponding to a particular spatial position.

In the monochromatic data matrix each column of the matrix is equivalent to one data vector  $\mathbf{p}(z_0)$ . For convenience the variable  $\omega_j$  is dropped in the notation. Every vector corresponds to a single shot experiment. So the diagonal corresponds to data for which the lateral position of the geophone is the same as the lateral position of the shot and is therefore the (monochromatic) zero offset section. This is also shown in figure 4.2. For the extrapolation of a data vector  $\mathbf{p}(z_i)$  a matrix vector multiplication is carried out. If  $\mathbf{W}(z_{i+1}, z_i)$  denotes the extrapolation operator, the extrapolation is given by

$$\mathbf{p}(z_{i+1}) = \mathbf{W}(z_{i+1}, z_i) \mathbf{p}(z_i) \quad (4.2)$$

Each row of  $\mathbf{W}$  corresponds to the Green's function in the Rayleigh type of extrapolation operators (see also chapter 2). So simultaneous monochromatic extrapolation of all shots is given by

$$\mathbf{P}(z_{i+1}) = \mathbf{W}(z_{i+1}, z_i) \mathbf{P}(z_i) \quad .$$

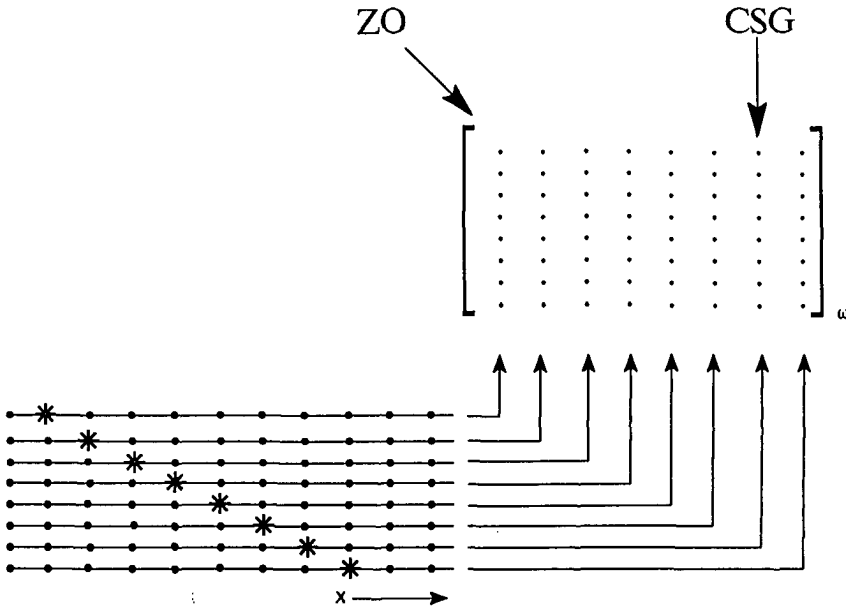


Figure 4.2 In the data matrix each column corresponds to a data vector. Different columns correspond to different shot locations.

### 4.1 THE FORWARD MODEL

In the seismic reflection method a source at the surface generates the illuminating wave field. Usually a simple point source or a small source array is used. This wave field propagates through the overburden to the target zone (figure 4.3) and gets distorted during propagation. At the target zone the illuminating wave field is no longer a simple wave field. The structures in the overburden cause the illuminating wave field to become rather complex. The propagated source wave field is given by

$$s^+(z_i) = W^+(z_i, z_0) s^+(z_0) \quad , \quad (4.3)$$

in which  $s^+(z_i)$  corresponds to the source wave field at the surface; the elements of  $s^+(z_i)$  correspond to the source wave field at spatial locations  $x$  and at depth  $z_i$ .  $W^+(z_i, z_0)$  represents a wave field propagation operator from depth  $z_0$  to  $z_i$ . The dot product of a row of  $W$  and  $s$  corresponds to the evaluation of the integral equation 2.30. The rows of  $W$  are related to the Green's functions.

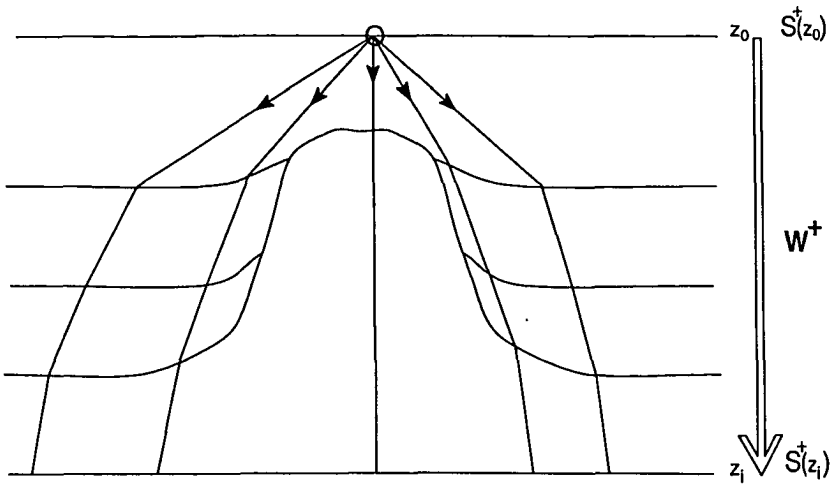


**Figure 4.3** The source wave field  $s^+(z_0)$  at the surface is propagated downward through the overburden to level  $z_1$  by applying a wave field extrapolation operator  $W^+$ .

The reflection response  $p^-(z_1)$  of the target at depth  $z_1$  due to  $s^+(z_1)$ , also propagates through the overburden to the surface and gets distorted during propagation. At the surface this reflection response is registered by the detectors:

$$p^-(z_0) = W^-(z_0, z_1) p^-(z_1) \quad , \quad (4.4)$$

where  $p^-(z_0)$  denotes the reflection response at the surface and  $W^-(z_0, z_1)$  determines how the reflection response at level  $z_1$  propagates upward to level  $z_0$ .

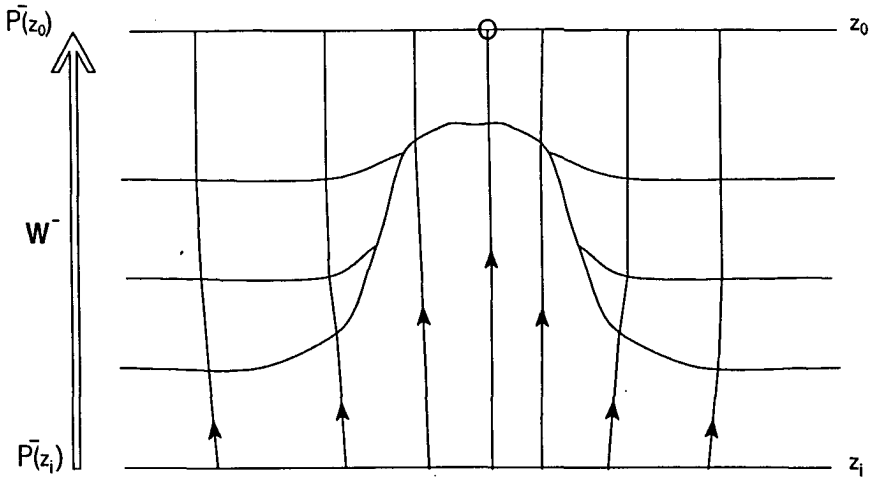


**Figure 4.4** The upgoing wave field at level  $z_i$ ,  $p^-(z_i)$  is propagated to the surface by applying a wave field extrapolation operator  $W^-$ .

At the target zone the incident wave field  $s^+(z_i)$  is related to the reflected wave field  $p^-(z_i)$  through the target reflection response:

$$p^-(z_i) = X(z_i) s^+(z_i) \quad (4.5)$$

The matrix  $X$  will denote the target reflection response operator. Since the redatuming aims at obtaining the reflection response  $X(z_i)$  of the target zone this matrix will be examined more closely in the next section.

The target response for primary waves due to sources  $s^+(z_i)$  at the surface is found by combining (4.3), (4.4) and (4.5):

$$p^-(z_0) = W^-(z_0, z_i) X(z_i) W^+(z_i, z_0) s^+(z_0) \quad (4.6)$$

In this relation both  $s^+(z_0)$  and  $p^-(z_0)$  are vectors containing the monochromatic source and detector data at the surface as shown in figure 4.1. However, many shots are available so the source and detector data vectors should be extended to matrices. Each column of the  $S$  matrix contains the source data for one shot. The corresponding column in the  $P$  matrix contains the reflection response for the same shot position as shown in figure 4.6.

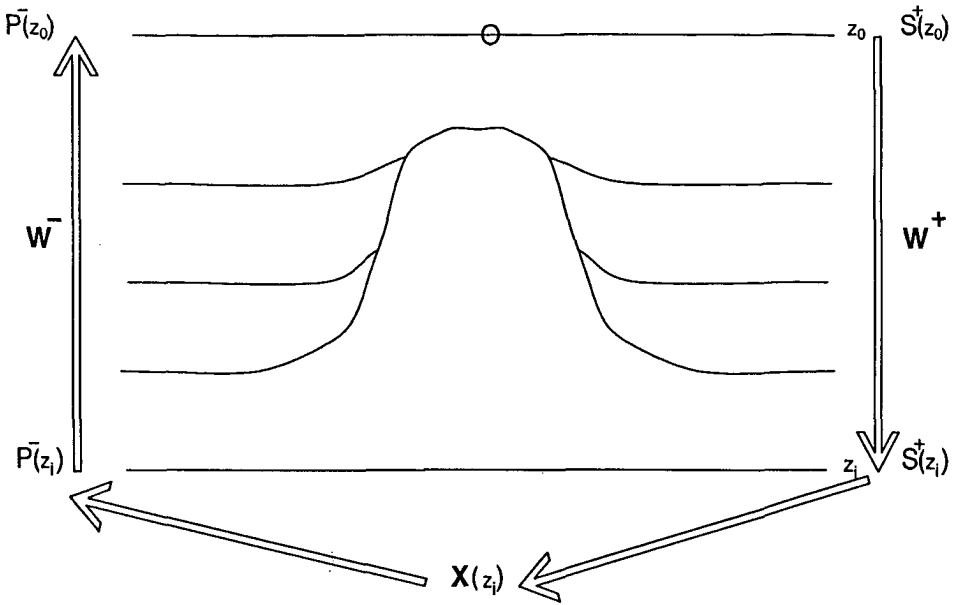


**Figure 4.5** The surface response  $p^-(z_0)$  due to a surface source wave field  $s^+(z_0)$  is obtained by applying a wave propagation operator  $W^+$  followed by a reflection response operator  $X(z_1)$  and a wave propagation operator  $W^-$  to bring the wave field back to the surface.

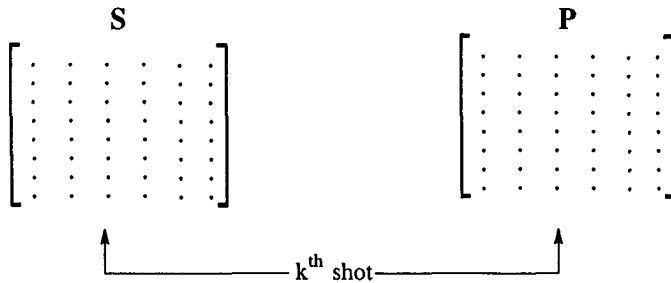


**Figure 4.6** Corresponding columns in the source data matrix  $S$  and the detector wave field matrix  $P$  relate to the same shot location.

So for a multi-shot experiment the forward model becomes:

$$\mathbf{P}^-(z_0) = \mathbf{W}^-(z_0, z_i) \mathbf{X}(z_i) \mathbf{W}^+(z_i, z_0) \mathbf{S}^+(z_0) \quad . \quad (4.7)$$

This equation describes the forward problem for a number of surface experiments where each source wave field  $\mathbf{s}^+(z_0)$  causes a reflection response  $\mathbf{p}^-(z_0)$  from the target zone. If some special acquisition parameters are present these may be incorporated in a detector matrix  $\mathbf{D}(z_0)$ :

$$\mathbf{P}^-(z_0) = \mathbf{D}(z_0) \mathbf{W}^-(z_0, z_i) \mathbf{X}(z_i) \mathbf{W}^+(z_i, z_0) \mathbf{S}^+(z_0) \quad . \quad (4.8)$$

If an array of geophones is used per station to suppress ground roll, the acquisition matrix becomes a band matrix instead of a diagonal matrix. However, since the emphasis is on the redatuming problem, the acquisition matrix will not be considered further on. We will assume that  $\mathbf{D}(z_0)$  and  $\mathbf{S}^+(z_0)$  are diagonal matrices.

For the migration the reflectivity matrix  $\mathbf{R}(z)$  should be determined for every depth level. In the redatuming application the target response  $\mathbf{X}(z_i)$  should be obtained for one depth level from the surface data. So the forward problem should be inverted for. The target reflection response  $\mathbf{X}(z_i)$  should be extracted from the surface data  $\mathbf{P}(z_0)$  by inverting (4.8).

## 4.2 THE TARGET RESPONSE X

In the redatuming the response from the target zone denoted by  $\mathbf{X}(z_i)$  should be obtained from the surface data. This response as it appears in the forward problem will be examined more closely.

The reflection response describes the relation between a down going incident wave field  $\mathbf{s}^+(z_i)$  and the up going reflected wave field  $\mathbf{p}^-(z_i)$ :

$$\mathbf{p}^-(z_i) = \mathbf{X}(z_i) \mathbf{s}^+(z_i) \quad . \quad (4.9)$$

For the case of a single reflector at  $z_i$  and a homogeneous halfspace below  $z_i$ ,  $\mathbf{X}(z_i)$  corresponds to the reflectivity properties  $\mathbf{R}(z_i)$  of the reflector. The reflection is defined as the relation between the incident wave field and the reflected wave field:

$$\mathbf{p}^-(z_i) = \mathbf{R}(z_i) \mathbf{s}^+(z_i) \quad . \quad (4.10)$$

If the reflectivity does not vary laterally the above equation may be written as

$$\mathbf{P}^-(x, z_i, \omega) = \mathbf{R}(x, z_i, \omega) * \mathbf{S}^+(x, z_i, \omega) \quad . \quad (4.11)$$

The reflection is written in terms of a spatial convolution (along the  $x$ -coordinate) of the reflectivity operator and the illuminating wave field. If the reflection operator is transformed from the space frequency domain to the wavenumber frequency domain by applying a Fourier

transform to  $R(x, z_i, \omega)$ , then each element of  $R(k_x, z_i, \omega)$  corresponds to a plane wave reflection coefficient:

$$\tilde{P}^-(k_x, z_i, \omega) = \tilde{R}(k_x, z_i, \omega) \tilde{S}^+(k_x, z_i, \omega) \quad (4.12)$$

$R(k_x, z_i, \omega)$  is the plane wave reflection coefficient for an angle of incidence  $\alpha$ , according to

$$\sin \alpha = \frac{k_x}{k}$$

and

$$k = \frac{\omega}{c} .$$

For one specific frequency  $R(k_x, z_i, \omega)$  is shown in figure 4.7. The reflected wave field is obtained by applying a plane wave reflection coefficient to each plane wave. If the reflection operator is applied in the  $x$  domain instead of the plane wave domain,  $R(k_x, z_i, \omega)$  should be transformed to the space domain. In figure 4.8 the transformed  $R(x, z_i, \omega)$  is shown. This operator should be spatially convolved with an incident wave field in order to obtain the reflected wave field (see equation 4.12). Each function  $R(x, z_i, \omega)$  represents one row of the reflectivity matrix in equation 4.10. Note that if the reflector is assumed to be locally reacting, the reflection operator  $R(x, z_i, \omega)$  becomes a spike.

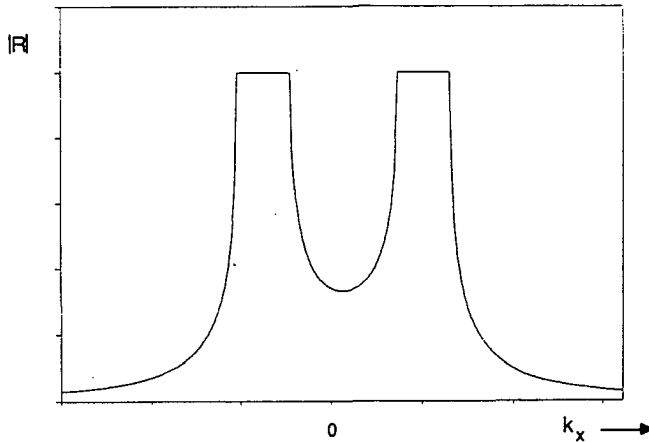


**Figure 4.7** The reflectivity  $R(k_x, \omega_i)$  is very similar to the plane wave reflection coefficient as a function the angle of incidence. The center of the horizontal axis corresponds to normal incidence. The points where the reflectivity function reaches 1 correspond to critical reflection. The points at which the function drops below 1 again are the  $90^\circ$  angle of incidence points.

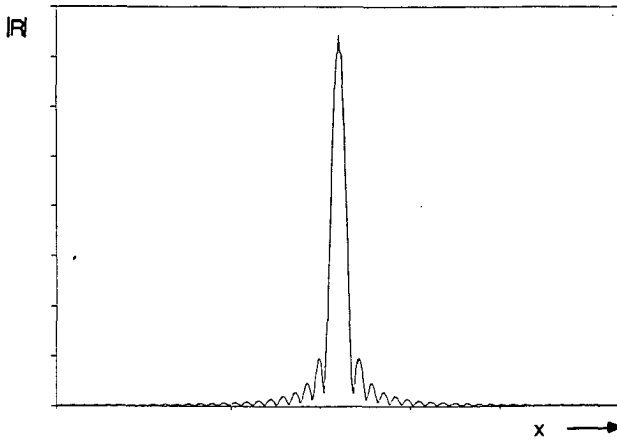


Figure 4.8 The reflectivity operator  $R(x, \omega)$  should be applied as a convolution operator to the data.

For a far more rigorous description of the concept of reflection in terms of convolution the reader is referred to Berkhout (1982).

In the above a single reflector is assumed at the target level. However, in general the target zone response is more complicated. For the forward model this response  $X(z_i)$  could be obtained through some modeling procedure. As discussed in chapter 2, the Kirchhoff integral can be used to model the wave propagation. However, in chapter 2 the discussion is focussed on modeling of propagation *through* the medium. The known wave fields are at one depth level whereas the unknown wave fields are at another depth level. For modeling the reflection response  $X(z_i)$  of the target structures both the down going wave field and the up going wave field should be modeled. A one-way approach is chosen so multiples are not included.

$$P^-(r_A, \omega) = -\frac{1}{4\pi} \int \frac{1}{\rho} \left[ P^+(r, \omega) \frac{\partial G^-(r, r_A, \omega)}{\partial n} - \frac{\partial P^+(r, \omega)}{\partial n} G^-(r, r_A, \omega) \right] dS \quad (4.13)$$

$r$  and  $r_A$  are on  $S$ , where  $S$  represents the datum just above the target.

In figure 4.9 the Green's function for some medium is shown. Note that the Green's function  $G^-(r, r_A, \omega)$  represents an up going scattered wave field arriving at  $r$  in  $S$ , related to a downward radiating source at  $r_A$  on  $S$  (figure 4.9). Expression 4.13 states that the up going wave field at  $r_A$  on  $S$  is obtained by applying the Kirchhoff integral to the down going wave

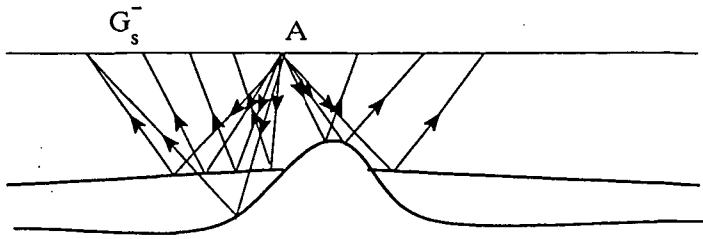


Figure 4.9 The target response  $X(z_i)$  may be written in terms of Green's functions  $G_s^-$ .

field on  $S$ . If the surface  $S$  is planar, equation 4.13 may be modified. As discussed in chapter 2, both terms in the above Kirchhoff integral become identical so

$$P^-(x_A, y_A, z_s, \omega) = -\frac{1}{2\pi} \int_S \frac{1}{\rho} \left[ P^+(x', y', z_s, \omega) \frac{\partial G^-(x', y', x_A, y_A, z_s, \omega)}{\partial n} \right] dx' dy' \quad (4.14)$$

or in matrix notation

$$p^-(z_s) = X(z_s) p^+(z_s) \quad (4.15)$$

where the rows of  $X(z_s)$  are given by the Green's function  $G^-$  according to equation 4.14.

### 4.3 THE REDATUMING

In the redatuming the objective is to obtain the target reflection response  $X(z_i)$  at the new datum from the surface data. From the previous relation it follows that the illuminating wave field  $W^+(z_i, z_0) S^+(z_0)$  has to be inverted for as well as the upward propagation  $W^-(z_0, z_i)$ . The redatumed reflection response is given by (figure 4.10).

$$\begin{matrix}
 \begin{bmatrix} \cdot & \cdot & \cdot & \cdot \\ \cdot & \cdot & \cdot & \cdot \\ \cdot & \cdot & \cdot & \cdot \\ \cdot & \cdot & \cdot & \cdot \end{bmatrix} & = & \begin{bmatrix} \cdot & \cdot & \cdot & \cdot \\ \cdot & \cdot & \cdot & \cdot \\ \cdot & \cdot & \cdot & \cdot \\ \cdot & \cdot & \cdot & \cdot \end{bmatrix} & \begin{bmatrix} \cdot & \cdot & \cdot & \cdot \\ \cdot & \cdot & \cdot & \cdot \\ \cdot & \cdot & \cdot & \cdot \\ \cdot & \cdot & \cdot & \cdot \end{bmatrix} & \begin{bmatrix} \cdot & \cdot & \cdot & \cdot \\ \cdot & \cdot & \cdot & \cdot \\ \cdot & \cdot & \cdot & \cdot \\ \cdot & \cdot & \cdot & \cdot \end{bmatrix} \\
 P_{z_i}^- & & [W^-]^{-1} & P_{z_0}^- & [W^+ S^+]^{-1}
 \end{matrix}$$

Figure 4.10 The redatuming in terms of matrix operations.

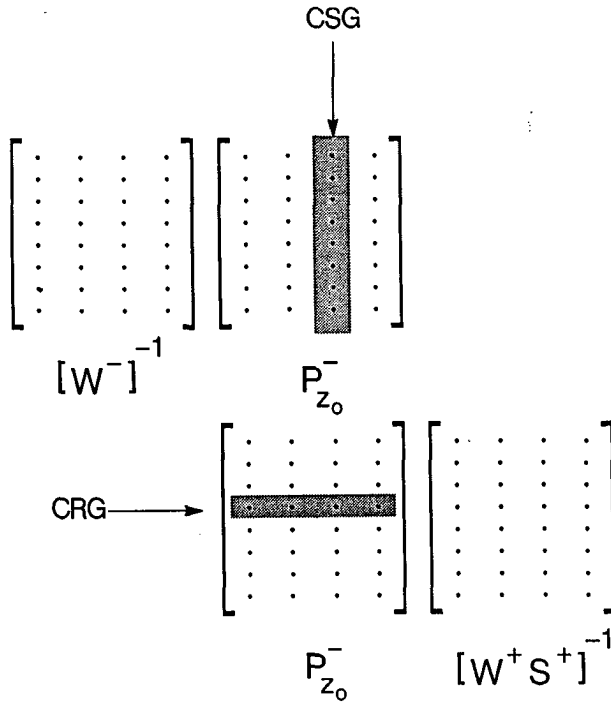


**Figure 4.11** The matrix operations for the redatuming involve an inverse extrapolation per CSG and a source wave field extrapolation per CRG.

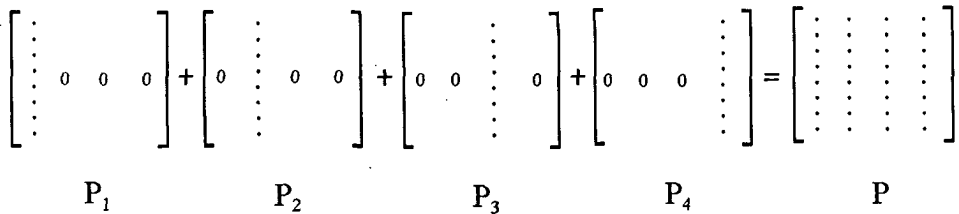


**Figure 4.12** In redatuming per shot gather each shot is processed separately. Addition of all partial redatuming results will yield the same response as as in figure 4.11

$$X(z_i) = [W^-(z_0, z_i)]^{-1} P^-(z_0) [W^+(z_i, z_0) S^+(z_0)]^{-1} \tag{4.16}$$

The inverse extrapolation operator  $\mathbf{W}^{-1}$  has been discussed in the previous chapter. In the relation above  $[\mathbf{W}^{-}(z_0, z_i)]^{-1} \mathbf{P}^{-}(z_0)$  describes the elimination of the overburden wave propagation effects for the reflected up going wave field. The registered wave field is inversely extrapolated down to the target zone. Since this matrix multiplication involves operation on the columns of  $\mathbf{P}^{-}(z_0)$  (figure 4.11) this inverse extrapolation is carried out per common shot gather (CSG). The other part of the right hand side of equation 4.16  $\mathbf{P}^{-}(z_0)[\mathbf{W}^{+}(z_i, z_0) \mathbf{S}^{+}(z_0)]^{-1}$  involves dot products of the rows of  $\mathbf{P}^{-}(z_0)$  with the columns of  $[\mathbf{W}^{+}(z_i, z_0) \mathbf{S}^{+}(z_0)]^{-1}$ . So this matrix multiplication which represents inversion of the illuminating wave field involves processing per common receiver gather (CRG). In the redatuming procedure proposed by Berryhill (1984) the inverse extrapolation per CSG and CRG also occurred. In practice this is a problem (especially for the 3-D case) since it involves changing the data organization during the processing. The data volume is quite large so this data reordering should be avoided. In the matrix notation the previous relation can easily be written in terms of processing per common shot gather. If we have only one shot record, the data matrix  $\mathbf{P}_k^{-}(z_0)$  is zero except for the  $k^{\text{th}}$

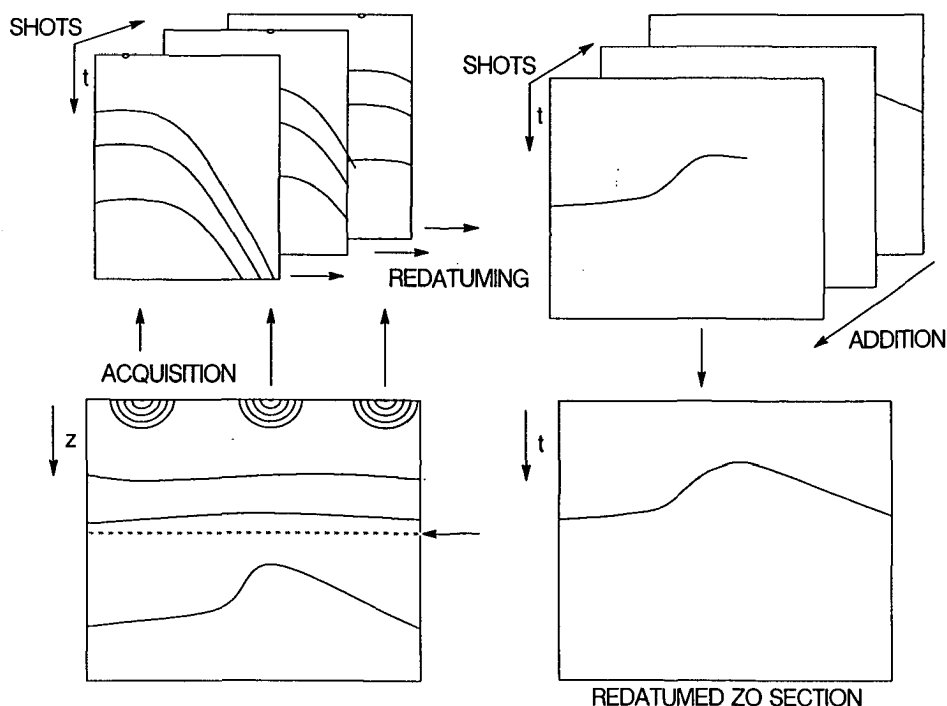


**Figure 4.13** The shot record redatuming involves a redatuming of each shot separately followed by an addition of all the redatumed shot data.

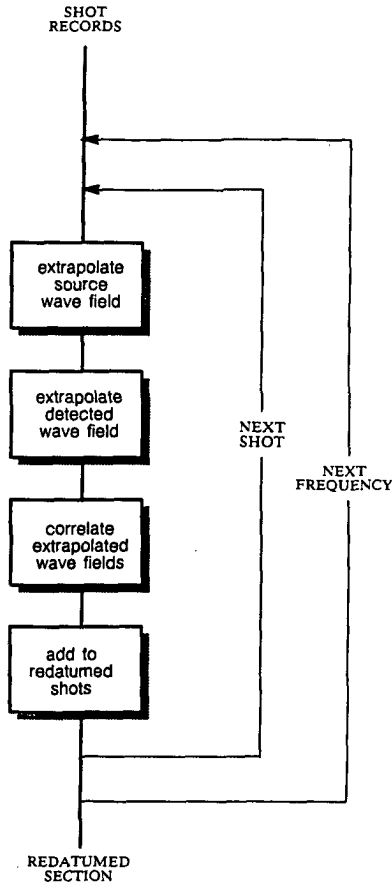


Figure 4.14 Flowchart for the shot record redatuming process.

column corresponding to the shot location  $x_k$ . Applying the previous relation results in a redatumed section for only one surface shot record:

$$X(z_1) = \left[ W^-(z_0, z_1) \right]^{-1} P_k^-(z_0) \left[ W^+(z_1, z_0) S^+(z_0) \right]^{-1} \quad (4.17)$$

Repeating this procedure for each shot record and adding the results, gives the redatumed reflection response. For many different shot locations this single shot record redatuming is given by

$$X = X_1 + X_2 + \dots + X_k + \dots + X_N \quad (4.18)$$

so

$$\mathbf{X}(z_i) = \left[ \mathbf{W}^-(z_0, z_i) \right]^{-1} \left[ \mathbf{P}_0^-(z_0) + \dots + \mathbf{P}_k^-(z_0) \dots + \mathbf{P}_N^-(z_0) \right] \left[ \mathbf{W}^+(z_i, z_0) \mathbf{S}^+(z_0) \right]^{-1}, \quad (4.19)$$

or

$$\mathbf{X}(z_i) = \left[ \mathbf{W}^-(z_0, z_i) \right]^{-1} \mathbf{P}^-(z_0) \left[ \mathbf{W}^+(z_i, z_0) \mathbf{S}^+(z_0) \right]^{-1}, \quad (4.20)$$

in which the data matrix  $\mathbf{P}^-(z_0)$  contains zeros except for the  $k^{\text{th}}$  column corresponding to shot position  $x_k$  (see figure 4.12). This relation is equivalent to the multi shot redatuming relation, so a processing per common shot gather in the redatuming procedure should be feasible. The procedure is shown schematically in figures 4.13 and 4.14. If the number of shot locations at the surface is less than the number of shots at the new datum the problem is ill-posed. Few surface registrations can not give a correct reflection response for many points at the new datum.

In conclusion, a wave propagation model together with sufficient surface shot records allows for the construction of a zero offset section (diagonal of  $\mathbf{X}$ ) or a set of common shot gathers (columns  $\mathbf{X}$ ) at a new datum. Furthermore the redatuming procedure allows for processing per surface shot record. The zero offset section which is obtained with redatuming is a true zero offset section. Unlike the conventional CMP stacking process, no hyperbolic assumptions are made about the move out curve. In the redatuming the move out elimination is based on the wave equation and the interval velocity model. The zero offset section is therefore truly zero offset.

#### 4.4 REDATUMING WITH THE FULL KIRCHHOFF OPERATOR

The redatuming process as discussed in the previous section assumes Rayleigh type of extrapolation operators. Only the acoustic pressure wave field is considered in the extrapolation. If the full Kirchhoff integral is applied, both the particle velocity and the pressure of the wave field should be extrapolated. The operator matrices and data matrices should contain the data and operators related to both wave field variables  $P$  and  $V_n$ . In matrix notation the matrices containing the wave field should consist of two submatrices containing the pressure data and the normal component of the particle velocity data:

$$\begin{bmatrix} \mathbf{P}^+ \\ \dots \\ \mathbf{V}_n^+ \end{bmatrix} \quad \text{or} \quad \begin{bmatrix} \mathbf{P}^- \\ \dots \\ \mathbf{V}_n^- \end{bmatrix}. \quad (4.21)$$

The extrapolation operator for this data matrix consists of 2x2 submatrices

$$\begin{bmatrix} \frac{1}{2} \mathbf{W}_{PP}^+ & | & \frac{1}{2} \mathbf{W}_{PV}^+ \\ \dots & \dots & \dots \\ \frac{1}{2} \mathbf{W}_{VP}^+ & | & \frac{1}{2} \mathbf{W}_{VV}^+ \end{bmatrix} \quad \text{or} \quad \begin{bmatrix} \frac{1}{2} \mathbf{W}_{PP}^- & | & \frac{1}{2} \mathbf{W}_{PV}^- \\ \dots & \dots & \dots \\ \frac{1}{2} \mathbf{W}_{VP}^- & | & \frac{1}{2} \mathbf{W}_{VV}^- \end{bmatrix} .$$

The submatrix  $\mathbf{W}_{PP}$  represents the P to P extrapolation operator.  $\mathbf{W}_{PP}$  corresponds to the first term of the integral in equation 2.11. The  $\mathbf{W}_{PV}$  represents the  $V_n$  to P extrapolation operator. This corresponds to the second term of the integral in equation 2.12.  $\mathbf{W}_{VP}$  is the P to  $V_n$  extrapolation operator and  $\mathbf{W}_{VV}$  is the  $V_n$  to  $V_n$  extrapolation operator based on the integral equation in relation ..... The full Kirchhoff extrapolation of the pressure and particle velocity is achieved with the following matrix multiplication.

$$\begin{bmatrix} \mathbf{P}^+(z_s) \\ \dots \\ \mathbf{V}_n^+(z_s) \end{bmatrix} = \begin{bmatrix} \frac{1}{2} \mathbf{W}_{PP}^+(z_s, z_0) & | & \frac{1}{2} \mathbf{W}_{PV}^+(z_s, z_0) \\ \dots & \dots & \dots \\ \frac{1}{2} \mathbf{W}_{VP}^+(z_s, z_0) & | & \frac{1}{2} \mathbf{W}_{VV}^+(z_s, z_0) \end{bmatrix} \begin{bmatrix} \mathbf{P}^+(z_0) \\ \dots \\ \mathbf{V}_n^+(z_0) \end{bmatrix} . \tag{4.22}$$

Note that this equation describes the downward extrapolation. A similar equation holds for the upward extrapolation.

The target response  $\mathbf{X}$  as defined in section 4.3 should also be built up from four submatrices.

$$\mathbf{X}(z_s) = \begin{bmatrix} \mathbf{X}_{PP}(z_s) & | & \mathbf{X}_{PV}(z_s) \\ \dots & \dots & \dots \\ \mathbf{X}_{VP}(z_s) & | & \mathbf{X}_{VV}(z_s) \end{bmatrix} . \tag{4.23}$$

Each submatrix represents the pressure or particle velocity response for a pressure or particle velocity input. With  $\mathbf{X}_{PP}$ ,  $\mathbf{X}_{VV}$ ,  $\mathbf{X}_{PV}$  and  $\mathbf{X}_{VP}$ , the response of the target for a wave field described in terms of pressure distribution and particle velocity is defined. The four responses however are not independent because for a given wave field, P and  $V_n$  are not independent. The forward model for both P and  $V_n$  becomes (figure 4.15):

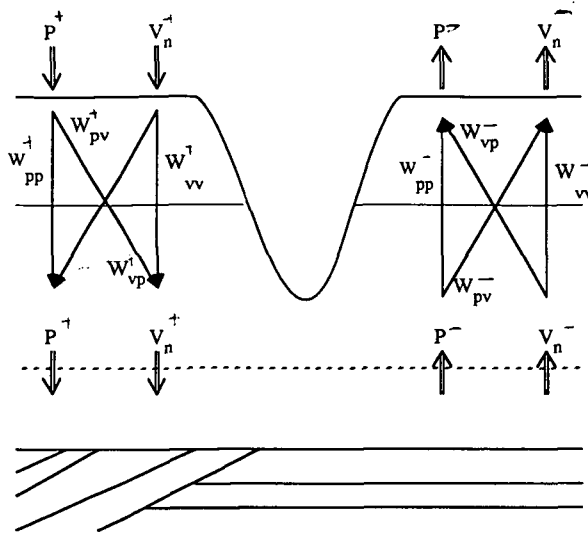


Figure 4.15 Forward modeling of the seismic surface response in terms of P and V<sub>n</sub>.

$$\begin{bmatrix} \mathbf{P}^-(z_0) \\ \dots \\ \mathbf{V}_n^-(z_0) \end{bmatrix} = \begin{bmatrix} \frac{1}{2}\mathbf{W}_{PP}^- & \frac{1}{2}\mathbf{W}_{PV}^- \\ \dots & \dots \\ \frac{1}{2}\mathbf{W}_{VP}^- & \frac{1}{2}\mathbf{W}_{VV}^- \end{bmatrix} \begin{bmatrix} \mathbf{X}_{PP}(z_s) & | & \mathbf{X}_{PV}(z_s) \\ \dots & \dots & \dots \\ \mathbf{X}_{VP}(z_s) & | & \mathbf{X}_{VV}(z_s) \end{bmatrix} \begin{bmatrix} \frac{1}{2}\mathbf{W}_{PP}^+ & \frac{1}{2}\mathbf{W}_{PV}^+ \\ \dots & \dots \\ \frac{1}{2}\mathbf{W}_{VP}^+ & \frac{1}{2}\mathbf{W}_{VV}^+ \end{bmatrix} \begin{bmatrix} \mathbf{P}^+(z_0) \\ \dots \\ \mathbf{V}_n^+(z_0) \end{bmatrix}, \quad (4.24)$$

where

$\begin{bmatrix} \mathbf{P}^-(z_0) \\ \dots \\ \mathbf{V}_n^-(z_0) \end{bmatrix}$  is the up going wave detected field at the surface and

$\begin{bmatrix} \mathbf{P}^+(z_0) \\ \dots \\ \mathbf{V}_n^+(z_0) \end{bmatrix}$  is the down going source wave field at the surface.

For notational convenience we omitted the arguments  $(z_s, z_0)$  and  $(z_0, z_s)$  in the downward and upward extrapolation operators, respectively.

However, finding both  $X_{PP}$  and  $X_{VV}$  and the cross terms  $X_{PV}$  and  $X_{VP}$  from the down going source wave field  $P^+$  and the up going wave field  $P^-$  on the new datum is not trivial. I have not found a way to construct the four dependent responses  $X_{PP}$ ,  $X_{VV}$ ,  $X_{PV}$  and  $X_{VP}$  from the up going and down going P and  $V_n$  at the new datum for any geometry. If the cross terms  $X_{PV}$  and  $X_{VP}$  could be eliminated, the reconstruction of  $X_{PP}$  and  $X_{VV}$  would be straightforward as will be shown below.

If the new datum would be a planar surface, assuming one-way wave fields, the dependency between  $X_{PP}$ ,  $X_{VV}$ ,  $X_{PV}$  and  $X_{VP}$  could be expressed explicitly, without any knowledge about the actual wave field. In chapter 2 it has been shown that for one-way Green's functions the contributions for both terms in the Kirchhoff integral are identical in case of integration over a planar surface. In analogy with the derivation of equation 2.30 and 2.31 from 2.11, we may therefore write equation 4.24 as

$$\begin{bmatrix} P^-(z_0) \\ \dots \\ V_n^-(z_0) \end{bmatrix} = \begin{bmatrix} \frac{1}{2}W_{PP}^- & | & \frac{1}{2}W_{PV}^- \\ \dots & \dots & \dots \\ \frac{1}{2}W_{VP}^- & | & \frac{1}{2}W_{VV}^- \end{bmatrix} \begin{bmatrix} X_{PP}(z_s) & | & \mathbf{0} \\ \dots & \dots & \dots \\ \mathbf{0} & | & X_{VV}(z_s) \end{bmatrix} \begin{bmatrix} \frac{1}{2}W_{PP}^+ & | & \frac{1}{2}W_{PV}^+ \\ \dots & \dots & \dots \\ \frac{1}{2}W_{VP}^+ & | & \frac{1}{2}W_{VV}^+ \end{bmatrix} \begin{bmatrix} P^+(z_0) \\ \dots \\ V_n^+(z_0) \end{bmatrix} \quad (4.25)$$

For the redatuming the following equation should be solved

$$\begin{bmatrix} P^-(z_s) \\ \dots \\ V_n^-(z_s) \end{bmatrix} = \begin{bmatrix} X_{PP}(z_s) & | & \mathbf{0} \\ \dots & \dots & \dots \\ \mathbf{0} & | & X_{VV}(z_s) \end{bmatrix} \begin{bmatrix} P^+(z_s) \\ \dots \\ V_n^+(z_s) \end{bmatrix}, \quad (4.26)$$

where

$$\begin{bmatrix} P^-(z_s) \\ \dots \\ V_n^-(z_s) \end{bmatrix} = \begin{bmatrix} \frac{1}{2}W_{PP}^- & | & \frac{1}{2}W_{PV}^- \\ \dots & \dots & \dots \\ \frac{1}{2}W_{VP}^- & | & \frac{1}{2}W_{VV}^- \end{bmatrix}^{-1} \begin{bmatrix} P^-(z_0) \\ \dots \\ V_n^-(z_0) \end{bmatrix} \quad (4.27)$$

and

$$\begin{bmatrix} \mathbf{P}^+(z_s) \\ \dots \\ \mathbf{V}_n^+(z_s) \end{bmatrix} = \begin{bmatrix} \frac{1}{2} \mathbf{W}_{PP}^+ & | & \frac{1}{2} \mathbf{W}_{PV}^+ \\ \dots & \dots & \dots \\ \frac{1}{2} \mathbf{W}_{VP}^+ & | & \frac{1}{2} \mathbf{W}_{VV}^+ \end{bmatrix} \begin{bmatrix} \mathbf{P}^+(z_0) \\ \dots \\ \mathbf{V}_n^+(z_0) \end{bmatrix} \quad (4.28)$$

Hence,  $\mathbf{X}_{PP}(z_s)$  is resolved from the downward extrapolated wave fields  $\mathbf{P}^-(z_s)$  and  $\mathbf{P}^+(z_s)$ , according to

$$\mathbf{X}_{PP}(z_s) = \mathbf{P}^-(z_s) [\mathbf{P}^+(z_s)]^{-1} \quad (4.29)$$

Similarly,  $\mathbf{X}_{VV}(z_s)$  is resolved from the downward extrapolated wave fields  $\mathbf{V}_n^-(z_s)$  and  $\mathbf{V}_n^+(z_s)$ , according to

$$\mathbf{X}_{VV}(z_s) = \mathbf{V}_n^-(z_s) [\mathbf{V}_n^+(z_s)]^{-1} \quad (4.30)$$

The P to P response  $\mathbf{X}_{PP}$  at the new datum  $z_i$  should be reconstructed from the inverse extrapolated source wave field  $\mathbf{P}^+(z_i)$  and the inverse extrapolated detected wave field  $\mathbf{P}^-(z_i)$ . This is similar to the procedure for the redatuming of P only, which has been discussed in the previous section. The  $\mathbf{V}_n$  to  $\mathbf{V}_n$  response  $\mathbf{X}_{VV}$  is reconstructed similarly from the particle velocities  $\mathbf{V}_n^+(z_i)$  and  $\mathbf{V}_n^-(z_i)$  at the new datum.

#### 4.5 APPLICATION OF REDATUMING IN LAYER REPLACEMENT

The redatuming process is primarily intended for bringing the acquisition surface down to the target area. However, if the main interests are the general geological features in the whole subsurface instead of only a small area, the datum should be the surface. However, especially in the case of marine data, an undulating sea floor may result in a distortion and disruption of reflection events from the underlying structures. Yilmaz and Lucas (1986) suggested the use of pre-stack redatuming to eliminate the water layer and to replace it by a layer with a velocity similar to the velocity in the shallow structures. This is accomplished by inverse extrapolating the detected data and the source data to the sea floor taking the wave propagation velocity in water. Next, the inverse extrapolated wave fields are forward extrapolated to the acquisition datum with a velocity which is close to the velocity of the first layer. The extrapolated wave fields are then used to reconstruct shot records. The distortion from the irregular water-bottom has now been eliminated in the surface data. The stacking process may yield a better result after the layer replacement.

#### 4.6 REDATUMING AND MIGRATION

In this section the relation between migration, redatuming and focussing analysis will be discussed. In seismics the migration is used to obtain an image of the reflectivity everywhere in the subsurface. The focussing analysis is a technique to verify if the migration velocities used in the migration process are correct. The migration and redatuming have many similarities (figure 4.16). In the migration, in order to image the reflectivity at a certain depth, the wave propagation effects for the shallower structures are eliminated. By taking the ratio of the up going wave field and the down going incident wave field at a depth, the reflectivity is estimated.

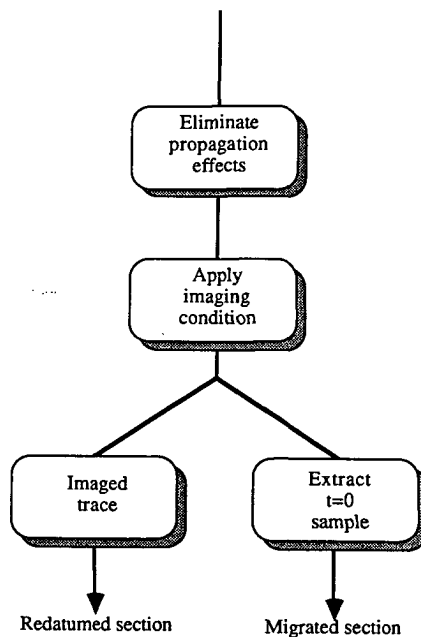


**Figure 4.16** In both redatuming as well as depth migration an elimination of overburden wave propagation effects takes place followed by an imaging step.

A more commonly used imaging condition is the correlation of the down going wave field and the up going wave field at  $t = 0$  s. This imaging condition is stable. In redatuming the process is very similar. The wave propagation effects for the overburden are eliminated as well. The imaging condition however should not result in the reflectivity at a single depth, but the full response for the lower structures. The ratio of the down going wave field and the up going wave field results in the reflectivity for  $t = 0$  s and the response of the lower structures at

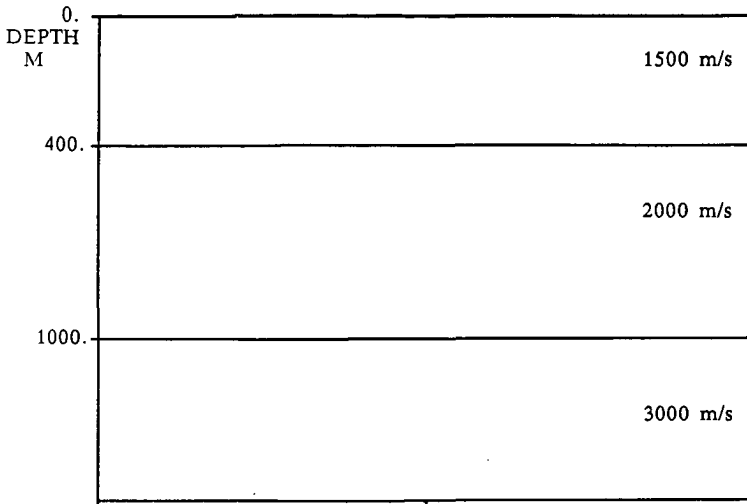


**Figure 4.17** Both depth migration and redatuming are carried out with the surface reflection data for both reflectors. The new datum coincides with the first reflector.

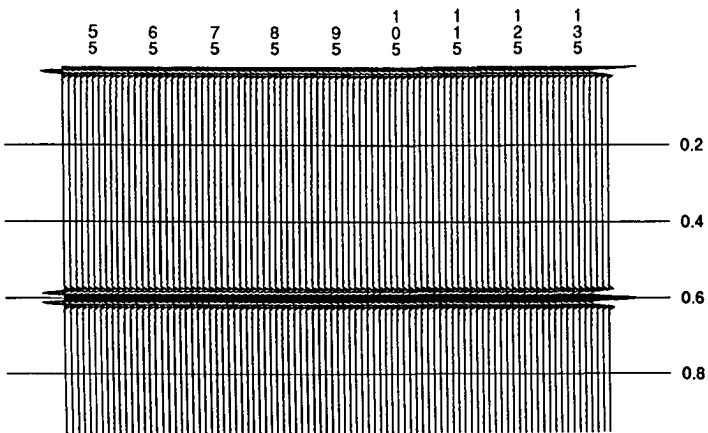


**Figure 4.18** True zero offset time section obtained with redatuming to the first reflector (again has been applied to emphasize the reflection from the second interface).

$t > 0$  s. For a simple medium this is shown in figure 4.17. A pre-stack redatuming is carried out at the level of the second reflector. A zero offset section after redatuming is shown in figure 4.18. The first reflector occurs at  $t = 0$  s. In the redatumed section sources and receivers are located at the new datum on top of the reflector. The travel time for the reflection response is therefore zero seconds. The second reflector occurs at the two way travel time. In the migrated section (figure 4.19) the vertical axis is depth instead of time. The reflectivity is obtained for every depth level in the subsurface. Whereas in the redatuming the amplitude of the second reflector is determined by both the propagation effects and the reflection properties.

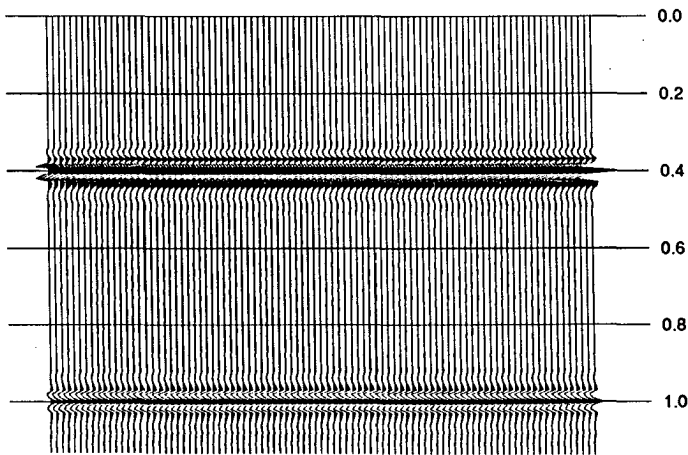
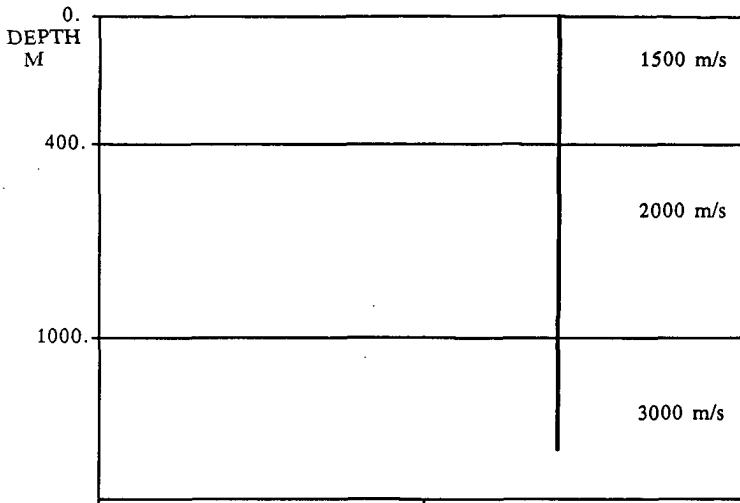


Figure 4.19 Depth migrated section.

The focussing analysis was first discussed by Yilmaz and Chambers (1984). However, they used time migration which does not result in an correct image in depth for laterally varying media. In 1986 Faye and Jeannot presented a paper where they used the focussing analysis with depth migration. In the focussing analysis the imaging condition is similar to the condition used in the redatuming process. After the correlation of the down going wave field and the up going wave field the whole result is used instead of only the zero time sample. By doing this analysis at a certain lateral position for every depth as shown in figure 4.20, as discussed by Cox in the TRITON reports (1987, 1988), a verification of the macro model may be carried out. In case of a correct velocity model, all energy should be concentrated around the zero time line. From the deviations of the focus energy from the zero time line a model update may be derived. For



**Figure 4.20** For the focussing analysis vertical new datum could be taken. If the interval velocities are incorrect the maximum reflection event does not occur at  $t = 0$  s.

simple horizontally layered media an analytical relation between model error and incorrect imaging position may be derived.

For more complex media iterative update procedures should be used. So redatuming to a vertical datum results in the focussing panels, which are used in the focussing analysis.

## 5

---

## APPLICATION OF THE REDATUMING

In this chapter the redatuming procedure, which has been discussed in the previous chapter has been applied to both synthetic data examples as well as a real data set. In the first section of this chapter the effects of a limited geophone spread and geophone sampling on the redatuming result are investigated. It is very interesting to study what information the registered data contains about the subsurface before interpreting the redatumed data.

In the next sections redatuming examples for synthetic data are discussed. The first synthetic example involves a single interface overburden with steep dips and strong lateral velocity variations. Through finite difference modeling synthetic data is obtained. The surface data is brought down through redatuming.

In the second synthetic example finite difference data has been modeled for a dome structure. Redatuming is carried out to obtain a true zero offset section for the structures below the dome. Finally in the last sections a real data example is discussed. The data was obtained through physical modeling in a water tank. The overburden for this model consists of a dome structure and a faulted structure. The redatuming is carried out to obtain an undistorted zero offset section of a deep planar reflector.

### 5.1 THE EFFECTS OF GEOPHONE SPREAD AND SPATIAL SAMPLING ON MIGRATION AND REDATUMING

In practice the geophones are spread out over a limited distance. So not all of the reflected wave field is registered at the surface. Furthermore the distance between the geophone stations and the

individual shot location is not always according to the spatial sampling Nyquist criterion. The number of geophone stations and the station spacing are strongly related to the costs of a survey. However, if insufficient geophone stations are used some data may be lost. The geophone spread is related to the angular illumination of the reflectors in the subsurface. The reflectivity as a function of incidence, which is investigated in amplitude versus offset techniques may give detailed information on the density and velocity structure at the reservoir. However, these techniques fail if insufficient angular illumination is available. Therefore the angular reflectivity which is available in the data given the subsurface structures and the geophone spread should be examined.

For the subsurface geometry from figure 5.1 the geophone spread and sampling have been varied. Sources and receivers are located at the surface. A redatuming to the level of the reflector is carried out for each of the acquisition configurations. Of course the effects of different geophone spreads and sampling depends on the subsurface geometry. It is not possible to give explicit analytical relations between some surface spread layout and the resulting effect after migration for a reflector at one kilometer depth, which holds for every subsurface structure. The dip and curvature in the overburden will strongly effect the wave propagation. However the experiments shown in this section should give some idea as to how different spread configurations may effect the image of a reflector in the subsurface after migration or redatuming. In terms of the response matrix  $\mathbf{X}$  as defined in the previous section, different parts of this matrix are obtained as output from the redatuming. Since the redatuming occurs at the level of a reflector with no reflections occurring from deeper structures the response matrix  $\mathbf{X}$  is equivalent to the reflectivity matrix  $\mathbf{R}$ . Either the diagonal of the  $\mathbf{R}$  matrix, a zero offset section

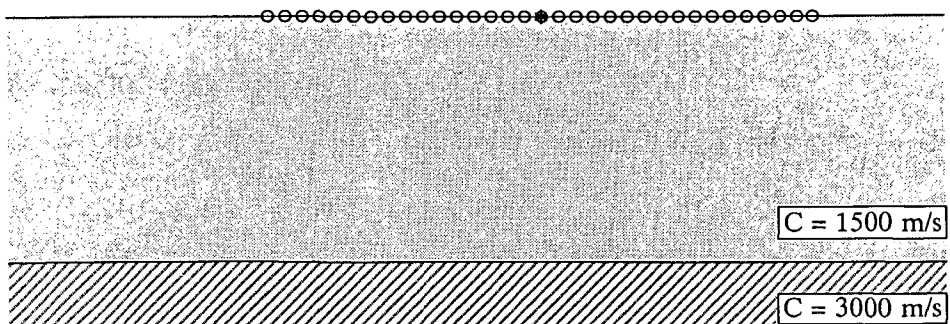


**Figure 5.1** The effect of cable truncation and acquisition geometry on redatuming is examined with the above subsurface model.

is considered, or a single row of the response matrix is regarded. The zero offset section relates most strongly to what an interpreter would like to have as output. However it contains not all of the available reflection information. A single row of the response matrix contains information about the reflection as a function of the angle of incidence. So a row of  $\mathbf{R}$  should tell use about the angular illumination of the reflector for some surface acquisition configuration. This is very important information since amplitude versus offset techniques use the angular reflection properties to estimate the lithological properties. If the angular illumination for a certain reflector is insufficient amplitude versus offset techniques will not give an accurate estimate of the lithologic parameters. In the experiments the row of the response matrix  $\mathbf{R}$  will be presented in the wave number domain. In this domain each element of  $\mathbf{R}$  corresponds to a plane wave reflection coefficient. In the space domain the  $\mathbf{R}$  matrix is a reflectivity operator in terms of convolutions which is very hard to interpret. In figure 5.2 the reflectivity for an interface between a 1500 m/s and a 3000 m/s layer is shown. The frequency is along the vertical axis. The wave number is along the horizontal axis. All straight lines going through the origin correspond to constant angle of incidence. Furthermore the figure is symmetrical in the vertical axis since the reflectivity for an angle of incidence of  $+\alpha^\circ$  is the same as the reflectivity for  $-\alpha^\circ$ . A cross section for constant frequency is also shown in figure 5.2. The horizontal axis is  $k_x$  but can also be interpreted as the angle of incidence according to

$$\sin \alpha = \frac{k_x}{k} \quad . \quad (5.1)$$

The figure corresponds to the familiar plane wave reflection as a function of the angle of incidence.

In the first set of experiments a split spread configuration is used. The spread length is varied from 3000 m to 200 m as is shown in figures 5.3a through 5.4c. The limited spread means that far offsets are not recorded. Therefore only a limited dip of the wave field is recorded. A high angle of incidence on the reflector would cause the reflected wave field to arrive at the surface beyond the last geophone. A row of the  $\mathbf{R}$  matrix, obtained after the redatuming will be presented in the wave number domain. The figures should give a clear indication which angular reflection coefficients are resolved by the migration process. Figures 5.5 through 5.10 show the resolved reflectivity functions for the migration of a 3000 m geophone spread through a 200 m geophone spread. For the maximum spread length the reflection coefficient is fully resolved by the migration process. A cross section of the migrated data for 30 Hz is depicted in the figures as well. The dashed line corresponds to the migrated data and the solid line is associated with the analytical solution. Beyond  $k_x = \omega/c$  ( $90^\circ$ ) the reflection coefficient is unresolved because the inverse wave propagation does not handle the evanescent waves properly. This is the case for all commonly used migration algorithms. For the propagating waves the migration results matches the analytical solution quite well. Some ringing occurs due to aperture truncation. As

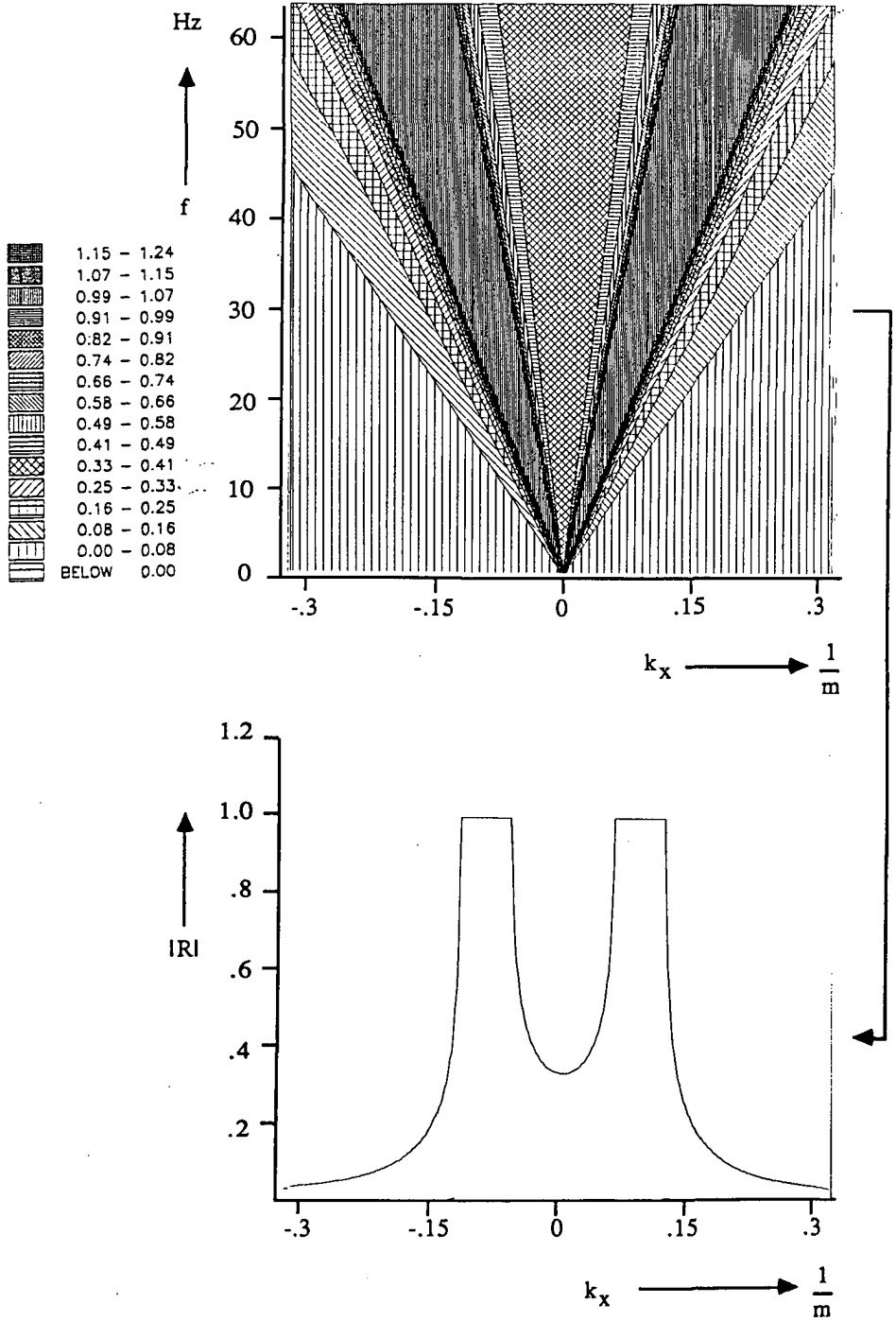


**Figure 5.2** The analytical reflectivity for the reflector from figure 5.1 in the  $k_x$ - $\omega$  domain. The lower figure is a horizontal cross section at 30 Hz showing the plane wave reflection coefficient as a function of the angle of incidence according to  $\sin \alpha = k_x/k$ .

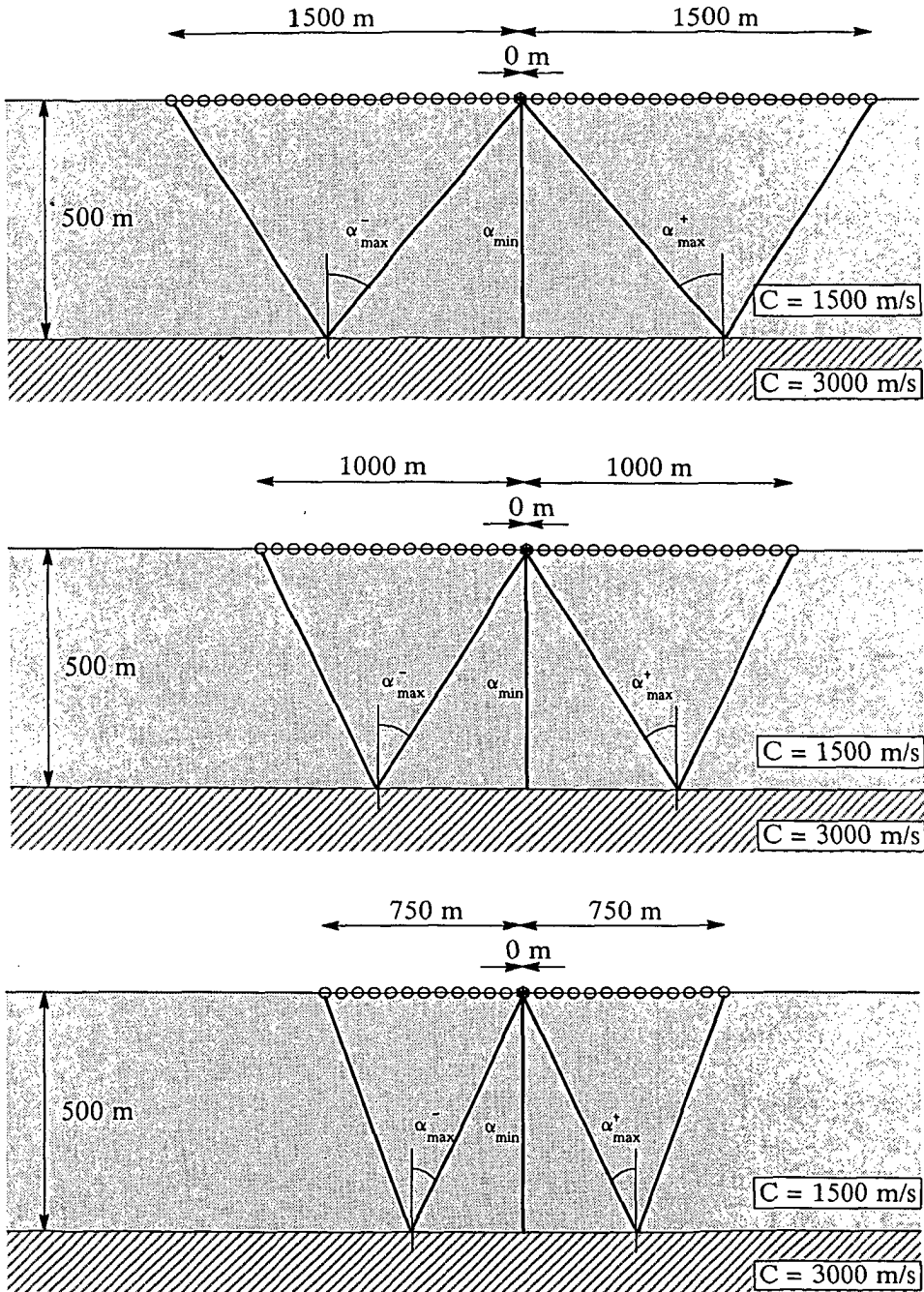
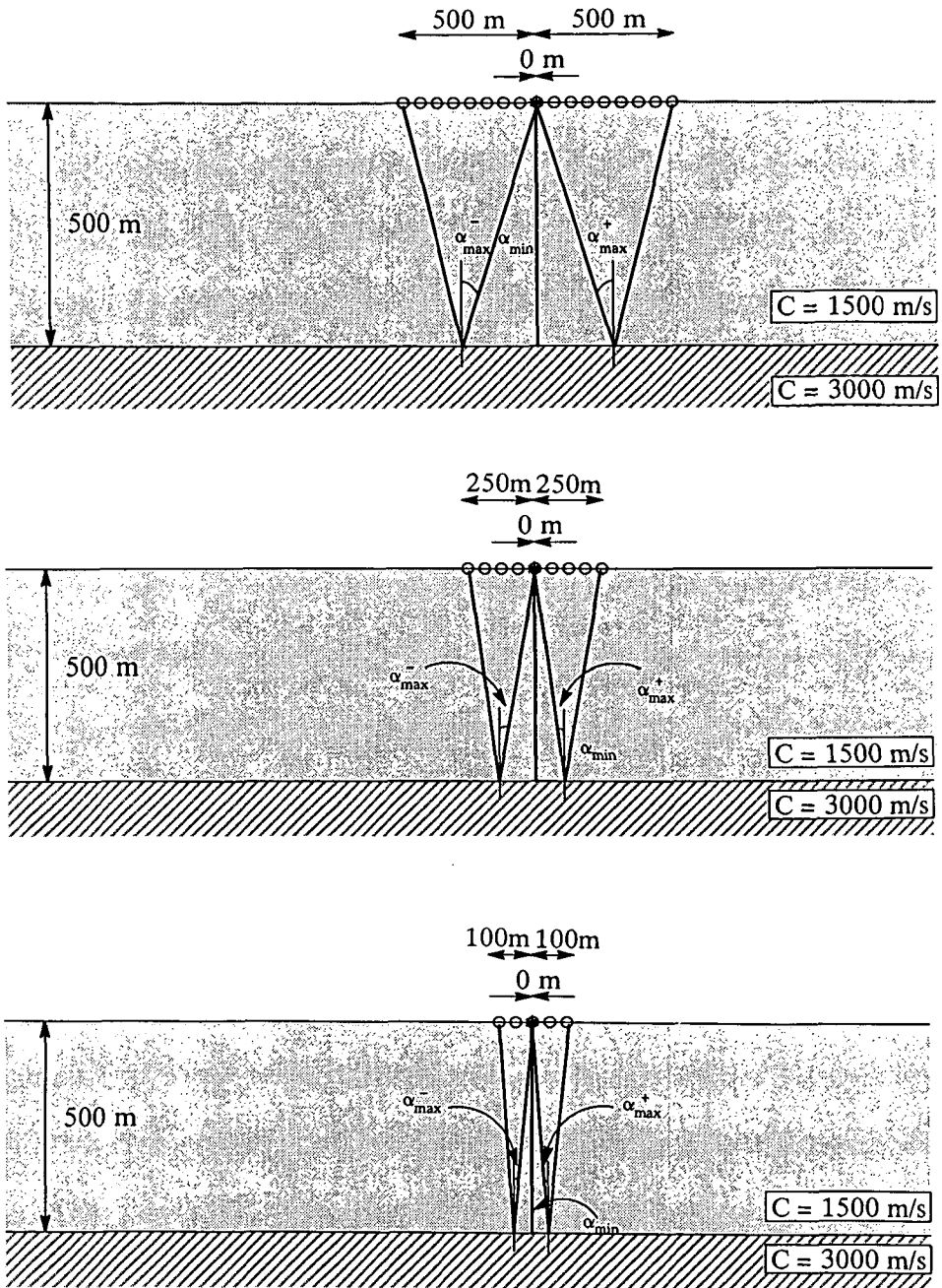
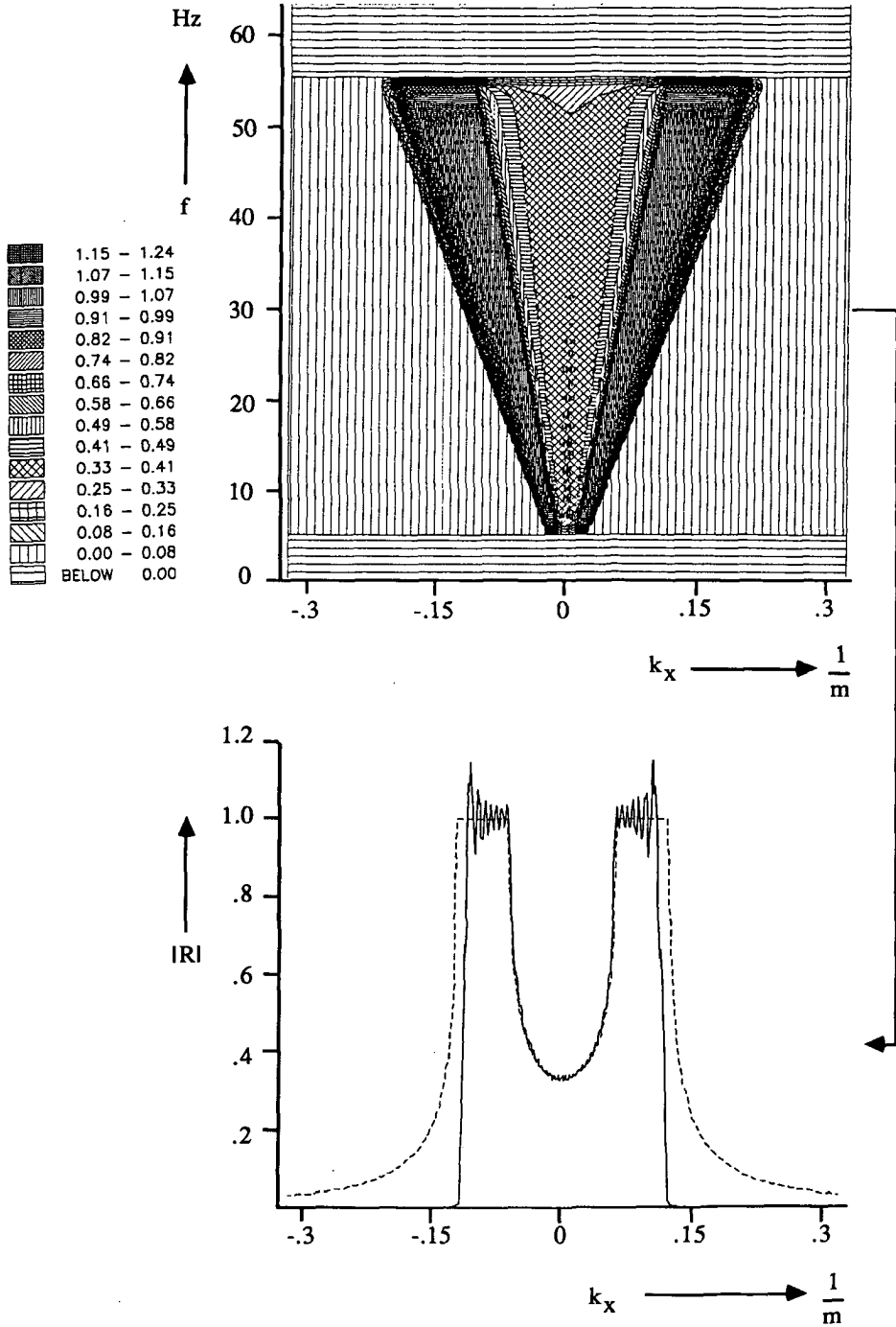


Figure 5.3 The cable length has been varied from 3 km in (a) to 1.5 km in (c). A redatuming is carried out to the reflector at 500 m depth.



**Figure 5.4** The cable length has been varied from 1 km in (a) to 200 m in (c). A redatuming is carried out to the reflector at 500 m depth.



**Figure 5.5** The reflectivity at 500 m depth obtained after redatuming for the acquisition geometry from figure 5.3a. In the lower figure a cross section at 30 Hz is compared with the analytical reflectivity shown as a dashed line.

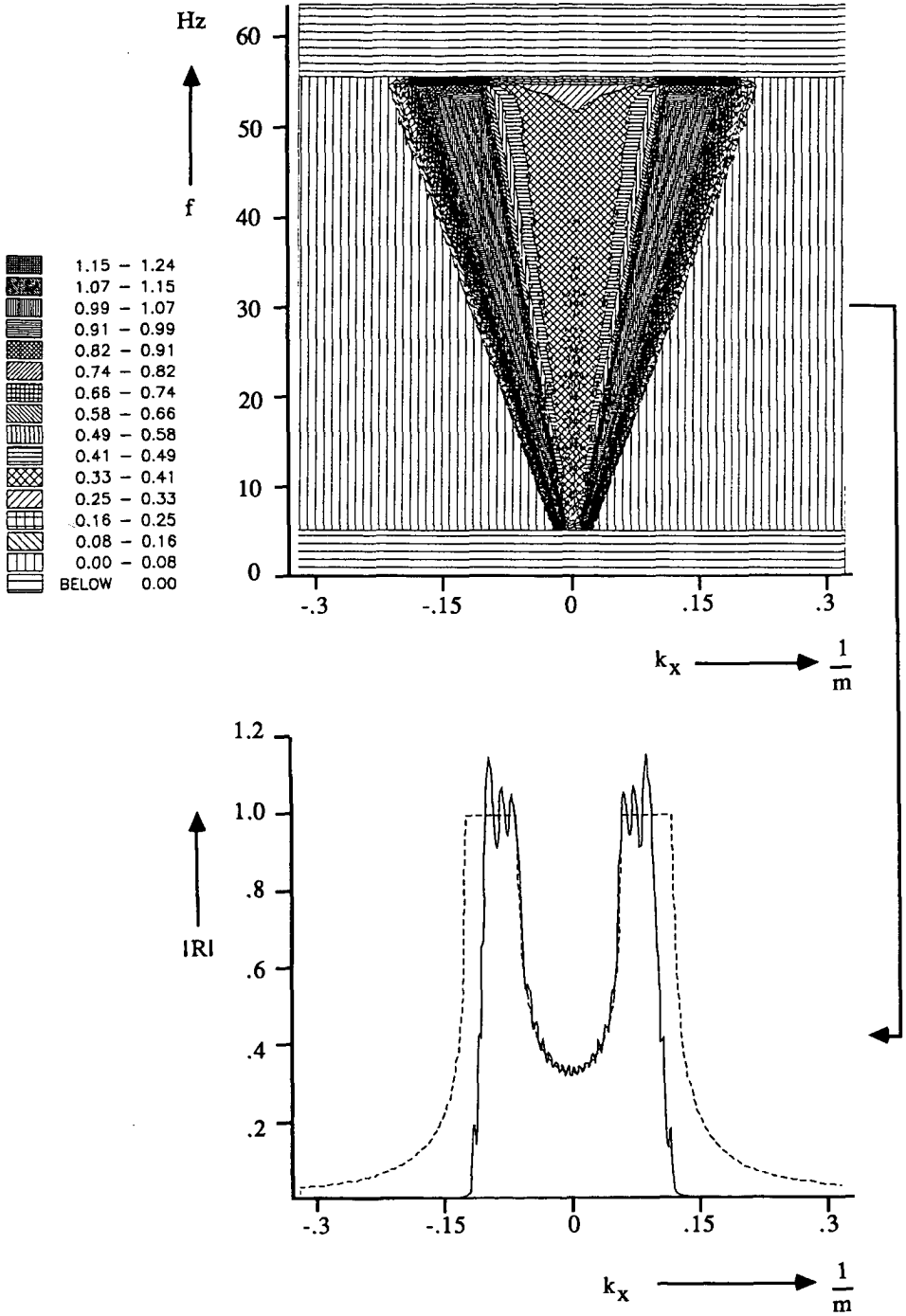


**Figure 5.6** The reflectivity at 500 m depth obtained after redatuming for the acquisition geometry from figure 5.3b. In the lower figure a cross section at 30 Hz is compared with the analytical reflectivity shown as a dashed line.

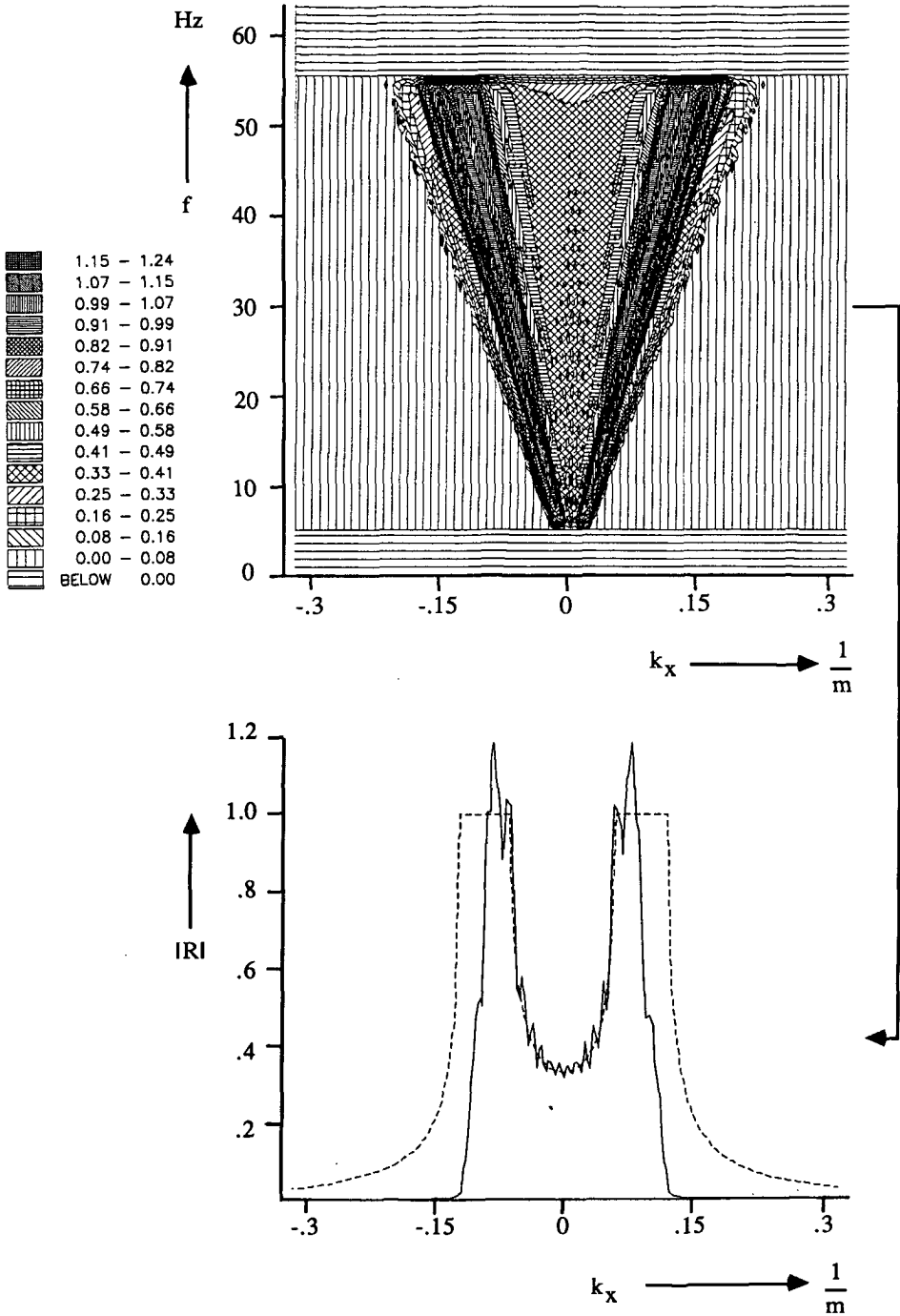


**Figure 5.7** The reflectivity at 500 m depth obtained after redatuming for the acquisition geometry from figure 5.3c. In the lower figure a cross section at 30 Hz is compared with the analytical reflectivity shown as a dashed line.

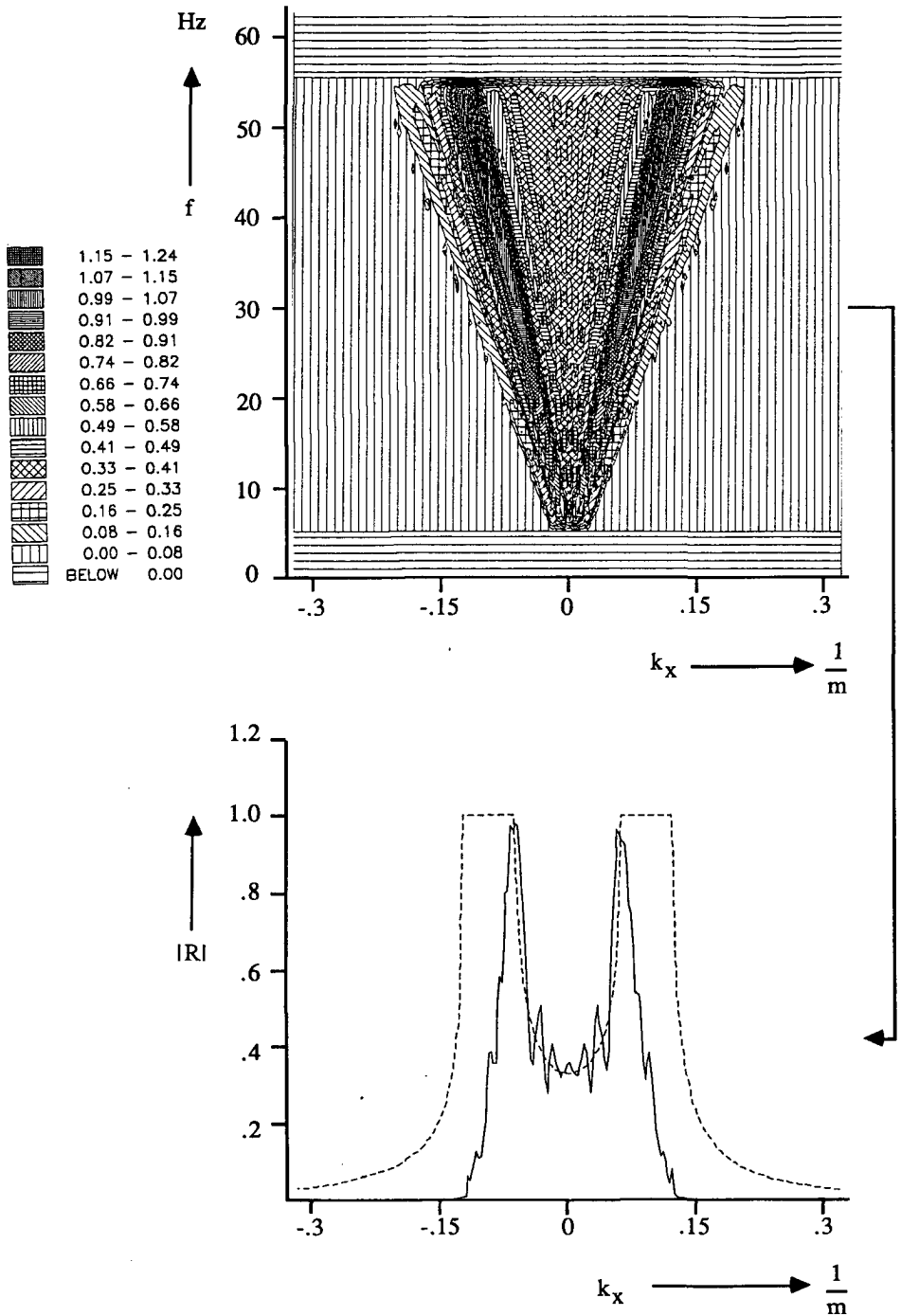


**Figure 5.8** The reflectivity at 500 m depth obtained after redatuming for the acquisition geometry from figure 5.4a. In the lower figure a cross section at 30 Hz is compared with the analytical reflectivity shown as a dashed line.

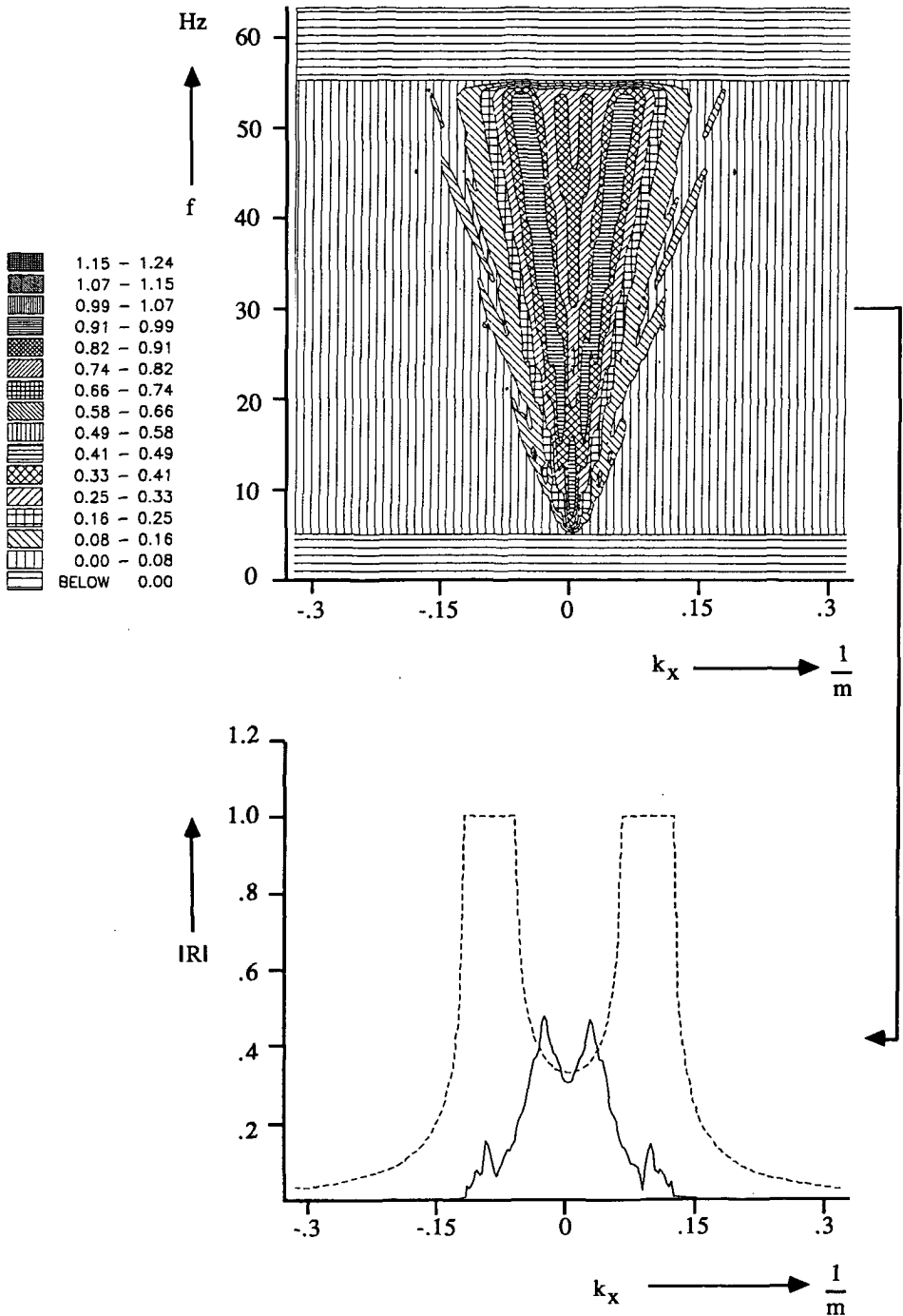


**Figure 5.9** The reflectivity at 500 m depth obtained after redatuming for the acquisition geometry from figure 5.4b. In the lower figure a cross section at 30 Hz is compared with the analytical reflectivity shown as a dashed line.

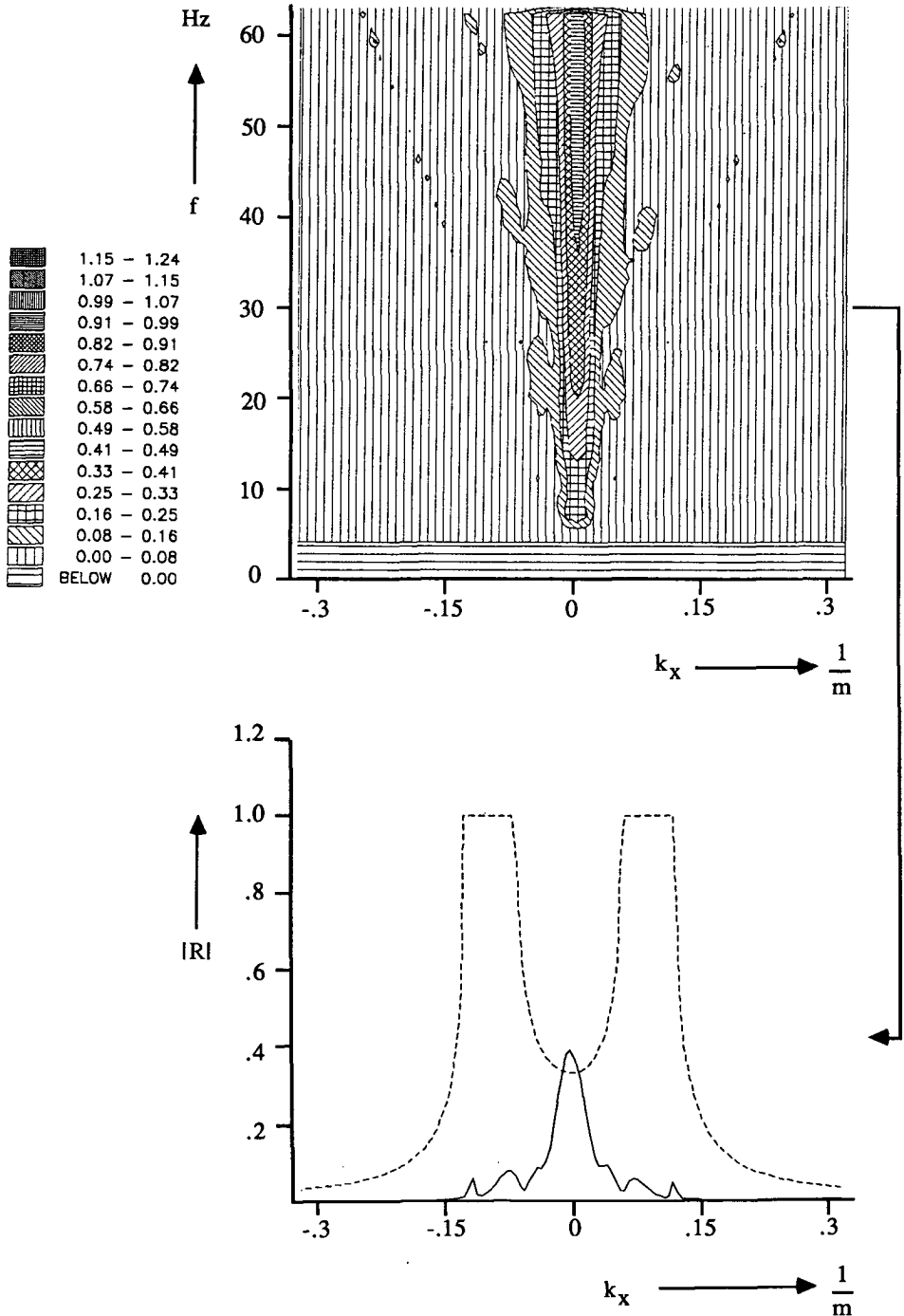


**Figure 5.10** The reflectivity at 500 m depth obtained after redatuming for the acquisition geometry from figure 5.4c. In the lower figure a cross section at 30 Hz is compared with the analytical reflectivity shown as a dashed line.

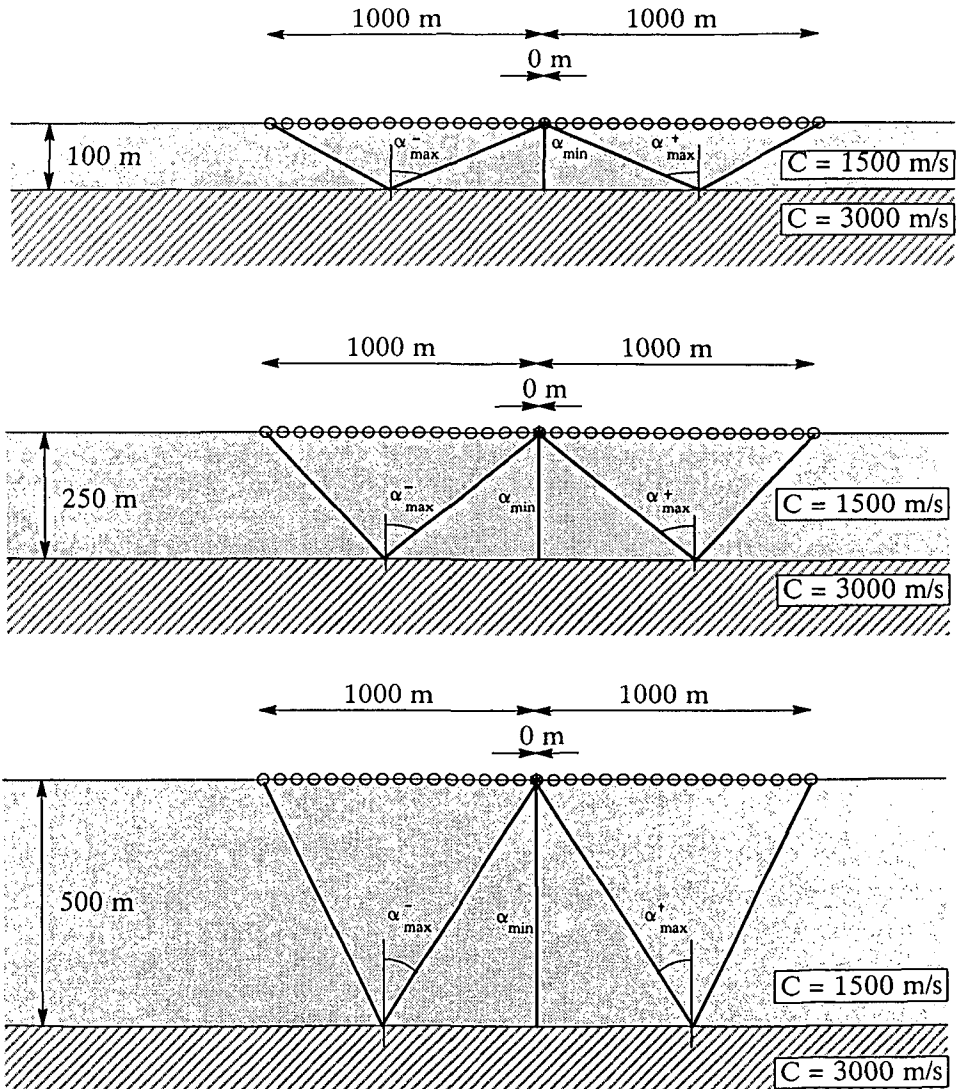
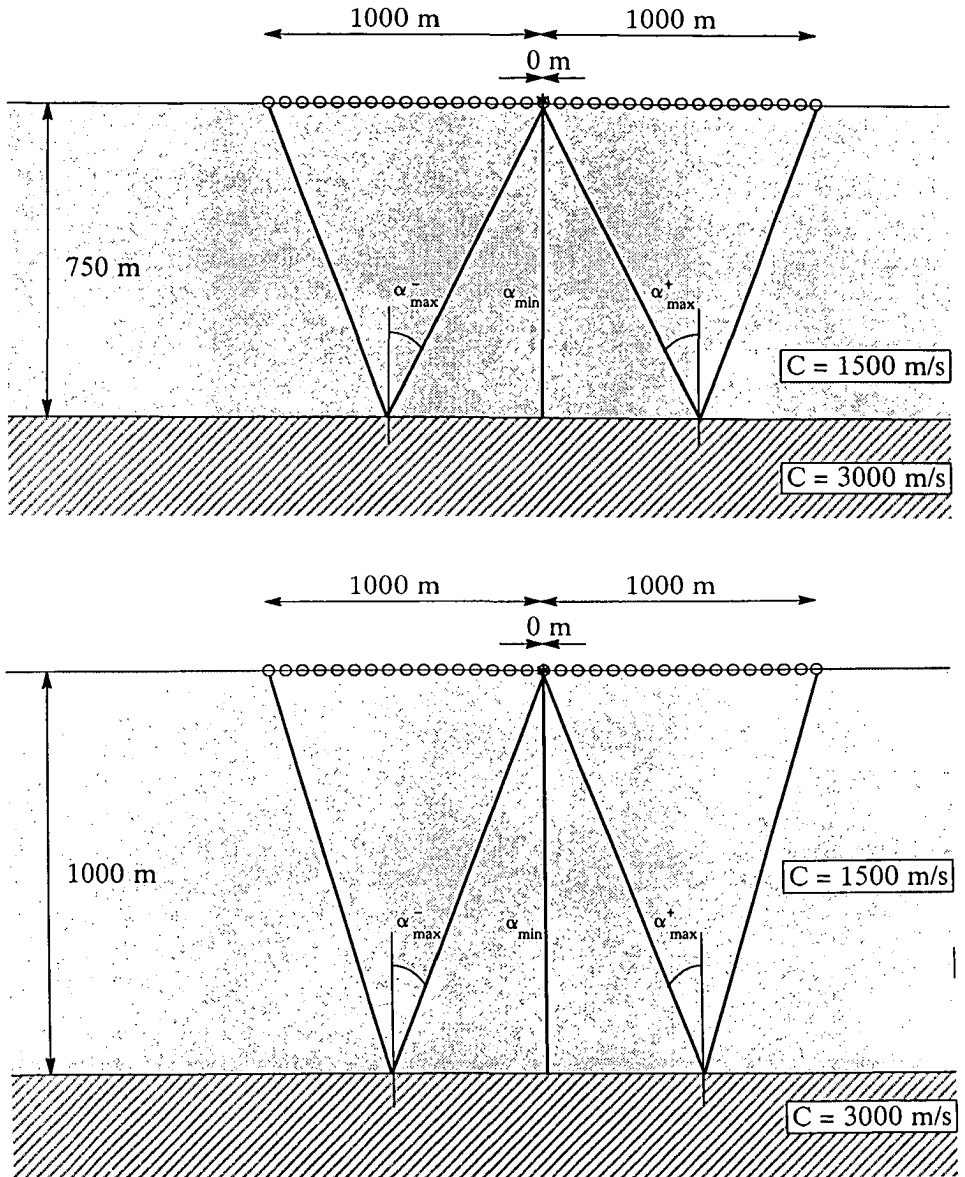
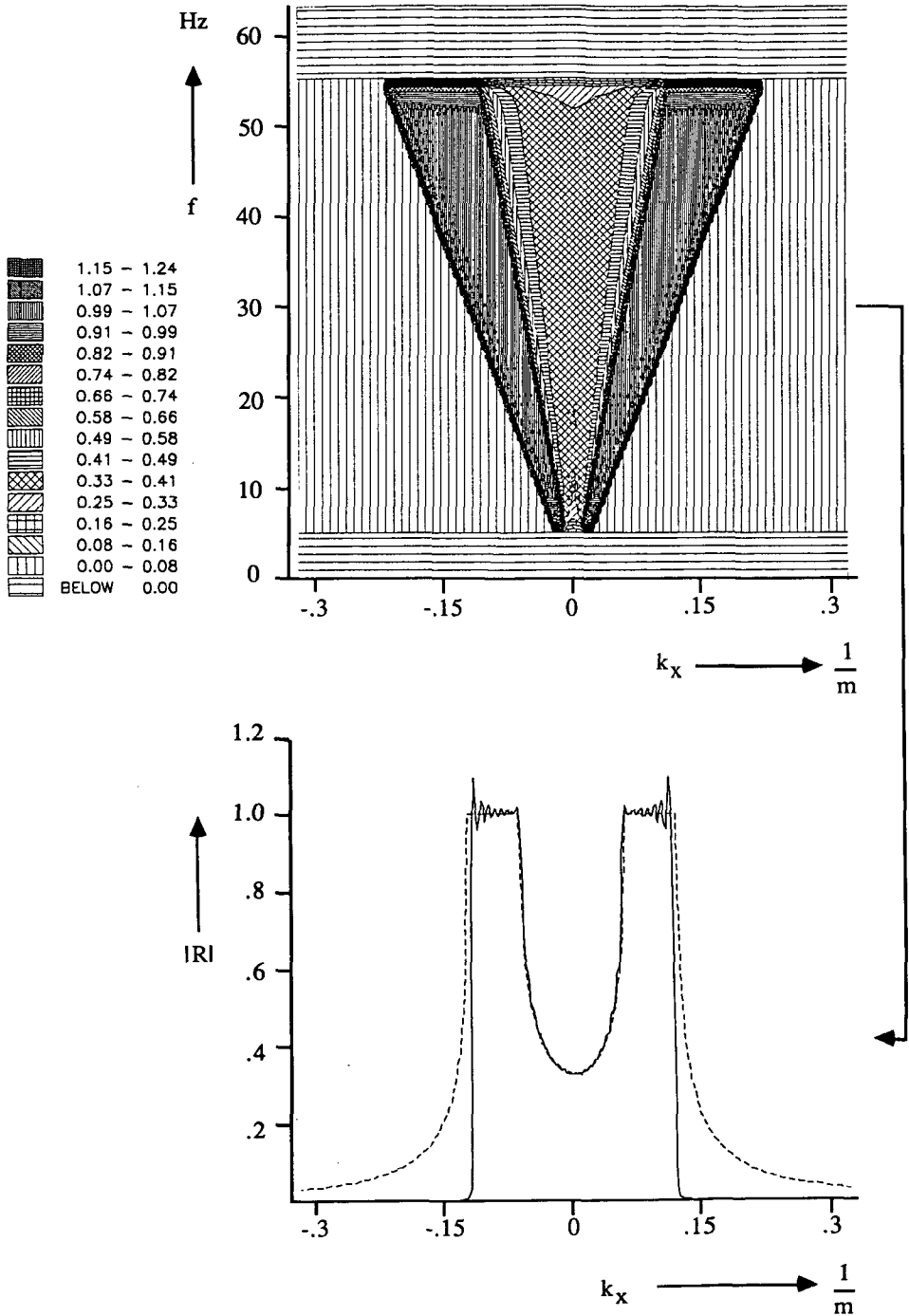


Figure 5.11 The reflector depth has been varied from 100 m in (a) to 500 m in (c). A redatuming is carried out to the reflector.



**Figure 5.12** The reflector depth has been varied from 750 m in (a) to 1 km in (b). A redatuming is carried out to the reflector.



**Figure 5.13** The reflectivity at 100 m depth obtained after redatuming for the acquisition geometry from figure 5.11a. In the lower figure a cross section at 30 Hz is compared with the analytical reflectivity shown as a dashed line.

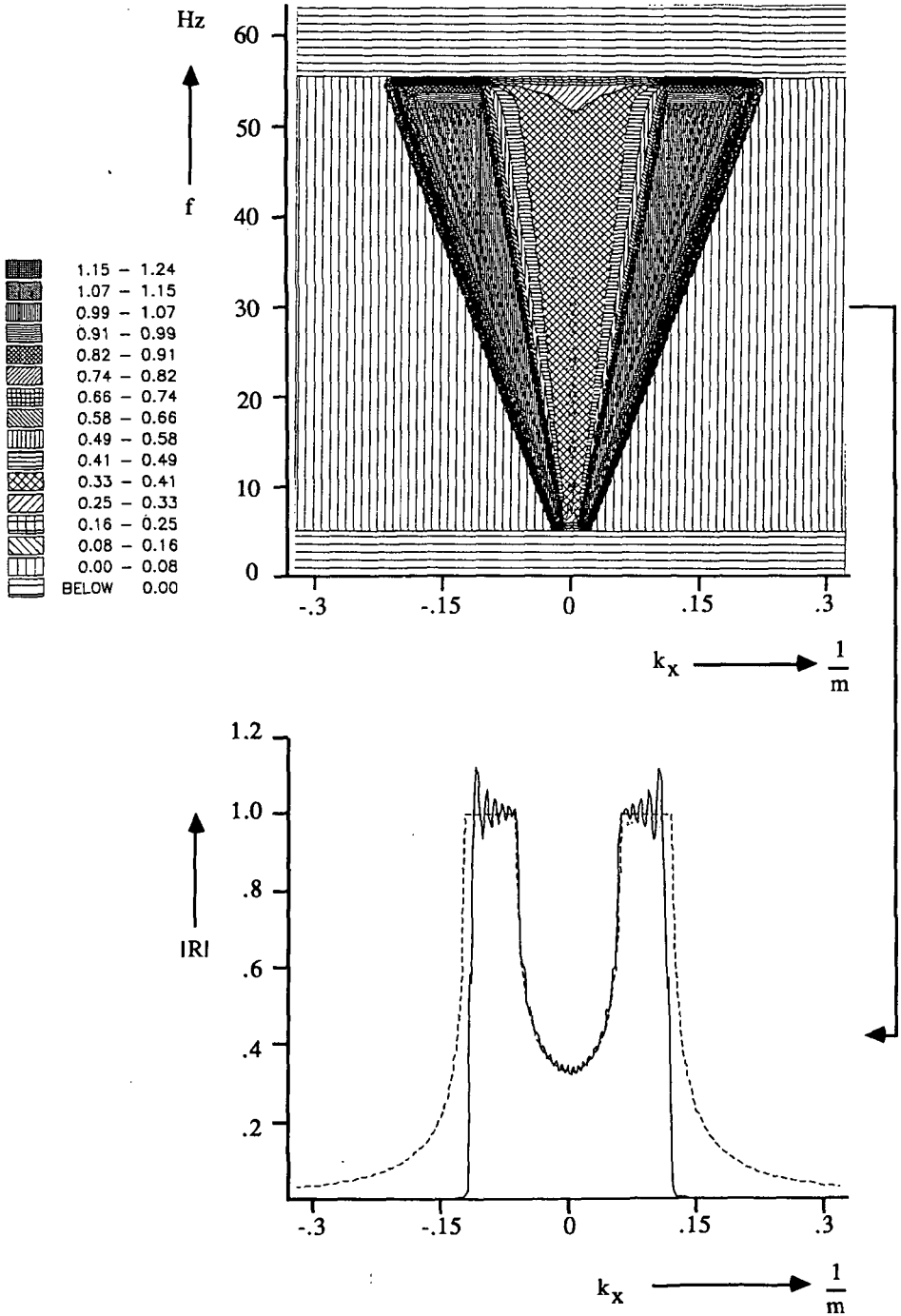
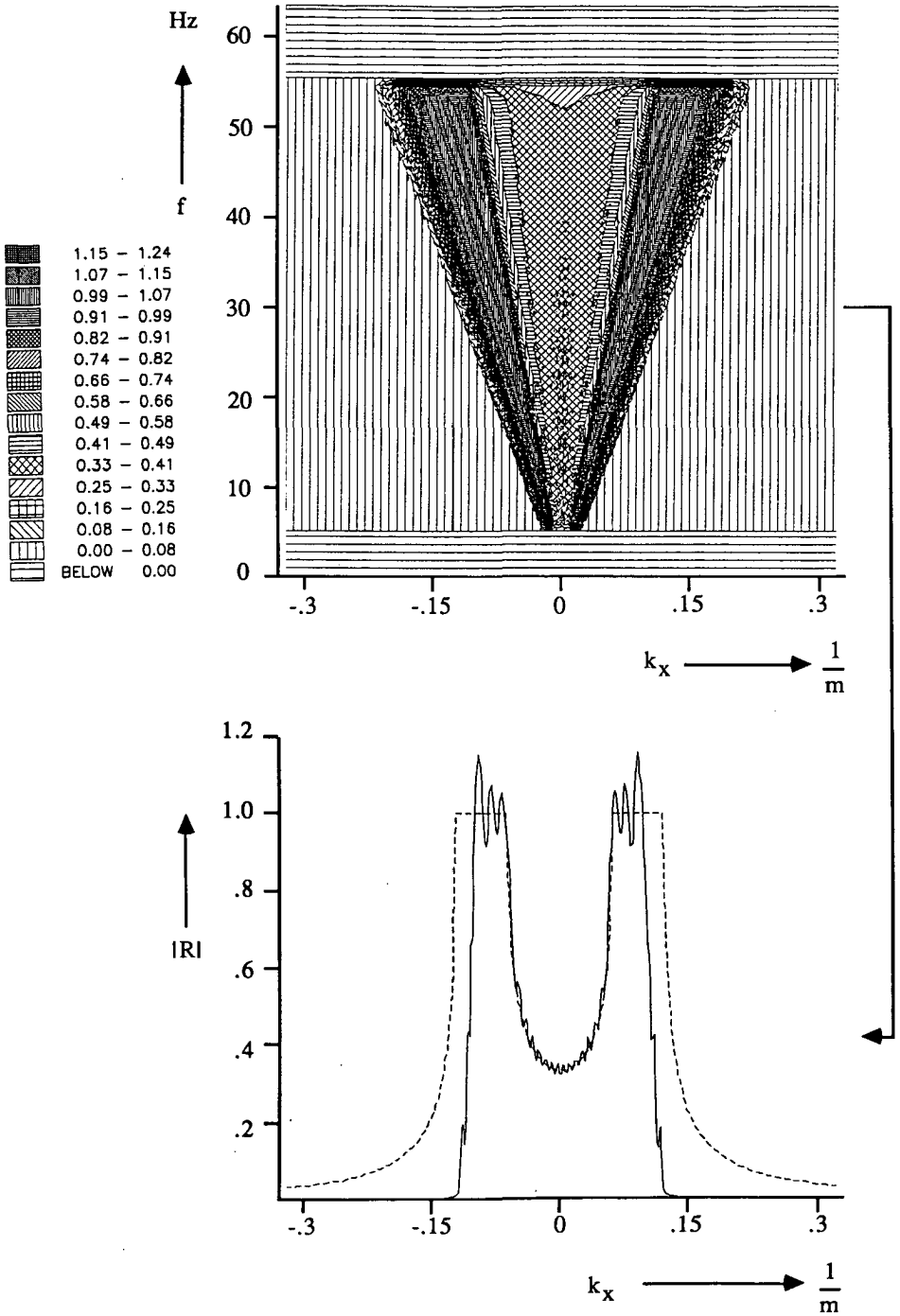


Figure 5.14 The reflectivity at 250 m depth obtained after redatuming for the acquisition geometry from figure 5.11b. In the lower figure a cross section at 30 Hz is compared with the analytical reflectivity shown as a dashed line.



**Figure 5.15** The reflectivity at 500 m depth obtained after redatuming for the acquisition geometry from figure 5.11c. In the lower figure a cross section at 30 Hz is compared with the analytical reflectivity shown as a dashed line.

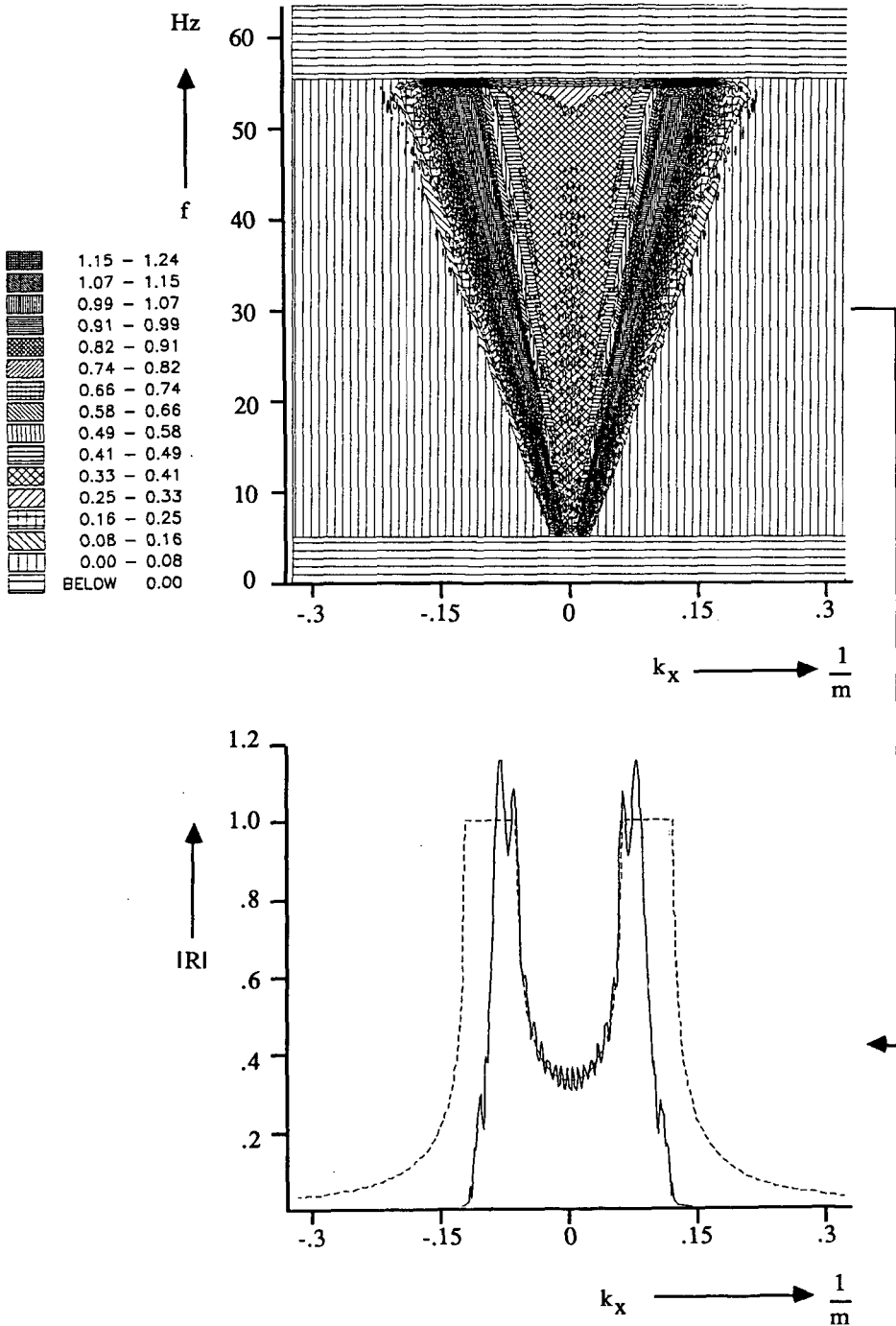
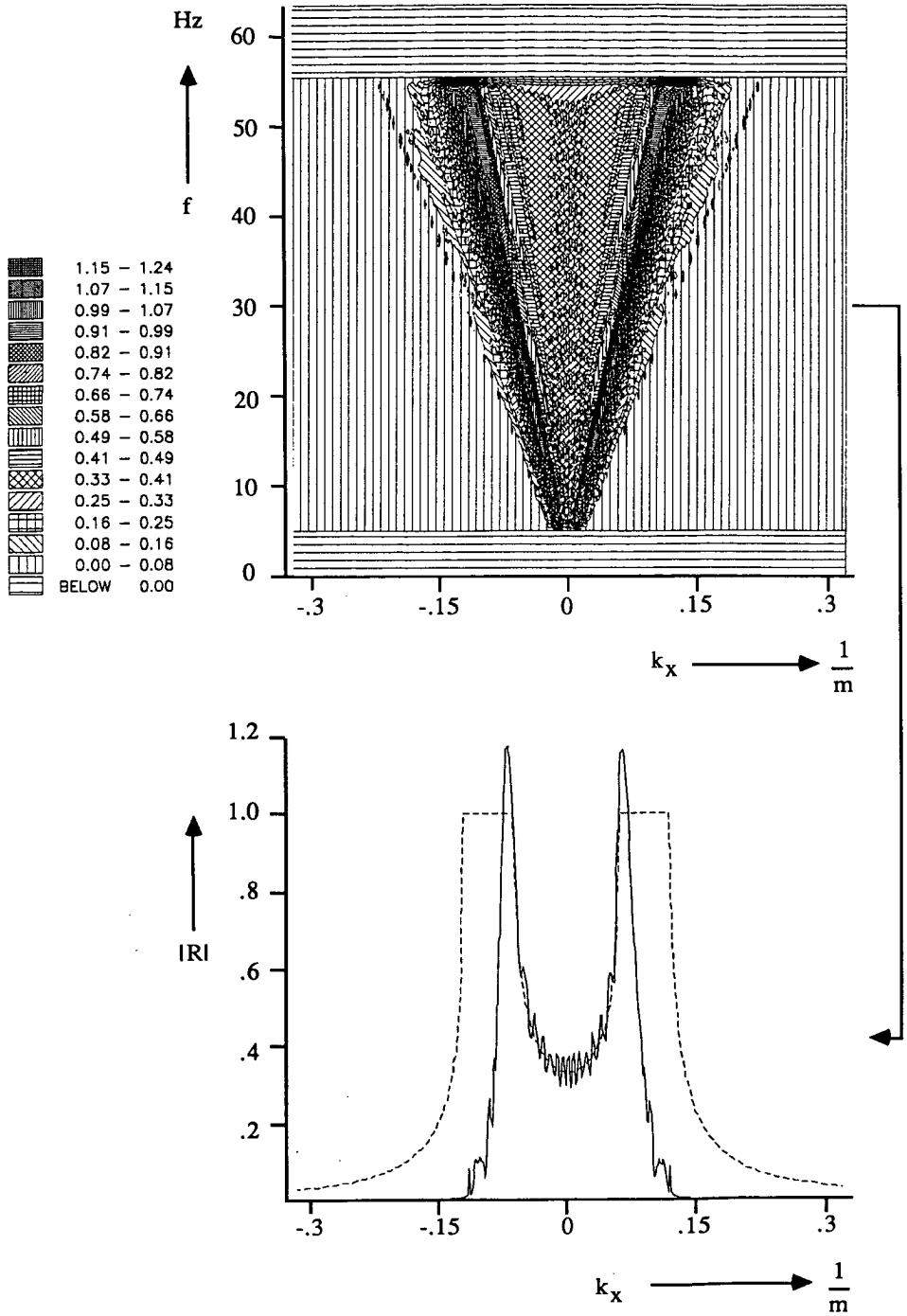
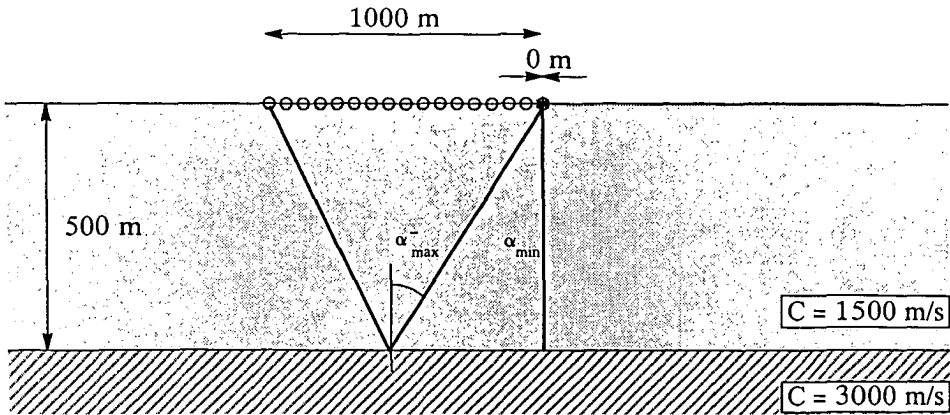


Figure 5.16 The reflectivity at 750 m depth obtained after redatuming for the acquisition geometry from figure 5.12a. In the lower figure a cross section at 30 Hz is compared with the analytical reflectivity shown as a dashed line.



**Figure 5.17** The reflectivity at 1 km depth obtained after redatuming for the acquisition geometry from figure 5.12b. In the lower figure a cross section at 30 Hz is compared with the analytical reflectivity shown as a dashed line.



**Figure 5.18** The geophones are taken only to the left hand side of the source. Therefore only the wave field which is reflected from the left to the right is registered.

the spread length is reduced the maximum angle of reflection which is resolved by the migration process decreases. For the minimum spread length the migration result is distorted. Reflection coefficients other than normal incidence are hardly resolved. A geometrical analysis shown in figures 5.3 and 5.4, which is basically a high frequency approximation, confirms the results.

For the second set of experiments the depth of the reflector has been varied (figures 5.11 and 5.12). For a fixed spread length an increasing reflector depth results in a decreasing angular illumination. Therefore the maximum angle of the plane wave reflection coefficient which is resolved by the migration will decrease for deeper reflectors. Figure 5.13 shows the migration results for a reflector depth of 100 m. The spread length is 2000 m symmetrical around the source. The reflection coefficients are fully resolved for the propagating waves. As the reflector depth is increased the maximum angle decreases (figures 5.13 through 5.17). Also the effect of ringing due to aperture truncation becomes more pronounced. For a reflector depth of 1000 m plane wave reflection coefficients up to  $26.6^\circ$  are resolved. This corresponds to the geometrical analyses shown in figures 5.11 and 5.12.

For the third set of experiments the spread is arranged a-symmetrical around the source. In figure 5.18 the acquisition geometry is shown. A geophone spread with offsets from 0 to  $-1000 \text{ m}$  has been used for the redatuming to the reflector at 500 m depth. For this experiment the wave field is always reflected from the right to the left. Therefore only negative angles of incidence are present in the data. So only the left part of the reflectivity information in the  $k_x-\omega$

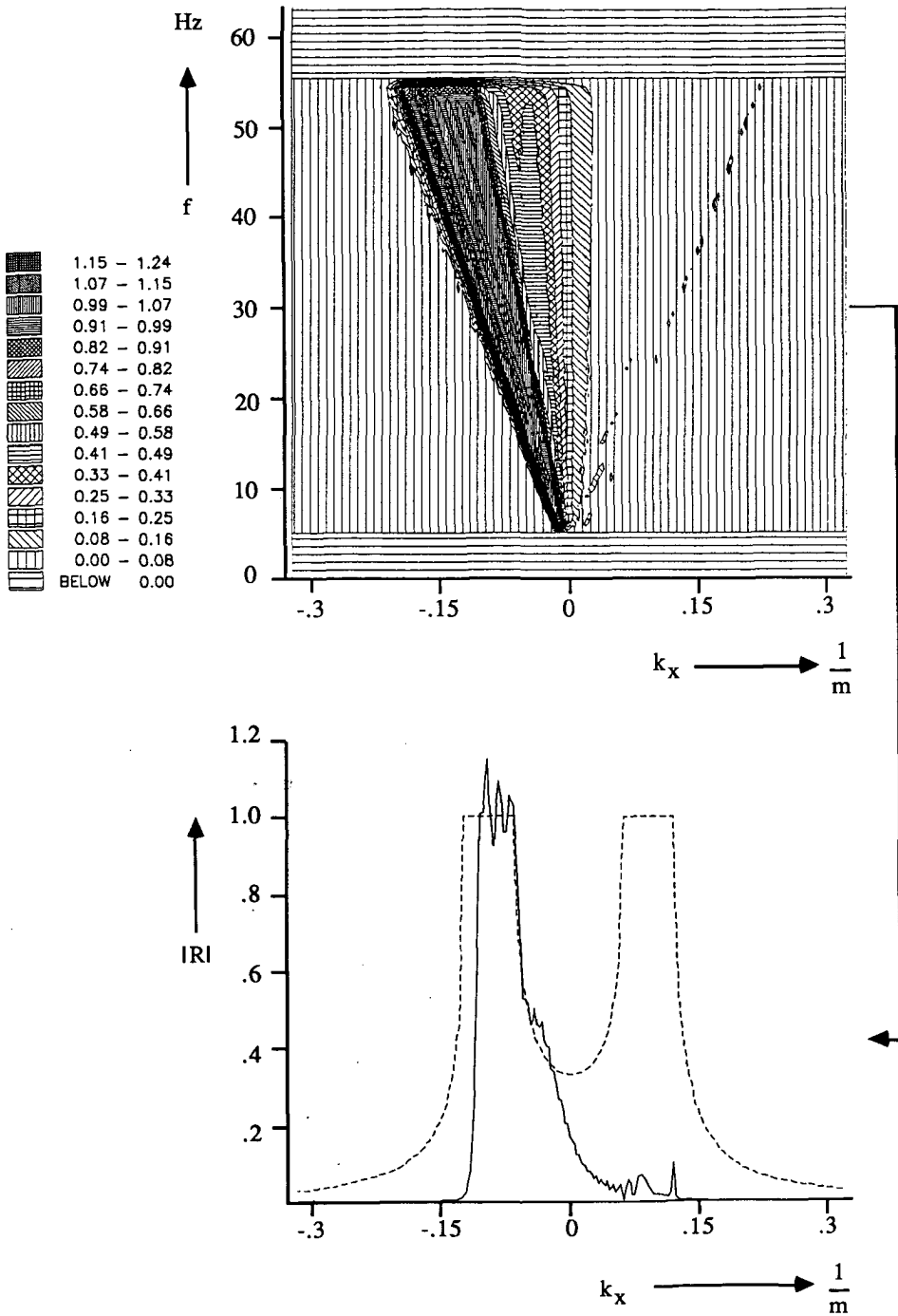
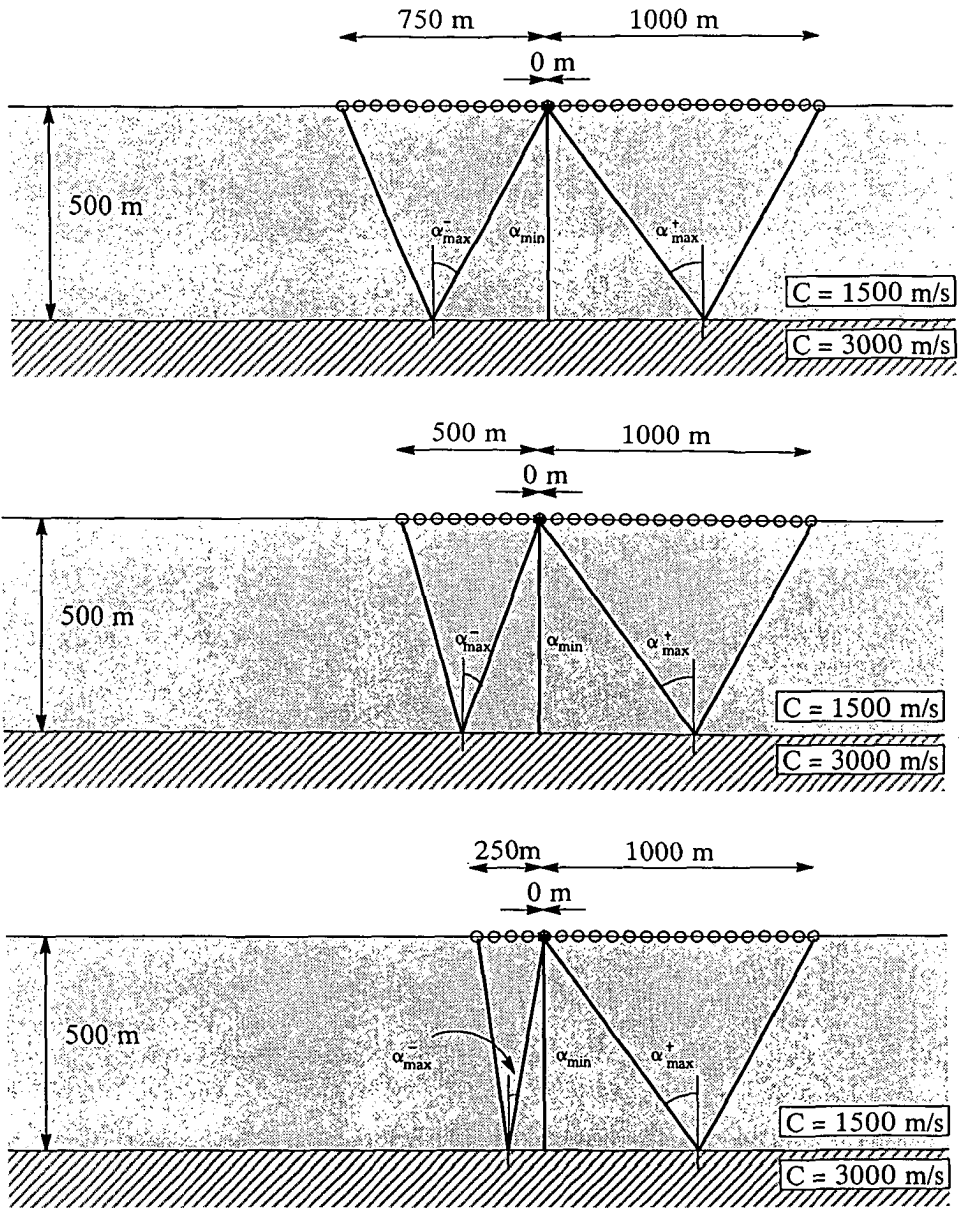
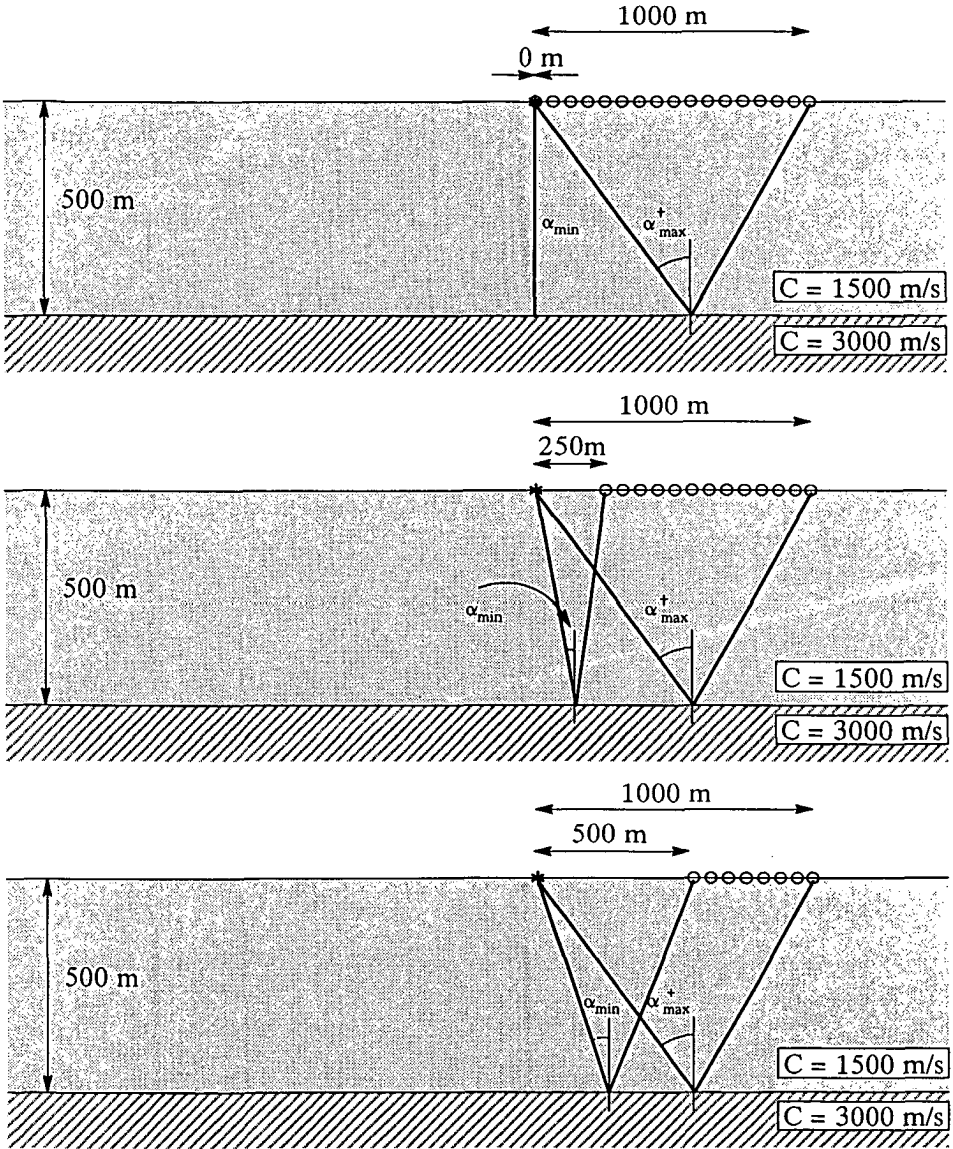


Figure 5.19 The reflectivity at 500 m depth obtained after redatuming for the acquisition geometry from figure 5.18. Only half of the reflectivity information is resolved.



**Figure 5.20** A-symmetrical geophone spreads are used in the modeling. The cable length is shortened by reducing the maximum offset to the left of the source.



**Figure 5.21** A-symmetrical geophone spreads are used in the modeling. The cable length is shortened by increasing the minimum offset while keeping the maximum offset constant.

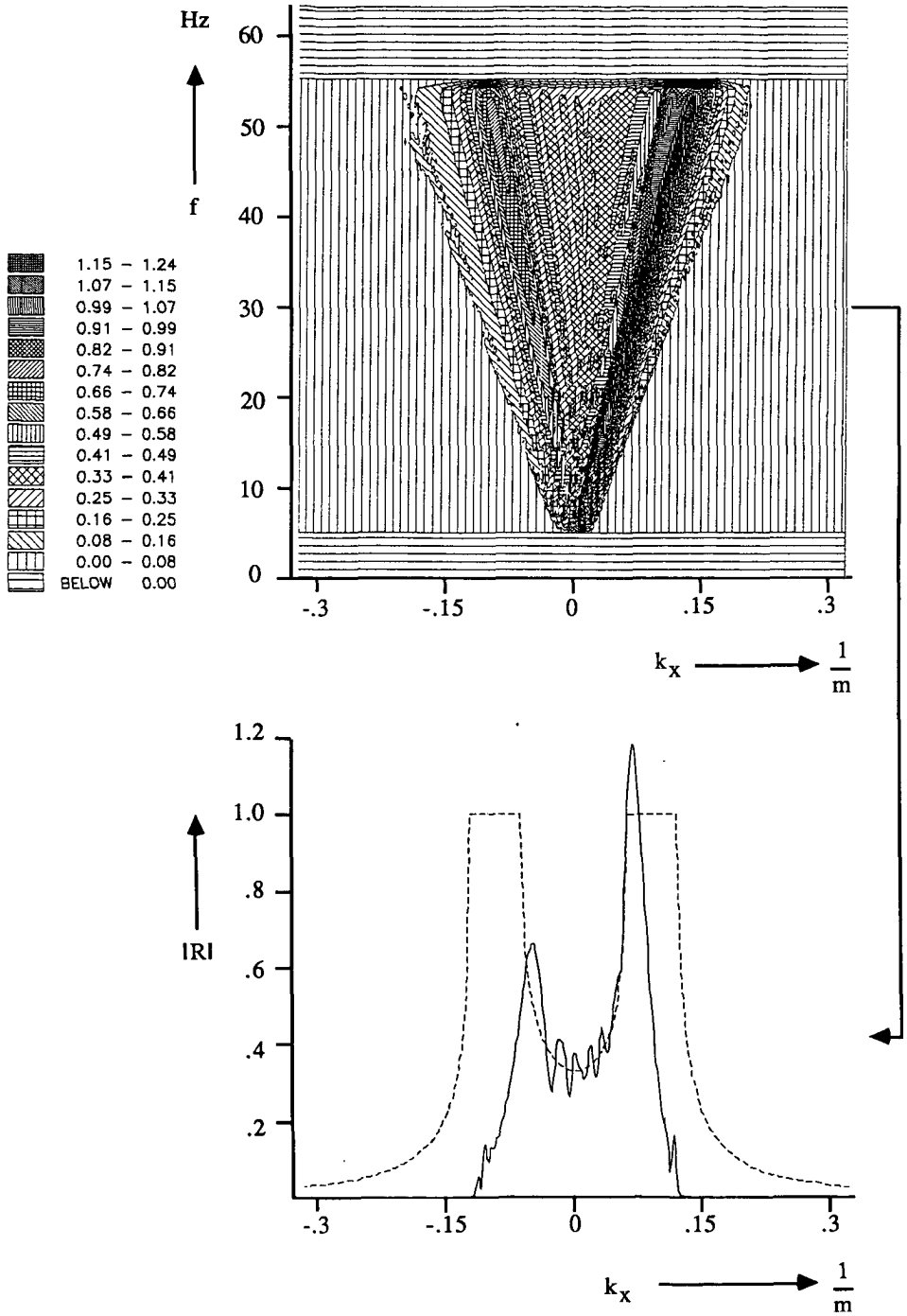


**Figure 5.22** The reflectivity information after redatuming to the reflector at 500 m depth. Due to the asymmetrical spread in figure 5.20a the resolved reflectivity is asymmetrical as well.

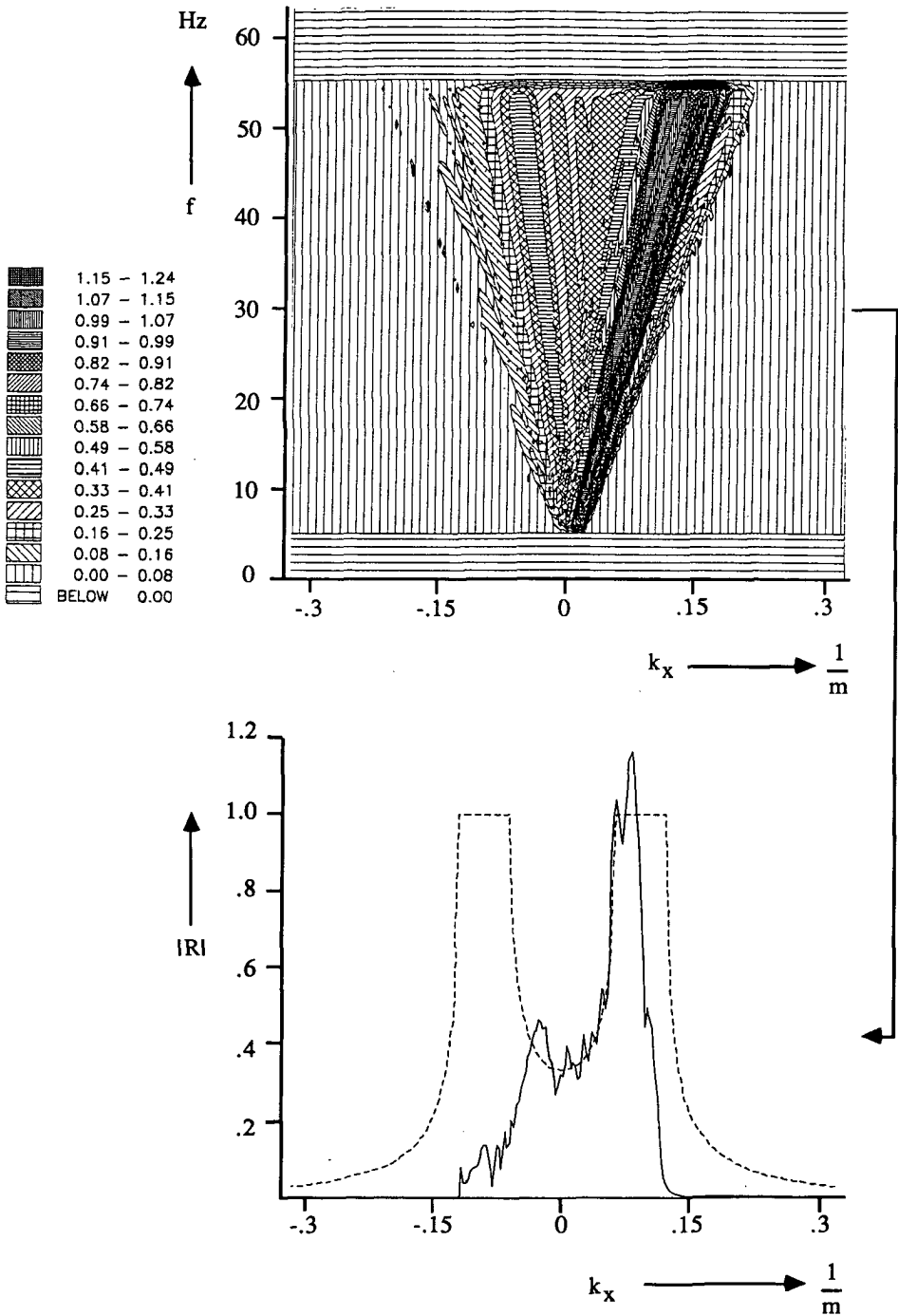


**Figure 5.23** The reflectivity information after redatuming to the reflector at 500 m depth. Due to the asymmetrical spread in figure 5.20b the resolved reflectivity is asymmetrical as well.

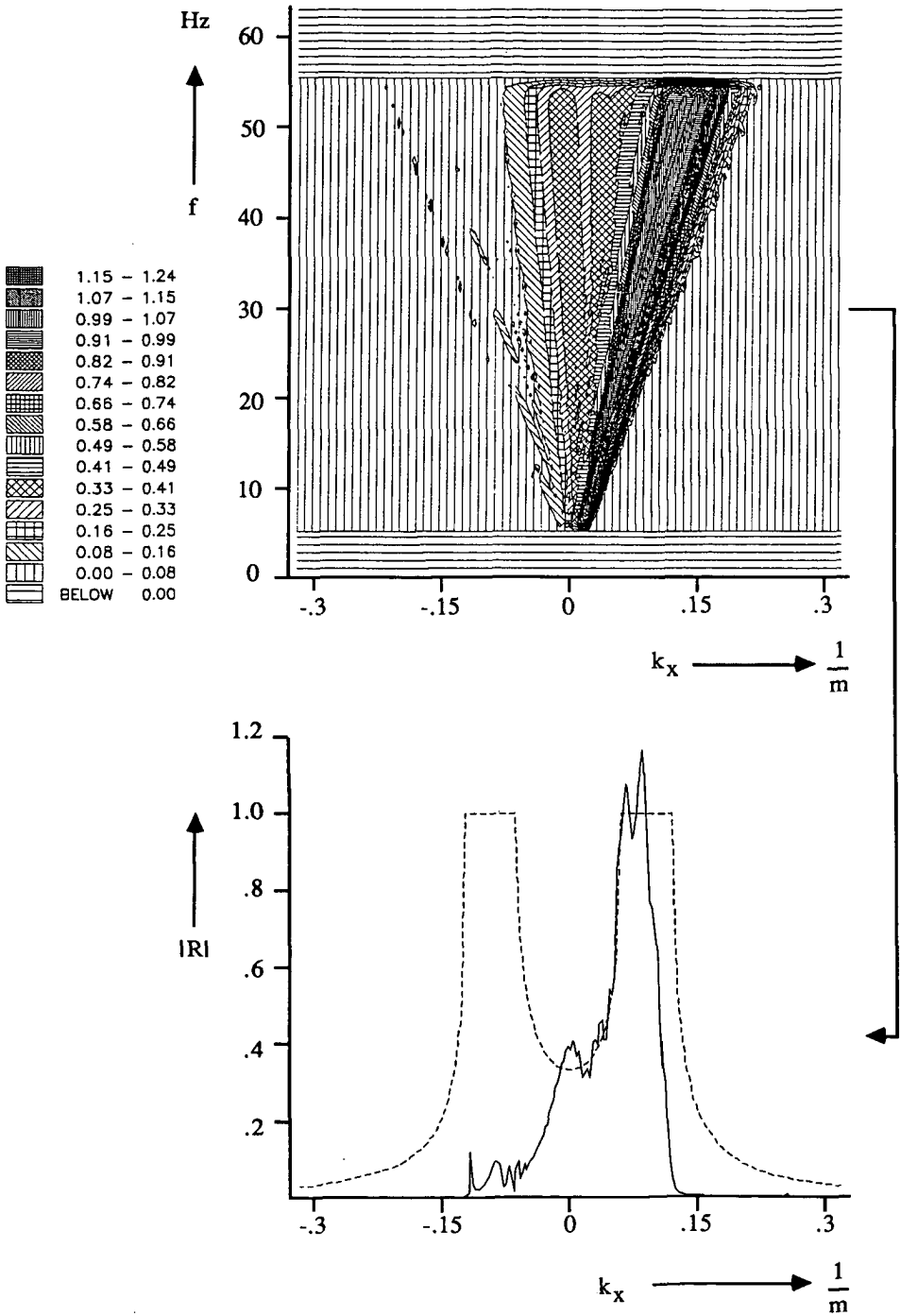


**Figure 5.24** The reflectivity information after redatuming to the reflector at 500 m depth. Due to the a-symmetrical spread in figure 5.20c the resolved reflectivity is a-symmetrical as well.

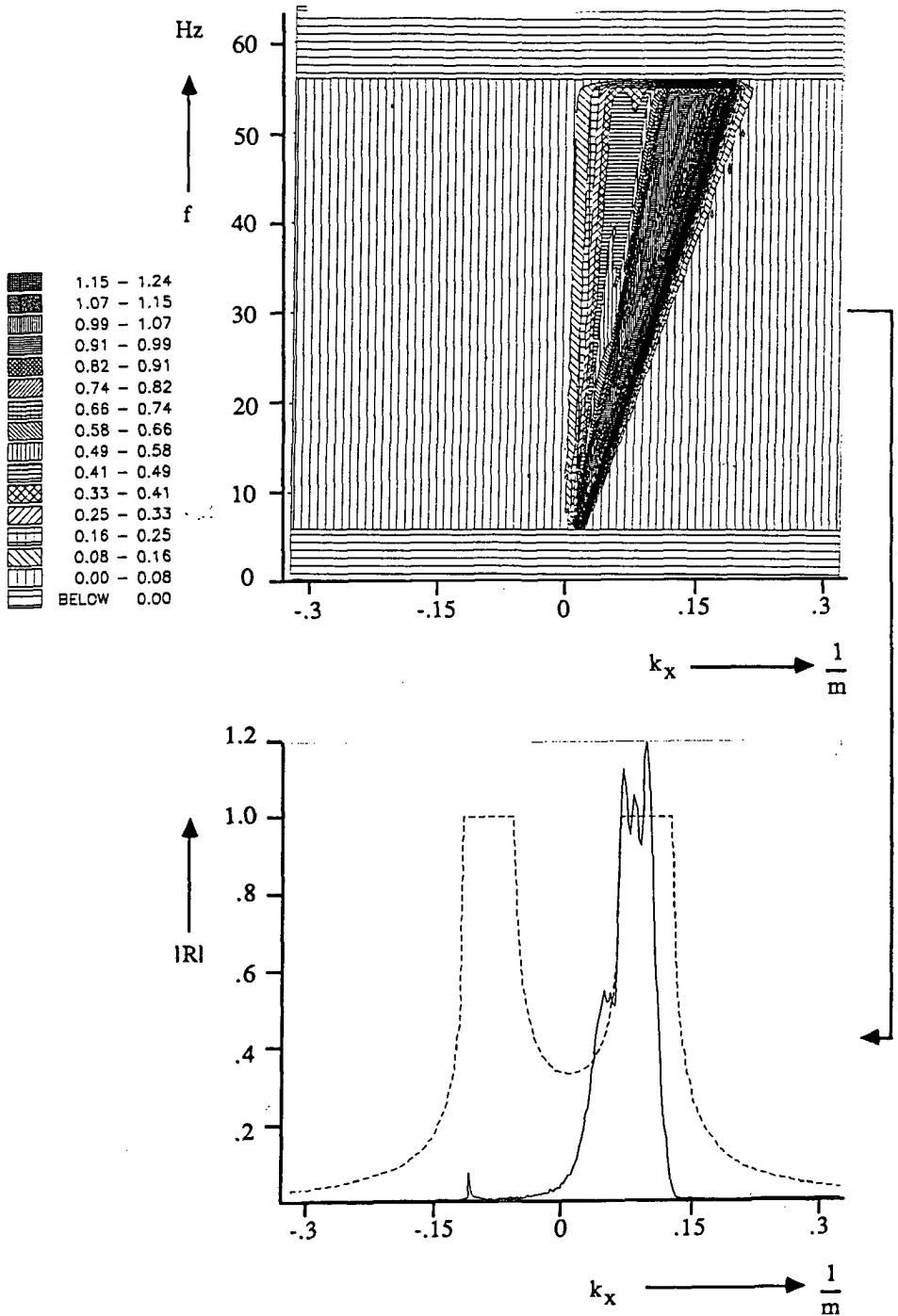


**Figure 5.25** The reflectivity information after redatuming to the reflector at 500 m depth. Due to the increasing minimum offset (figure 5.21a), the reflectivity for low angles of incidence is not resolved.

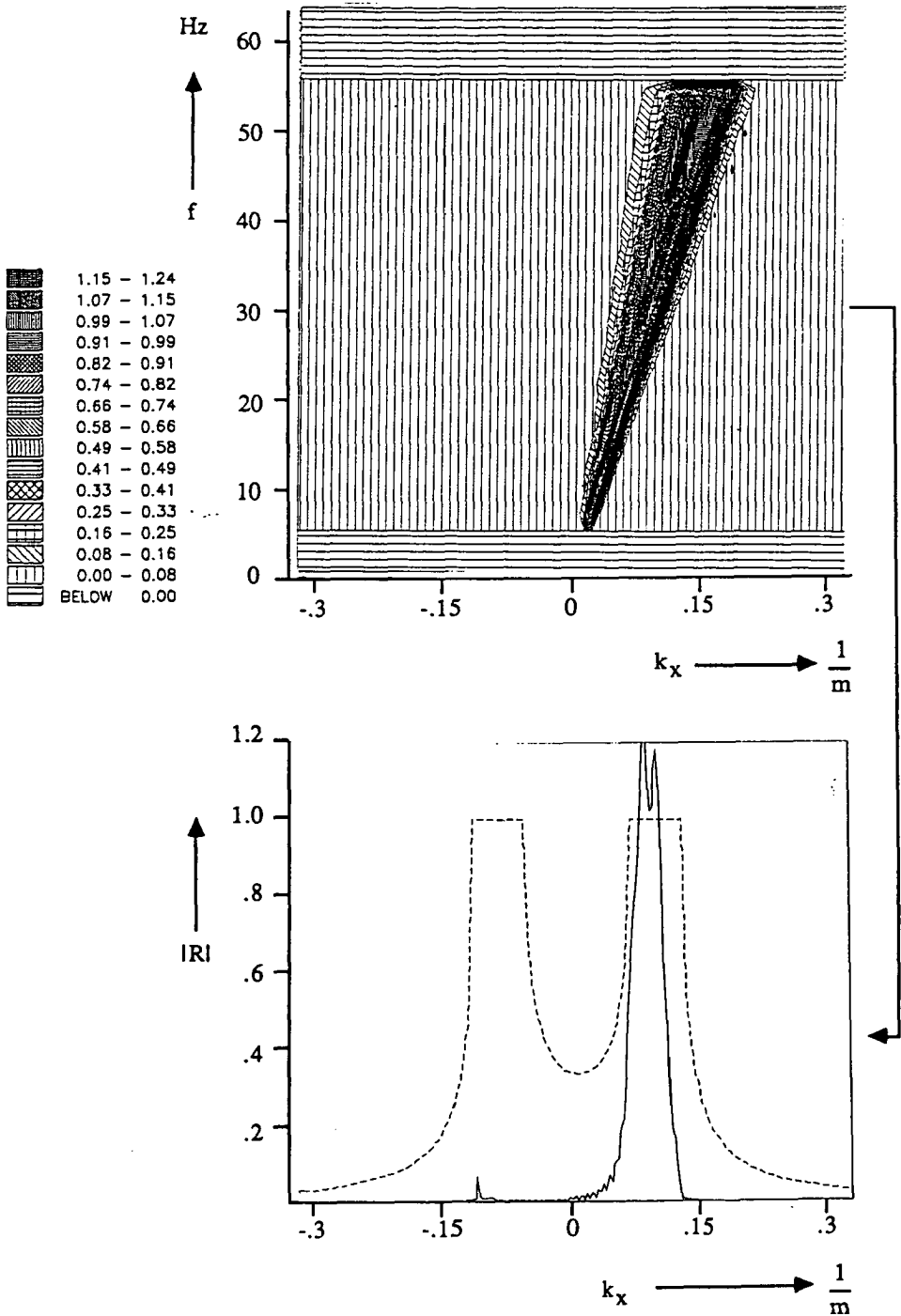


**Figure 5.26** The reflectivity information after redatuming to the reflector at 500 m depth. Due to the increasing minimum offset (figure 5.21b), the reflectivity for low angles of incidence is not resolved.

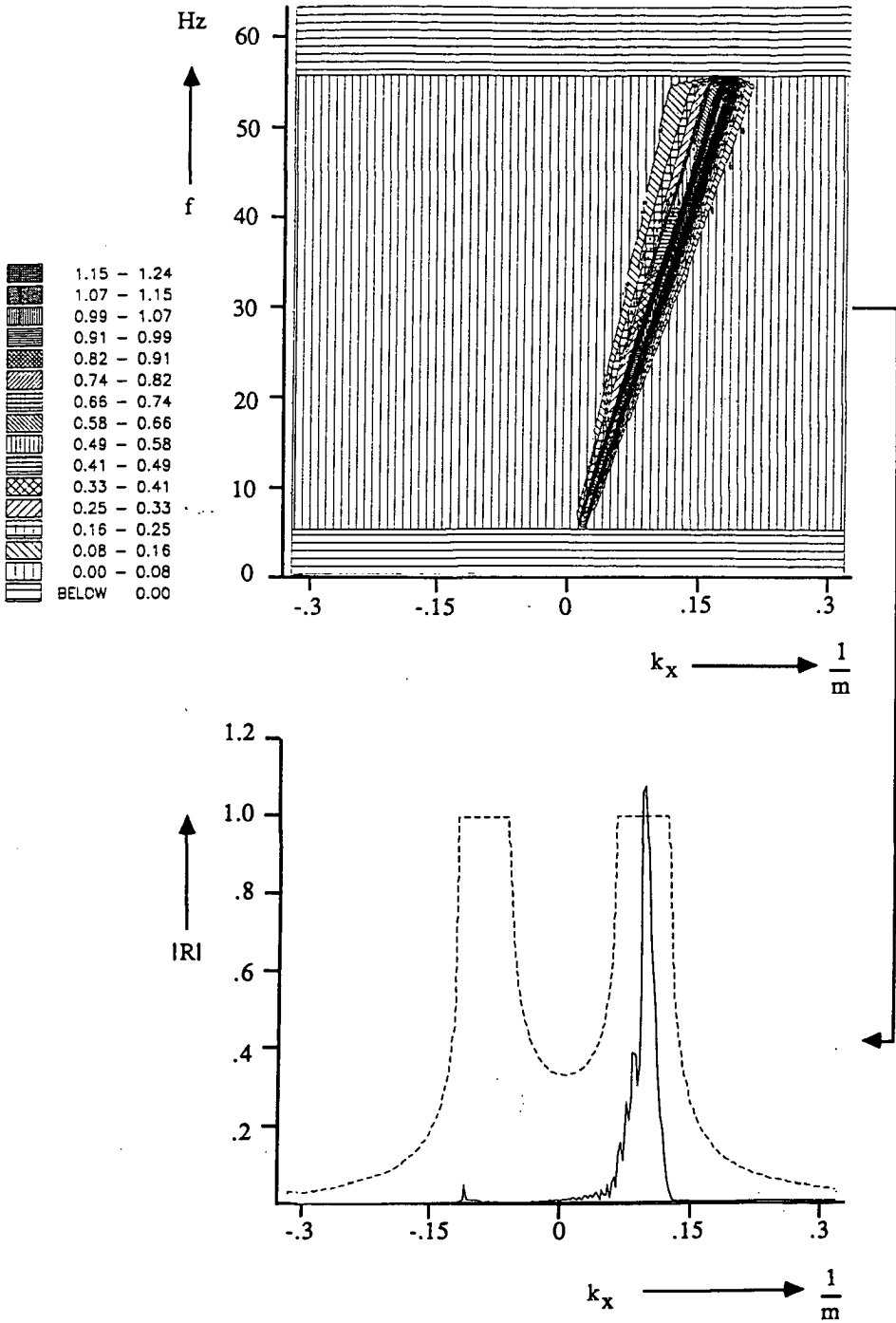


**Figure 5.27** The reflectivity information after redatuming to the reflector at 500 m depth. Due to the increasing minimum offset (figure 5.21c), the reflectivity for low angles of incidence is not resolved.

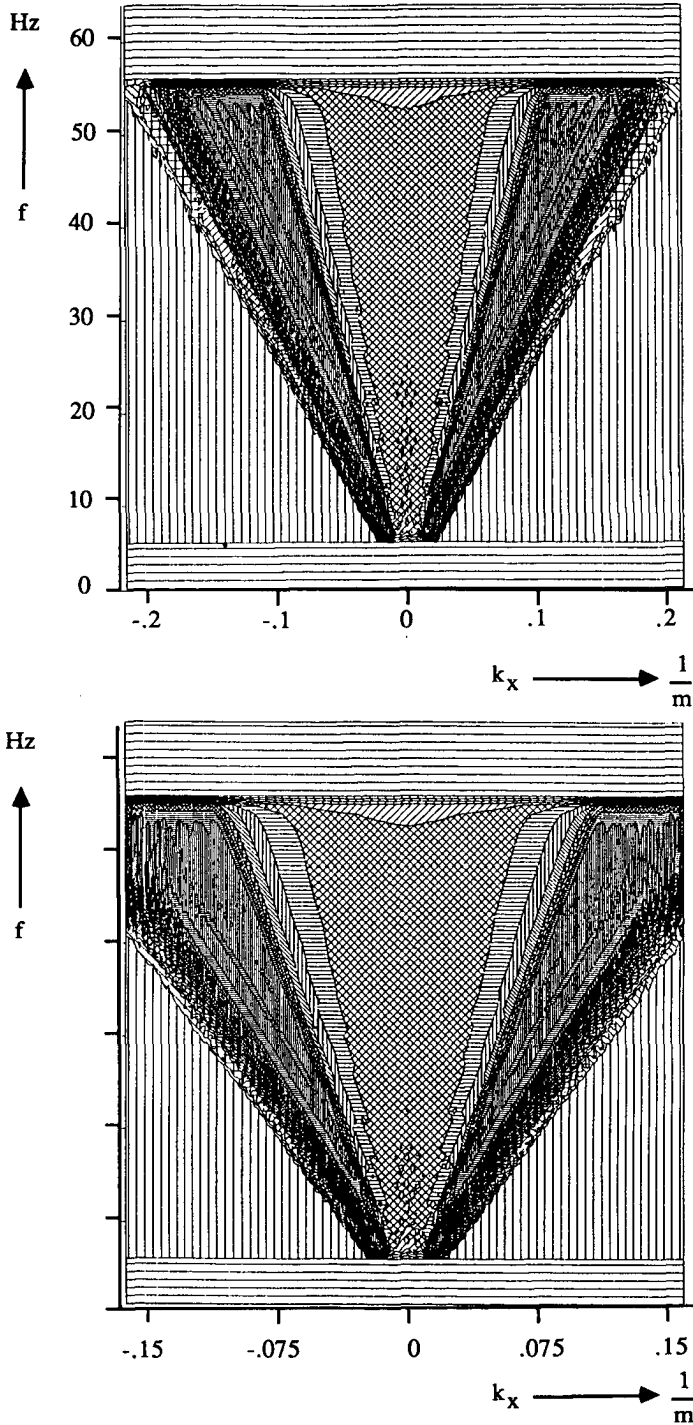


**Figure 5.28** In the acquisition configuration from figure 5.3b the spatial sampling has been increased to 15 m (a) and 20 m (b). For high frequencies aliasing occurs and the maximum angle of incidence for the reflectivity is decreased.

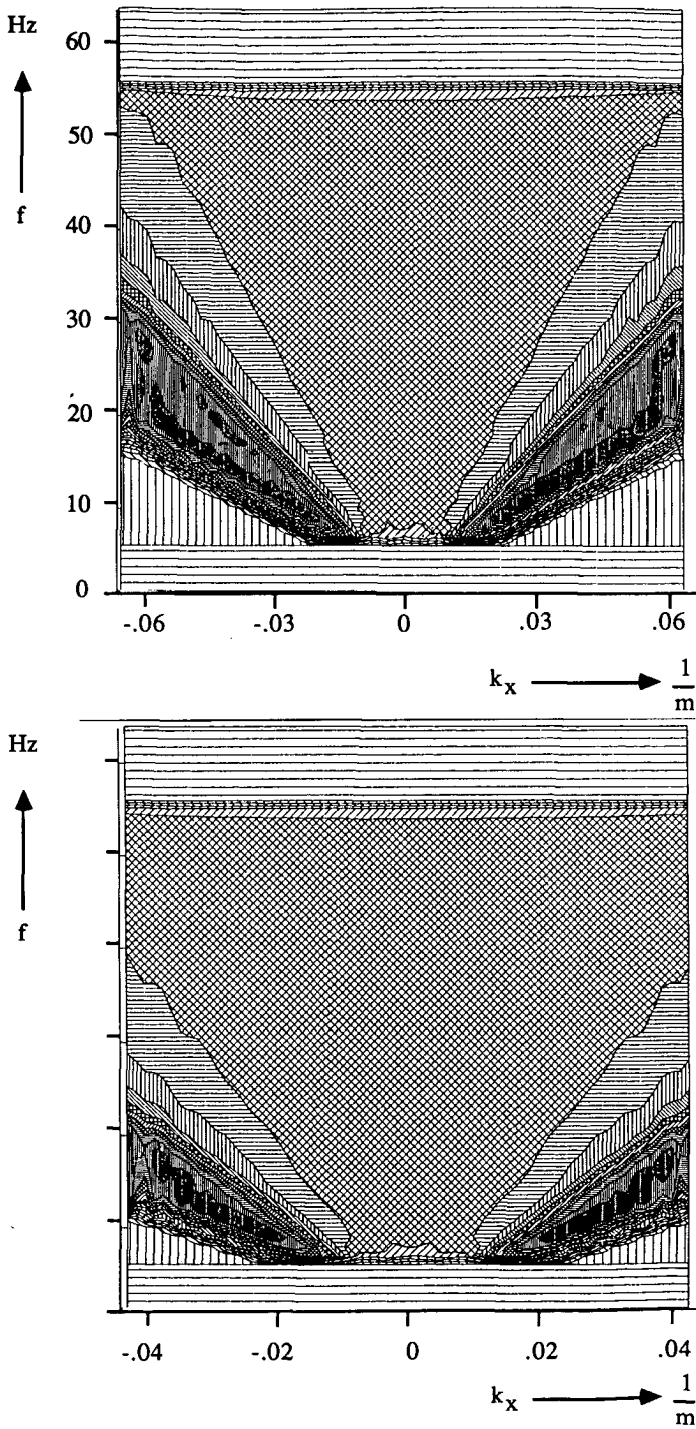


**Figure 5.29** In the acquisition configuration from figure 5.3b the spatial sampling has been increased to 50 m (a) and 75 m (b). Aliasing occurs, so the reflectivity may only be resolved for small angles on incidence.

domain has been resolved as is shown in figure 5.19. For the geometries shown in figure 5.20 and 5.21 the following offset ranges have been chosen:  $-750 - 1000$  m,  $-500 - 1000$  m,  $-250 - 1000$  m,  $0 - 1000$  m,  $250 - 1000$  m,  $500 - 1000$  m. The redatuming results are shown in figures 5.22 through 5.27. The results show very nicely how, depending on the acquisition configuration different parts of the reflectivity information are resolved from the data by the redatuming or depth migration. This means that the zero offset data will be different as well. For complex overburdens, the wave propagation through this overburden may cause the angular illumination of the target zone to change laterally. Imaging conditions which do not incorporate this effect may result in a distorted zero offset section. For this thesis this effect has not been studied. I would suggest further research into this interesting subject.

In the last set of experiments the spatial sampling interval has been varied. If the spatial sampling criterion is violated the maximum plane wave reflection coefficient which is resolved from the migration will be less than  $90^\circ$ . In figures 5.28 and 5.29 the redatuming results for a spatial sampling increment for 15 m, 30 m, 50 m and 75 m respectively are shown. No spatial anti-aliasing filtering has been applied. For the high frequencies the maximum angle for which the reflectivity is resolved decreases for increasing spatial sampling distance. For low frequencies however, the full angular reflectivity may be resolved from the data. In the space time domain the data is distorted because the aliased data is not separated from the unaliased data.

From these experiments we can conclude that the acquisition configuration which is chosen, is related to the information which may be extracted from the data. The use of relatively expensive true amplitude wave field extrapolation operators is not sensible, if incomplete data is recorded because of insufficient surface coverage.

## **5.2 STRONG DIP IN LATERAL VELOCITY VARIATIONS, A SYNTHETIC EXAMPLE**

The redatuming procedure discussed in the previous example has been applied to the data generated for the model shown in figure 5.30. The model is geologically not very feasible. However, various features such as steep dip and strong lateral velocity variations are present in this model. The effects resulting from these features may be studied in this model. The detectors are placed from 0 m to 2500 m at the surface. A dipole source with a signature shown in figure 5.31 is placed at the surface. The shot spacing is 10 m with the first shot at 0 m and the last shot at 2500 m. Finite difference modeling has been used to obtain the synthetic data. All model boundaries, including the surface have been taken reflection free. The zero offset section for this model is shown in figure 5.32. The deepest reflection is distorted because of the overburden wave propagation effects. This makes interpretation of the response from this reflector difficult.

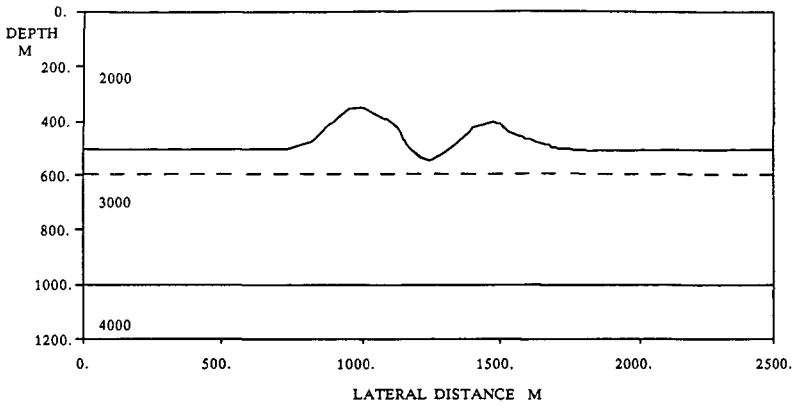


**Figure 5.30** Macro model with strong lateral velocity variations and steep dips in the overburden. The surface data is redatumed to the new datum at 600 m.

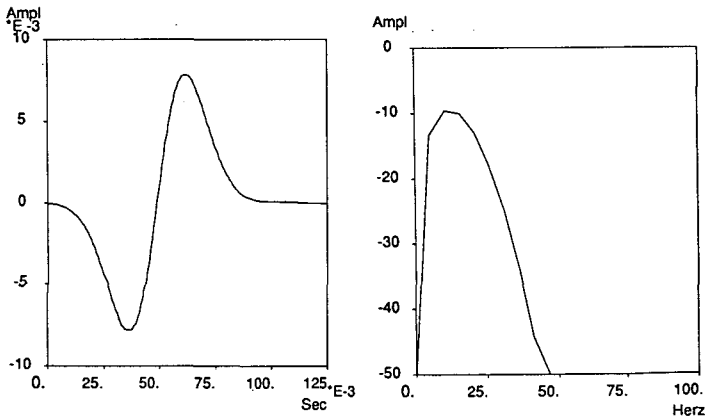


**Figure 5.31** Source signature which has been used in the modeling of the surface data for the subsurface model from figure 5.30.

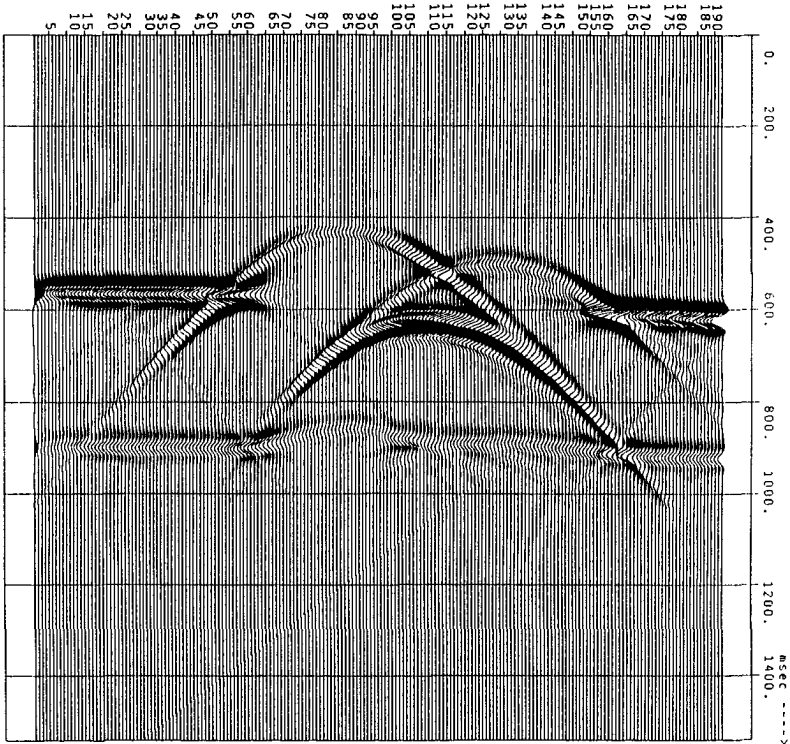


**Figure 5.32** The zero offset section for the subsurface model from figure 5.30. The lower reflection response is distorted because of overburden wave propagation effects.

For the redatuming the source wave field and the geophone data are recursively inverse extrapolated from the surface to the interface at 500 and on to the interface at 600. At this level the redatuming is carried out. Different operators have been used in the redatuming. The commonly used Rayleigh operator, involving a pressure to pressure extrapolation only has been used. Secondly the full Kirchhoff operator has been used. Both pressure and particle velocity data are extrapolated with this operator. The redatumed true zero offset section at  $z = 600$  m is shown in figure 5.33. Since the procedure is carried out in the space frequency domain, the

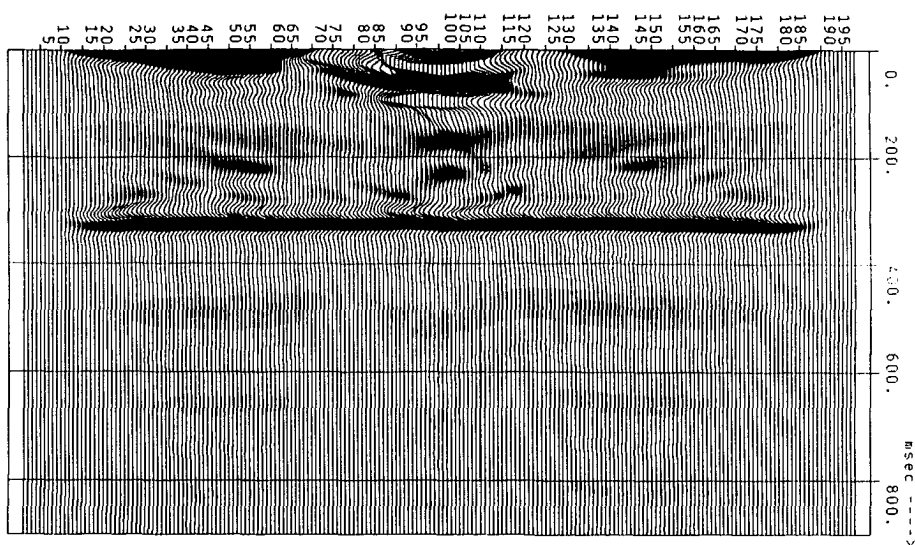
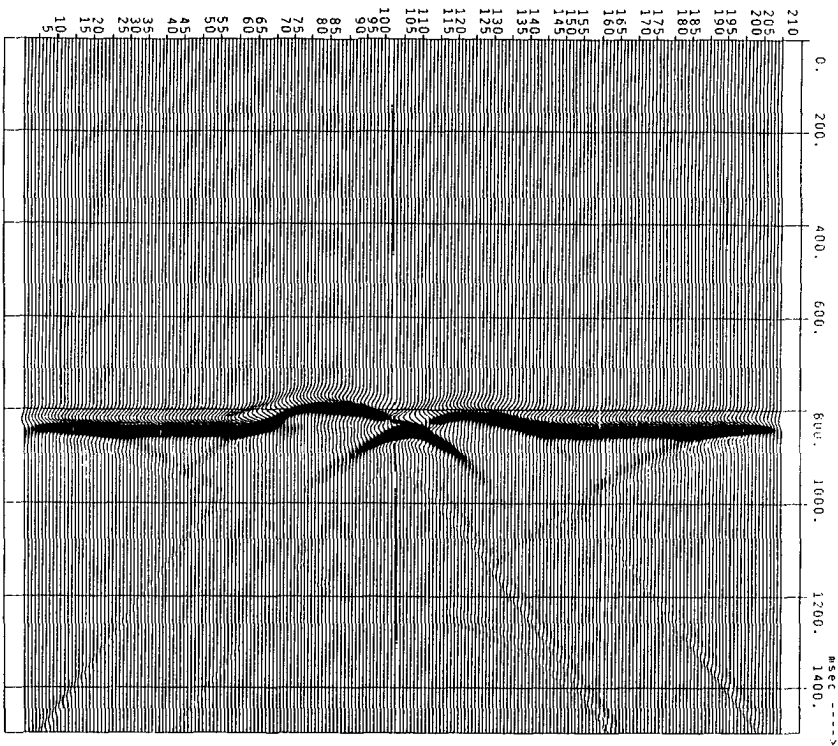


Figure 5.33 The true zero offset section at the new datum. The full Kirchhoff integral has been recursively applied.

reflections from the top reflector are now moved into negative time. In the ZO section obtained with the Kirchhoff operator the response from the deepest reflector is now flat. Because of the strong dip in the overburden some of the reflection energy from the deepest reflector reaches the surface beyond the last geophone. In the wave extrapolation the Kirchhoff integral should be taken from  $-\infty$  to  $+\infty$ . However, in practice we only have a limited cable length. Integration over this limited surface is only correct if the wave field outside the cable has decreased in amplitude sufficiently and the wave field may be approximated by zero amplitude. If the assumption about the amplitude decrease of the wave field is violated, distortion occurs. In migration the distortion occurs at the left and right extreme of the line. After migration smiles appear resulting from the truncation of the geophone cable. For redatuming similar effects occur. The response in figure 5.33 also shows some smile type of distortion.

In figure 5.34 a zero offset section is shown, which has been modeled with finite difference for the model from figure 5.30. The exploding reflector model was used with only buried sources on the deepest reflector. In the figure diffraction events are indicated which propagate beyond the last geophone. For offset data similar events will be lost resulting in the redatumed zero offset section to show smiles. In figure 5.35 the redatumed zero offset section has been



**Figure 5.34** The zero offset reflection response of the deepest reflector obtained with exploding reflector modeling. The steeply dipping events are internal reflections in the top reflector.

obtained with a Rayleigh type of operator. This operator is not correct for curved interfaces and does not handle the boundary conditions correctly. Two strong additional events are present in the data which may be incorrectly interpreted. In the section 'A comparison of the Kirchhoff integral and the Rayleigh integral' in chapter 2 a similar event appeared in one of examples. The event could be eliminated by limiting the operator angle to  $90^\circ$ . In figure 5.36 the Rayleigh operator with angle limitation has been used to obtain the redatumed zero offset section. The addition event is reduced in amplitude, however it has not been eliminated. In the section 'Recursive application of the full Kirchhoff integral for recursive inverse wave field extrapolation' in chapter 3 internal reflections in an anticlinal structure resulted in additional events, if the Rayleigh operator is used for inverse wave field extrapolation. The recursive application of the Kirchhoff integral did eliminate these internal reflections (figure 5.37)

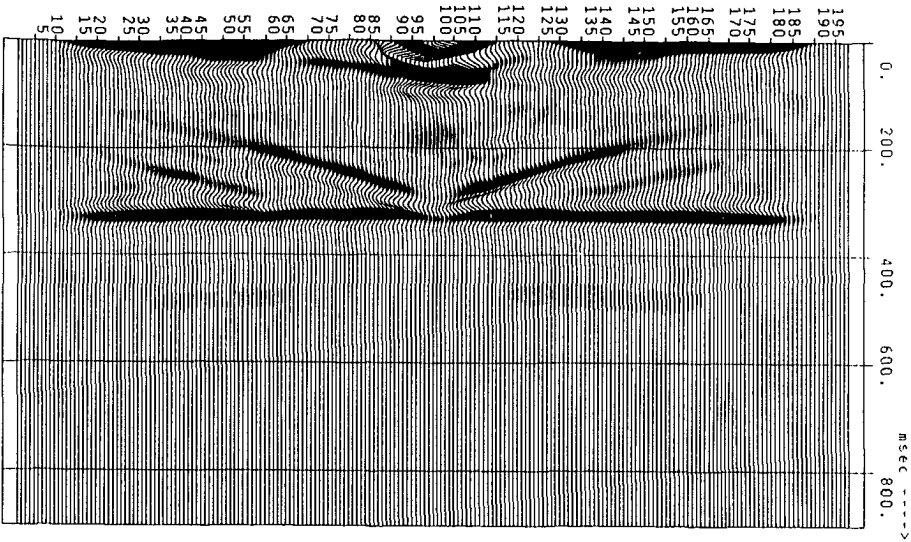


**Figure 5.35** The zero offset section at the new datum. The Rayleigh integral instead of the full Kirchhoff integral has been used in the inverse wave field extrapolation. Additional events are present in this section.

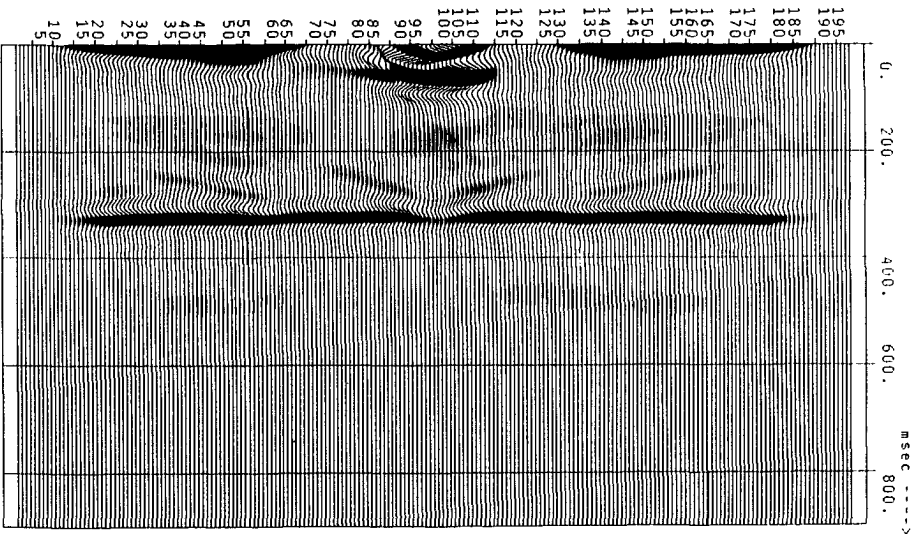


**Figure 5.36** The zero offset section at the new datum for which the angle limited Rayleigh extrapolation operator has been used. The additional event is reduced, however an amplitude anomaly still exists in the reflection event.

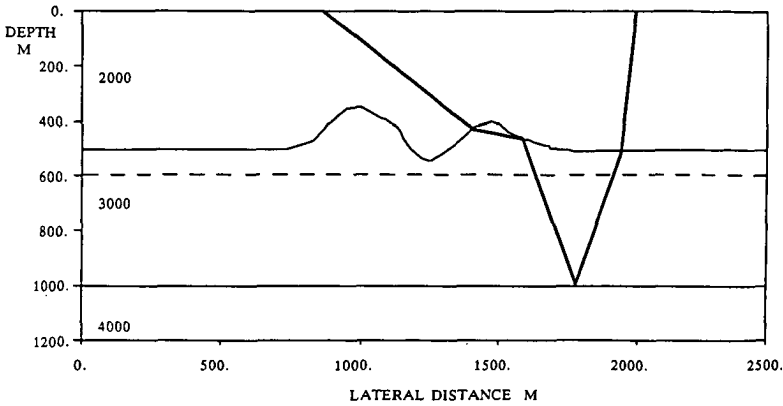


**Figure 5.37** A ray path in the model from figure 5.30 indicating the internal reflection in the top reflector.

resulting in an undistorted back propagated wave field. The additional event shown in figure 5.35 could therefore well be such an internal reflection in the top reflector. Therefore the full Kirchhoff integral should be applied in the case of high velocity contrasts and strong lateral velocity variations in the overburden. However if reflection energy is not registered because of a limited cable length, smiles will occur in the redatumed result. All effort which is put in using an operator which preserves the amplitude information may be lost because of these distortion.

### 5.3 DOME STRUCTURE, A SYNTHETIC EXAMPLE

For this example a model of a dome structure has been chosen (figure 5.38). This type of structure typically occurs in the North Sea. For the modeling an acoustic finite difference modeling scheme has been used. The model has been compressed vertically to reduce computation time for the modeling. The acquisition parameters are listed below

Shot spacing:	25 m
Group spacing:	15 m
Number of channels:	511
Number of shots:	201
Near offset:	0 m
Far offset:	5000 m
Sample interval:	6 ms (resampled)
Trace length:	3 s

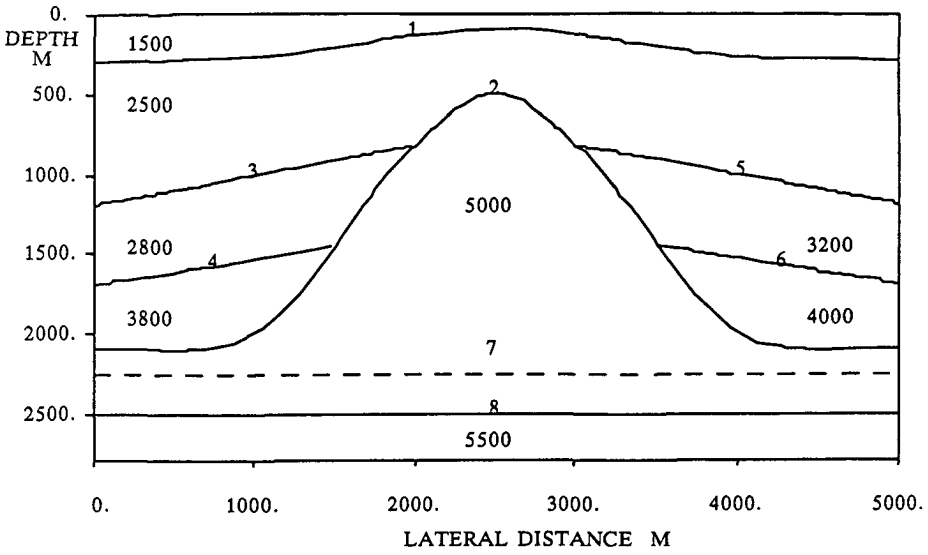


**Figure 5.38** The redatuming is used to improve the quality of the reflection from the reflector at 2500 m for this dome structure. The new datum is at 2250 m.

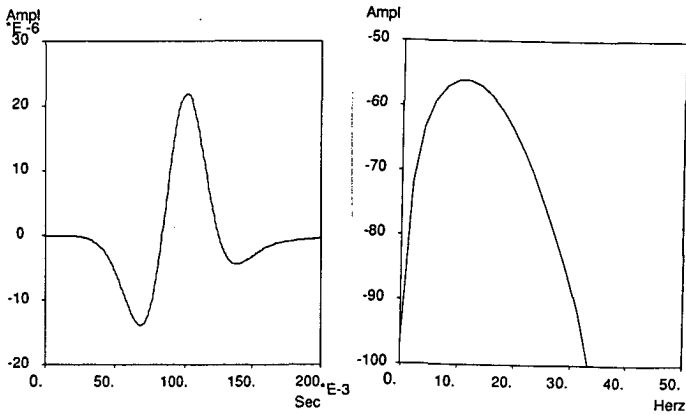


**Figure 5.39** The source signature used in the finite difference modeling of the surface data for the model from figure 5.38.

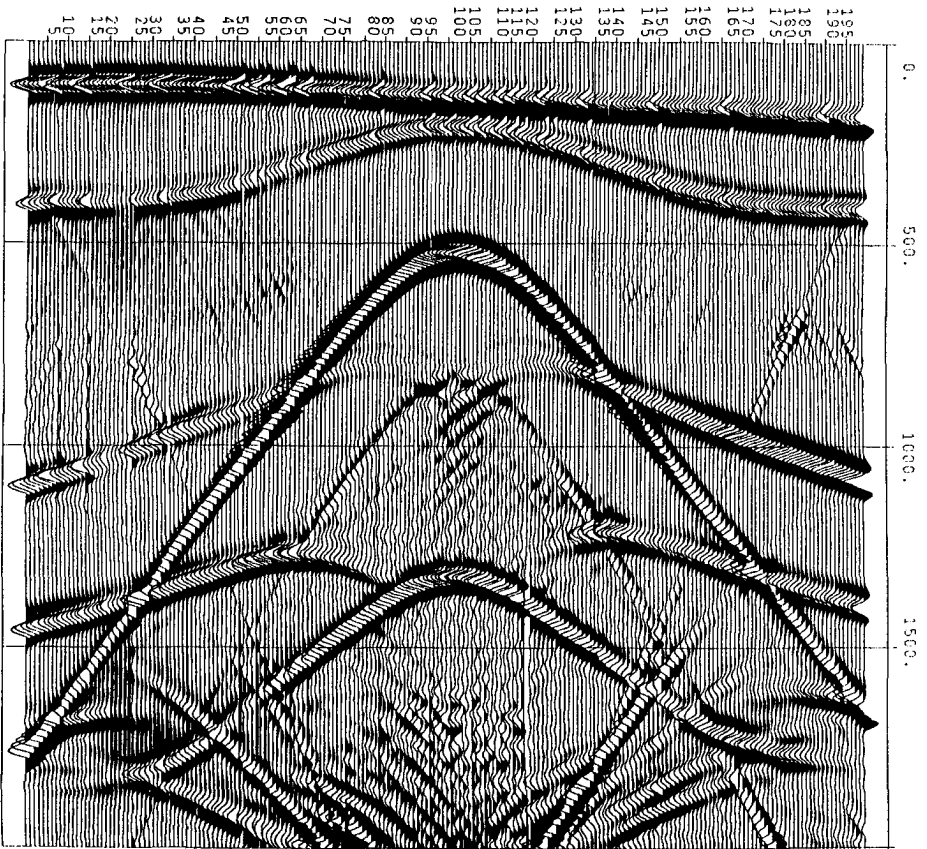


**Figure 5.40** The zero offset section at the surface of the dome model. The reflection from the deepest reflector is pulled up because of lateral velocity variations in the overburden. Additional diffraction events are present because of the gain which has been applied to the data for plotting.

The source signature is shown in figure 5.39. The somewhat low maximum frequency of 35 Hz resulted from stability conditions for the finite difference modeling. The near offset section is shown in figure 5.40. The response from the deepest reflector shows a pull up under the dome, because of the strong lateral velocity change in the overburden. A recursive redatuming procedure has been applied. In the recursive extrapolation the wave field is inversely extrapolated across each homogeneous layer. In the first step the source wave field and the detected wave field are extrapolated from the surface to interface 1. The next extrapolation step takes the wave fields from interface 1 to interface 3, 5 and the segment of interface 2, which is

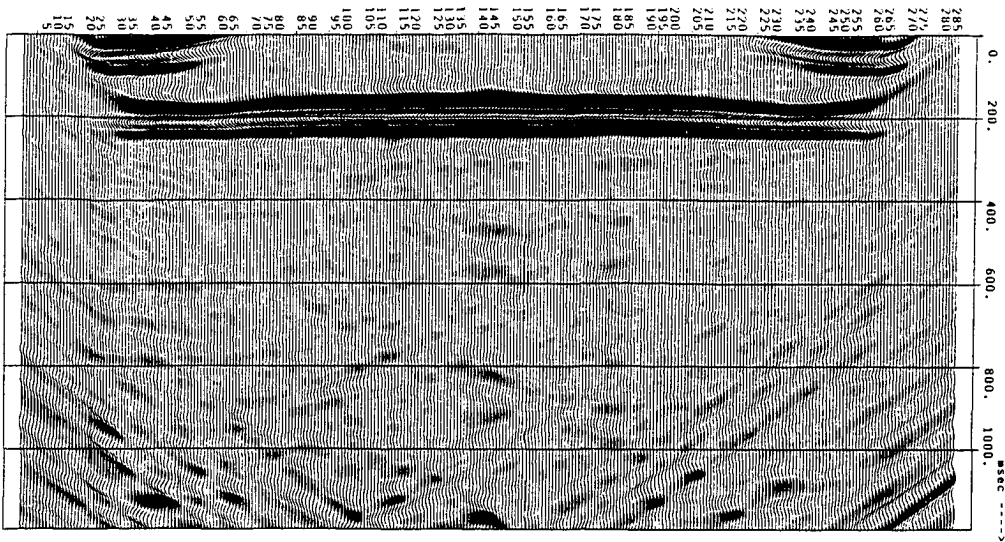


**Figure 5.41** The true zero offset section at 2250 m in the dome model. The overburden wave propagation effects have been eliminated.

between interfaces 3 and 5. On the left side the wave fields are then extrapolated from 3 to 4 and part of 2. Followed by an extrapolation from 4 to the left part of 2. On the right hand side the wave fields are extrapolated from 5 to 6 and the part of 2 between 5 and 6. Followed by an extrapolation from 6 to the right most part of 2. Finally the source and the detected wave fields are extrapolated from 2 to 7 at which level a reconstruction of a true zero offset section shown in figure 5.41 occurs. All overburden wave propagation effects have been eliminated and the response is horizontal without the pull up. Smile like distortions are present at the left and right hand side of the data due to the truncation of the geophone cable at the surface. However no artifacts are present for the part of the reflector which has sufficient surface coverage. So the redatuming yields a zero offset section which is better suited for structural or stratigraphic interpretation purposes, than a surface zero offset section.

### 5.4 A REAL DATA EXAMPLE

For the last example of redatuming a real data set has been used. The data has been obtained through physical modeling in a water tank. The dimensions of the model have been scaled down and the frequency of the source has been scaled up. The data from water tank modeling is generally quite similar to real seismic data. The acquisition parameters are listed below.

---

Shot spacing:	24.384 m
Group spacing:	24.384 m
Number of channels:	48
Number of shots:	296
Configuration:	Entel spread
Near offset:	243.84 m
Far offset:	1389.9 m
Sample interval:	4 ms (resampled)
Trace length:	2 s

In the stacking velocity analysis the CMP gathers stacked for a wide range of stacking velocities. Unfortunately, the offset range is too small to determine the correct stacking velocities. The data has been stacked for different constant stacking velocities. The results are shown in figures 5.42, 5.43 and 5.44 in which the stacked sections for stacking velocities of 3000 m/s, 3500 m/s and 4500 m/s are shown. All major events are present in all sections. Stacking with different velocities resulted in a constructive stacking of the events along the move-out curves. This gives us an indication that only little velocity information is available in the data. In order to obtain a macro model for the data, pre-stack travel time inversion has been used. In this procedure an interval velocity model is automatically modified to produce a better match between model travel times and measured travel times. An interpretation of the stacked section has been made to determine the major reflection events. Note that the event between 1. and 1.1 s to the left and right of the dome has a negative polarity. So a velocity inversion occurs at the interface corresponding to this event. In order to obtain pre-stack travel times 17 CMP gathers have been selected of which 8 are shown in figures 5.45 and 5.46. In each of the CMP gathers the events related to the interpreted time horizons in the stacked section are picked. The pre-stack travel time picks are shown in figures 5.47 and 5.48. The vertical bars in these figures indicate at which offsets the travel times have been picked. Furthermore, the height of these bars indicate the uncertainty in the picks. Due to noise and picking inaccuracy, the travel time picks may be off several milliseconds. The pre-stack travel time inversion procedure uses the interpretation and the travel time picks to estimate the macro model. So the position of the major reflectors and the interval velocities should be estimated. For an extensive discussion on the pre-stack travel time inversion, which has been used the reader is referred to Van der Made (1987).

The estimated macro model is shown in figure 5.49 together with the zero offset rays. In order to assess the correctness of the macro model the data mismatch should be analyzed. In the diagram for the model driven processing shown again in figure 5.50, the data mismatch analysis corresponds to the quality control procedure. Before carrying out the computationally expensive

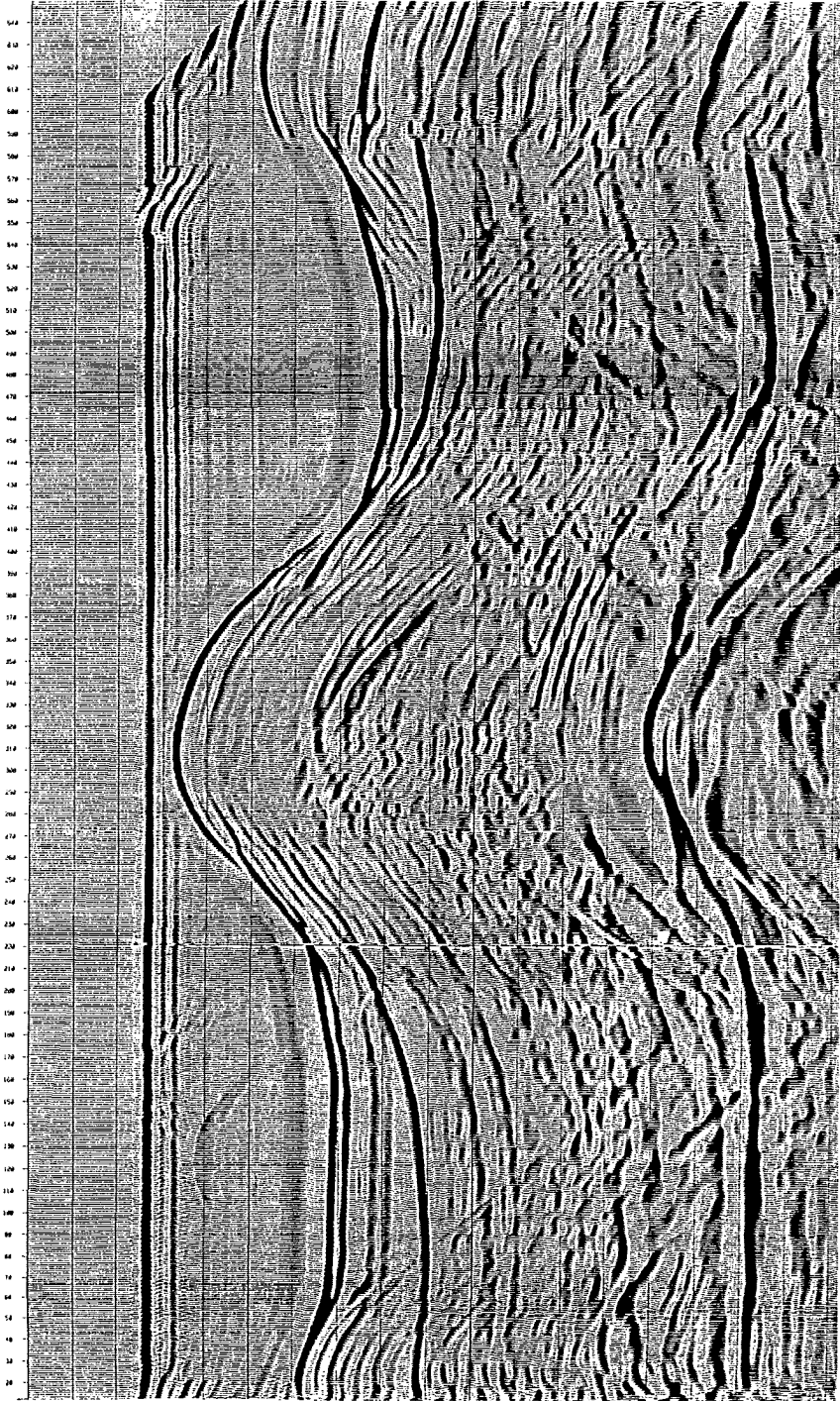


Figure 5.42 A constant velocity stack (3500 m/s) of the water tank data. Courtesy Marathon Oil company.

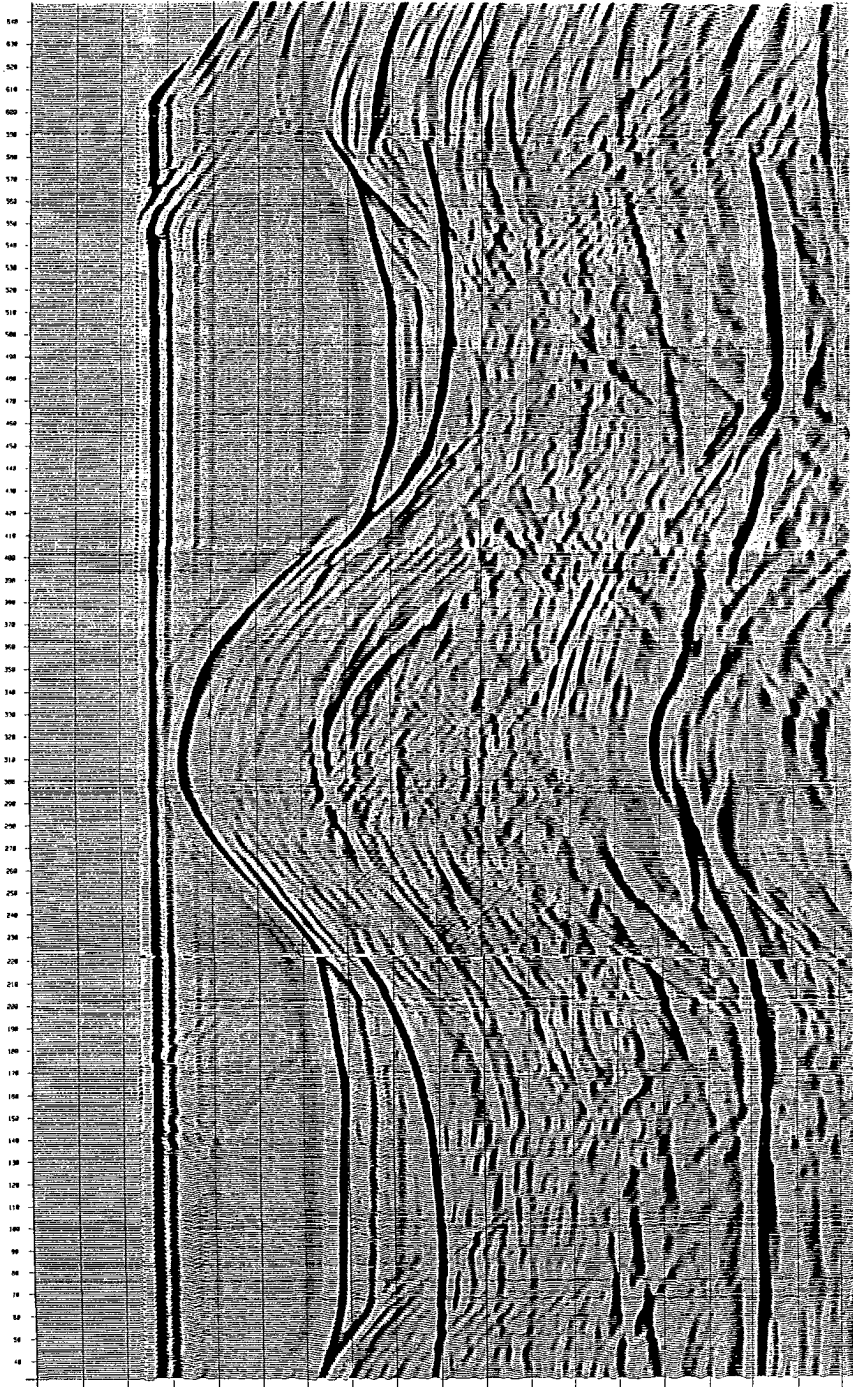


Figure 5.43 A constant velocity stack (4000 m/s) of the water tank data. Courtesy Marathon Oil company.

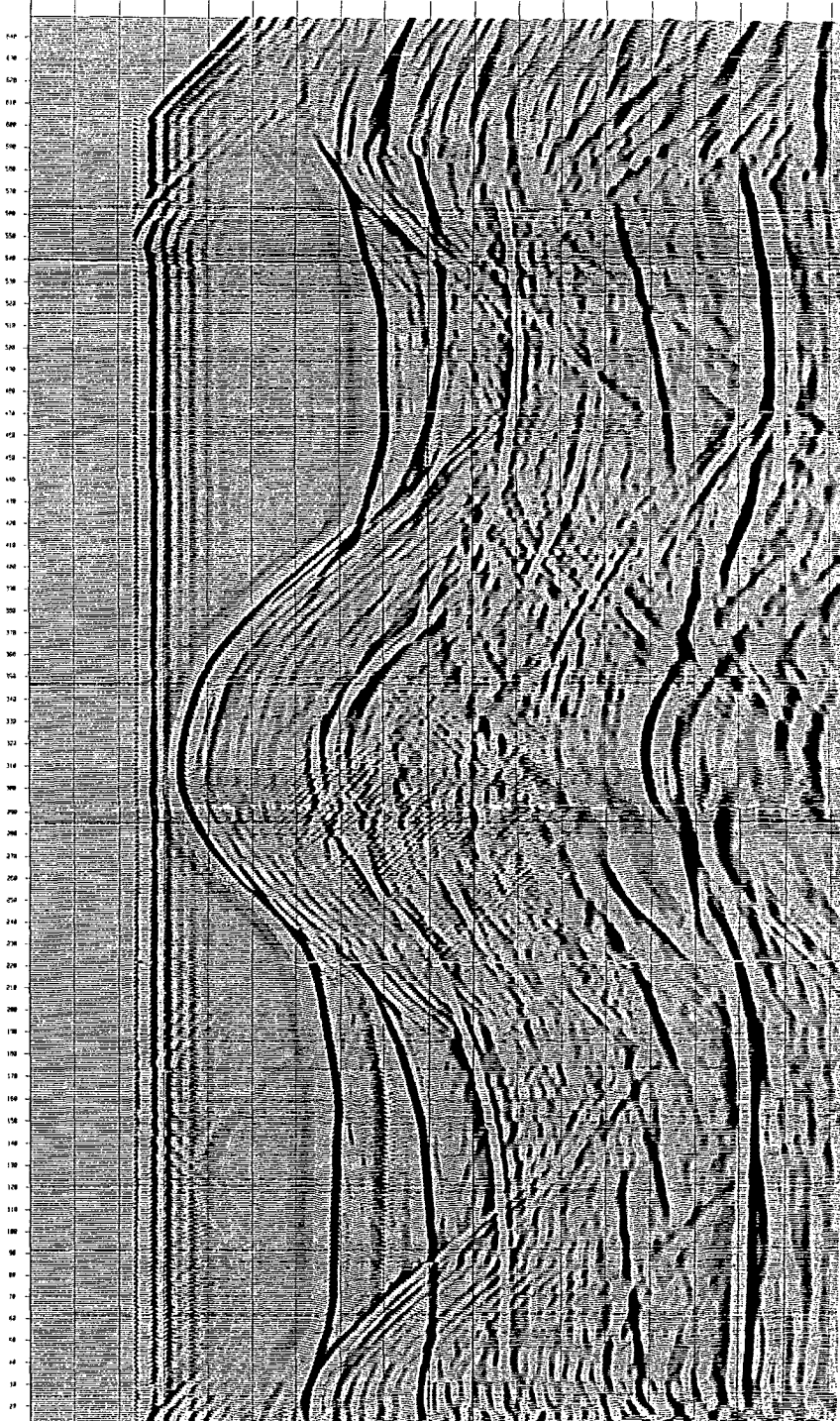


Figure 5.44 A constant velocity stack (4500 m/s) of the water tank data. Courtesy Marathon Oil company.

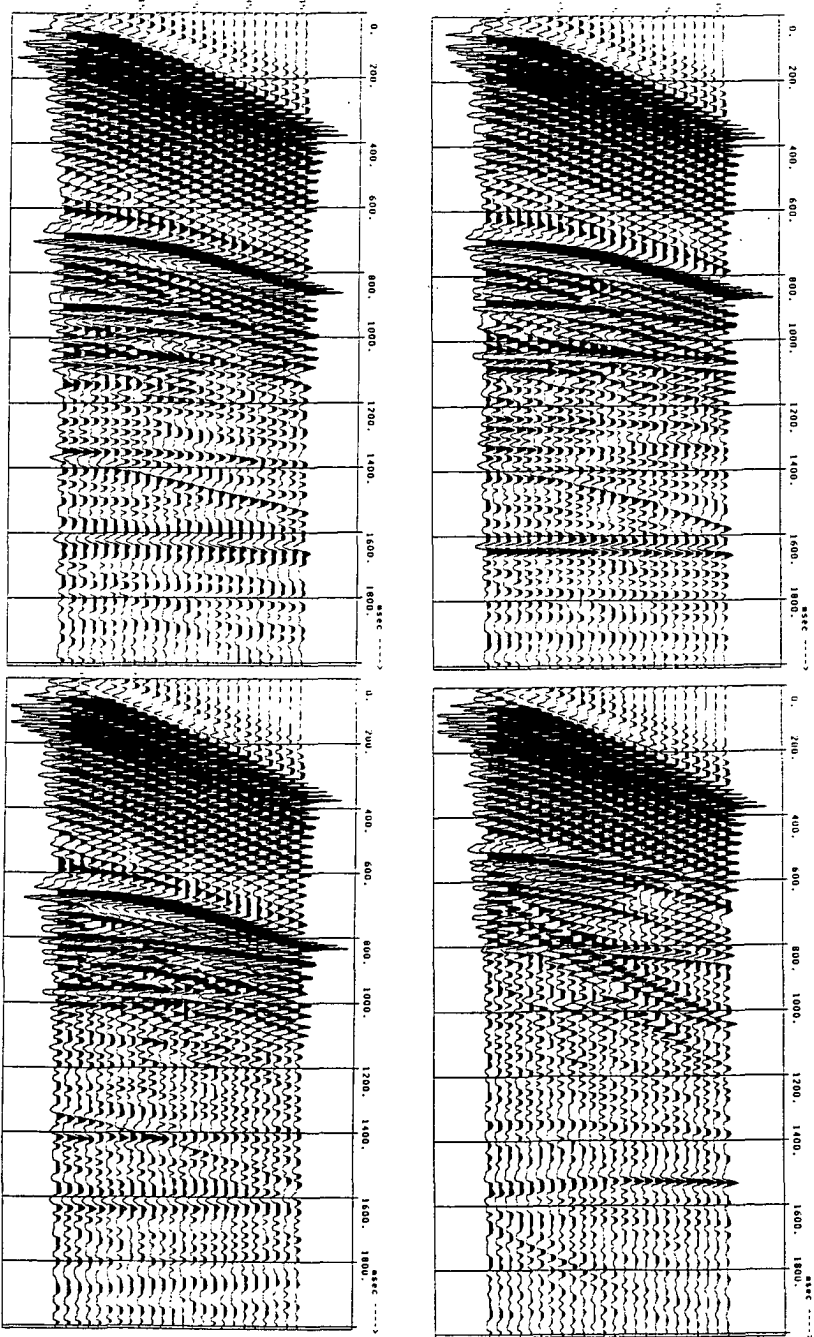


Figure 5.45 The CMP gathers at CDP locations 100, 150, 200 and 250. The gathers have been plotted with agc to make the deeper events visible.

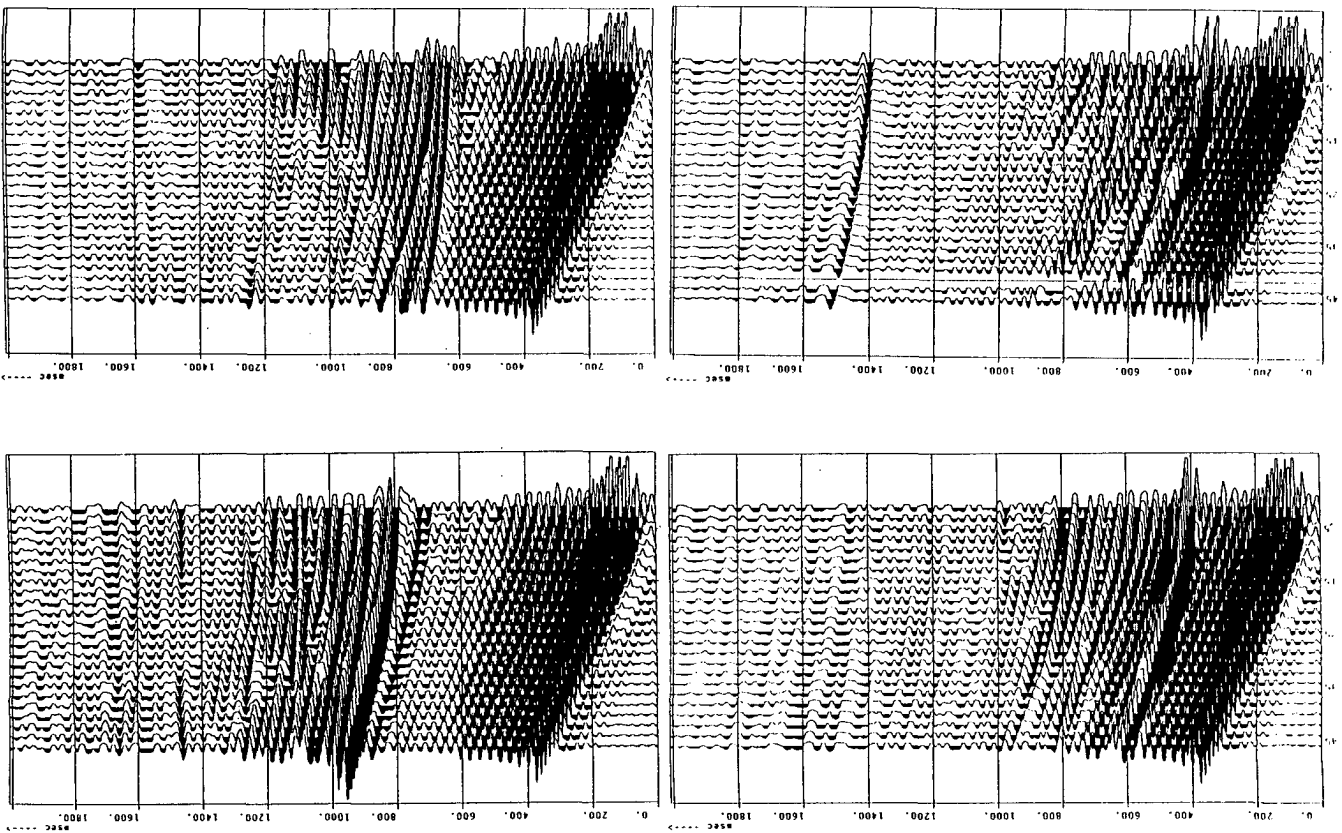
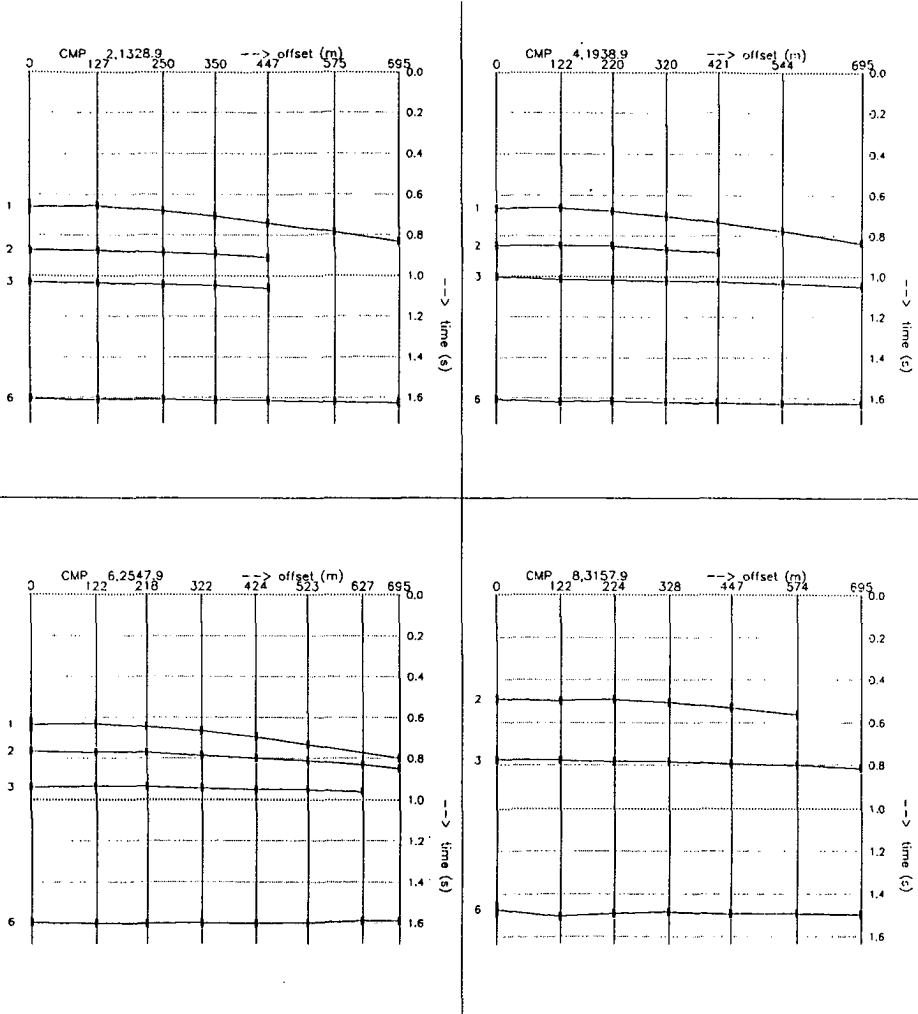
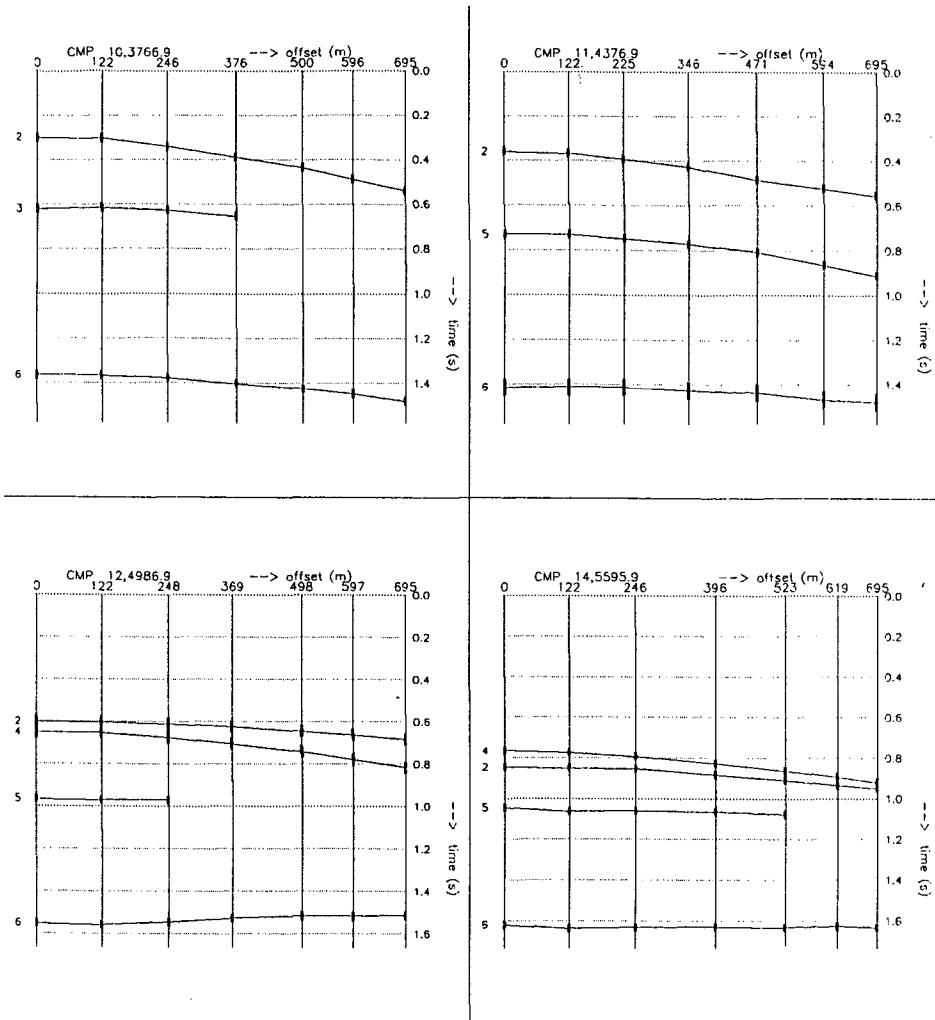


Figure 5.46 The CMP gathers at CDP locations 300, 350, 400 and 450. The gathers have been plotted with age to make the deeper events visible.



**Figure 5.47** The picked travel times from the CMP gathers 100, 150, 200 and 250 which have been used in the macro model estimation.

redatuming the correctness of the macro model is verified. For different CMP gathers, the data mismatch is shown in figures 5.51 through 5.54. The measured travel times are depicted as solid lines and the modeled travel times, depicted as dashed lines, are shown for each event. The modeled travel times are obtained by ray-tracing in the estimated macro model. If the modeled travel times and the measured travel times coincide, then the estimated model explains



**Figure 5.48** The picked travel times from the CMP gathers 300, 350, 400 and 450 which have been used in the macro model estimation. Eight out of the 17 CMP gathers which have been used are shown in these figures.

the data. The redatuming has been applied to the shot gathers taking the estimated model as the macro model. The new datum has been chosen at a depth of 3 km. The source wave fields and the registered wave fields have been recursively extrapolated from the surface to 3 km depth, the new datum. The true zero offset section at the new datum is shown in figures 5.55 and 5.56. Both the full Kirchhoff operator has been applied (figure 5.55) as well as the Rayleigh operator (figure 5.56). The response from the deepest reflector is now horizontal. The pull up due to

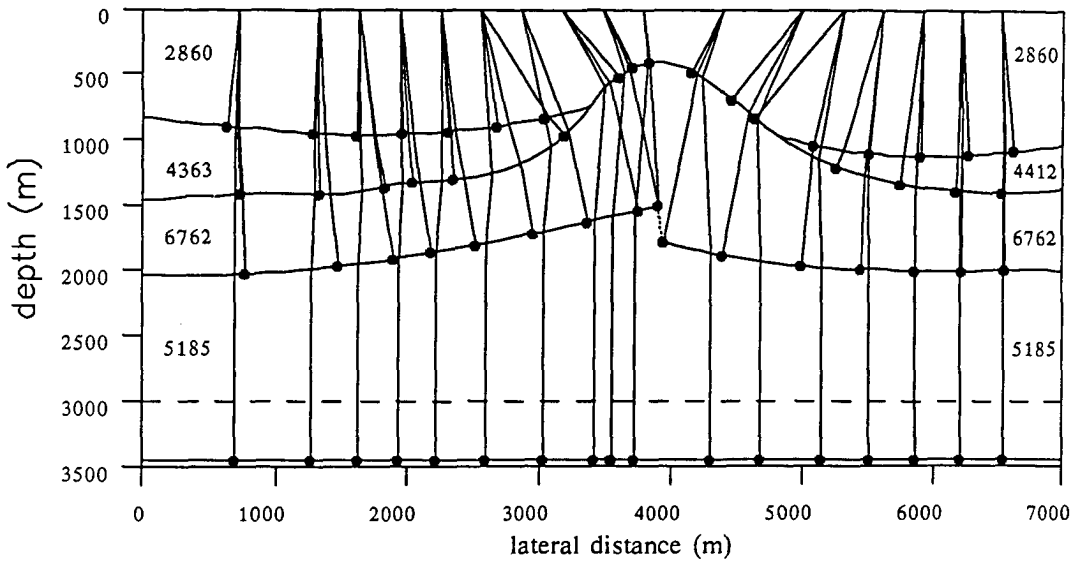


**Figure 5.49** The estimated macro model from the picked travel times. The zero offset rays are shown to give an indication of the CMP coverage. The interval velocities are indicated inside the layers.

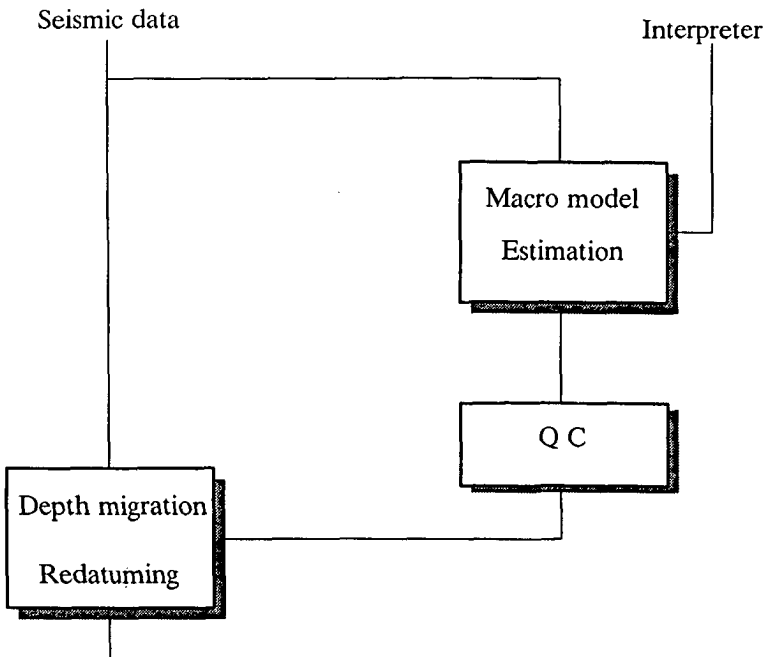


**Figure 5.50** In the model driven processing the macro model is estimated separately from the actual processing. Through quality control the accuracy of the macro model is assessed.

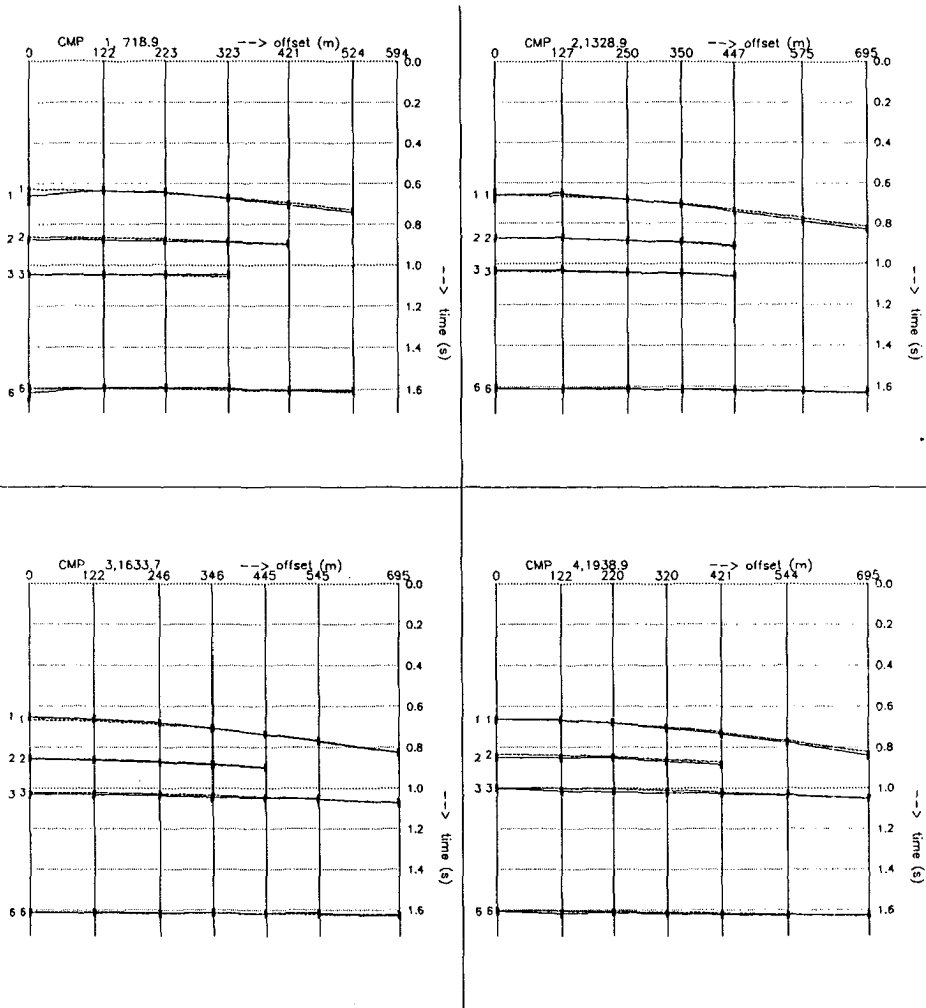


**Figure 5.51** The modeled travel times (dashed lines) and the measured travel times (solid lines) for CMP's 50, 100, 125 and 150. Since measured and modeled travel times coincide the data is explained by the estimated macro model.

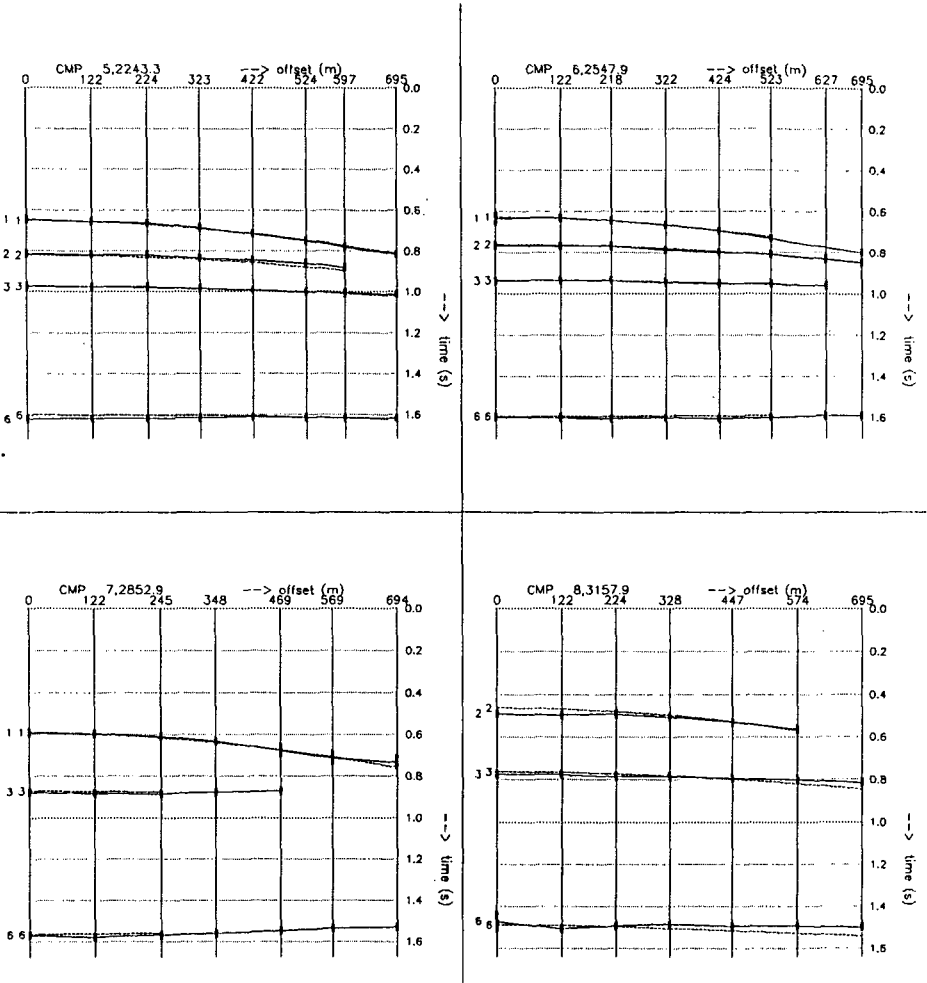


**Figure 5.52** The modeled travel times (dashed lines) and the measured travel times (solid lines) for CMP's 175, 200, 225 and 250. Since measured and modeled travel times coincide the data is explained by the estimated macro model.

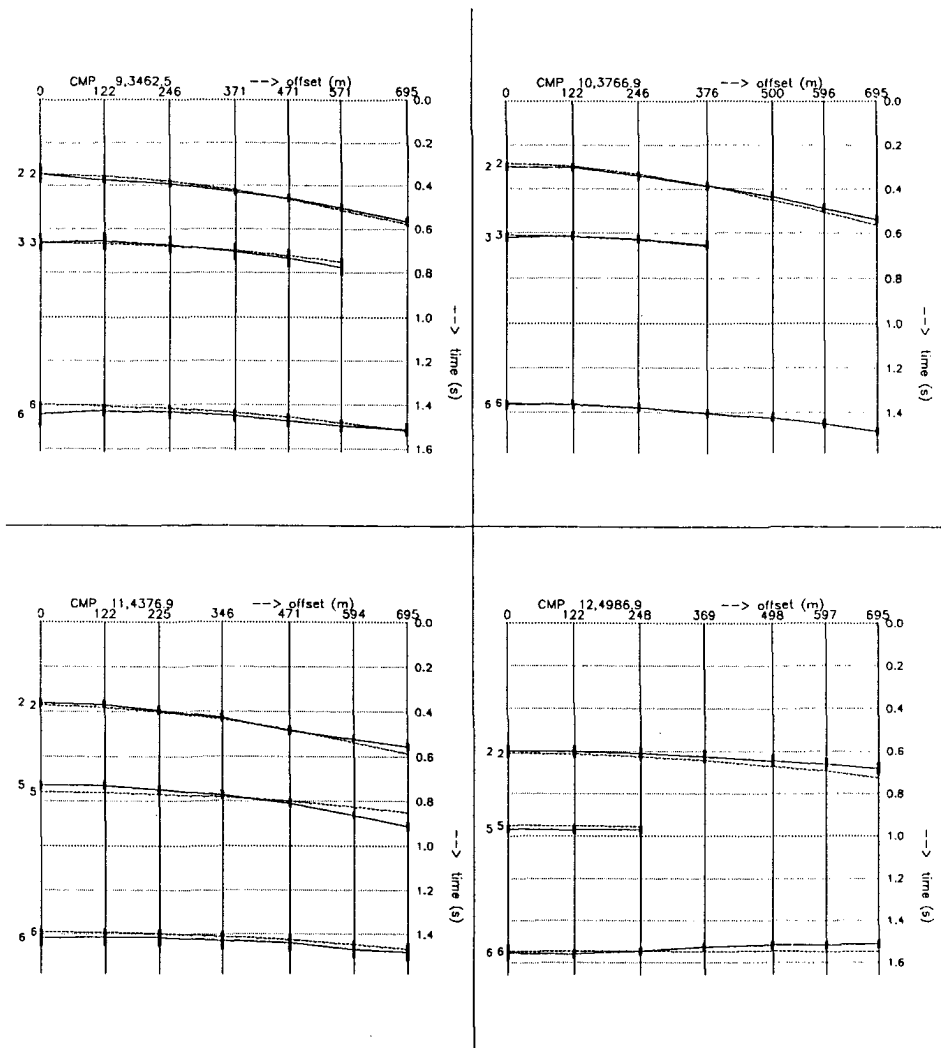


**Figure 5.53** The modeled travel times (dashed lines) and the measured travel times (solid lines) for CMP's 275, 300, 350 and 400. Since measured and modeled travel times coincide the data is explained by the estimated macro model.

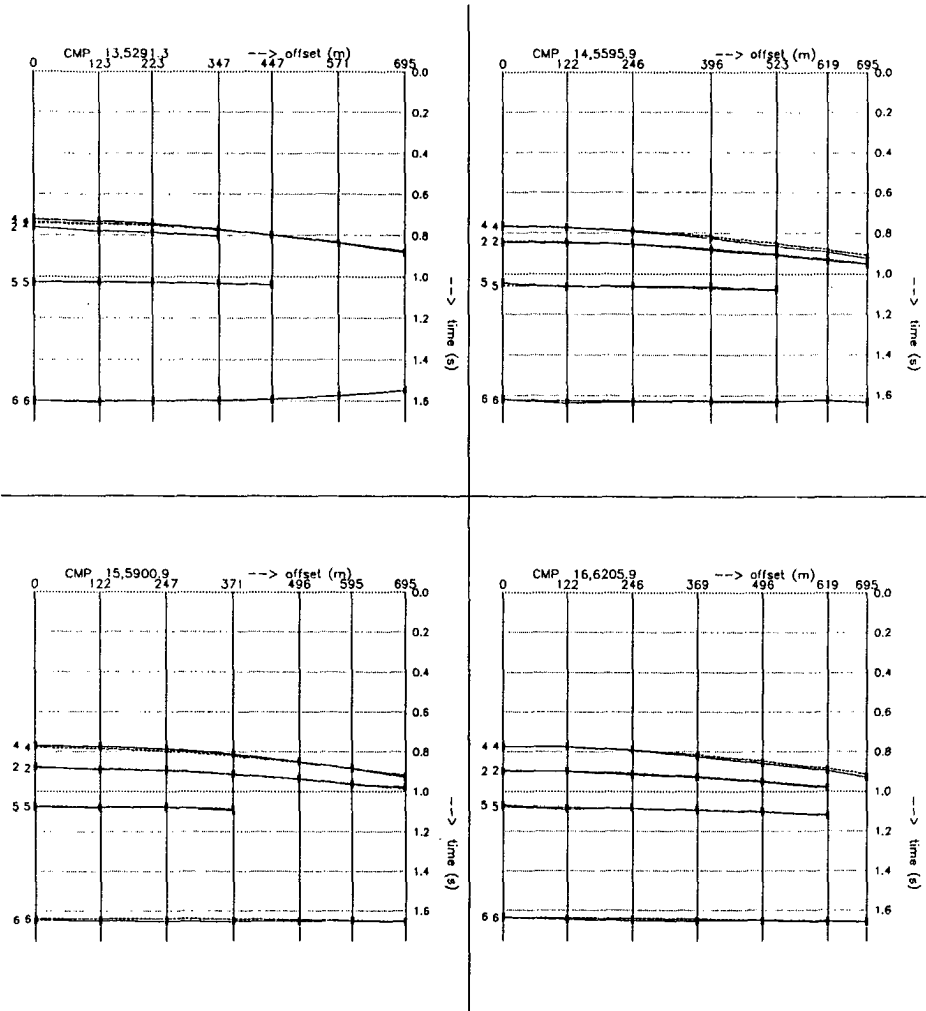


**Figure 5.54** The modeled travel times (dashed lines) and the measured travel times (solid lines) for CMP's 425, 450, 475 and 500. Since measured and modeled travel times coincide the data is explained by the estimated macro model.

lateral velocity variations in the overburden has been eliminated. To the left and right of the dome, the reflector response is continuous and of good quality. Below the dome structure however, the response is distorted. Either the macro model is not correct for this region or insufficient surface data has been used. The modeled travel times did coincide with the picked travel times, so the estimated overburden structure does explain the reflection data. Furthermore

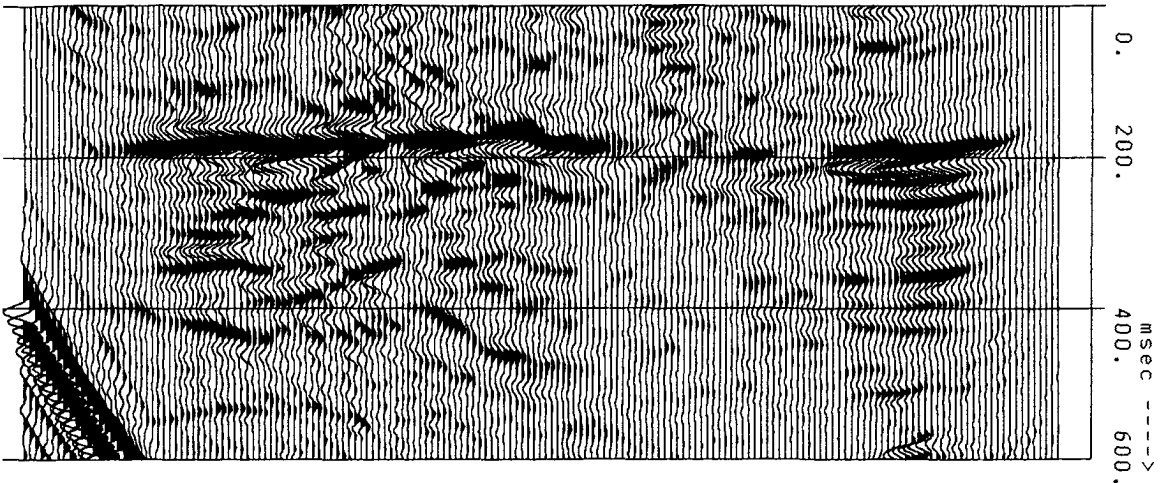


**Figure 5.55** The true zero offset section at the new datum obtained with a Rayleigh integral based operator.

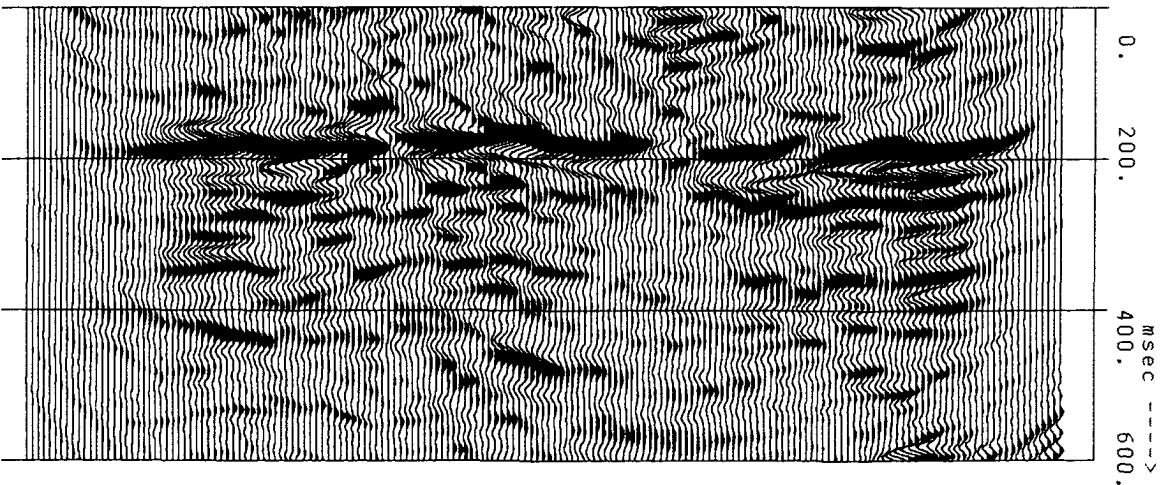


**Figure 5.56** The true zero offset section at the new datum obtained with the full Kirchhoff integral based operator.

the zero offset section at the new datum obtained with the full Kirchhoff integral is different from the zero offset section obtained with the Rayleigh integral. The amplitude recovery of the Kirchhoff integral based operator is much better below the dome. The high velocity contrast at the top of the dome causes a high transmission loss which is not inverted for when using the

Rayleigh integral. The other anomalies may be related to insufficient surface coverage. Most of the reflection energy from the 3.5 km deep reflector may have been lost in the only 1 km long geophone cable.

The experiments discussed in this chapter show that the redatuming eliminates overburden wave propagation effects resulting in a true zero offset section which is superior to a surface zero offset section. Furthermore it can be concluded that insufficient surface coverage may result in an undesired loss of reflection information for particularly the deep structures.

## APPENDIX A

---

 THE KIRCHHOFF INTEGRAL FOR  
 2-D HOMOGENEOUS MEDIA

In this appendix the 2-D Kirchhoff integral for homogeneous media will be derived. In the recursive application of the Kirchhoff integral both pressure and normal components of the particle velocity are required at each surface over which the integral is taken. Therefore both the pressure  $P$  as well as the particle velocity  $V$  should be extrapolated. An expression for the extrapolation of the particle velocity will be derived as well.

Consider the Kirchhoff integral for the geometry form figure A-1 (relation 2.11)

$$P(\mathbf{r}_A, \omega) = -\frac{1}{4\pi} \int_S \frac{1}{\rho(\mathbf{r})} \left[ P(\mathbf{r}, \omega) \frac{\partial G(\mathbf{r}, \mathbf{r}_A, \omega)}{\partial n} - \frac{\partial P(\mathbf{r}, \omega)}{\partial n} G(\mathbf{r}, \mathbf{r}_A, \omega) \right] dS \quad (\text{A-1})$$

For a homogeneous medium we can take an analytical Green's function

$$G(\mathbf{r}, \mathbf{r}_A, \omega) = \rho \frac{e^{-jk r}}{r} \quad (\text{A-2})$$

with

$$\mathbf{r} = (x, y, z)$$

$$\mathbf{r}_A = (x_A, y_A, z_A)$$

$$r = |\mathbf{r} - \mathbf{r}_A|$$

$$k = \omega/c.$$

After substitution in (A-1) and taken the normal pointing inward, the following 3-D Kirchhoff

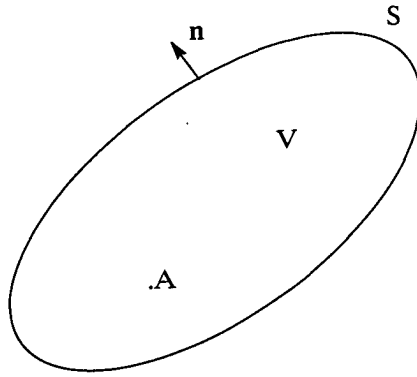


**Figure A-1** Closed domain for obtaining the wave field in A from the wave field on the surface S with the Kirchhoff integral.

integral is obtained

$$P(\mathbf{r}_A, \omega) = \frac{1}{4\pi} \int_S \frac{1 + jkr}{r} \cos \phi_1 \frac{e^{-jkr}}{r} P(\mathbf{r}, \omega) + j\omega\rho V_n(\mathbf{r}, \omega) \frac{e^{-jkr}}{r} dS \quad (A-3)$$

For the 2-D approximation assume an invariant medium in the y-direction. Furthermore assume that the wave field  $P(\mathbf{r}, \omega)$  has been caused by a line source in the y-direction. Since both the wave field and the medium are invariant in the y-direction, the integration in this direction may be carried out for (A-3) resulting in

$$P(\mathbf{r}_A, \omega) = \frac{1}{4\pi} \int_L -jk\pi \cos \phi_1 H_1^{(2)}(kr) P(\mathbf{r}, \omega) + \omega\rho\pi H_0^{(2)}(kr) V_n(\mathbf{r}, \omega) dL \quad (A-4)$$

where  $H_0^{(2)}$  and  $H_1^{(2)}$  are Hankel functions of the second kind. In the recursive extrapolation integral (A-4) is applied repeatedly. So we need the normal component of the particle velocity in  $\mathbf{r}_A$  as well (figure A-2),

$$V_n(\mathbf{r}_A, \omega) = \mathbf{V}(\mathbf{r}_A, \omega) \cdot \mathbf{n}_A \quad (A-5)$$

and

$$\mathbf{V}(\mathbf{r}_A, \omega) = -\frac{1}{j\omega\rho} \nabla_A P(\mathbf{r}_A, \omega) \quad (A-6)$$

Substitution of (A-6) in (A-5) yields

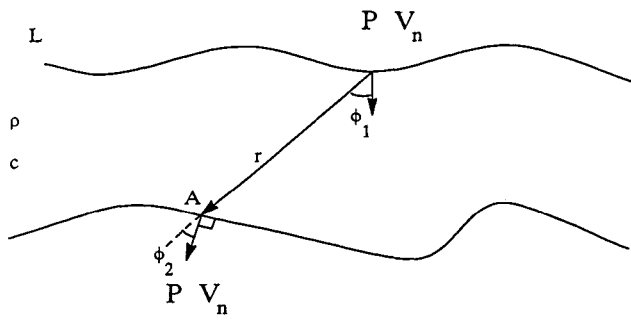


Figure A-2 In recursive application of the full Kirchhoff integral, both pressure and particle velocity data should be calculated on each interface.

$$V_n(\mathbf{r}_A, \omega) = -\frac{k}{j\omega\rho} \frac{\partial P}{\partial kr} \cdot \frac{\partial r}{\partial n_A} \quad (A-7)$$

For the derivatives of the Hankel functions the following can be found in Abramowitz and Stegun (1970):

$$\frac{\partial}{\partial kr} H_1^{(2)}(kr) = H_0^{(2)} - \frac{1}{kr} H_1^{(2)}(kr) \quad (A-8)$$

and

$$\frac{\partial}{\partial kr} H_0^{(2)}(kr) = -H_1^{(2)}(kr) \quad (A-9)$$

Substitution of A-8, A-9 and A-4 in A-7 yields

$$V_n(\mathbf{r}_A, \omega) = \frac{-k}{j\omega\rho_0 4\pi} \int_L \left\{ -jk\pi \cos \phi_1 \left[ H_0^{(2)}(kr) - \frac{1}{kr} H_1^{(2)}(kr) \left( \frac{\partial r}{\partial n_A} \right) - \frac{1}{k} H_1^{(2)}(kr) \left( \frac{\partial}{\partial n_A} \right) \left( \frac{\partial r}{\partial n} \right) \right] P(r, \omega) - \omega\rho\pi H_1^{(2)}(kr) V_n(r, \omega) \left( \frac{\partial r}{\partial n_A} \right) \right\} dL \quad (A-10)$$

For the derivatives of r to the normal we can write

$$\left( \frac{\partial r}{\partial n} \right) = \cos \phi_1 \quad (A-11)$$

$$\left( \frac{\partial r}{\partial n_A} \right) = \cos \phi_2 \quad (A-12)$$

and

$$\left( \frac{\partial}{\partial n_A} \right) \left( \frac{\partial r}{\partial n} \right) = \frac{1}{r} \left[ -\frac{1}{2} \cos(\varphi_1 - \varphi_2) + \frac{1}{2} \cos(\varphi_1 + \varphi_2) \right] . \quad (\text{A-13})$$

Substitution of A-11, A-12 and A-13 in A-10 yields

$$\begin{aligned} V_n(\mathbf{r}_A, \omega) = & \frac{-k}{j\omega\rho 4\pi} \int_L \left\{ -jk \left[ \cos \varphi_1 \cos \varphi_2 H_0^{(2)}(kr) - \right. \right. \\ & \left. \left. \frac{1}{kr} \left( \cos \varphi_1 \cos \varphi_2 - \frac{1}{2} \cos(\varphi_1 - \varphi_2) + \frac{1}{2} \cos(\varphi_1 + \varphi_2) \right) H_1^{(2)}(kr) \right] P(\mathbf{r}, \omega) - \right. \\ & \left. \omega\rho_0\pi \cos \varphi_2 H_1^{(2)}(kr) V_n(\mathbf{r}, \omega) \right\} dL . \quad (\text{A-14}) \end{aligned}$$

With A-4 and A-14 a 2-D recursive wave field extrapolation may be carried out.

## REFERENCES

- Berkhout, A.J., 1982, Seismic migration, imaging of acoustic energy by wave field extrapolation, A. theoretical aspects, 2nd ed.: Elsevier, Science Publ Co.
- Berkhout, A.J., 1984, Seismic migration, imaging of acoustic energy by wave field extrapolation, B. practical aspects: Elsevier, Science Publ Co.
- Berkhout, A.J., 1984, Seismic resolution: Geophysical Press.
- Berkhout, A.J., and Wapenaar, C.P.A., 1988, True amplitude extrapolation of primary seismic waves I: One-way versions of the Kirchhoff integral, *Geophysics*, 54.
- Berryhill, J.R., 1979, Wave-equation datuming: *Geophysics*, 44, 1329–1344.
- Berryhill, J.R., 1984, Wave-equation datuming before stack: *Geophysics*, 49, 2064–2066.
- Bleistein, N., 1984, *Mathematical methods for wave phenomena*: Academic Press Inc.
- Carter, J.A., and Frazer, L.N., 1984, Accomodating lateral velocity changes in Kirchhoff migration by means of Fermat's principle: *Geophysics*, 49, 46–53.
- Castle, R.J., 1982, Wave-equation migration in the presence of lateral velocity variations: *Geophysics*, 47, 1001–1011.
- Faye, J.P., and Jeannot, J.P., 1986, Pre-stack migration velocities from focussing analysis, Presented at the 56th Ann. Intern. Mtg., Soc. Explor. Geophys., Atlanta.
- Gazdag, J., 1978, Wave equation migration with the phase shift method: *Geophysics*, 43, 1342–1351.
- Hilterman, F.J., Amplitudes of seismic waves — a quick look: *Geophysics*, 40, 754–762.
- Hubral, P., 1983, Computing true amplitude reflections in laterally inhomogeneous earth: *Geophysics*, 48, 1051–1062.
- Jain, C.J., deFigueiredo, R.J.P., 1982, Concepts and techniques in oil and gas exploration, SEG.
- Kelly, K.R., Ward, R.W., Treitel, .S, and Alford, R.M., Synthetic seismograms: a finite-difference approach: *Geophysics*, 41, 2–27.

- Kinniging, N.A., Budejicky, V., Wapenaar, C.P.A., and Berkhout, A.J., 1988, Efficient 3-D shot record redatuming: submitted for publication in *Geophysics*.
- Kunh, J.M., and Alhilali, K.A., Weighted factors in the construction and reconstruction of acoustical wave fields: *Geophysics*, 42, 1183-1198.
- Larner K.L., Hatton, L., and Gibson, B., 1981, Migration of seismic data from inhomogeneous media: *Geophysics*, 46, 761-767.
- Ooms, F.P.J., 1987, A new approach to velocity analysis in shot record migration, Msc thesis, Delft University.
- Schneider, W.A., 1978, Integral formulation for migration in two and three dimensions: *Geophysics*, 43, 49-67.
- Stolt, R.H., 1978, Migration by Fourier transform: *Geophysics*, 43, 23-48.
- Stolt, R.H., and Jacobs, B., 1985, *Seismic migration*: Geophysical Press.
- TRITON, 1986, 1987 and 1988, Research project progress reports, Delft University.
- Van Riel, P., and Berkhout, A.J., 1985, Resolution in seismic trace inversion by parameter estimation: *Geophysics*, 50, 1440-1455.
- Van der Made, P.M., 1988, Determination of macro subsurface models by generalized inversion, Doctoral thesis, Delft University of technology.
- Wapenaar, C.P.A., 1986, Pre-stack migration in two and three dimensions, Doctoral thesis, Delft University of technology.
- Wapenaar, C.P.A., Peels, G.L., Budejicky, V. and Berkhout, A.J., 1988, Inverse extrapolation of primary seismic waves: Submitted.
- Wapenaar, C.P.A., and Peels, G.L., 1987, True amplitude wave-field extrapolation of primary waves: Submitted to *Geophysics* for publication in *Geophysics*.
- Wiggins, J.W., 1984, Kirchhoff integral extrapolation and migration of non planar data: *Geophysics*, 49, 1238-1248.
- Yilmaz, O., and Darran, L., 1986, Pre-stack layer replacement: *Geophysics*, 51, 1355-1369.
- Yilmaz, O., and Chambers, R.E., 1984, Migration velocity analysis by wave field extrapolation: *Geophysics*, 49, 1664-1674.

---

## SUMMARY

One of the main purposes of seismics is to detect hydrocarbon reservoirs beneath the surface. At the surface echo acoustical measurements are carried out. In order to obtain an image of the subsurface, the surface measurements are downward continued into the subsurface. This is achieved by applying back propagation operators to the surface data. In this thesis back propagation or inverse wave field extrapolation is investigated. Special attention has been paid to the preservation of the amplitude information in the registered wave field, when the inverse wave field extrapolation is applied.

In the first chapter the macro model is discussed. In order to apply the inverse wave field extrapolation the wave propagation velocity in the subsurface is required. The actual velocity profile of the subsurface entails very detailed variations. However, the wave propagation effects are described sufficiently well if only a sparse model of the subsurface is used. A representation in terms of various layers with simple or constant velocity profiles is sufficient to describe the wave propagation effects. Various modeling experiments are discussed in chapter 1 to confirm this.

For the modeling of the seismic wave propagation the Kirchhoff integral may be used. In chapter 2 the Kirchhoff integral is derived. The frequently used Rayleigh integrals are also discussed. The integrals may be interpreted in terms of the Huygens' principle. This is illustrated in a modeling experiment, in which artifacts, which occur if the Rayleigh integral is used can be explained with the Huygens' principle. Furthermore the role of the Green's function in the Kirchhoff integral is discussed. The Green's function turns out to be a useful

tool for obtaining a Kirchhoff integral best suited for specific acquisition geometries or conditions.

In chapter 3 inverse wave field extrapolation operators are discussed. Application of these operators results in an elimination of wave propagation effects. It is shown that a full Kirchhoff inverse wave field extrapolation operator preserves the amplitude information, for inverse extrapolation from curved interfaces in homogeneous media. For arbitrarily media the amplitude errors are of the order of  $R^2$ , where  $R$  is the reflectivity of the inhomogeneities. However, if the full Kirchhoff integral is applied recursively the transmission effects at layer interfaces is correctly inverted for.

In chapter 4 the redatuming procedure is discussed. This procedure allows for the acquisition level to be brought down into the subsurface. This means that a true zero offset section or shot records may be constructed just over a target area. The high quality zero offset section, which is obtained with these procedure could be used for detailed stratigraphic interpretation.

In chapter 5 the redatuming is applied to both synthetic as well as real data sets. If insufficient surface coverage is available due to limited geophone cable length, the response from the target may become distorted after redatuming. However, if sufficient data is gathered at the surface, the zero offset response from the target zone significantly improves in quality if the acquisition surface is brought down to the target level.

---

## SAMENVATTING

Een van de belangrijkste doelstellingen van seismisch onderzoek is het aantonen van carbonaat reservoirs in de ondergrond. Daartoe worden echo akoestische metingen aan het oppervlak verricht. Om een beeld van de ondergrond te verkrijgen worden onder andere de oppervlaktemetingen de ondergrond in verplaatst. Dit wordt bereikt door een achterwaartse golfveld propagatie operator toe te passen. In deze thesis is deze achterwaartse propagatie of inverse golfveld propagatie operator onderzocht. Een speciaal aandachtsgebied is het behoud van de amplitude informatie tijdens de inverse golfveld propagatie.

In het eerste hoofdstuk wordt het macro model beschouwd. Om de inverse golfveld extrapolatie operator te kunnen toepassen dient de propagatie snelheid in het medium bekend te zijn. Het werkelijke snelheidsprofiel van de ondergrond is zeer gedetailleerd. Echter worden de propagatie eigenschappen van een medium voldoende nauwkeurig beschreven met een minder gedetailleerd snelheidsprofiel. Een representatie in termen van een aantal lagen met eenvoudige of constante snelheidsprofielen is voldoende om de golfpropagatie eigenschappen te beschrijven. Verschillende modelleringsexperimenten, welke in hoofdstuk 1 besproken worden, bevestigen dit.

Voor het modelleren van golfveld propagatie kan de Kirchhoff integraal worden gebruikt. In hoofdstuk 2 wordt deze Kirchhoff integraal afgeleid. De veelvuldig gebruikte Rayleigh integraal wordt ook besproken. Deze integralen kunnen worden geïnterpreteerd in termen van het Huygens' principe. Dit wordt geïllustreerd aan de hand van een modelleringsexperiment, waarin artefacten, welke ontstaan bij het gebruik van de Rayleigh integraal met behulp van het

Huygens' principe kunnen worden verklaard. Verder wordt ook de rol van de functie van Green in de Kirchhoff integraal besproken. Deze functie blijkt bijzonder geschikt te zijn om als instrument te gebruiken, dat toestaat de Kirchhoff integraal in een vorm te krijgen, die het beste bij een bepaalde geometrie past.

In hoofdstuk 3 worden een aantal inverse golfveld extrapolatie operatoren besproken. Het toepassen van zo'n operator resulteert in het wegnemen van golfveld propagatie eigenschappen. Aangetoond wordt dat toepassing van de volledige Kirchhoff integraal voor de inverse golfveld extrapolatie van een gekromde laag in een homogeen medium de amplitude informatie correct behandelt. Voor een inhomogeen medium zijn de amplitude fouten in de orde van meervoudige gereflecteerde golven. Indien echter de volledige Kirchhoff integraal in inhomogene media recursief wordt toegepast, worden transmissie effecten aan laagovergangen op correcte wijze geëlimineerd.

In hoofdstuk 4 wordt de redatuming procedure behandeld. Met behulp van redatuming kan het acquisitie oppervlak het medium in worden verplaatst. Dit betekent, dat een echte zero-offset sectie of schot gathers kunnen worden geconstrueerd vlak boven een interessante laag, in plaats van aan het oppervlak. Een dergelijke hoge kwaliteit zero-offset sectie kan worden gebruikt voor stratigrafische interpretatie.

In hoofdstuk 5 worden toepassing van de redatuming op zowel synthetische als echte gegevens besproken. Indien onvoldoende waarnemingen aan het oppervlak zijn verricht door een te korte geofoon kabel, kan de reflectie van de interessante lagen worden verstoord in de redatuming. Indien echter wel voldoende waarnemingen zijn geregistreerd, kan een zero-offset sectie worden geconstrueerd op de nieuwe datum, die beter van kwaliteit is dan de zero-offset sectie aan het oppervlak.

---

## CURRICULUM VITAE

- 1 maart 1961 : geboren te Zoetermeer
- 1967–1973 : Lager onderwijs
- 1973–1979 : Middelbaar onderwijs (Atheneum)
- 1979–1985 : studie voor natuurkundig ingenieur aan de Technische Universiteit Delft, 4e-jaars onderzoek naar spectral balancing bij de vakgroep seismiek en akoestiek. Het 5e-jaars onderzoek op het gebied van redatuming vond plaats bij dezelfde vakgroep.
- 1984–1985 : Studenten assistent bij het derde geldstroom project PRINCEPS.
- 1985–1987 : Onderzoeker bij de vakgroep seismiek en akoestiek aan de Technische Universiteit Delft bij het PRINCEPS project en het TRITON project.
- 1988-heden : werkzaam bij Jason Geosystems.